

INSTITUT POLYTECHNIQUE DE GRENOBLE

N° attribué par la bibliothèque

THESE

pour obtenir le grade de

DOCTEUR DE L'Institut Polytechnique de Grenoble

Spécialité : « Matériaux, Mécanique, Génie Civil, Electrochimie »

préparée au laboratoire Sciences et Ingénierie des Matériaux et des Procédés

dans le cadre de l'Ecole Doctorale « *Ingénierie - Matériaux, Mécanique, Environnement, Energétique*, »

Procédés, Production »

présentée et soutenue publiquement

par

Pierre LHUISSIER

le 21 Septembre 2009

Random hollow spheres stackings : structure, behaviour and integration into sandwich structures.

Empilements aléatoires de sphères creuses : structure, comportement et intégration dans des structures sandwich.

Directeur de thèse: Yves BRECHET

Co-encadrants: Luc SALVO

Marc FIVEL

JURY

M. André ZAOUI
M. Samuel FOREST
M. Thomas PARDOEN
M. Jacques DESRUES
M. Yves BRECHET
M. Luc SALVO

- , Président
- , Rapporteur
- , Rapporteur
- , Examineur
- , Directeur de thèse
- , Co-encadrant

Remerciements

Une thèse : trois ans de travail, une soutenance et des cheveux en moins? C'est un peu réducteur.

Une thèse, en tout cas à Grenoble au GPM2, c'est d'abord du plaisir au quotidien. Si je commence par les pauses café, on pensera que je n'ai pas travaillé, mais c'est croire que je ne travaille que devant mon PC. Quand j'ai skié, parfois voir même souvent avec des membres du laboratoire que je ne citerai pas, c'est que j'avais besoins de prendre un peu de recul sur mon sujet. Et c'est là déjà un point important à souligner ; on m'a laissé gérer mon étude et j'en suis reconnaissant à mes encadrants. Si vous les voyiez ces encadrants, Yves et Luc, vous vous rendriez compte... Ils ont trop d'idées. Un quart d'heure de réunion et vous avez pour six mois de travail, mais ils m'ont offert la possibilité d'exploiter aussi mes pistes. Ils sont sur une dizaine de fronts différents dans la journée, mais quand j'étais acculé avant une conférence ou en fin de thèse, ils m'ont porté à bout de bras. Vous cherchez un contact, ils l'ont. Vous voulez faire une expérience, ils vous trouvent un laboratoire. Bref, je ne vois pas bien comment j'aurais pu être mieux encadré. Bon, on n'oubliera quand même pas le "*et si on*" de Luc ou le "*improvisation à la Prévert*" de Yves qui annoncent un Hirochima sur votre travail.

Mais les conseils, au GPM2, vous pouvez aussi les trouver dans les autres bureaux. Pour un doctorant, quel bonheur que toutes ces portes ouvertes. A chacun sa spécialité, vous pouvez piocher un peu partout. Un aperçu? Georges vous livre un cours prêt à dispenser (plus ça serait une version audio du cours). Christophe vous donne tous les bons plans ski (et accessoirement un code DEM). Edgar vous fait un café à réveiller les morts. Rémy peut vous vendre des actions COMSOL et Marc du foie gras. Plus fort que l'humeur de Stéphane Guillon sur France Inter vous avez la pause café de Jean-Jacques au GPM2. Grâce à Didier vous connaîtrez tous les rouages du cycle de recyclage du papier. Avec Michel vous goûterez aux délices d'un petit déjeuner en terrasse à Budapest. N'oublions pas enfin les deux "petits jeunes", Seb et Emilie, que j'ai vu plus souvent par terre hors du labo (au ski ou dans un bar) que dans leur bureau.

Mais, malgré ces mines d'informations, vous ne pouvez pas faire une thèse. En effet, il y a bien un moment où vous devrez faire des expériences. Là, plusieurs possibilités : soit vous savez jouer au foot, soit vous êtes un fille. Vous n'êtes pas dans cette situation, va falloir patienter... Bon, d'accord, j'exagère un peu. Il faut dire que je ne les ai pas ménagés Frank et Charles. C'est toujours en urgence que je leur ai mis la main dessus. Et de la même manière, c'est toujours lorsque votre programme est serré que vous vous rendez compte qu'il vous faut une mise à jour de Gnuplot sur tel ou tel dinosaure, et que du coup vous arrivez en courant dans le bureau de Valérie.

Cependant, on vous donne un ongle et bien évidemment vous voulez le bras. Les équipements de votre laboratoire ne vous suffisent pas. Pas de problème! Vous voulez aller au synchrotron, on a des entrées pour vous. Vous souhaitez visiter Lyon, Eric et Jérôme vous proposent leur cave 3 étoiles du MATEIS, et si vous passez le vendredi après-midi vous avez même droit au petit verre de rouge. Vous voulez faire un tour en Suisse, Claudio et Andreas vous accueillent à bras ouverts à Lausanne. Vous avez juste envie de traverser la rue, pas de soucis, Pierre et Pascal se débrouillent pour vous trouver un créneau chez eux, au 3S-R.

Et maintenant que vous avez fait affaire avec pleins de gens, vous avez envie d'en causer. Et comme d'habitude, au GPM2, on vous dit qu'il n'y a pas de soucis. Enfin, disons pas de soucis pour vous. Parce que les soucis c'est plutôt à Claire et à Claude que vous les donnez quand vous leur signalez 3 jours avant que vous partez en conférence et que vous en revenez avec seulement la moitié des justificatifs. Mais non, elles vous disent toujours avec un grand sourire : "*pas de problème, je vais m'arranger*". Incroyable, je ne sais pas comment elles font.

Et puis ils y a tous les "*petits*", les "*insignifiants*" comme on les appelle quand on est docteur : les doctorants ou thésards. Vous en côtoyez un certain nombre pendant votre thèse, et c'est une chance, parce qu'à deux on fait deux fois plus de travail qu'à un, mais on peut se débrouiller pour le présenter deux fois, n'est-ce pas Alex et Jean-Phi? Mais avant toute c'est la SOLIDARITE dans la grande famille des thésards. Quand vous voyez Jennifer sur son tableau de paramètres de 1 mètres 50 de large, Antoine dans son dixième mois de bibliographie, Laurent avec ses plaques de verre ou Greg cherchant la virgule dans son code ABAQUS, vous ne pouvez pas ne pas éprouver de compassion.

Vous n'oubliez pas, lors de vos premières années de thèse, de respecter les plus anciens en leur demandant combien de pages ils ont écrit pendant que vous étiez en montagne. Ju et Jue, Remi sensei, Sylvain et Ludo s'en souviennent sûrement encore.

Arrive, alors le moment de synthétiser vos travaux ; c'est dur. Lire et évaluer cette synthèse ça doit l'être encore plus. Mais il y a des gens qui vous disent : "avec plaisir". Les pauvres, ils ne connaissaient pas mon anglais...

Bref, pour tous ces moments là, et aussi pour beaucoup d'autres (en général avec les "*insignifiants*" ou associés), un grand **MERCI** à tous. Ce ton un peu taquin n'est là que pour rappeler que qui aime bien châtie bien.

Contents

French summary - Résumé de la thèse en Français

Introduction	3
1 Motivations	3
2 Contexte de l'étude	4
3 Démarche	5
Empilement aléatoires de sphères creuses	7
1 Élaboration	7
2 Structure du matériau	8
3 Comportement mécanique	9
Structures sandwich	19
1 Structures étudiées	19
2 Indentation de plaques sandwich	21
3 Flexion de poutres sandwich	24
Conclusions et perspectives	29

General introduction

I Generalities and overview

1	Sandwich structures : interest and properties	39
1.1	Optimization of the weight of a beam with prescribed flexural stiffness	41
1.2	Sandwich beams and plates	42
1.3	Summary on sandwich structures	54
2	Generalities and performances of cellular materials	55
2.1	The contribution of material tailoring on properties	57
2.2	Hollow spheres stacking	60
2.3	Summary on cellular materials	69

II Starting point, investigation strategy and experimental methods

1	Starting point : State of the art	73
2	Strategy of this PhD	75
3	Investigations tools for the hollow sphere materials	77
3.1	Experimental tools	79
3.2	Simulation tools	86

III Hollow spheres stackings

	Hollow spheres stackings : presentation of the samples	93
1	Samples	93

1	Structural characterization	95
1.1	Microscopic scale	97
1.2	Macroscopic scale	101
1.3	Mesoscopic scale	103
2	Discrete Element Method applied to hollow spheres stackings	107
2.1	Interaction laws for the contact between spheres	109
2.2	Macroscopic loading on a random stacking of hollow spheres	116
3	Macroscopic behavior	121
3.1	Uni-axial compressive tests	123
3.2	Uni-axial tensile tests	132
3.3	Multi-axial compressive tests	138
4	Phenomenological modeling	145
4.1	Experiments	147
4.2	Damaging	147
4.3	Densification	151
4.4	Equivalent homogeneous medium by phenomenological approach	152
4.5	Summary on the mesoscopic metamorphism	155

IV Sandwich structures

	Sandwich structure : presentation of the samples	161
1	Analysis of hollow spheres stacking in sandwich structures	165
1.1	Structural characterization	167
1.2	Macroscopic behavior	171
2	Four-point bending	175
2.1	Experiments	177
2.2	Results	177
2.3	Numerical simulations	184
2.4	Comparison of experiments and models	186

3 Behavior under indentation loading	195
3.1 Experiments	197
3.2 Load-indentation responses	197
3.3 Energy absorbed	203

Conclusions and perspectives

Appendices

A Experimental techniques	217
A.1 Digital image correlation	219
A.2 Tensile tests	220
A.3 Bending tests	221
B Sensitivity of the mechanical behaviour of hollow spheres stacking to the strain rate and to the loading-unloading sequences	225
B.1 Strain rate sensitivity	227
B.2 Unloading sequences sensitivity	227
C Discrete Element Method	229
C.1 Discrete Element Method	231
D Sandwich structures with architected core	233

Bibliography	243
---------------------	------------

French summary - Résumé de la thèse en Français

Introduction

Cette partie est un résumé de la thèse en Français. Il présente les motivations, la démarche et les principaux résultats de ces travaux. Il faut cependant garder à l'esprit qu'il s'agit d'une vulgarisation du manuscrit, et que pour toute exploitation rigoureuse de ces travaux, il est impératif d'avoir recours aux résultats présentés dans le manuscrit original.

1 Motivations

Cette thèse traite de l'intégration de matériaux architecturés dans des structures sandwich. Mais pourquoi des matériaux architecturés?

L'optimisation de structures pour des applications mobiles passe par un compromis entre la masse et les propriétés mécaniques requises. En architecturant les matériaux, comme c'est le cas pour les mousses (Figure 1), on diminue leur densité et on peut ainsi espérer augmenter leur performance. L'architecture étudiée dans cette thèse est celle de mousses. Les mousses métalliques sont divisées

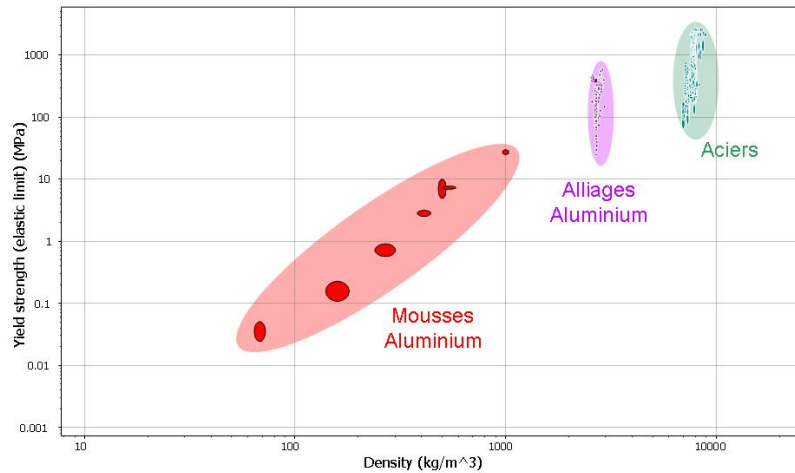


Figure 1: Carte d'Ashby de la limite élastique en fonction de la densité. Alliages d'aluminium massifs et mousses d'aluminium, ainsi que les aciers massifs y sont présentés.

en deux grandes catégories : les mousses à porosité fermée, composées de cellules isolées les unes des autres, et les mousses à porosité ouverte, dont l'unique cellule percole à travers toute la structure. La figure 2 montre une photo de chacun de ces types. La mousse étudiée ici est un peu particulière, il s'agit

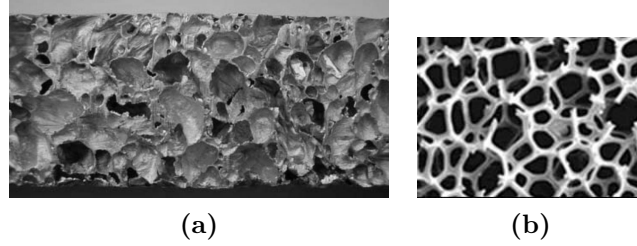


Figure 2: Les deux grandes familles de mousses. **a-** Mousse à porosité fermée. **b-** Mousse à porosité ouverte.

d'empilements de sphères creuses. Ce matériau peut être observé à plusieurs échelles. Tout d'abord à l'échelle de l'échantillon (quelques centimètres) le matériau est considéré homogène, il est caractérisé par des propriétés appelées macroscopiques. A l'échelle de la cellule (quelques millimètres), les sphères creuses ainsi que les cols entre ces sphères sont parfaitement décrits. Cette échelle sera appelée échelle mésoscopique. Enfin, l'échelle que l'on considérera comme microscopique est celle de la paroi (une centaine de micromètres). Elle permet de caractériser la rugosité et la porosité de la paroi

Ce matériau est multifonctionnel et grandement modifiable, lui permettant ainsi de s'adresser à une vaste gamme d'applications. L'aspect cellulaire permet de jouer sur les caractéristiques des cellules élémentaires (les sphères) ainsi que sur leur assemblage (cols, empilement ...), le procédé d'élaboration par métallurgie des poudres offre des libertés sur le choix du matériau constitutif, enfin la topologie, simultanément d'une mousse à porosité ouverte (l'espace entre les sphères) et d'une mousse à porosité fermée (le volume intérieur des sphères), donne accès aux avantages des deux catégories.

Cependant trois points amènent à ne pas utiliser le matériau tel quel :

- Le niveau des contraintes en jeu est faible (environ 10MPa) ce qui rends le matériau très sensible aux sollicitation localisées.
- Au cours de la déformation (laquelle peut être très importante) le module de décharge diminue, traduisant ainsi un endommagement du matériau.
- Le niveau des contraintes est fortement influencé par la densité du matériau, permettant ainsi d'accéder à une grande gamme de propriétés

Aux vues de cette sensibilité à l'endommagement, l'utilisation couplée avec un matériau enveloppe dense, semble nécessaire. La grande capacité de déformation et la grande plage de variation des propriétés sont par contre des avantages important dans la perspective d'utilisation de structures avec un tel cœur¹. Les structures sandwichs, avec des peaux en acier et un cœur d'empilement de sphères creuses, tels que présentés sur la figure 3.

2 Contexte de l'étude

Au début des années 2000, S. Gasser (Elastoplasticité et acoustique, ONERA, 2003) et M.W. Sanders (Elastoplasticité, MIT, 2002) ont étudié le comportement d'empilements réguliers de sphères creuses. Si ce sont les premières études sur ce matériau, on comprends aisément que l'aspect aléatoire des empilements doit être pris en compte, puisque l'utilisation à grande échelle d'empilement réguliers serait

¹La capacité de déformation est très importante pour les aspect d'absorption d'énergie. La variabilité des propriétés du matériau cœur permet l'optimisation de structures et étant la plage d'application du matériau.

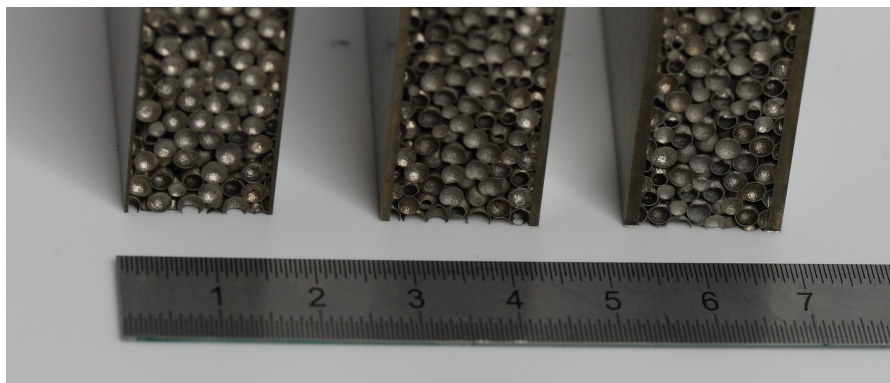


Figure 3: Structures sandwich avec un cœur d'empilement de sphères creuses et des peaux d'acier de diverses épaisseurs.

utopique. Ainsi a vu le jour le projet MAPO (MATériaux POreux), initié par l'ONERA et le CNRS, qui a englobé notamment trois thèses sur les empilements aléatoires de sphères creuses : F. Mamoud (Élasticité et fluage, ONERA, 2007), O. Caty (Fatigue, MATEIS, 2008) et A. Fallet (Initiation de la plasticité et endommagement, Grenoble INP, 2008). Parallèlement à cela, au sein du laboratoire SIMaP, deux doctorants ont étudiés les milieux enchevêtrés : C. Barbier (Modélisation par méthode discrète) et J-P. Masse (Comportement et intégration dans des structures sandwich fines). Les travaux de cette thèse se situe à mi-chemin entre ces deux thématiques : la modélisation d'empilements aléatoires de sphères creuses et leur intégration dans des structures sandwichs.

Il est à noter qu'au commencement de cette thèse, peu de données expérimentales sur les empilements de sphères creuse étaient disponibles. Il n'y avait pas de modèles de comportement pour les grandes déformations et finalement peu de connaissances sur les mécanismes d'endommagement de ce matériau. Enfin aucune données expérimentales exploitables ne pouvaient être trouvées sur les structures sandwich avec un tel cœur.

3 Démarche

La démarche d'étude se divise en deux grandes parties :

- l'étude et la modélisation des empilements aléatoires
- l'étude et le modélisation de structures sandwich

Chacune de ses parties repose sur des approches expérimentales et des modèles analytiques et numériques. Dans la première partie on cherche à relier les paramètres élémentaires de la structure du matériau (taille de col, épaisseur de coque ...) au comportement macroscopique de celui-ci. L'approche expérimentale est menée à plusieurs échelles : observation de la structure élémentaire, étude des mécanismes de déformation basée sur des essais in situ en tomographe aux rayons X, essais mécaniques macroscopiques. Sur le base de ces données, un modèle phénoménologique propose un lien entre le comportement macroscopique et les mécanismes d'endommagement. Les prédictions reste cependant limitées aux paramètres structuraux des empilements testés. Ainsi une seconde approche basée sur un couplage d'éléments finis et de méthode des éléments discrets est présentées. Elle permet d'étudier l'influence de tous les paramètres structuraux.

Dans la seconde partie, des structures sandwich, avec des peaux en acier et un cœur d'empilements de sphères creuses, sont étudiées. Les modèles analytiques classiques, et des simulations par éléments finis sont utilisées en complément d'expériences aussi bien pour la flexion 4-points de poutre que pour l'indentation de plaques.

Empilement aléatoires de sphères creuses

1 Élaboration

Les empilements de sphères creuses utilisés dans cette thèse sont élaborés par métallurgie des poudres (procédé IFAM, figure 1). Des billes de polystyrène expansé passent dans un lit fluidisé de poudre

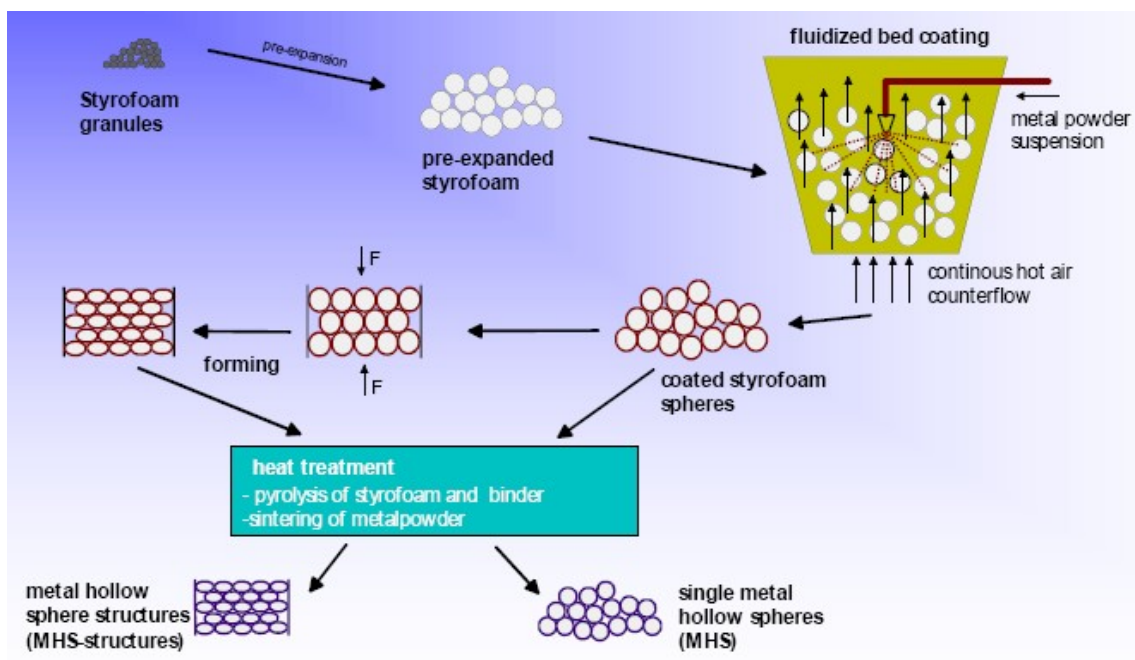


Figure 1: Procédés IFAM d'élaboration des empilements de sphères creuses.

métallique et de liant organique. Les sphères au vert obtenues sont empilées et compactées par procédé mécanique. Des cycles thermiques assurent alors de le dégazage du polystyrène et le frittage simultané des coques et des cols entre les particules. Grâce au procédé d'élaboration, il est envisageable de jouer quasiment indépendamment sur tous les paramètres structuraux : diamètre des sphères, taille de cols, épaisseur de coque, nombre de contacts... Il est à noter que tous les échantillons utilisés lors de cette thèse ont été élaborés et fournis par la compagnie PLANSEE (Reute, Autriche) et était constitués d'acier inoxydable 314 (norme AISI).

2 Structure du matériau

Les empilements ont été étudiés par tomographie aux rayons X (synchrotron ESRF ligne ID19 et tomographe de laboratoire Phénix à l'INSA Lyon) couplée à de l'analyse d'images 3D. Les différents paramètres structuraux ont été mesurés pour les échantillons disponibles. Le tableau 1 les récapitule sommairement. Le seul paramètre structurant variant significativement entre les échantillons est

		A	B	C
Rayon des sphères	R (mm)	1.31	1.31	1.31
Rayon des cols	a (μm)	418	400	388
Épaisseur des coque	t (μm)	56	72	88
Densité relative	ρ^*/ρ_s	0.070	0.092	0.113
Nombre de coordination	z	7.9	8.2	7.6

Table 1: Paramètres structuraux moyens des échantillons étudiés.

l'épaisseur de paroi, laquelle impacte directement la densité.

L'observation des parois par microscopie optique permet de quantifier leur porosité (environ 4%) et leur rugosité (amplitude d'environ $20\mu m$). La figure 2 illustre ces irrégularités. La mesure des cols basée

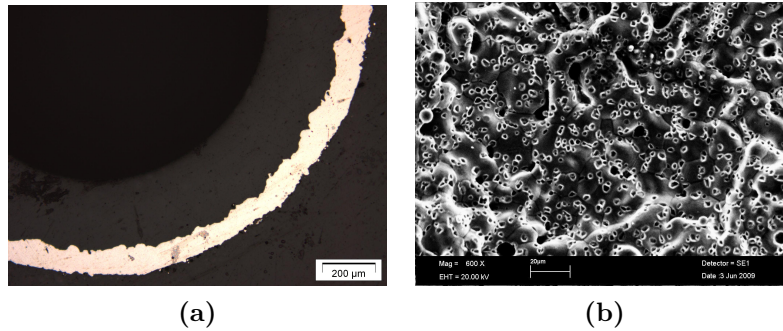


Figure 2: Micrographie optique illustrant la porosité des parois (a) et leur rugosité (a).

sur l'observation par tomographie aux rayons X surestime l'aire de contact réel entre les sphères. Des observations par microscope électronique à balayage montrent qu'en périphérie des cols, le contact est limité à quelques micro-piliers (figure 3). Les mesures des cols sont donc surestimées d'environ 30%

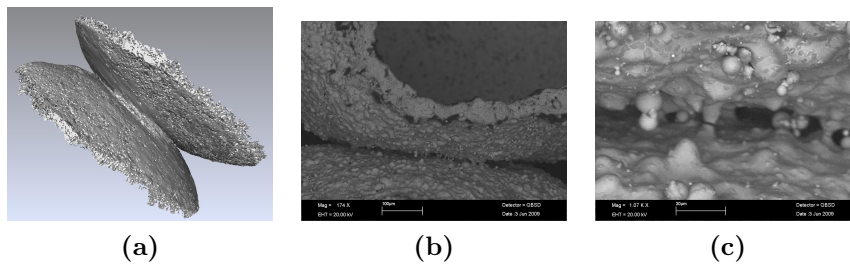


Figure 3: Comparaison des observations d'un col par tomographie aux rayons X (a) et par microscope électronique à balayage (a- grossissement $x174$, b- grossissement $x1070$) .

3 Comportement mécanique

3.1 Compression uniaxiale

Les essais mécaniques menés en compression uni axiale font apparaître des champs de déformations homogènes dans le matériaux (figure 4), et montrent la capacité du matériau à endurer de très forte déformations. Ces observations se traduisent sur les courbes contraintes-déformations par une faible

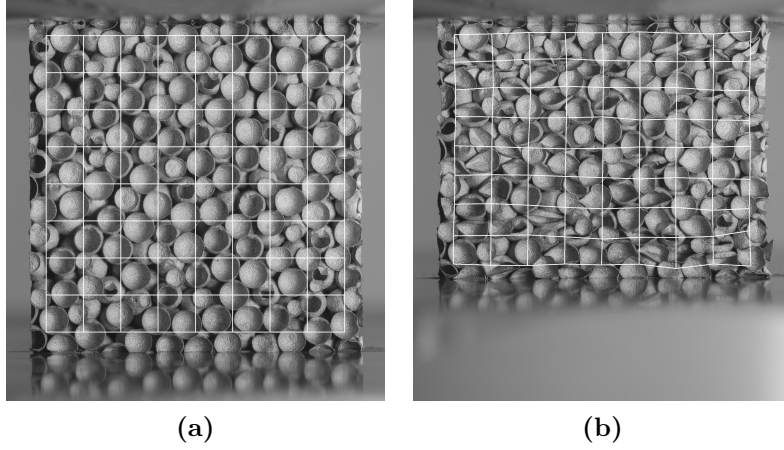


Figure 4: Compression uni axiale d'un cube d'empilement de sphères creuses. La grille obtenue par corrélation d'image 2D rend compte de l'homogénéité de la déformation.

dispersion et par un écrouissage faible et régulier (figure 5a). On retrouve l'allure des courbes de compressions classiques de mousses caractérisées par une zone élastique, puis par un long plateau plastique suivi par un fort accroissement de la contrainte qui correspond à ce qu'on appelle la densification. Ces trois domaines se retrouvent sur les courbes d'évolution du module de décharge avec la déformation (figure 5b). Lors des premiers pourcents de déformations on observe une forte diminution du module de décharge, ce qui traduit un endommagement du matériau. Puis, sur une large plage de déformation correspondant au plateau de contrainte, le module de décharge reste constant, avant d'augmenter significativement lors de la densification. Lorsque la densité initiale de la mousse augmente, les niveaux de

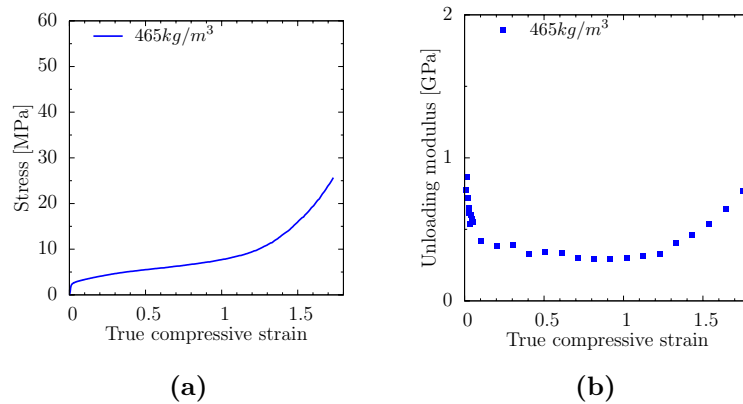


Figure 5: Compression uni axiale d'un cube d'empilement de sphères creuses. **a-** Courbe contrainte-déformation. **b-** Évolution du module de décharge avec la déformation.

contraintes et de modules sont aussi augmentés (figure 6). Par contre les déformations de transitions

entre les différentes phases précédemment citées ne sont pas affectées par la densité initiale du matériau. On peut modéliser l'évolution d'une propriété P de la mousse par une loi puissance de la densité initiale (équation 1) dont l'exposant varie entre 1.2 et 2.1 selon la propriété concernée.

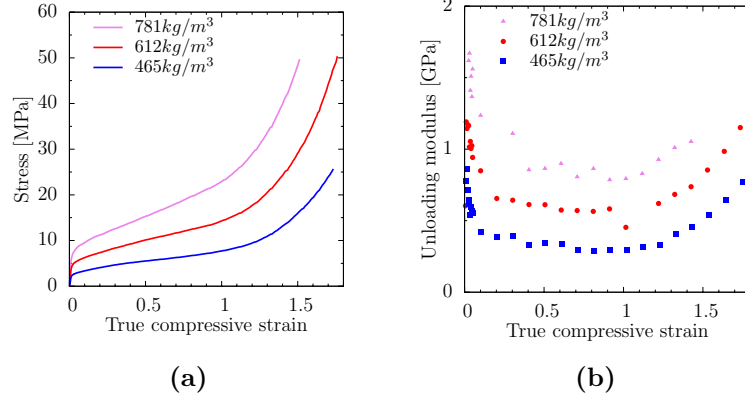


Figure 6: Influence de la densité initiale de la mousse. **a-** Courbe contrainte-déformation. **b-** Évolution du module de décharge avec la déformation.

$$P = P_0 \rho^n \quad (1)$$

3.2 Mécanismes locaux de déformation

La tomographie aux rayons X, couplée à de l'analyse d'images 3D, permet la compréhension des mécanismes locaux liés à l'endommagement initial ou à la densification.

3.2.1 Endommagement

Les observations sur des essais in situ montrent qu'un critère pertinent pour qualifier un col comme endommagé est le rapprochement des centres de gravité des deux sphères en contact (figure 7a). La fraction f des cols endommagés peut être décrite par une loi de type Weibull de la déformation (équation 2, figure 7b).

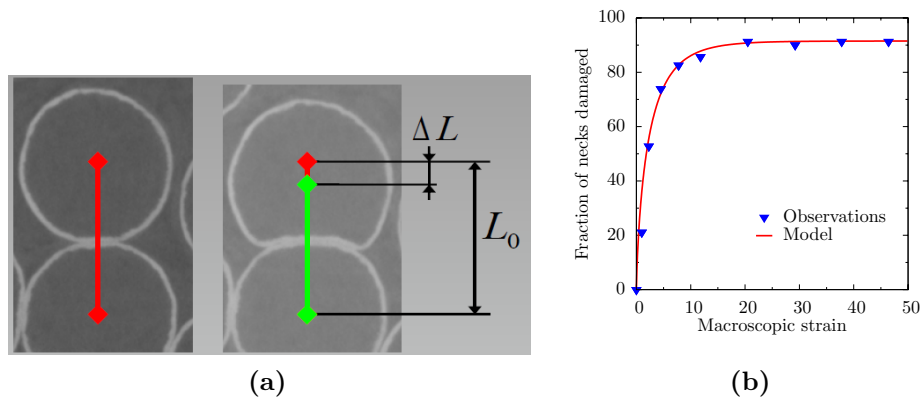


Figure 7: **a-** Critère de qualification d'un col endommagé. **b-** Quantification de la fraction de cols endommagés avec la déformation.

$$f(\varepsilon) = 0.9 \left[1 - e^{\left(\frac{\varepsilon}{\varepsilon_u}\right)^{0.75}} \right] \quad (2)$$

On observe que la majorité des cols sont endommagés dès les premiers pourcents de déformation, traduisant ainsi l'homogénéité du comportement du matériau.

3.2.2 Densification

L'occlusion de la porosité ouverte (l'espace entre les sphères) peut être liée au plateau de contrainte, alors que la densification correspond à l'occlusion de la porosité fermée (le volume intérieur des sphères). En effet ce dernier est très peu impacté par le changement de forme des cellules lors de l'occlusion de la porosité ouverte. La figure 8 présente l'état de la mousse à plusieurs stades de déformation, alors que la figure 9 présente une coupe du matériau, facilitant ainsi la visualisation des mécanismes mentionnés.

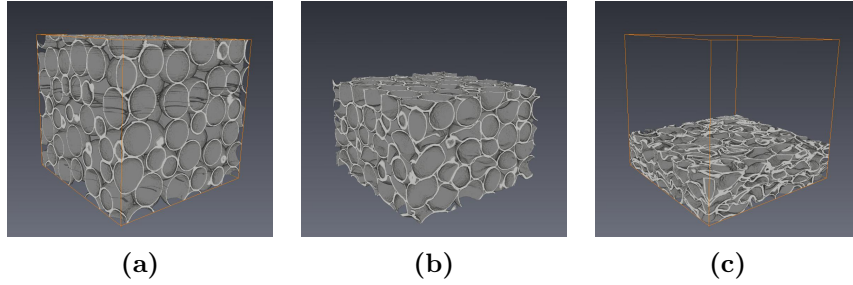


Figure 8: *Reconstruction numérique d'un cube sollicité en compression uni axiale, observé en tomographe RX.*

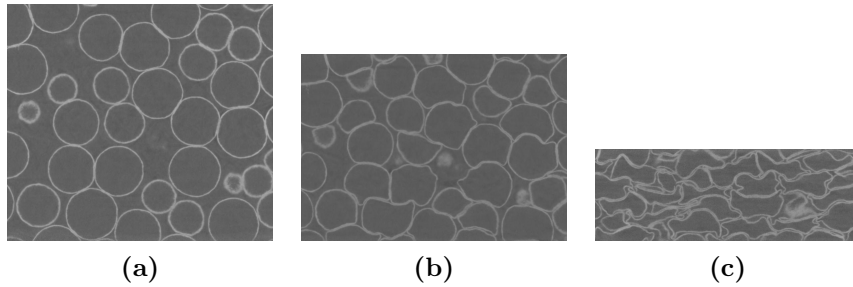


Figure 9: *Section d'un cube sollicité en compression uni axiale, observé en tomographe RX.*

3.3 Modèle phénoménologique

Un modèle phénoménologique est établi. Il intègre trois phases (figure 10) : une phase saine (le matériau avant sollicitation), une phase endommagée (la fraction du matériau dont les cols sont endommagés) et une phase densifiée (là où la porosité ouverte a disparue). Les transitions entre les phases sont décrites par des lois de Weibull telles que celle obtenue pour la quantification de la fraction de cols endommagés. Les degrés de liberté restant (propriétés de phases endommagées et densifiées) sont ajustés sur un essai de compression (figure 11). L'influence de la densité initiale du matériau est prise en compte par les lois puissance précédemment proposées. Le modèle décrit alors correctement le comportement de la mousse, aussi bien pour l'évolution de la contrainte que du module de décharge, avec la déformation (figure 12).

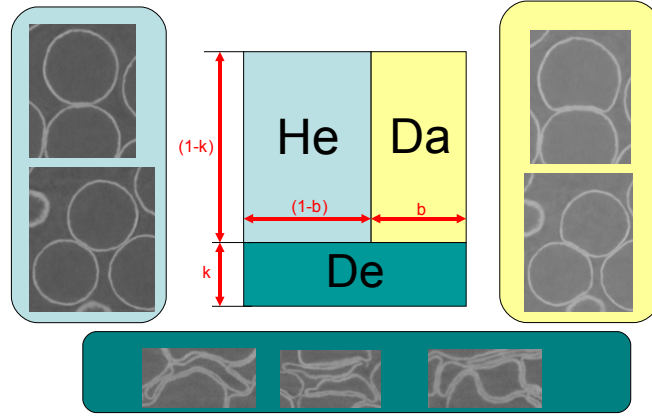


Figure 10: Décomposition du matériau en 3 phases. Deux phases saines et endommagées en parallèles, placées en série avec une phase dite densifiée.

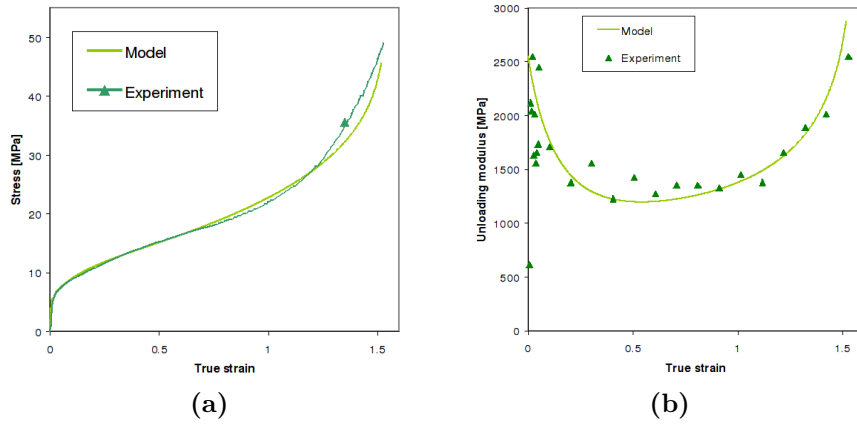


Figure 11: Réponse du modèle pour la courbe de contrainte-déformation (a) et pour l'évolution du module de décharge avec la déformation (b).

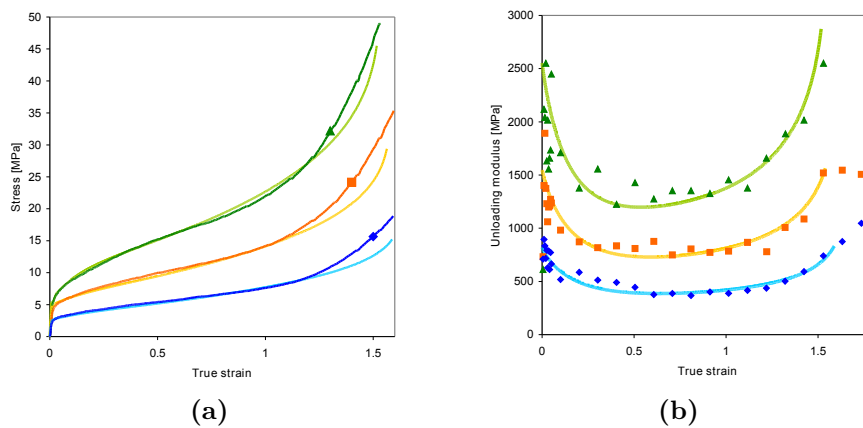


Figure 12: Comparaison du modèle aux expériences

3.4 Méthode des Eléments Discrets : DEM

Si le modèle précédent permet de prédire le comportement d'un empilement de sphère creuse dont la densité initiale se trouve dans une gamme pertinente il ne permet pas d'estimer l'influence d'autres

paramètres structuraux (tailles de cols, nombre de coordination ...) que ceux des empilements étudiés. C'est pourquoi une seconde approche de modélisation est proposée, basée sur un couplage entre des modélisations Eléments Finis et une Méthode des Éléments Discrets.

3.4.1 Principe de la méthode

L'objectif de la méthode est de simuler un empilement de plusieurs milliers de sphères (Figure 13a) grâce à une discrétisation en particules dont les interactions sont déterminées par des lois de contact. La finesse du comportement est contenue dans ces lois de contacts. Celles-ci sont déterminées par simulations Éléments Finis pour simplement *deux demi-sphères liées par un col* (Figure 13b). Les

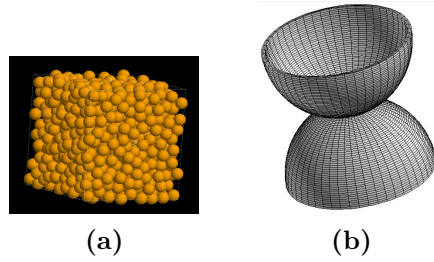


Figure 13: Les deux échelles de la méthode couplée DEM-EF.

lois sont décomposées en sollicitations élémentaires. Le principe de superposition des sollicitations est assumé (malgré les non linéarités des lois de contact). La figure 14 présente les sollicitations élémentaires considérées : compression, traction, cisaillement, roulement et pivotement. Un faisceau de réponses est

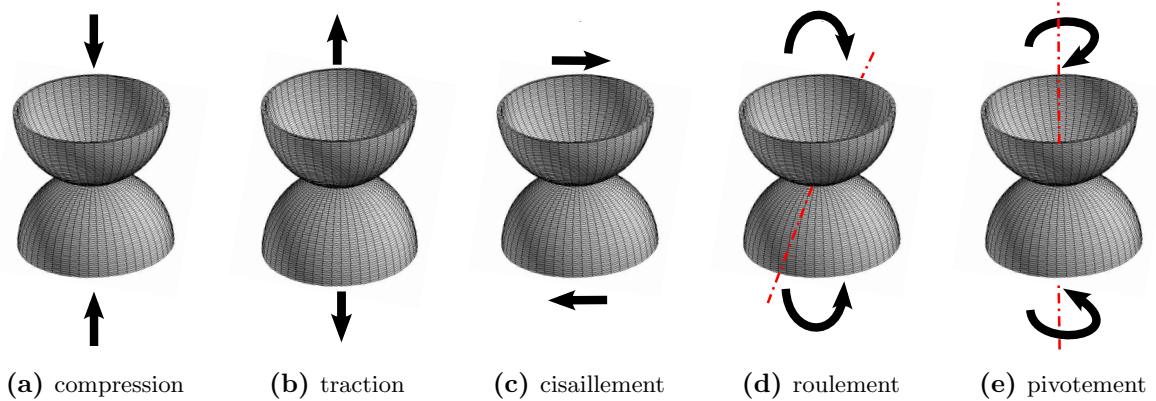


Figure 14: Sollicitations élémentaires entre deux sphères.

obtenu pour chacune des sollicitations élémentaires pour des épaisseurs de coques et des tailles de cols variés (Figure 15a). Les réponses sont ajustées sur un modèle de comportement paramétrique des paramètres structuraux (taille de col et épaisseur de coque). Par la suite, ces lois de contact sont introduites dans le code DEM. On peut alors observer l'influence des paramètres structuraux sur la réponse macroscopique d'un empilement (Figure 15b).

3.4.2 Limitations de la méthode

Telle que présentée précédemment, cette méthode a été appliquée par Fallet [Fallet, 2008] grâce au code DEM DP3D [Martin *et al.*, 2003]. Cependant, dans son état la méthode était très limitée : elle ne

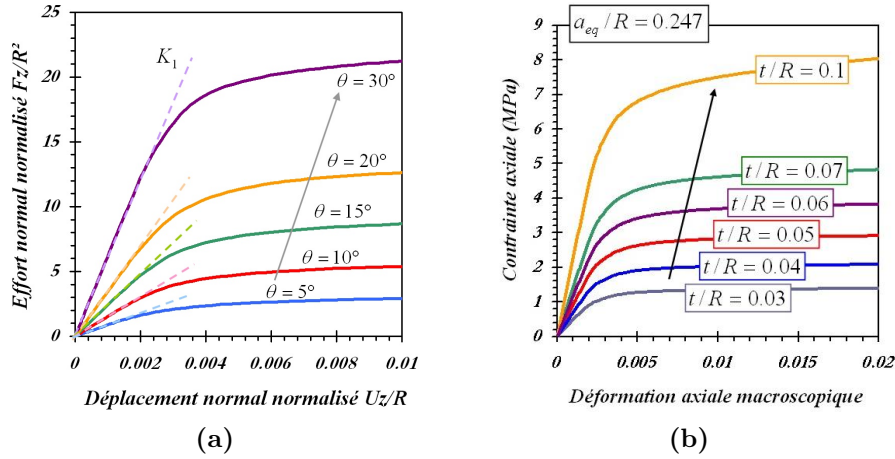


Figure 15: Faisceau de réponses élémentaires.

s'attachait qu'à la prédiction du niveau de contrainte dans les 2 premiers pourcents de déformation. Les modules ne pouvaient être évalués qu'au travers de la pente de charge.

3.4.3 Extension de la méthode

Le champ de prédiction de la méthode a été étendu, permettant par la même de confirmer les choix de modélisation grâce à des confrontations à l'expérience plus convaincants.

La plage des déformations accessibles a été étendue. Les lois de contacts ont donc été prédites jusqu'à environ 15% de déformation et des lois plus sophistiquées ont été utilisées pour les décrire correctement sur cette plage de déformation (Figure 16a). Les lois de contacts entre deux sphères non liées par un col²

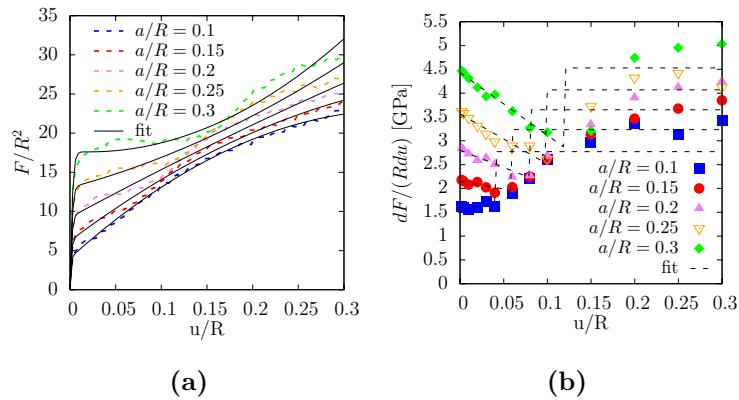


Figure 16: Faisceau de lois de contacts élémentaires (a) et de modules de décharges du contact (b).

ont aussi été évaluées afin de prendre en compte les nouveaux contacts générés lors de la déformation de l'empilement.

Le module de décharge des contacts a été évalué au cours de la déformation et représenté par des lois paramétriques (figure 16b), afin d'avoir accès à l'évolution du module de décharge de l'empilement au cours de la déformation.

Enfin l'influence du choix des conditions aux limites utilisées pour l'évaluation des lois de contact a

²Deux sphères dont la mise en contact est postérieure à l'élaboration.

été estimée, notamment dans le cas du cisaillement. Il a été montré que le passage de contraintes en déplacement à des contraintes en réaction globale avait un impact très fort sur la réponse pour cette sollicitation (figure 17). Dans un premier temps, la réponse la plus rigidifiante à été retenue (pour rester en accord avec les modélisation de Fallet).

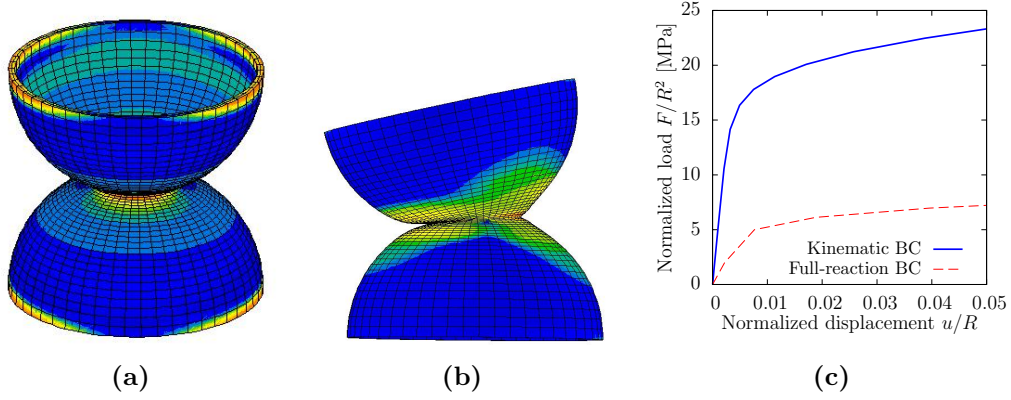


Figure 17: Comparaison des réponses (c) pour des conditions aux limites en déplacements (a) et en effort (b).

3.4.4 Confrontation modèles-expériences

Les résultats des essais de compressions uni axiales sont comparés aux modèles bruts. Dans ces conditions les modèles surestiment largement les niveaux de contraintes en jeu (figure 18a). Mais d'après ce qui précède, il est légitime de corriger la taille des cols (jusqu'ici surestimés d'environ 20%) et de choisir une loi de contact en cisaillement moins rigide (condition aux limites en effort). Sous réserve de ces corrections, les courbes contraintes-déformations des expériences sont correctement décrites par le modèle, du moins pour les deux mousses de forte densité (figure 18b). Les modèles corrigés prédis-

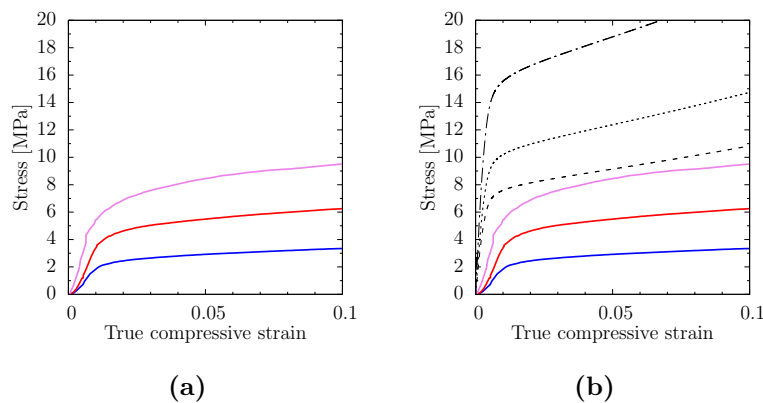


Figure 18: Comparaison des expériences (traits pleins en couleurs) et des modèles (traits pointillés noirs) sans correction (a) et avec correction de la taille de col et de la loi de cisaillement (b).

ent aussi correctement les modules de décharges, que ce soit les valeurs des modules ou l'évolution de ceux-ci (figure 0.3.4.4). Sachant que ces modélisations ne tiennent pas compte de l'endommagement du matériau constitutif, on peut affirmer que la décroissance du module de décharge est en partie due à un aspect géométrique. Cependant l'endommagement du matériau constitutif devra être pris en compte

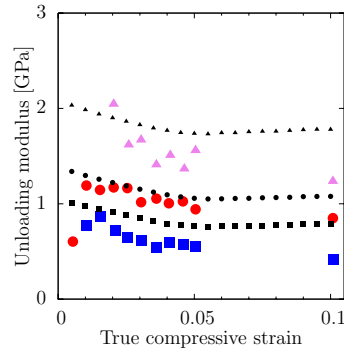


Figure 19: Comparaison des expériences (gros motifs en couleurs) et des modèles (petits motifs noirs) avec correction de la taille de col et de la loi de cisaillement.

pour décrire complètement la décroissance du module de décharge.

Ces modèles permettent donc de prédire le comportement des empilements de sphères creuses en fonction des paramètres structuraux (taille de col, épaisseur de coque, nombre de coordination ...) en compression uni axiale. Cependant l'endommagement de structures sandwich engendre en général des états de contraintes du cœur qui ne sont pas simples. La prédiction du comportement de telles structures passe par une connaissance du comportement du matériau cœur pour des états de chargements complexes.

3.5 Chargements multi axiaux

Deux méthodes expérimentales ont été utilisées pour étudier le comportement des mousses sous chargement multi axial.

La première méthode, appelée ici “3 axes” est basée sur un chargement par plateaux asservis d'un cube entaillé selon ses arêtes (figure 0.3.5). Ces expériences ont été réalisées à l'Ecole Polytechnique Fédérale de Lausanne sur des volumes utiles cubiques de respectivement 10 et 13 mm de côté. La

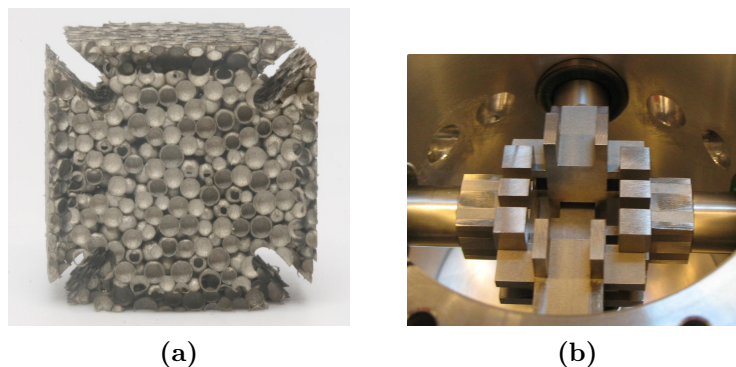


Figure 20: Échantillon et plateaux pour l'essai “3 axes”.

seconde méthode, dite ici “en milieu confiné”, est issue du monde de la mécanique des roches. Un échantillon cylindrique enveloppé d'une ou plusieurs gaines en néoprène est inséré dans une enceinte. Une pression de confinement est imposée, tandis d'un piston vient appliquer un déviateur selon l'axe du cylindre (figure 0.3.5). Cette technique, utilisée au laboratoire 3S-R à Grenoble, est applicable (et à été appliquée) dans un tomographe. Les échantillons avait un diamètre de 10mm pour une longueur de

20mm. Chacune de ces technique a des avantages et des inconvénients, mais il est important de noter

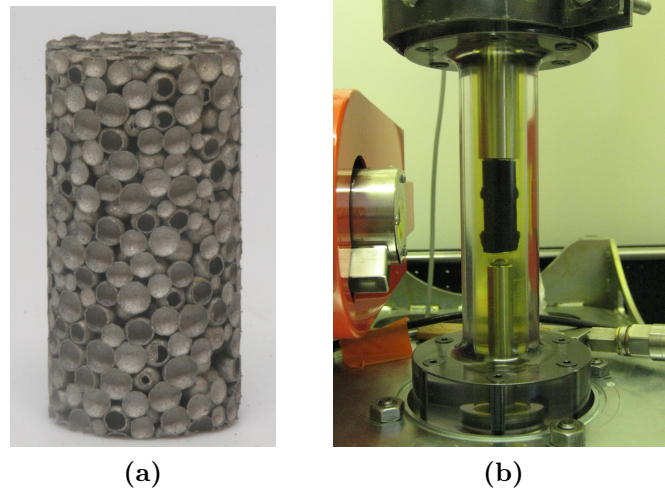


Figure 21: Échantillon et cellule pour l'essai “en milieu confiné”.

que dans le cas présent la taille caractéristique des échantillons (10 mm) était faible au regard de la taille des cellules (1.3 mm de diamètre dans le cas le plus favorable).

La méthode “3 axes” permet de retrouver l'influence de la densité sur la surface de plasticité. Cependant ces expériences ne permettent pas de déterminer le critère de plasticité le plus pertinent. En effet, compte tenu du nombre de points et de la dispersion, un critère elliptique tel que classiquement utilisé pour les mousses (figure 22a) peut aussi bien être choisit qu'un critère de type Drucker-Prager (figure 22b). Le faible nombre de points obtenus “en milieu confiné” ne permet pas de trancher.

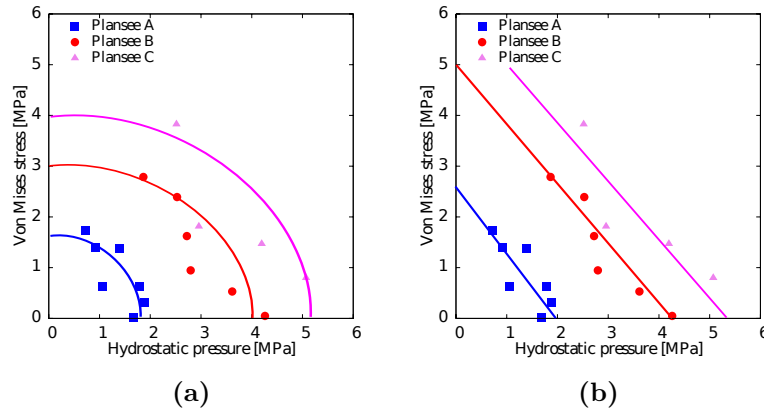


Figure 22: Surfaces de plasticités selon la densité initiale des mousses. Les critères elliptiques (a) et de Drucker-Prager (b) sont tracés.

La comparaison des essais multi axiaux et des modélisations éléments discrets montrent que ces modèles sont capables de décrire la forme de la surface de plasticité des empilements de sphères creuses. Le niveau de contrainte pourrait être mieux décrit, mais compte tenu du volume des échantillons testés, et de la dispersion qui en découle, cet ajustement semble inapproprié (figure 0.3.5).

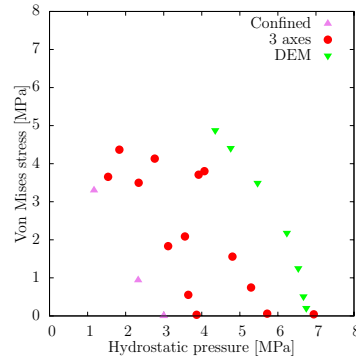


Figure 23: Comparaison des essais “3 axes” et “en milieu confiné” avec le modèle éléments discrets.

Conclusion

Dans cette partie nous avons rassemblé une grande quantité de données expérimentales aussi bien en compression et en traction uni axiale qu'en compression multi axiale, et ceci en ayant fait varié la densité initiale des mousses ainsi que les volumes sollicités. Là où aucun modèle en grande déformation n'existait, nous avons proposé un modèle phénoménologique basé sur trois phases. Une modélisation couplée DEM-EF nous donne accès aux paramètres d'entrée de ce modèle avec l'évolution des paramètres structuraux du matériau. Des pistes de compréhension des mécanismes d'endommagement du matériau ont été mises en avant grâce à la comparaison des modèles et des expériences. Enfin, s'il n'a pas été possible de choisir le critère de plasticité, il a été montré que la méthode de modélisation DEM-EF permettait de reproduire le comportement du matériau sous sollicitations complexes.

Structures sandwich

1 Structures étudiées

1.1 Jeu d'échantillons

Les structures sandwich étudiées ont été élaborées et fournies par PLANSEE (Reutte, Autriche). Elles consistent en des peaux en acier inoxydable 314 (norme AISI) brasées sur un cœur d'empilement de sphères creuses de densité 600kg/m^3 . Le jeu d'échantillons est constitué de 12 structures avec 3 épaisseurs de peau (t) de 0.4, 1.0 et 1.5mm, et de 4 épaisseurs de cœur (c) de 14, 18, 24 et 28 mm. La figure 1 présente une micrographie de l'interface peau/cœur ainsi qu'un aperçu du jeu d'échantillons.

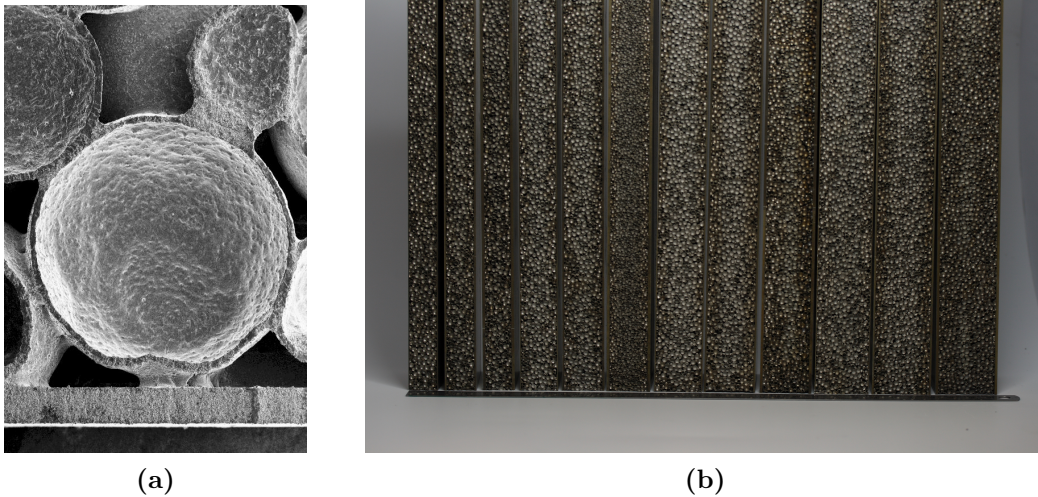


Figure 1: *a-Micrographie Électronique à Balayage de l'interface entre la peau et le cœur. b-Présentation du jeu de structures sandwich étudiées.*

1.2 Propriétés du cœur

Lors du procédé d'intégration dans les structures sandwichs, les empilements de sphères creuses sont fortement modifiés. Une analyse du matériau cœur, après son intégration, montre que les parois poreuses (figure 2a) sont devenues denses (figure 2d), que les surfaces de contacts entre sphères, initialement faibles (figure 2b), sont considérablement élargies (figure 2e), et enfin que la structure initialement saine (figure 2c) présente des parois ou des cols rompus *avant toute sollicitation* (figure 2f). Les observations par tomographie aux rayons X montrent que l'endommagement du matériau dépend fortement de l'épaisseur du cœur. Lorsque l'épaisseur de cœur est faible le matériau semble peu endommagé (figure 3a), alors que pour les cœurs épais les sphères sont indentées et les parois partiellement déchirées

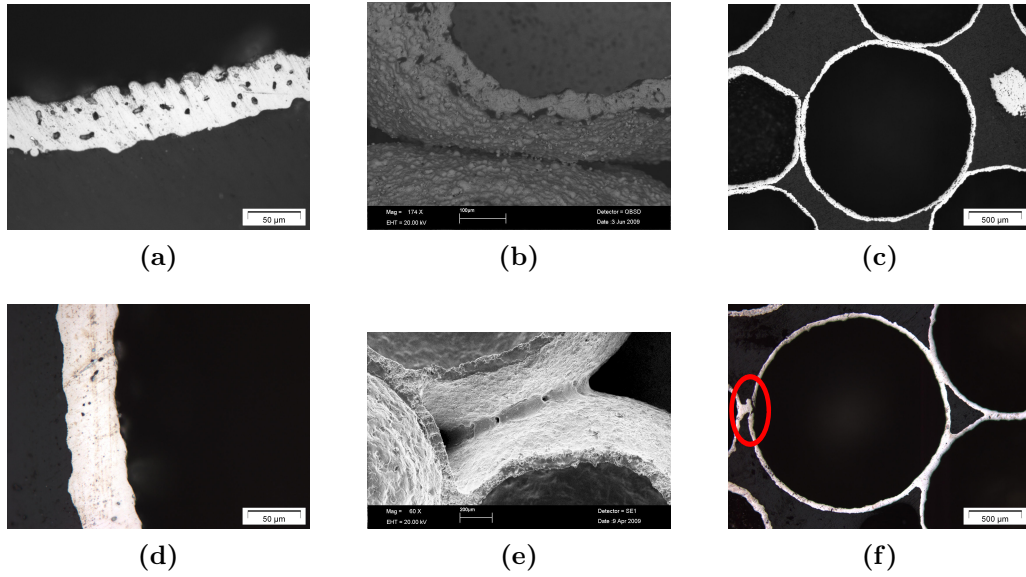


Figure 2: Matériau cœur avant intégration (a,b,c) et après intégration (d,e,f) dans les structures sandwich.

avant toute sollicitation (figure 3b). Cette influence de l'épaisseur du cœur se retrouve lors d'essais de compression du matériau cœur (prélevé dans des structures sandwich d'épaisseur de cœur variables). La figure 3c fait apparaître l'influence de l'épaisseur du cœur sur les propriétés mécaniques du matériau ayant subi le procédé d'intégration dans une structure. Le comportement est donc variable et diffère fortement du comportement du matériau avant intégration. Les modifications engendrées par le

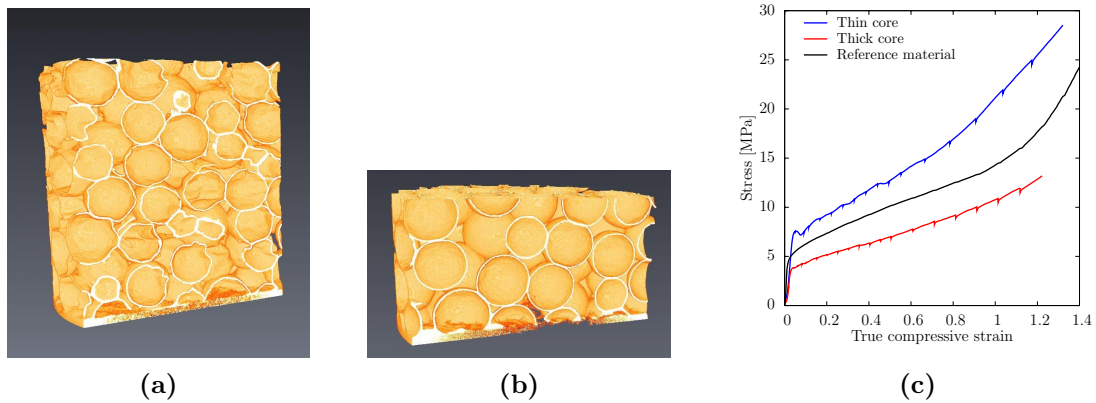


Figure 3: a,b- Observation par tomographie R-X de structures sandwich d'épaisseur de cœur fine (a) et épaisse (b). c- Courbes contrainte-déformation d'essais de compression sur le matériau cœur issu de sandwiches d'épaisseur de cœur variables et comparaison au comportement du matériau n'ayant pas subi de procédé d'intégration dans une structure.

procédé d'intégration sont trop importantes pour permettre l'utilisation des modèles de comportement des empilements de sphères creuses développés dans la première partie. Les analyses sur les structures sandwich seront donc basées sur les propriétés du matériau cœur issues de l'expérience. Le comportement est choisi bilinéaire et sera supposé dépendre de l'épaisseur du cœur (figure 4).

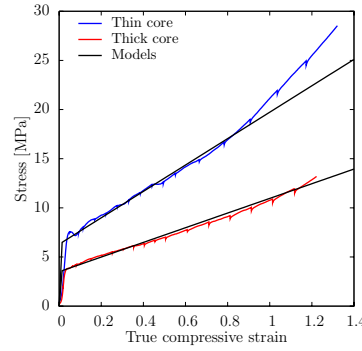


Figure 4: *Modélisation bilinéaire du comportement en compression du matériau cœur selon l'épaisseur du cœur.*

2 Indentation de plaques sandwich

2.1 Expériences

Des essais d'indentation sur des plaques sandwichs ont été menés avec des indents sphériques de rayons 8 et 15 mm. La face des plaques opposée à l'indent reposait sur un support sur toute sa surface. Les essais ont été menés à une faible vitesse de chargement (0.05mm/s) jusqu'à une charge maximale de 19kN (figure 5). L'aire de la surface indentée a été évaluée. Parallèlement, des simulations éléments

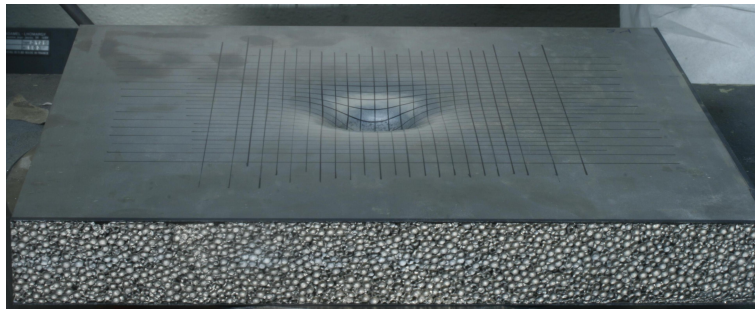


Figure 5: *Essais d'indentation d'une plaque sandwich.*

finis des structures ont été conduites. Une modélisation 2D axi-symétrique a été choisie (figure 6). Une loi de comportement élastoplastique avec un critère de Von Mises et une loi d'écrouissage d'Hollomon a été attribuée aux peaux. Une loi de comportement élastoplastique de milieu poreux avec un critère elliptique et un écrouissage linéaire a été attribué au cœur.

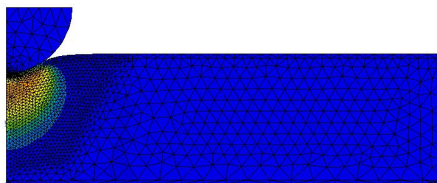


Figure 6: *Modélisation par éléments finis 2D axi-symétrique d'un essai d'indentation d'une plaque sandwich.*

2.2 Influence de l'épaisseur du cœur

Les essais ont fait apparaître que pour une même épaisseur de peau, la réponse dépendait de l'épaisseur du cœur (figure 7). Des simulations éléments finis ont été utilisées afin de découpler l'effet d'épaisseur

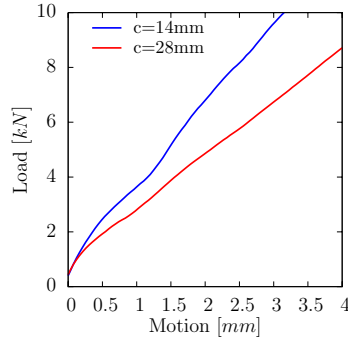


Figure 7: Influence de l'épaisseur du cœur sur la réponse à l'indentation de plaques sandwich.

de cœur de l'effet de propriété mécanique du cœur (figure 8). Il a été montré que les propriétés du cœur

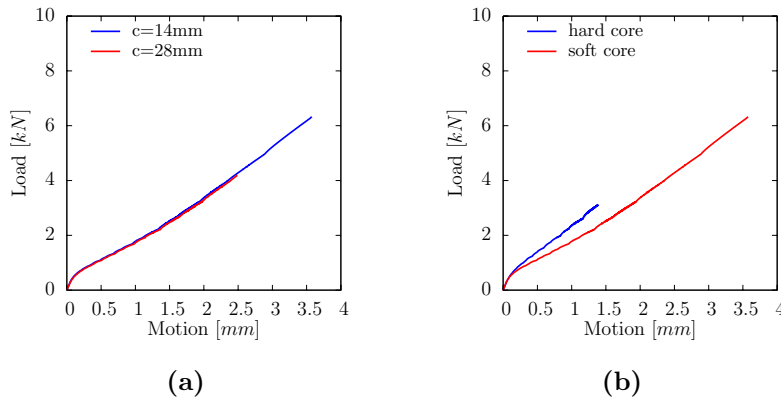


Figure 8: Simulations par éléments finis de l'indentation de plaques sandwich. **a-** A propriétés mécaniques du cœur équivalentes, deux structures avec des cœurs d'épaisseurs variables ont la même réponse à l'indentation. **b-** A épaisseur de cœur identique, des propriétés mécaniques de cœur variable entraînent une modification de la réponse du même ordre de grandeur que celle observée sur les expériences.

étaient responsables de ces variations et que dans la gamme de dimensions considérées, l'épaisseur de cœur avait une influence négligeable.

2.3 Influence de l'épaisseur de peau et de la taille de l'indent

Pour des structures avec des peaux épaisses (supérieures ou égales à 1 mm) on observe une diminution de la rigidité apparente de la structure quand la taille de l'indent diminue (figure 9). Quand l'épaisseur de peau est faible (0.4 mm) le même comportement est observé pour les faibles charges. Quand la charge augmente et que l'indent est petit le peau supérieure est perforée, et de par la même la réaction de la structure chute drastiquement (figure 10). Cette transition est importante si l'on s'intéresse à l'énergie que peut absorber la structure pour une charge maximale imposée. Si le cahier des charges nous impose un indent de 15 mm de rayon et une charge maximale de 19 kN, l'énergie maximale est

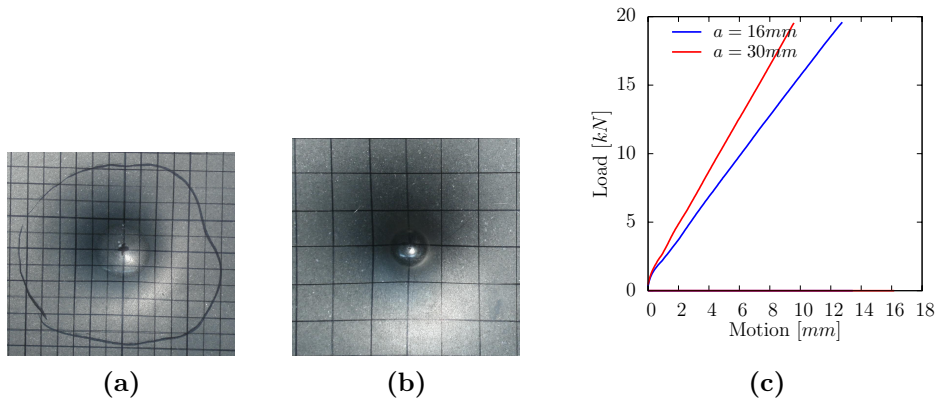


Figure 9: Influence de la taille de l'indent sur des sandwichs à peau épaisse (épaisseur supérieure à 1 mm) sur la réponse à l'indentation de plaques sandwich.

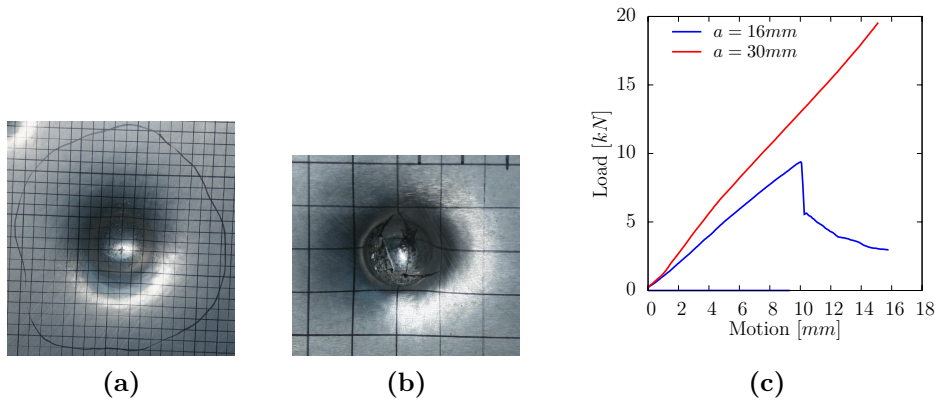


Figure 10: Influence de la taille de l'indent sur des sandwichs à peau fine (épaisseur de 0.4 mm) sur la réponse à l'indentation de plaques sandwich.

absorbée par les structures à faible épaisseur de peau (figure 11), qui sont par la même les structures les plus légères. Si le cahier des charges impose un rayon d'indent de 8 mm, on se rends alors compte que

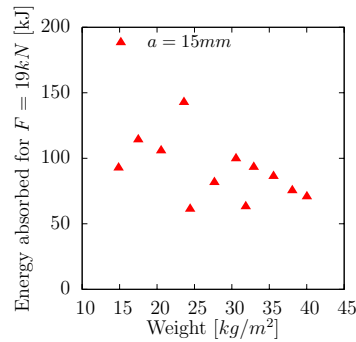


Figure 11: Énergie absorbé par les plaques sandwich en fonction de leur masse pour une charge maximale de 19 kN et un rayon d'indent de 15 mm.

les structures que se ne sont plus les mêmes structures qui absorbent le plus d'énergie (figure 12). Les structures avec des peaux fines ont en effet été perforée. Ainsi dans l'optique d'absorber le maximum

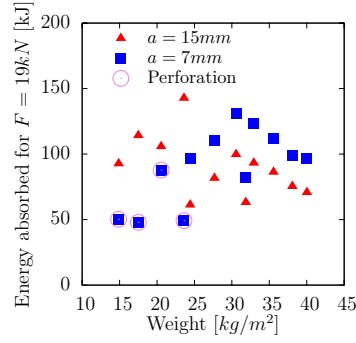


Figure 12: Énergie absorbé par les plaques sandwich en fonction de leur masse pour une charge maximale de 19 kN et des rayons d'indent de 15 mm et 8 mm.

d'énergie pour une charge maximale imposée, il faut choisir la structure avec les peaux les plus fines qui permettent d'éviter la perforation pour la taille d'indenteurescrit.

Les structures lors de leur emploi sont cependant rarement en appuis sur toute leur face inférieure. Une configuration plus réaliste de l'utilisation de ces structures correspond à des sollicitations en flexion.

3 Flexion de poutres sandwich

3.1 Expériences

Des essais de flexion 4-point sur des poutres sandwichs de largeur 50 mm ont été réalisés. Les conditions aux limites étaient des appuis simples sur des rouleaux de 10 mm de rayon. Les essais ont été mené à une faible vitesse de chargement (0.05 mm/s). Plusieurs paramètres ont été enregistrés au cours de la déformation dont notamment la réaction F et un paramètre d'épaisseur e (figure 13). Ce dernier contient simultanément une information de variation d'épaisseur de la structure et de courbure dans le zone centrale de la poutre. Parallèlement, des simulations éléments finis des structures ont été

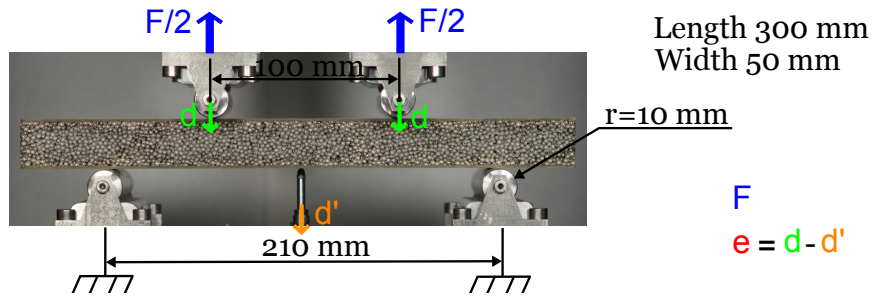


Figure 13: Essais de flexion 4-point d'une poutre sandwich.

conduites. Une modélisation 2D en déformations planes a été choisie (figure 14). Une loi de comportement élastoplastique avec un critère de Von Mises et une loi d'écrouissage d'Hollomon a été attribuée aux peaux. Une loi de comportement élastoplastique de milieu poreux avec un critère elliptique et un écrouissage linéaire a été attribué au cœur.

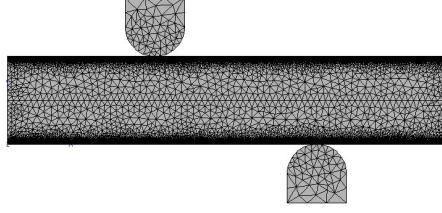


Figure 14: Modélisation par éléments finis 2D en déformations planes d'un essai de flexion 4-point d'une poutre sandwich.

3.2 Modes d'endommagement

Lors des essais de flexions 4-point sur les structures sandwich avec un cœur d'empilement de sphères creuses trois modes d'endommagements ont été observés : la plastification des peaux, le cisaillement du cœur et l'indentation. Les profils des structures après une déflexion d'environ 30 mm sont univoques (figure 15). Cependant l'endommagement intervient pour des déflexions de quelques millimètres. Pour ces

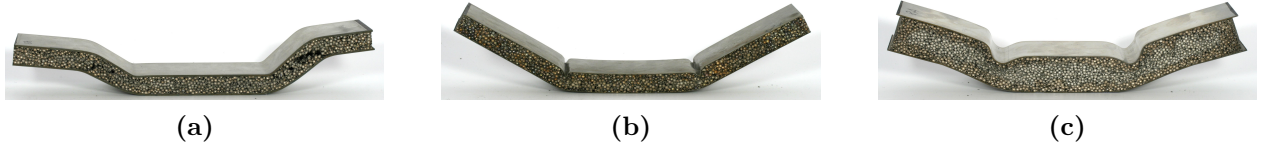


Figure 15: Profils des modes d'endommagements des structures sandwichs : (a) cisaillement du cœur, (b) plastification des peaux, (c) indentation.

déflexions, le mode d'endommagement ne peut être déduit du profil de la structure. L'allure des courbes des paramètres F et e en fonction de la déflexion sont des signatures des modes d'endommagements (figure 16), de même que l'évolution du module de décharge avec la déflexion. Les mêmes critères

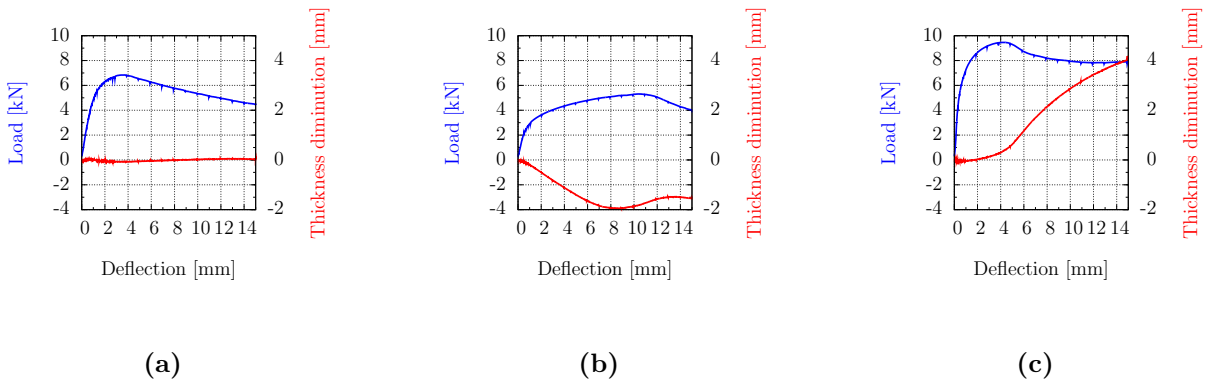


Figure 16: Signature des modes d'endommagements des structures sandwichs grâce à l'évolution de la réaction F et du paramètre d'épaisseur e avec la déflexion : (a) cisaillement du cœur, (b) plastification des peaux, (c) indentation.

de définition du mode d'endommagement peuvent être appliquées aux simulations par éléments finis des structures. Enfin pour chacun des modes d'endommagement, Ashby [Ashby *et al.*, 2000] propose des modèles analytiques. Ainsi, que ce soit pour les expériences, pour les simulations par éléments finis, ou pour les modèles analytiques, la force critique et le mode d'endommagement prépondérant

de chaque structure peuvent être déterminés. Ainsi on peut représenter les structures et leur mode d'endommagement dans des cartes fonction des épaisseurs de peau et de cœur normalisés. La figure 17 compare les cartes établie sur la base des expériences, sur la base des modèles analytiques et sur la base des simulations par éléments finis. Pour les structures où un mode d'endommagement est clairement

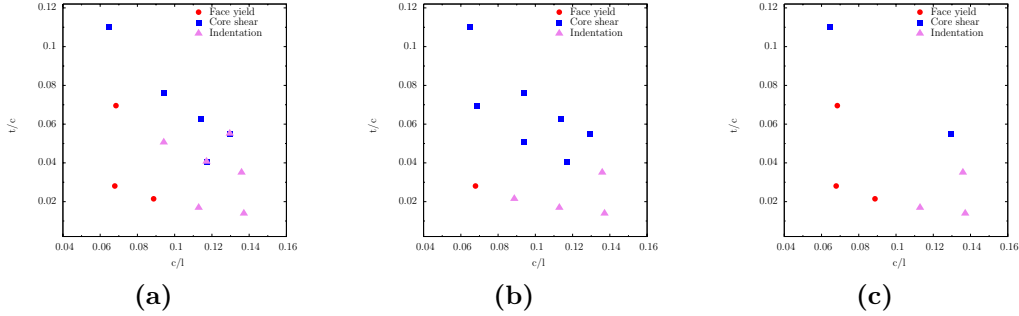


Figure 17: Carte des modes d'endommagements des structures sandwichs en fonction de l'épaisseur de peau normalisée (t/c) et de l'épaisseur de cœur normalisée (c/L) pour les expériences (a), les modèles analytiques (b) et pour les simulations par éléments finis (c).

prépondérant, les modèles analytiques sont en accord avec l'expérience. Par contre, lorsque deux modes sont en compétition (les forces critiques associées à ces deux modes sont proches), les modèles analytiques pêchent par leur simplicité et ne prédisent pas correctement le mode d'endommagement. Pour les simulations par éléments finis réalisées, les modes d'endommagement sont correctement prédits pour toutes les structures.

Si l'on s'intéresse aux forces critiques en jeu, les modèles analytiques et numériques décrivent correctement les niveaux de ces forces pour les sandwich à peau épaisses, mais beaucoup moins bien les structures avec des peau fines (figure 18).

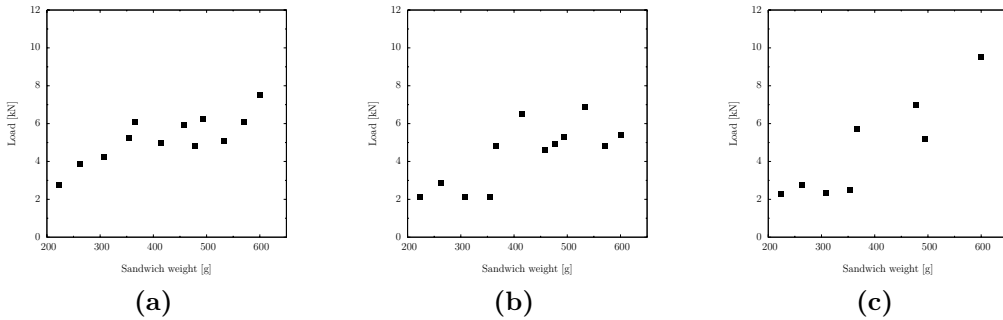


Figure 18: Forces critiques des structures sandwichs en fonction de leur masse pour les expériences (a), les modèles analytiques (b) et pour les simulations par éléments finis (c).

Cette déviation au comportement observée peu être imputée aux propriétés des peaux qui se sont avérées avoir un coefficient d'écrouissage plus important que supposé.

Conclusion

Une étude paramétrique a été menée sur des structures sandwichs avec un cœur d'empilements de sphères creuses. La trop importante modification du matériau cœur lors de son intégration dans les

structures sandwich n'a pas permis d'utiliser directement les résultats de la première partie, le comportement du matériau cœur a donc été ajusté sur des essais de compression. Le comportement des structures sandwich a été étudié au travers de la flexion 4-point de poutres et de l'indentation de plaques. Des modèles analytiques et numériques ont été systématiquement comparés aux expériences, soit pour valider ces modèles, soit pour permettre de découpler des paramètres liés dans l'expérience.

Conclusions et perspectives

Objectif et méthode

L'objectif de cette étude était de caractériser le comportement mécanique d'empilements aléatoires de sphères creuses et de valider des modèles le décrivant dans le but de pouvoir prédire les propriétés mécaniques de structures avec un tel cœur. Le problème a été traité, au travers d'échelles croissantes, par une combinaison d'expériences, d'observations et de modèles.

Ainsi la première étape a été de relier la structure élémentaire du matériau à un comportement de milieu homogène équivalent. La caractérisation de la structure du matériau, grâce à des techniques d'analyses d'images en 2 dimensions et en 3 dimensions, a fourni les informations nécessaires à la modélisation du contact entre deux sphères. Ensuite ces lois ont été implémentées dans un code éléments discrets afin de modéliser des empilements. Le comportement des empilements aléatoires de sphères creuses a été étudié pour les principales classes de chargements (sauf le cisaillement). Les modèles par Méthode des Éléments Discrets et les modèles analytiques ont été calibrés. Parallèlement, une étude du matériau par des essais in situ en tomographe aux rayons X a permis de comprendre les relations entre les mécanismes de déformation locaux et le comportement macroscopique.

Ensuite des structures sandwich avec un cœur d'empilements de sphères creuses ont été sollicitées en flexion 4-point et en indentation. Les structures ont été modélisées grâce à des simulations par éléments finis et grâce à des modèles analytiques.

Principaux résultats

Empilements aléatoires de sphères creuses

- Les empilements aléatoires de sphères creuses ont été entièrement caractérisés depuis l'échelle de la rugosité et de la porosité des parois jusqu'à l'échelle d'un Volume Élémentaire Représentatif pour la densité initiale.
- Le comportement des empilements de sphères creuses a été étudié pour les chargements de traction et de compression uni-axiaux et pour les chargements compressifs multi axiaux. Le grand nombre d'essais réalisés avec diverses densités initiales de mousse et avec des tailles d'échantillons variés constituent une base de donnée de confiance pour la description des empilements de sphères creuses..
 - Pour les chargements compressifs uni-axiaux, aussi bien les courbes contrainte-déformation que les courbes d'évolution du module de décharge avec la déformation sont bien décrits

pour les faibles déformations grâce à la combinaison des observations des microstructures des coques et des cols avec une modélisation par Méthode des Éléments Discrets. Le comportement à grande déformation est reproduit par un modèle phénoménologique reposant sur les observations mésoscopiques par tomographie R-X couplés à des analyses d'images 3D.

- Pour la sollicitation en traction uni axiale, les mécanismes microscopiques et mésoscopiques responsable du comportement macroscopique ont été identifiés jusqu'en grandes déformations. La DEM qui ne prend pas en compte l'endommagement du matériau constitutif ne peut pas les décrire. Les améliorations nécessaires pour une meilleure description du comportement en traction avec ce modèle ont été mises en avant.
- Deux techniques ont été utilisées pour les essais de compression multi axiaux. La dispersion entre les expériences ne permet pas de conclure avec certitude si le critère de plasticité est elliptique ou linéaire. La forme de la surface de plasticité est à peu près décrite par le DEM. Cependant plus d'expériences sont requises pour diminuer la dispersion et permettre de choisir le critère de plasticité le plus pertinent.

Structures sandwich

- L'évolution de la structure du matériau cœur lors du procédé d'intégration dans les structures sandwichs a été étudiée. Ce procédé engendre une modification considérable de la structure des empilements de sphères creuses.
- Des sandwichs structures avec un cœur d'empilements de sphères creuses et des épaisseurs de peau et de cœur variables ont été sollicités en flexion 4-point et en indentation.
 - Une carte d'endommagement des dimensions de la structure a été obtenue pour les essais de flexion. Les modèles éléments finis ont décrit la même partition entre les modes d'endommagement. Les modèles analytiques peuvent aussi décrire ces modes mais avec une moins bonne précision.
 - Les données nécessaires pour l'optimisation de structure sandwich, tant en conditions d'utilisation, que dans le cas d'absorption d'énergie, ont été obtenues grâce aux essais de flexion.
 - La courbe de charge-indentation des plaques sandwich peut être reproduite approximativement par un modèle de membrane plastique avec une contribution découplée du cœur à la charge. Le modèle décrit l'influence de l'épaisseur de peau, de l'épaisseur de cœur et de la taille de l'indent, mais il ne prédit pas précisément la rupture. Les modélisations par éléments finis donnent de bon résultats pourvu que le comportement du matériau de la peau soit bien connu.

Perspectives

Les observations et expériences réalisées lors de cette étude permettent de proposer diverses continuations à ce travail, lesquelles perspectives peuvent être à court ou à plus long terme.

Perspectives à court terme

Amélioration de la Méthode des Éléments Discrets appliquée aux empilements de sphères creuses

Le point clef pour améliorer la description des empilements de sphères creuses avec la DEM est à trouver dans les lois de contact. Ces lois de contact doivent décrire l'endommagement du matériau constitutif avec la déformation. L'utilisation d'un modèle pour le matériau qui prends en compte l'endommagement ou d'éléments particuliers (comme les éléments décohésifs) pour les modélisations par éléments finis du contact entre deux sphères devrait permettre cela. Des observations par micro-tomographie des cols devraient donner les informations pour une meilleure description de la forme des cols et particulièrement pour la surface de contact réelle. L'accès au procédé d'élaboration des sphères pour pouvoir solliciter de vrais cols permettrait de quantifier l'importance relative des rigidités pour les différentes sollicitations élémentaires. Ces expériences sont difficilement réalisable sans procédé d'élaboration puisque l'usinage nécessaire à l'isolement de deux sphères les endommage presque inévitablement.

Une autre approche consisterait en la calibration des lois de contact par corrélation avec les essais de tomographie in situ. Puisque la connection entre les observations tomographiques et la DEM existe, il ne "reste qu'à" implémenter une routine d'optimisation dans le code DEM.

La définition "à priori" d'un seuil, dépendant de la taille de col et de l'épaisseur de coque, pour la rupture du contact entre deux sphères est aussi potentiellement intéressant. Cette méthode a l'avantage de garder inchangés les lois de contact (si ce n'est pour le critère de rupture). La encore "il n'y a qu'à" connecter de manière appropriée quelques routines dans le code DEM, puisque ce comportement existe déjà pour d'autres types de particules.

Description des propriétés mécaniques

Plusieurs essais simples devraient permettre de mieux décrire le comportement mécanique des empilements de sphères creuses.

- Des essais pour divers chargements sur des empilements de sphères creuses après qu'il ai été intégrés dans des structures sandwich devraient permettre de mieux comprendre l'influence des différents paramètres structuraux.
- Des essais multi axiaux sur des échantillons pus grands, avec des conditions aux limites en pression, devraient améliorer la description de la surface de plasticité. L'évolution de la surface de plasticité pour des grandes déformations serait intéressante pour modéliser le comportement sous indentation de structures avec un tel cœur.
- Des essais de compression à grande vitesse de déformation donneraient plus d'information sur l'intérêt potentiel de ce matériau comme cœur pour les structures de protection.

Structures sandwich

- Des simulations par éléments finis de l'indentation de structures sandwich avec divers critères de plasticité pour le cœur permettraient de quantifier son impact sur la réaction de la structure. Le couplage entre les peau et le cœur, ainsi que l'influence de l'épaisseur du cœur seraient ainsi clarifiés.

- Des essais d'impact à grande vitesse permettraient de tester la capacité de ces structures à être utilisées comme bouclier comme est utilisé le radom dans un avion contre les impacts d'oiseaux.
- L'étude des mécanismes d'initiation du déchirement aiderait à choisir le matériau de peau lors des phases de conception.

Perspectives à long termes

Modification de la structure du matériau

La variation de la structure des empilements de sphères creuses pourrait être réalisée avec plusieurs objectifs.

La génération d'empilements avec de faibles tailles de cols (et donc avec une importante porosité ouverte) pourraient repousser la déformation à densification. Cependant si c'est le niveau des contraintes qui doit être élevé, des empilements multi-modaux ou des empilements avec des ellipsoïdes creux seraient potentiellement intéressants.

Dans le but d'améliorer les propriétés d'absorption acoustique du matériau, il serait intéressant de générer des trous dans les coques.

Structures sandwich

Toujours autour du concept de structures sandwich, trois directions principales sont suggérées.

- Des structures sandwichs avec un cœur empilements de sphères creuses élaborés, si possible, "tout en un" pourraient résoudre quelques un des problèmes rencontrés dans cette étude. Tout d'abord plus aucun usinage des empilements ne serait requis avant l'intégration dans les structures, et cela réduirait le nombre de traitements thermiques. Ensuite la surface de contact augmentée entre l'empilement et les peaux, grâce à l'étape de compaction, devrait permettre de diminuer l'intensité du traitement thermique de brasage. Une structure avec des propriétés mécaniques mieux contrôlées pourrait ainsi être obtenue. Le procédé pourrait alors être appliqué à des structures incurvées. De même des structures sandwich avec des peaux ondulées pourraient facilement être obtenues.
- Des structures sandwich avec des peaux grillagées permettraient de combiner les propriétés acoustiques des empilements de sphères creuses, en connectant la porosité ouverte avec l'espace externe, avec les propriétés mécaniques de la structure sandwich.
- La génération de structure avec une échelle d'architecture supplémentaire permettrait de s'attaquer à des problèmes comme ceux de la mise en forme. Un exemple d'une telle architecture du cœur est décrite dans l'annexe D.

General introduction

General Introduction

Properties of metallic materials have been improved either by modification of their composition, or by application of thermo-mechanical treatments. The relevant scale in this case ranges from ångström (atoms) up to millimeter (grain size).

When looking for large building, architects made them higher by combining elements (beams, plates ...) to realize structures. The matter distribution is optimized in order to carry a sufficient load without increasing too much the weight. In this case, the relevant scale is the whole structure itself. Another field of performance is open when considering the architecturing of the material ; the organization of the matter at an intermediate scale. Sponges and bread are familiar examples of such architected materials. Similar to these examples, but with more direct engineering interest, are metallic foams; as presented in figure 1.

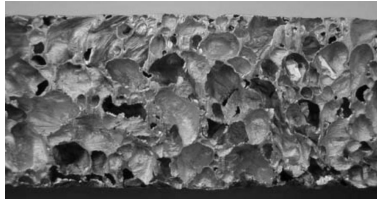


Figure 1: *A metallic foam with cells with millimeter size.*

Within the global framework of automotive challenges (reduction of weight, reduction of acoustic emission, enhancement of safety for passengers), architected materials are of interest. Among them, a particular type of foams, hollow spheres stackings (figure 2), have potential abilities to match a drastic set of both structural and functional requirements : good acoustic absorption, lightweight and high temperature operating conditions, where the candidate must moreover presents sufficient mechanical properties to act as part of the structure.

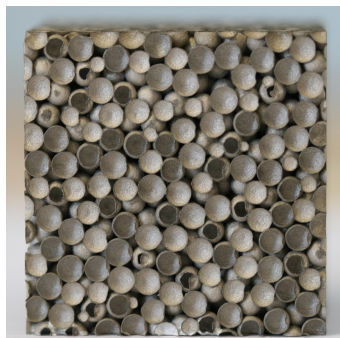


Figure 2: *A hollow spheres stacking.*

Thus in this PhD we will focus on mechanical properties of hollow sphere stackings, first as a single material, and then as integrated into a sandwich structure.

The manuscript is structured as following :

- **Part I : Generalities and overview** This part will give all the information required to understand the following. A first chapter addresses the sandwich structures. Properties and classical models used to describe them are presented. Then the next chapter deals with the hollow spheres stackings. The architecture of the material and its properties are reviewed.
- **Part II : Starting point, investigation strategy and experimental methods** At this point, a summary on the starting point of this PhD, and especially on hollow spheres stackings knowledge, is performed. Then the strategy of investigation is summarized. Next a chapter present all the experimental methods used in this PhD.
- **Part III : Hollow spheres stackings** First the available samples are presented. Then hollow spheres stackings structure is studied at various scale levels : the scale of the microstructure which corresponds to the heterogeneities of the *constitutive material*, the mesoscale which is the dimension of the architecture of the material, and the macroscopic scale which is the sample scale. Next the modeling of hollow spheres stackings by Discrete Element Method is described. The contact laws are presented and the sensitivity of the method to various input parameters are studied.
Then the macroscopic behaviour of hollow spheres stackings is investigated. The mechanical behaviour is studied for uni-axial compressive and tensile loading and for multiaxial compressive loading. The influence of the structural parameter is discussed. Discrete Element Method simulations are compared to the experiments in order to quantify the ability of this model to predict the mechanical behaviour of hollow spheres stackings.
Then deformation mechanism at the mesoscale are studied. A model based on the phenomenological description of the material damage and densification is presented.
- **Part IV : Sandwich structures** The process of integration of hollow spheres stackings into sandwich structures lead to important changes in the material properties. Thus hollow spheres stackings structure and properties, *as core material*, are studied.
Then the behaviour of sandwich structures loaded under four-points bending is investigated. The influence of various dimensional parameters is quantified. Analytical models and Finite Element simulations are compared to experiments. Their potential to describe the structure behaviour is discussed.
Last we will focus on the energy absorption of the sandwich structures using indentation tests. The responses of the structure and the models are compared.

Part I

Generalities and overview

Introduction

This part aims at giving an overview of the context of this PhD. The benefits of the distribution of matter in a material are considered at two scales. At the scale of a structure, this distribution is studied by partition between a face material and a core material in sandwich structures. At the scale of the cells of a cellular material, this distribution is studied on a special pattern : a stacking of hollow spheres.

In a first chapter sandwich structures based on cellular materials are introduced. Analytical models describing their mechanical behaviour and their damaging modes are shown.

The second chapter deals with hollow spheres stackings. Their structure and architecture are first described, as well as the process needed to obtain such structures. Then properties and behaviour at various scales (micrometer to centimeter) are reviewed and compared with other classical foams. Homogeneous medium models describing the foams behaviour are introduced, and finally, assets and weaknesses of hollow spheres stackings are outlined.

Chapter 1

Sandwich structures : interest and properties

Contents

1.1	Optimization of the weight of a beam with prescribed flexural stiffness	41
1.2	Sandwich beams and plates	42
1.2.1	Behavior under four points bending of sandwich beams	43
1.2.1.1	Properties	43
1.2.1.2	Analytical models	44
1.2.1.3	Failure modes	46
	Face yield	47
	Core shear	47
	Interface debonding	47
	Face wrinkling	48
	Indentation	48
1.2.1.4	Maps	49
	Failure mode map	49
	Properties map	51
1.2.2	Indentation resistance of sandwich plates	51
1.3	Summary on sandwich structures	54

To begin this chapter, a simple and classical example is investigated to illustrate the role of matter's distribution within a structure on its macroscopic behaviour. The concept of sandwich issues from it. Then classical behavior and damage models for sandwich beams loaded in four-points bending are presented.

1.1 Optimization of the weight of a beam with prescribed flexural stiffness

The main property of a structure is its ability to carry load. In many situations, some part of this structure is submitted to flexural loading. In order to design it, the behavior is studied under simple loading conditions. The simplest test related to flexural behavior is the loading of a beam with pure flexural moments. It has the advantage to be independent of the length of the beam *while it is consistent with beam theory*.

A simple analysis of a beam subjected to pure flexural loading, leads to well known but nevertheless interesting conclusions. It aims at minimizing the weight of that beam when the constraints of a constant flexural stiffness, a constant width, and a constant thickness are imposed. The degrees of freedom are given by the matter distribution within a cross section. At a given point, the material is assumed to present a porosity ρ . The Young Modulus of the constitutive material is supposed to be linked to its density by a power law (as it is often assumed for foams). Assuming a constant bending stiffness, the optimal distribution of porosity can be analysed via a level set method [Allaire *et al.*, 2007]. The initial state is a monolithic beam of density of 50%. The evolution of the density repartition within the cross section from the initial state to the optimal repartition through an intermediate stage is shown on figure 1.1 .

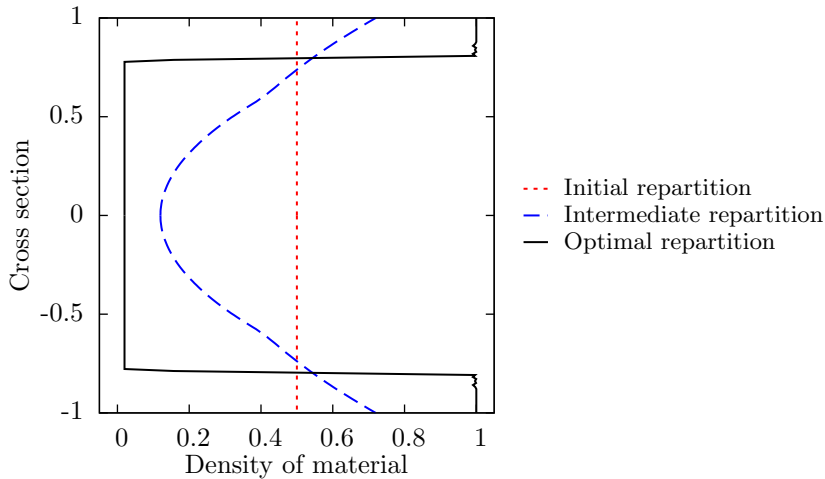


Figure 1.1: Evolution of the density distribution within a cross section for an heterogeneous beam loaded with pure flexural moment with constant flexural stiffness and minimum weight objective.

The optimal distribution shows a maximal density on the faces of the beam while it removes material from the core of the beam. This distribution is consistent with common intuition that requires to

position materials with high stiffness far from the neutral axis for a double reason. First the largest is the distance of a force to the neutral axis, the most important is the flexural moment. This force is obviously a combination of a surface with a stress that is itself the product of the Young Modulus and of the strain. This is the point which enhance this effect because the beam theory hypothesis of a rigid cross section leads to a linear repartition of strains. Therefore, the further from the neutral axis is the matter, the more important is its influence on the flexural stiffness. Figure 1.2 illustrates density, strain, stress and elementary flexural moment distribution in a section for respectively an homogeneous and an heterogeneous distribution of material in the beam. The normalized gain of mass between the

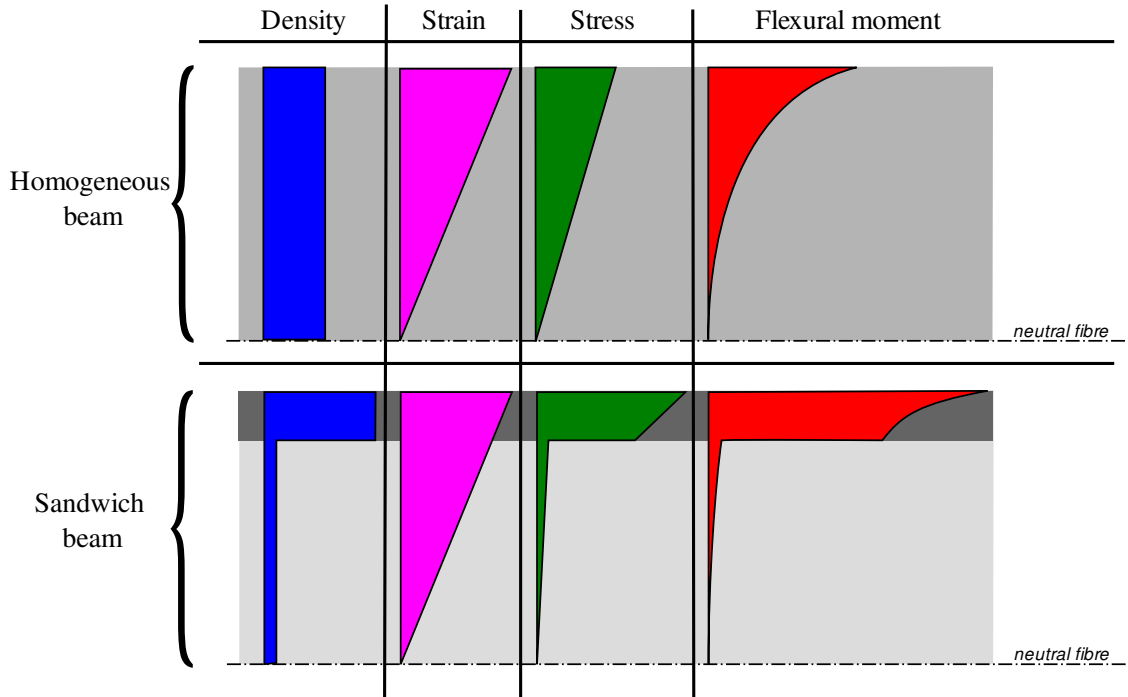


Figure 1.2: Distribution of density, strain, stress and elementary flexural moment in an homogeneous beam and in a sandwich beam.

homogeneous beam and the optimized configuration is of about 80% in that case. These observations directly shows the potential of using heterogeneous structures when the heterogeneity in on the length scales comparable to the scale of the component. The density repartition directly introduces the concept of sandwich, where a light core material is associated to a stiff face material. The impact on structures performances is huge.

1.2 Sandwich beams and plates

In this PhD, two types of loading on sandwich structures have been investigated. First the ability of the structure to carry a load has been studied through four points bending tests. Thus classical models used to describe their behavior are recalled in this section. Then one particular failure mode, indentation, is investigated on sandwich plates.

1.2.1 Behavior under four points bending of sandwich beams

As mentioned in paragraph 1.1, the sandwich structures are able to improve considerably the flexural stiffness of a beam. The optimization was realized in pure bending conditions, but whatever the limit conditions, the main point to keep in mind when optimizing a structure is : “*What is the model used to describe the behavior ?*”. From Euler and Bernoulli, who first drew the bases of beam theory, through Timoshenko [Timoshenko and Young, 1965] who implemented the shear contribution, to multiple orders theory [Reddy, 1984] [Touratier, 1991] and stratified theory [Zenkert and Fund, 1997], a large variety of models are available. A brief overview of some of these models will allow to see more clearly what can be predicted and optimized. But, before that, it is necessary to define what is to be known for a sandwich structure loaded in four points bending.

1.2.1.1 Properties

When loading a sandwich in four points bending, one still keeps several degrees of freedom once the dimensions of the sandwich are chosen. Inner and outer span can be modified, as their type of interaction with the structure. This means that pushers can be either rolls (whose diameter is also a free parameter) or some of them can be clamped to the structure. All these parameters can have an influence on the properties measured.

For the sake of simplicity, in the following, outer rollers will be always positioned below the structure, and they will be clamped to the frame, that means that they won't move in the laboratory frame. Figure 1.3 recaps all geometrical parameters and symbols used in analyzing four point bending of a symmetrical sandwich structure. Therefore a load is applied on the upper rollers (also inner rollers), the structure shape is changing, and often displacement of upper rollers is recorded. This displacement will be called “*deflection*”. One can also place any sensor under the central cross section of the structure to obtain what will be called “*maximal deflection*”. During the load removal, the stiffness of the beam can be measured. When the load increases above a certain threshold, it can lead to an irreversible damage of the structure that can be observed by a residual permanent deflection. This threshold load is called “*critical load*” or also “*damaging load*”. If the load still increases, the structure will be carried to failure at the “*ultimate load*”, the maximal load that the structure can endure. From the load versus deflection curve, “*elastic energy*” and “*plastic energy*” absorbed can be extracted. A typical load versus deflection curve is plotted on figure 1.4 . It illustrates how to obtain the previously mentioned parameters. To obtain an optimal structure fulfilling all the requirements, we have to be able to predict the structure performances depending on its parameters (that means, constitutive materials, and dimensions). Two options are open. The first one is to set up some analytical models that can, under some hypothesis, give relations between parameters and properties. It would be then quite easy, in principle, to get the optimal solution. The second one assumes that some parameters are already fixed, and that it remains only two or three degree of freedom, and is based on experimental sweeping of the sets of parameters. This would be very cumbersome if a large number of materials combination and geometries have to be realized and experimentally tested, so numerical experiments are often chosen. It remains that this second technique is preferentially used as a second step of optimization. This will be the general strategy : first analytical models are used to predict some potentially interesting combinations of materials and dimensions, and then numerical, and real, experiments are realized for sets of parameters close to these optima.

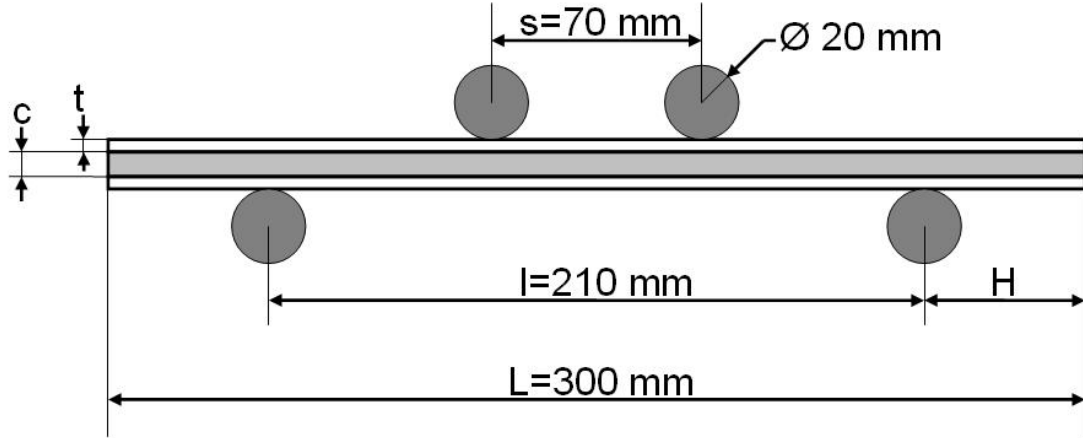


Figure 1.3: Geometrical parameters and symbols used in analyzing four points bending of a symmetrical sandwich structures.

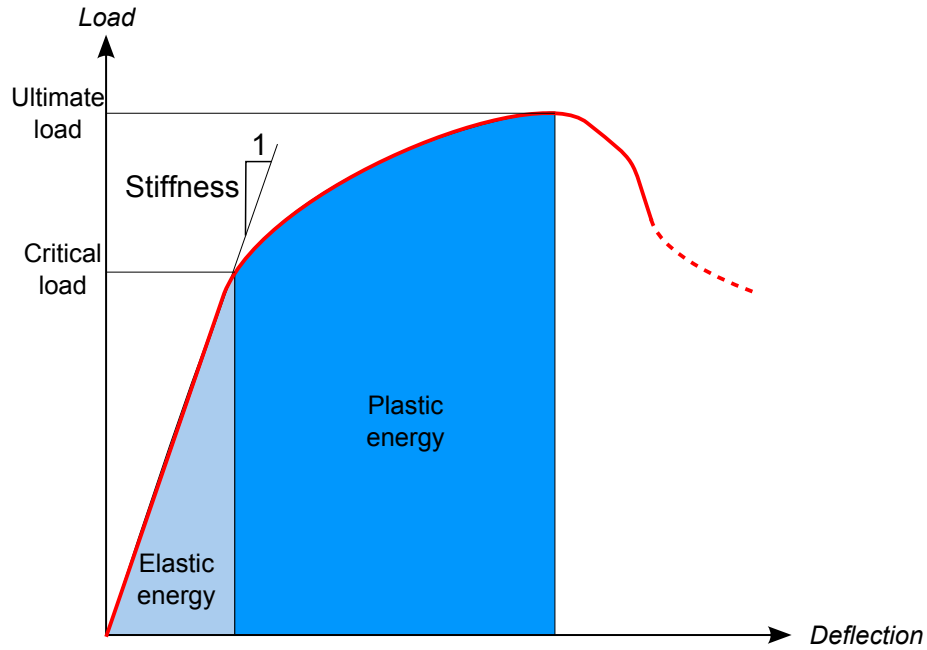


Figure 1.4: Classical load versus deflection curve of a sandwich loaded in four points bending.

1.2.1.2 Analytical models

Simplest models to predict the behavior of a sandwich structure are based on elastic beam theory, also called “*Euler-Bernoulli beam theory*”. This theory studies the behavior of a solid obtained by a normal extrusion of a surface (the “*cross section*”) along a continuous line (the “*neutral fiber*”). It was first designed for monolithic structures loaded in elastic regime. It relies on the hypothesis that cross sections are nondeformable and remains normal to the neutral fiber. It gives for a rectilinear beam subjected to bending a proportional relation between load F and deflection δ . This relation can be

decoupled in two terms as shown in equation 1.1 .

$$\delta = \alpha_1(\text{boundaries}, L) \cdot \alpha_2(E, S) \cdot F \quad (1.1)$$

The first pre-factor α_1 only depends on the boundaries conditions and on the longitudinal dimensions, while the second term α_2 only depends on the cross section properties (dimensions and material). Thus, for a given set of requirements, when boundaries conditions and longitudinal dimensions are fixed, flexural stiffness δ/F is completely defined by the cross section pre-factor α_2 . It can be expressed by equation 1.2 where E is the Young Modulus of the constitutive material (supposed to be elastically isotropic), and I is the moment of inertia.

$$\alpha_2 = \frac{1}{E \cdot I} \quad (1.2)$$

This models assumes a linear distribution of strains in the cross section with respect to the distance to the neutral axis. In pure flexural conditions, the maximal stress within the structure is linked to the macroscopic flexural moment (and thus to the load F , depending on the boundaries conditions). Therefore with that simple model, flexural stiffness, critical load and elastic energy absorbed can be predicted, for a monolithic beam. When studying a sandwich structure, one wants to use this model. The idea is just to adapt the term α_2 relative to the cross section in equation 1.1 . For a beam of width b , with a core and face of properties (thickness and Young modulus) of respectively (c, E^c) and (t, E^f) , an equivalent flexural compliance (invert of the stiffness) EI_{eq} is proposed in equation 1.3 . It contains the compliance of the core, the compliance of both faces *relatively to their owns neutral fibers*, and the compliance of both faces relatively to their distance to the sandwich neutral fiber. Last term is responsible for the huge gain of properties of sandwich structures compared to mono material beams.

$$(EI)_{eq} = \frac{E^c b c^3}{12} + \frac{E^f b t^3}{6} + \frac{E^f b t (t + c)^2}{2} \quad (1.3)$$

Nevertheless, this method needs some improvement, because the shear deformation of a sandwich beam is not negligible under some boundaries conditions, because of the usually weak shear modulus of the core. So, Timoshenko's beam theory will be considered as a better approximation. It adds a degree of freedom by allowing cross section not to be orthogonal to the neutral fiber. As a result, it allows to take into account the shear deformation. Thus 1.1 becomes :

$$K = \frac{\delta}{F} = \frac{\alpha_1(\text{boundaries}, L)}{(EI)_{eq}} + \frac{\alpha_3(\text{boundaries}, L)}{(AG)_{eq}} \quad (1.4)$$

where

$$(AG)_{eq} = \frac{b(c + t)^2 G^c}{c} \quad (1.5)$$

and α_3 only depends on the boundaries conditions and on the longitudinal dimensions, and G^c is the shear modulus of the core. This last model has been developed by Allen [Allen, 1969].

From this model, flexural stiffness, critical load and elastic energy absorbed can be predicted for a sandwich structure. To go further in depth two options are offered. The first one aims at predicting the ultimate load and how much energy will be absorbed plastically. The second one tries to predict what is the damaging mechanism. The last point will be treated in next section (1.2.1.3).

When trying to explore the behavior beyond the elastic domain, one have to re-examine the relation

between load and deflection. It is then necessary to re-evaluate the hypothesis of beam's theory. Cross section are assumed to remain planar, and therefore strain variation is linear. In pure bending, strain is null on the neutral fiber. The integration of the elementary flexural moments over the cross section gives a relation between the flexural moment \mathcal{M} and the gradient among longitudinal direction of the cross section rotation $\theta_{,x}$. This integration is divided into two parts depending on the phase considered in equation 1.6 .

$$\mathcal{M} = 2 \cdot \int_0^{c/2} y \sigma^c(\theta_{,x} y) dy + 2 \cdot \int_{c/2}^{e/2} y \sigma^f(\theta_{,x} y) dy \quad (1.6)$$

where $\sigma_c(\varepsilon)$ and $\sigma_f(\varepsilon)$ respectively represent the material behavior of core and faces. In that case, any non linear behavior is acceptable. But because the response become complex due to these non linear behaviors, the resolution has to be carried out numerically. It will not therefore be possible to invert the problem to get the optimal solution. Nevertheless it is a very “low cost” technique to obtain the behavior of the structure up to ultimate load. A very large number of sandwich realizations can be simulated, and thus a wide range of parameters can be swept. An example of the response obtained for a sandwich with elasto-plastic materials presenting a linear hardening is shown on figure 1.5 .

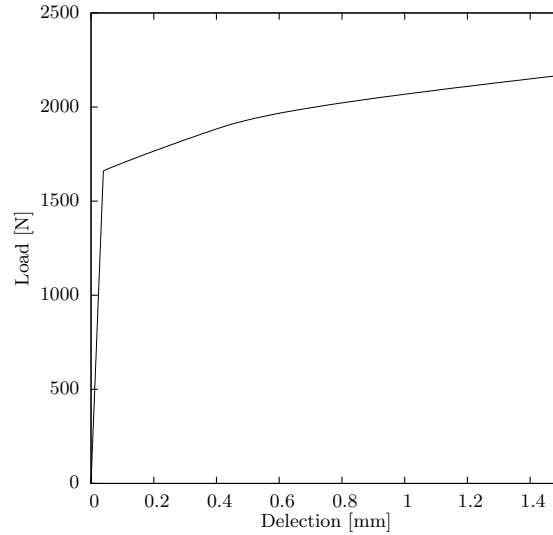


Figure 1.5: Load versus deflection response of a sandwich loaded in four points bending with elasto-plastic materials with linear hardening. Response based on Timoshenko beam theory.

Models are becoming more complex but no ultimate load seems to appear. Even if a failure criterion is added to the material behavior, some damaging phenomena may be lacking. Actually damage is local and does not necessarily impact, at least initially, the macroscopic behavior. In order to avoid to neglect a damage mechanism, there is no choice than to do a focus on possible damage modes, also called failure modes.

1.2.1.3 Failure modes

Ashby et al. summarized some of the failure modes that a sandwich might be subject to in [Ashby et al., 2002] : face yield, core shear and indentation ; to which interface debonding and face wrinkling has to be added.

Face yield Face yield damaging mode occurs when faces are undergoing an irreversible deformation. It can easily be predicted thanks to the fact that the maximal strain in faces occurs at the largest distance from the neutral fiber of the sandwich. This failure mode is not catastrophic because of the progressive hardening of faces. The critical load for face yielding is given by equation 1.7. Core is assumed to remain in elastic domain and σ_y^f is the yield stress of the constitutive material of the faces.

$$\mathcal{F}_{faceyield} = \frac{8EI_{eq}\sigma_y^f}{(L-s)cEf} \quad (1.7)$$

If the constitutive material of the faces can endure large strain and has hardening abilities, the structure will smoothly strengthen when damaging. This damaging process is thus stable for a given load. By increasing the deflection another failure mode will finally become dominant and the ultimate failure may occur more suddenly. So when face yield is the first damaging mode, another mode is often responsible of the final failure. Most of the damage is localized between the inner rollers where bending moment is maximal and constant.

Core shear Core shear is due to a too important shear stress in the core. But because of its low density, and because of localized high shear strains, this failure mode is also mainly controlled by the face behavior. Its critical load corresponds to the formation of several plastic hinges in the faces (their number depending of the overhang). This failure mode can also be quite easily implemented in a beam theory based model. Allen [Allen, 1969] showed that a transition between two core shear failure modes (called A and B) occurs for an overhang of H_c given by equation 1.8, with τ_y^c being the shear stress for collapse of the core. If $H < H_c$ then the core shear mode that may occur is the mode A with 4 plastic hinges in the faces and the critical load is given by equation 1.9. Else if $H > H_c$ then the core shear mode that may occur is the mode B with 8 plastic hinges in the faces and the critical load is given by equation 1.10. Figure 1.6 presents both models and the true shape of a sandwich structure failing by core shear.

$$H_c = \frac{t^2\sigma_y^f}{2c\tau_y^c} \quad (1.8)$$

$$\mathcal{F}_{coreshearA} = \frac{2bt^2}{l}\sigma_y^f + 2bc\tau_y^c \left(1 + \frac{2H}{l}\right) \quad (1.9)$$

$$\mathcal{F}_{coreshearB} = \frac{4bt^2}{l}\sigma_y^f + 2bc\tau_y^c \quad (1.10)$$

If the shear deformation ability of the core material is weak, this damaging mode will lead to failure within only a small increment of deflection. All the damage is localized in the parts of the beam subjected to shear loading (ie the portions located between the inner and the outer rollers).

Interface debonding Interface debonding failure mode is controlled by the quality of the interfaces between core and faces. The cohesion properties are hardly quantifiable when one of the material yield stress is weak. Qualitatively it can be observed that the interface is more loaded when the two materials are rigid than when one of them is soft. In the later case, deformation preferably occurs in the soft material. Since properties of the interfaces are much more scattered and anyway less accessible to full characterization than material properties, and since this failure mode is catastrophic, the type and the

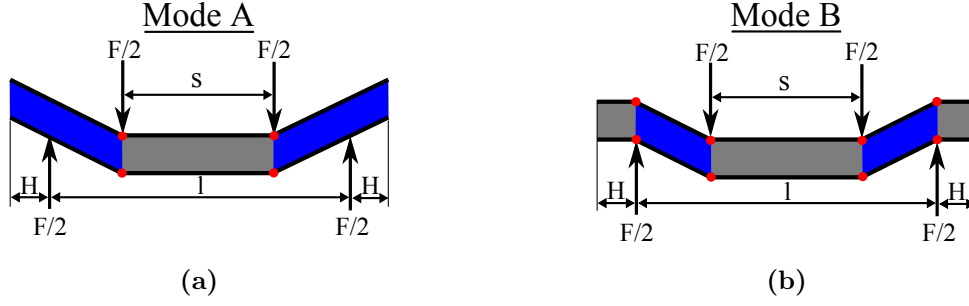


Figure 1.6: Core shear failure mode. Models for mode A (a) and mode B (b), red point are locations of plastic hinges, blue area are the core portions undergoing shear strain.

process used for interface bonding are usually chosen to ensure a cohesion superior to the core material failure limit.

Face wrinkling Face wrinkling is due to a compressive instability of a face. Periodic hollow core favors this phenomenon but prescribes the wave length. When modeling the core material by a homogeneous material, the damaging stress is given by the buckling load of a plate (a face) supported by a medium (the core). [Allen, 1969] expound the expression of the critical stress to be :

$$\sigma_{critic} = B(E^f)^{1/3}(E^c)^{2/3} \text{ where } B = 3[12(3 - \nu^c)^2(1 + \nu^c)^2]^{-1/3} \quad (1.11)$$

with ν^c the Poisson ratio of the core material. When face yield damaging has already occurred, face wrinkling can become dominant. [Zenkert and Fund, 1997] show that the above formula can be used provided E^c is substituted with E^r given by equation 1.12 with H^f being hardening modulus of faces.

$$E^r = \frac{4E^f H^f}{(\sqrt{E^f} + \sqrt{H^f})^2} \quad (1.12)$$

This failure mode can also be initiated by indentation damaging.

Indentation Indentation is a local penetration of the face in the core. It depends on the shape and size of the roller but also on the properties and dimensions of the structure.

Ashby [Ashby *et al.*, 2000] proposed a model for the damaging by indentation assuming that the core behaves as a plastic foundation and that 4 plastics hinges occur within the face. The wavelength λ is the free parameter allowing the minimisation of the load which is given by Equation 1.13 with σ_y^c being the yield stress of the core material.

$$\mathcal{F}_{indentation} = 4bt\sqrt{\sigma_y^c \sigma_y^f} \text{ and } \lambda = 2t\sqrt{\frac{\sigma_y^c}{\sigma_y^f}} \quad (1.13)$$

Zenkert [Zenkert *et al.*, 2004] proposed a model of indentation based on the behavior of an elastic face relying on a elastic foundation of stiffness E^c/c . Damaging occurs when the core reaches a plastic strain. Then the damaging load is given by Equation 1.14, with I_f being the moment of inertia of one face around its own neutral fiber. In this model the core thickness has an influence ; the thicker the

core, the more resistant to indentation the structure³. Figure 1.7 presents schematics corresponding to the two models.

$$\mathcal{F}_{indentation} = 4\sigma_y^c \left(\frac{ct^3}{3} \cdot \frac{E^f}{E^c} \right)^{1/4} \text{ and } \lambda^4 = \frac{E^c}{4cE^fI^f} \quad (1.14)$$

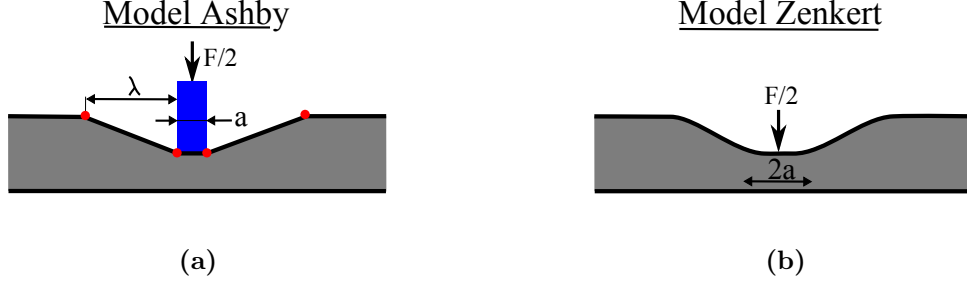


Figure 1.7: Indentation failure mode. Models of Ashby (a) and Zenkert (b), red points are locations of plastic hinges.

This damaging mode is often a key point in the design of a structure. Actually, when a sandwich structure is considered under operating conditions, damage by indentation is visible and thus is often redhibitory, while face yield, for example, is hardly visible and furthermore does not weaken the structure, being thus a more acceptable damaging mode. Nevertheless if one of the structure requirements is also to absorb energy, then indentation has some advantages. It is a failure mode that has the ability to dissipate a large amount of energy at approximately constant load with a limited translation of the opposite face, which is not the case of face yield even if the energy absorbed in that case is larger. So it has a great potential for protective structure in any moving system.

1.2.1.4 Maps

For a given couple of material integrated in a sandwich structure, face thickness c and core thickness t can be varied. It is interesting to describe the structure properties using map depending of the structure dimensions. In order to allow comparison with other maps, adimensional parameters will be used as axes, nevertheless the map plotted is only valid for a given outer-span length l . Usually adimensional parameters are t/c and c/l .

Failure mode map For each pair of dimension (normalized thicknesses of the face and the core), failure load for each of the previously mentioned failure mode can be calculated. The mode that will actually occurs will be the one with the lower failure load. Thus depending on the dimensions the failure mode can change. Figure 1.8 presents a failure map of the normalized dimensions. It can be enhanced with iso-values of "safety factor" defined as the equal relative distances (in load) between the prevalent mode and the next dominant mode (equation 1.15 where F_1 and F_2 are the critical loads of respectively the prevalent mode and the next dominant mode).

$$S_f = \frac{F_2 - F_1}{F_1} \text{ with } F_2 > F_1 \quad (1.15)$$

³Since only irreversible deformations are looked for, when the core is thicker, the motion of the upper face can be higher before the strain in the core reaches the plastic strain.

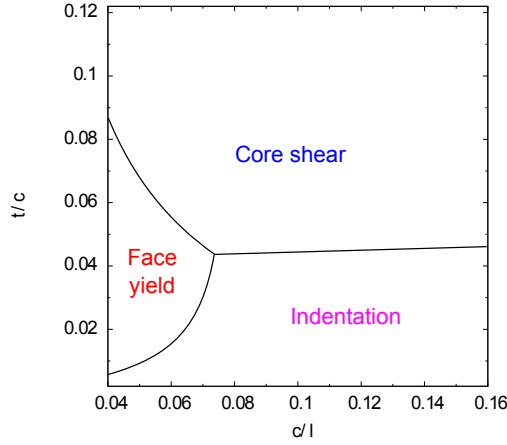


Figure 1.8: Failure mode map.

Figure 1.9a shows such a failure map with the lines of iso-values of "safety factor".

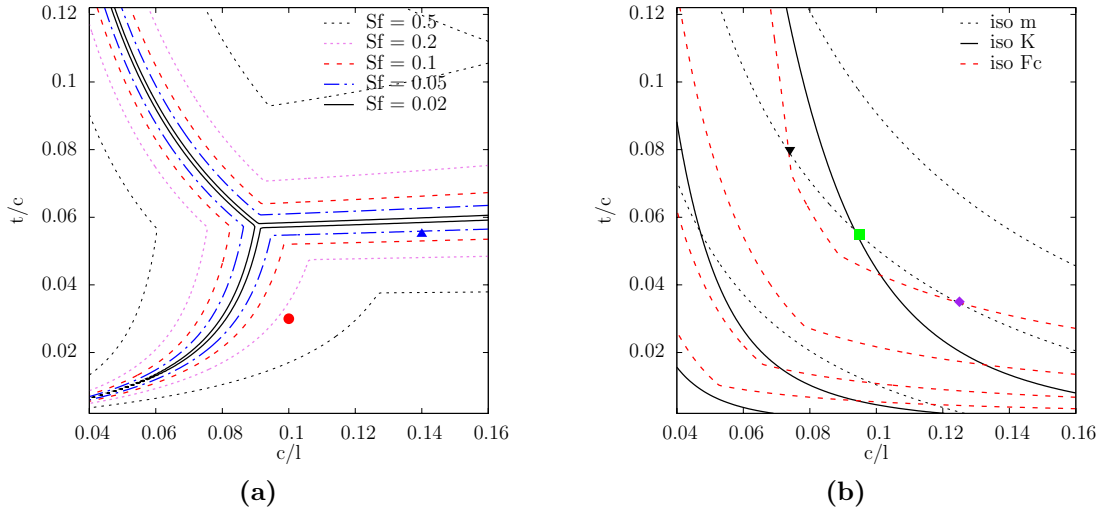


Figure 1.9: **a**-Failure mode map with lines of iso-values of the safety factors (S_f). Sandwich structure corresponding to the circular point (red) would fail by indentation since other critical load are at least 20% higher, while the sandwich structure corresponding to the triangle (blue) may as well fail by indentation or by core shear since the difference between the two critical loads are only of a few percents. **b**-Map with lines of iso-values of the stiffness (solid black lines), the weight (dotted grey lines) and the critical load (dashed red lines). Distance between lines of iso-values is not regular. The three structures (black triangle, green square and purple diamond points) have the same mass (dotted grey lines). Black triangle and purple diamond fail at the same load which is lower than the green square structure failure load (red dashed line). Black triangle, green square and purple diamond have increasing stiffness (solid black line).

If iso-values are low that means that the occurrence of the dominant mode is not ensured. This map is of great interest to validate qualitative models. Actually it can be that models depict well the occurrence of the mode but predict poorly the load response. Theses maps can also be used to design a structure when a failure mode have to be avoided or when one wants that its structure fails in a given

mode.

Properties map Lines of iso-values of weight, stiffness, critical load, and so on, can be plotted in this kind of map. These maps can be superimposed as between them as with the failure map (Figure 1.9b). When looking for optima locations in this map, one can find numerically, for each imposed stiffness or critical load, the couple of dimensions (t, c) that minimize the weight of the sandwich structure⁴. For a more transparent representation of the respective roles of t and c , those optima locations can be plotted in a map t versus c . Figure 1.10 presents both maps. One can clearly see that, for a given weight, one has to choose between stiffness and strength. If one is looking for stiffness the trend is to maximize the core thickness with rather thin faces. If the critical load is aimed at, the situation is more complex. For low prescribed value, there is a clear advantage to increase the face thickness. For higher values, a kind of compromise between faces and core thicknesses has to be searched for.

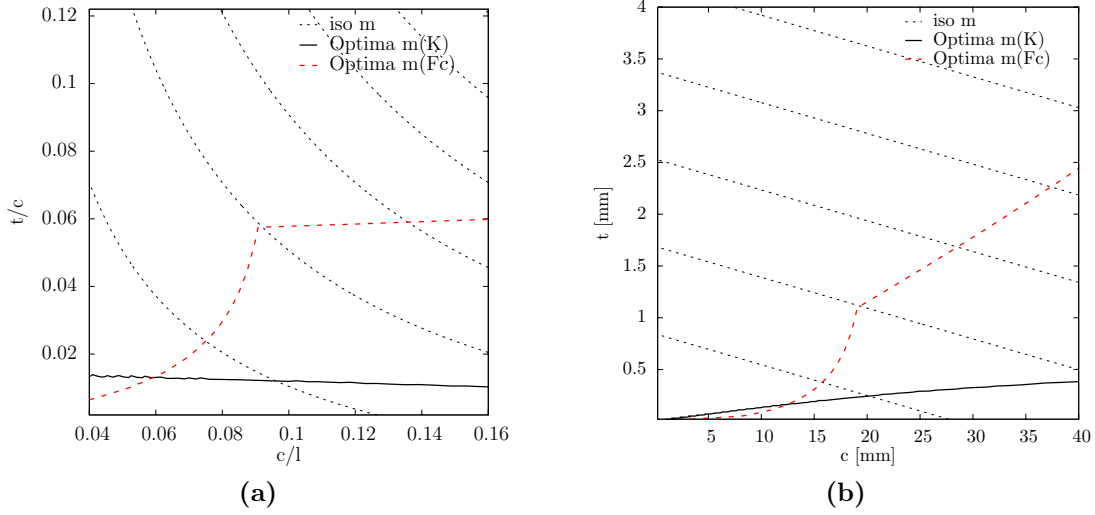


Figure 1.10: Location of sandwich structures with minimal weight for a constrain over the stiffness (solid black line) and for a constrain over the critical load (dashed red line). **a-** Axes are c/l and t/c . **b-** Axes are c and t .

1.2.2 Indentation resistance of sandwich plates

When impact protection is a main requirement for the structure, for example in the case of plane radom for birds impacts, the indentation mode have to be considered. The problem of indentation can be tackled from various angles.

The structure can either endure both indentation and bending, or it can rely on a plane which ensures that only indentation loading is applied.

- When indentation and bending are considered simultaneously on sandwich structures, the partition between the damage due to indentation and others failure modes is not trivial. Moreover, when bending is considered, perfect boundary conditions are difficult to ensure. Thus, for tests of blast loading ([Andrews and Moussa, 2009], [Hanssen *et al.*, 2002]) or tests for high-speed impact ([Tagarielli *et al.*, 2007], [Radford *et al.*, 2006]), clamped boundaries conditions are applied. The

⁴Which is equivalent to look for the stiffest or largest critical load for each imposed weight.

membrane behaviour of the faces is a key point. Nevertheless if the core is crushable, inserts in the core have to be used to allow a clamped boundary condition. Another option consists in the three points bending loading of a simply supported beam at low velocity ([McCormack *et al.*, 2001], [Steeves and Fleck, 2004]). But if this loading favours indentation compared to four points bending, other failure modes can still occurs. If one wants to ensure that indentation damage occurs whatever the dimensions and the core and face material, other boundaries conditions have to be used. For more information about the combination of bending and indentation, [Abrate, 1997] presents overview of the model used for sandwich structures with laminated facing, and [Fatt and Park, 2001] elaborates progressively a model taking account both the bending, the indentation and dynamic effects.

- In order to isolate the indentation behaviour, one can make the sandwich plate to rest on a rigid foundation. Then, either a beam or a plate can be loaded with respectively a cylinder or a sphere. For beams, 2D models presented in 1.2.1.3.0 have to be considered. When plates are loaded with an indent, depending on the depth of indentation, the system is often modeled either by a smooth indent in contact with a semi-infinite smooth medium ([Yang and Sun, 1982]), or by a rigid indent in contact with an elastic layer bonded on a semi-infinite rigid substrat ([Stevanovic *et al.*, 2001], [Lee *et al.*, 2008]). The thickness of the core is taken into account by elastic Winkler foundations as described in [Abrate, 1997] and in [Shuaib and Soden, 1997]. [Fatt and Park, 2001] proposed a partition of models depending on the depth of indentation (figure 1.11). For low indentation

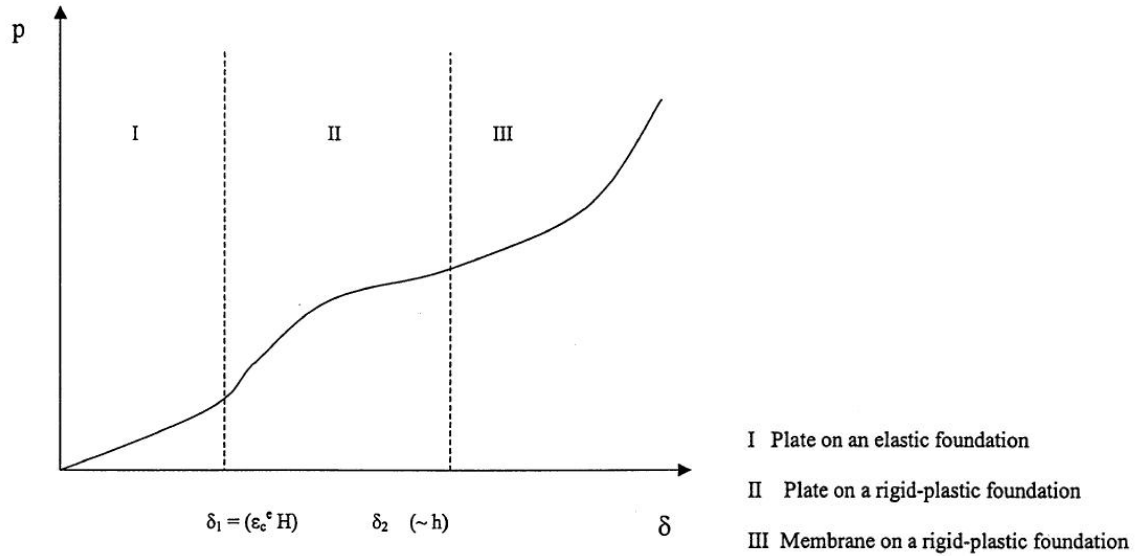


Figure 1.11: Depending on the depth of indentation three regimes can be identified for the upper face sheet [Fatt and Park, 2001]. ϵ_c^e is the core elastic limit, H is the core thickness and h is the face thickness.

depth, the load is well described by a plate on an elastic foundation. If indentation becomes large enough, the core yields and the load can be described by a plane on a rigid-plastic foundation. For indentation deeper than a face thickness, the load is better described by a membrane on a rigid-plastic foundation.

[Türk and Fatt, 1999] proposed to model the indentation with an elastic membrane resting on a rigid-plastic foundation. The profile of the membrane is prescribed both by the indentation depth ω_0 , by

the radius of the indent R and by the radius of indented area ξ where the foundation is plastified (figure 1.12). The hemispherical indenter is approximated as a flat-nose indenter of respective radius

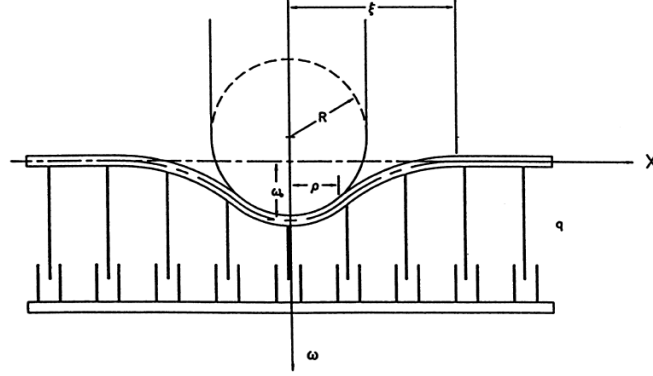


Figure 1.12: Description of the indentation profile [Türk and Fatt, 1999].

$R_e = 0.4R$. By minimization of the energy dissipated both in the foundation and in the membrane, he obtained expressions of respectively the radius of indented area (equation 1.16) and of the indentation depth (equation 1.17) as function of the indentation depth.

$$\xi = R_e + \sqrt{\frac{9(P - \pi\sigma_y^c R_e^2)}{8\sigma_y^c}} \quad (1.16)$$

$$\omega_0 = \sqrt[3]{\frac{9(P - \pi\sigma_y^c R_e^2)^2}{64\sigma_y^c C_1}} \quad (1.17)$$

C_1 is a material constant defined by :

$$C_1 = 8 \left[\frac{1}{45}(A_{11} + A_{22}) + \frac{1}{49}(2A_{12} + 4A_{66}) \right] \quad (1.18)$$

where A_{ij} are the membrane extensional stiffness which depend on the shell thickness t , the Young's modulus E_f and the Poisson ratio ν_f for an isotropic monolithic membrane (Eq. 1.19).

$$\begin{aligned} A_{11} &= A_{22} = \frac{E_f t}{1 - \nu_f^2} \\ A_{12} &= \nu_f A_{11} = \frac{\nu_f E_f t}{1 - \nu_f^2} \\ A_{66} &= \frac{E_f t}{2(1 + \nu_f)} \end{aligned} \quad (1.19)$$

It is important to notice that even if it can be considered as an upper bound for the indentation load at large indentation, the model does not take into account the shearing interaction between the face and the core. Even more, the core hardening has also been neglected.

Another simple analytical model that can be used is the indentation of a perfectly plastic membrane with clamped boundary conditions. [Simonsen and Lauridsen, 2000] proposed a parametric description of the load-indentation curve as function of the angle ψ_C from horizontal to the plate at the extreme contact point C (figure 1.13). The load-indentation curve is described by :

$$\begin{cases} P = 2\pi N_0 R_b \sin^2 \psi_C \text{ with } N_0 = 2\sigma_y^{f*} t / \sqrt{3} \\ \frac{\delta}{R_b} = 1 - \cos \psi_C + \sin^2 \psi_C \ln \left[\frac{R/R_b + \sqrt{(R/R_b)^2 - \sin^4 \psi_C}}{\sin \psi_C (1 + \cos \psi_C)} \right] \end{cases} \quad (1.20)$$

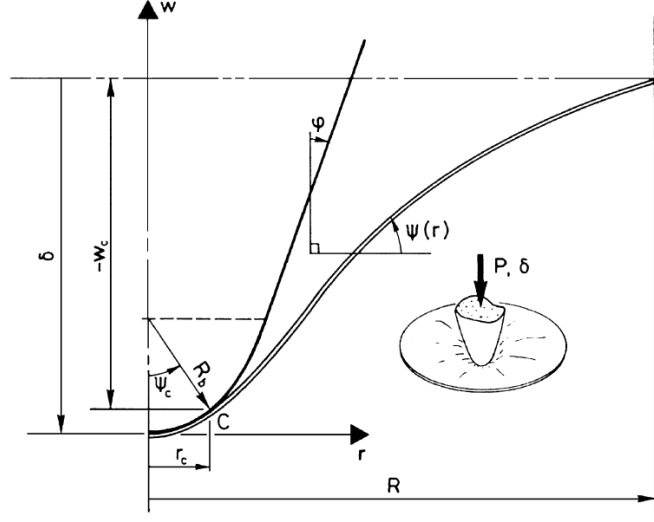


Figure 1.13: Description of the indentation profile [Simonsen and Lauridsen, 2000].

The modified yield stress σ_y^{f*} is defined as the average of the yield stress σ_y^f and of the failure stress σ_u^f (Eq. 1.21).

$$\sigma_y^{f*} = \frac{\sigma_y^f + \sigma_u^f}{2} \quad (1.21)$$

[Simonsen and Lauridsen, 2000] improved the model by taking into account for the hardening of the membrane, but no analytical solution are proposed. It remains that an empirical expression for both the deflection at failure δ_f (Eq. 1.22) and the energy absorbed at failure \mathcal{E} (Eq. 1.23) thanks to a simple necking criterion. The material stress is assumed to follow a power law of the strain (Eq. 1.24).

$$\delta_f = 1.41n^{0.33}R^{0.48}R_b^{0.52} \quad (1.22)$$

$$\mathcal{E} = \pi C_0 t R R_b \left[0.318 \left(\frac{R_b}{R} \right)^{0.607 - 0.387 R_b / R + 1.20 (R_b / R)^2} + 0.067(n - 0.2) \right] \quad (1.23)$$

$$\sigma = C_0 \varepsilon^n \quad (1.24)$$

1.3 Summary on sandwich structures

Association of two materials within a sandwich structure has an important potential to improve the specific ability (in relation to the weight) to carry load. Analytical models describe accurately the behaviour of a sandwich beam while it undergoes only elastic deformation. Damage mechanisms can also be studied thanks to analytical models, nevertheless their predictions are limited to thresholds. A parametric study of the performances of the structures depending on their dimensions can be analysed easily in a map. When the sandwich structures undergo indentation of depth larger than the face thickness, models describing the load-indentation curves are often based on a membrane behaviour of the face.

Chapter 2

Generalities and performances of cellular materials

Contents

2.1	The contribution of material tailoring on properties	57
2.1.1	Stiffness at minimum weight	58
2.1.2	Energy absorbed for a prescribed maximal load	59
2.2	Hollow spheres stacking	60
2.2.1	Structural and architectural parameters	60
2.2.2	Processing	61
2.2.3	Local phenomena, macroscopic behavior and scaling laws	63
2.2.3.1	Local aspect	63
2.2.3.2	Macroscopic aspect	63
	Simple compression	63
	Tension	65
	Multi-axial compression tests	65
2.2.3.3	Representative Volume Element	66
2.2.3.4	Equivalent homogeneous medium	66
2.2.3.5	Scaling laws	67
2.2.4	Assets and weaknesses	67
2.2.4.1	Assets	68
	Cellular material	68
	Powder techniques processing	68
	Open porosity foam	69
	Close cell foam	69
2.2.4.2	Weaknesses	69
2.3	Summary on cellular materials	69

In this chapter the organization of matter is seen at a smaller scale, the scale of cells in a cellular material. First the benefit of this local distribution of matter on the macroscopic properties is investigated through various examples. Then we will focus on a particular cellular material : hollow spheres stackings. After a brief presentation of the structure and architecture of the material, the elaboration process is described. Then local phenomena occurring during deformation are reviewed. Macroscopic mechanical properties and the classical models used to describe them are presented and compared to other metallic foams. An overview of the assets and weak points of this material are finally outlined.

2.1 The contribution of material tailoring on properties

It has been seen in section 1.1 that the organization of matter at a macroscale (millimeter and above) and the association of materials can lead to a substantial improvement of the performances of a structure, while keeping its mass constant. The same conclusions are true at a smaller scale : the scale of the constitutive material. Tailoring of the matter distribution leads to a lower density material but it also decreases some mechanical properties. There is a competition between both parameters. Figure 2.1 shows locations of bulk and foamed aluminum alloys in an Ashby map of the Young modulus versus the density. It is noticeable that the bulk material presents the best specific Young modulus (E/ρ). Nevertheless specific properties do not lead to the optimal material in any configuration. Indeed, the example of the optimization at given stiffness of the weight of a beam loaded in pure bending will show how these foams may be of interest.

When looking for other properties such as the ability of the material to absorb energy, the foamed

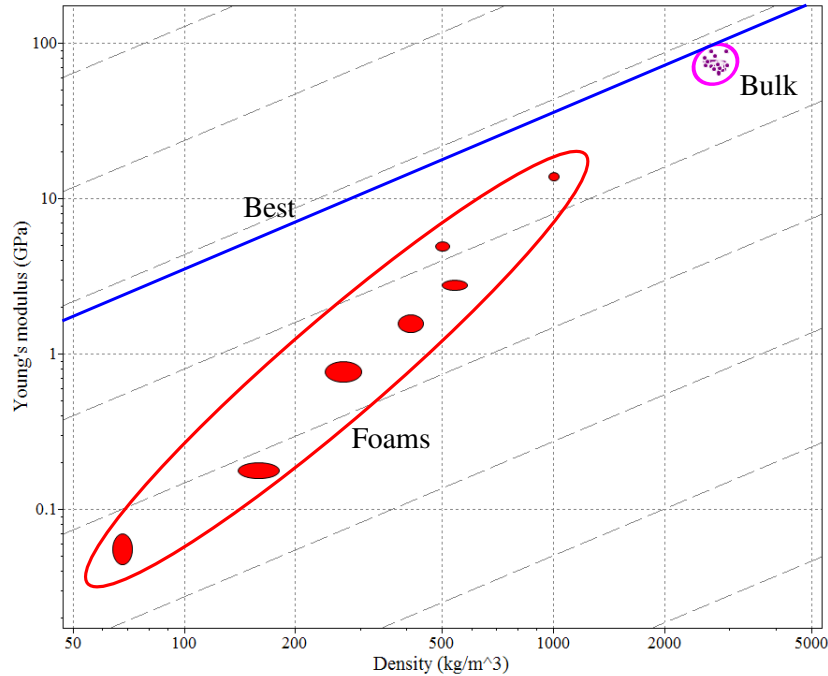


Figure 2.1: Ashby map of Young's modulus versus density of various aluminum foams and bulk aluminum alloys. Dashed lines indicates iso-values of E/ρ .

materials may become the best choice. It will be seen further in depth in the case of the optimization of the energy absorbed for a chosen maximal load.

This micro-architecture also has the ability to increase other properties such as acoustic absorption. The large number of degrees of freedom micro-architecture makes available might allow to get an optimal material for a multiple set of requirements.

2.1.1 Stiffness at minimum weight

The problem is similar to the one of section 1.1 : the minimization of the weight of a beam for a prescribed stiffness in the case of pure bending conditions, but now the constitutive material (E, ρ) and the beam thickness (c) are the free parameter.

Bending stiffness K and linear density m_x are related to the dimensions of the beam and to the properties of the material by :

$$\begin{cases} K = \frac{\mathcal{M}}{\theta_{,x}} = EI = \frac{Ebc^3}{12} \\ m_{,x} = \rho bc \end{cases} \quad (2.1)$$

The property to minimize is m_x , the geometrical degree of freedom is c and thus we obtain a relation between E and ρ that will help us to chose the optimal material.

$$\min(m_x) = \min \left(\frac{12\rho b^{2/3} K^{1/3}}{E^{1/3}} \right) \quad (2.2)$$

Since K and b are fixed, the optimal material is the one who maximize $\frac{E^{1/3}}{\rho}$. The equi-performance line on a Ashby map have thus a slope of 3 (and not 1 as in figure 2.1). When using this slope, as sketched in figure 2.2, it is obvious that foams are now more interesting than the bulk material. Nevertheless it should be kept in mind that if the weight is minimum, there is so far no constrain on the thickness c of the structure, and therefore the softer the material, the thicker will be the structure.

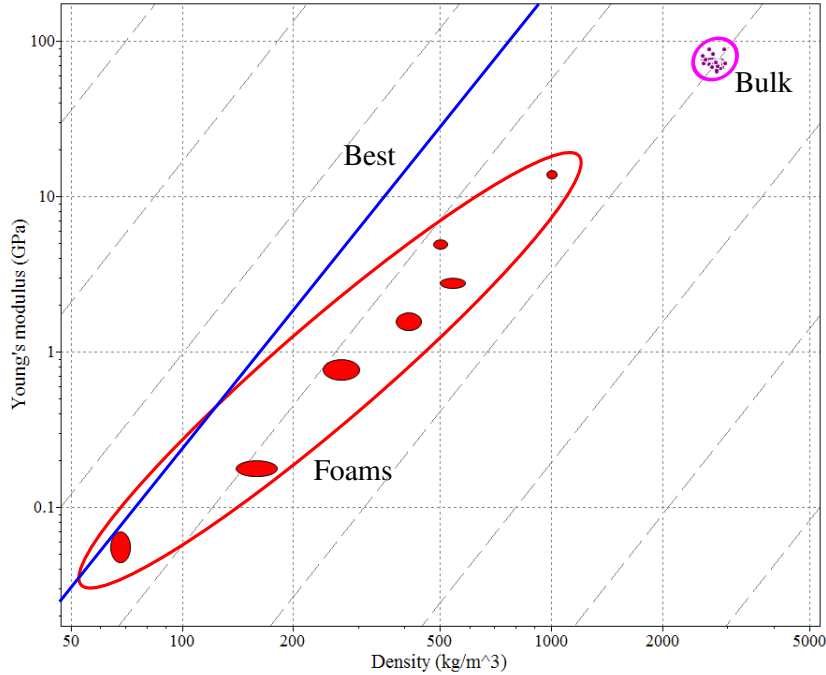


Figure 2.2: Ashby map of Young's modulus versus density of aluminum foams and bulk aluminum alloys. Dashed lines indicates iso-values of $E^{1/3}/\rho$.

2.1.2 Energy absorbed for a prescribed maximal load

The objective is now absorbing energy in compression loading with a constraint on the maximal admissible load, the problem is the following. We assume that the length (l) of the samples and the admissible load (F) are prescribed. The cross section area (S) is a free geometrical variable. Materials behavior is modeled thanks to a bi-linear law. Energy absorbed by unit volume e is thus given by :

$$e = \frac{\sigma_{Max} + \sigma_{yield}}{2} \left(\varepsilon_{Max} - \frac{\sigma_{yield}}{E} \right) + \frac{\sigma_{yield}^2}{2E} \quad (2.3)$$

The global absorbed energy \mathcal{E} and the maximal load F are related to the dimensional parameters and to the material properties by :

$$\begin{cases} \mathcal{E} = elS \\ F = \sigma_{Max}S \end{cases} \quad (2.4)$$

So the optimal material maximizes :

$$\max(\mathcal{E}) = \max \left[\left(1 + \frac{\sigma_{yield}}{\sigma_{Max}} \right) \frac{\varepsilon_{Max} - \varepsilon_{yield}}{2} + \frac{\sigma_{yield}}{\sigma_{Max}} \frac{\varepsilon_{yield}}{2} \right] \quad (2.5)$$

Qualitatively, the last equation shows that the optimal material is the one that can undergo the maximal elongation ($\varepsilon_{Max} - \varepsilon_{yield}$) and that presents a low hardening (that maximizes $\frac{\sigma_{yield}}{\sigma_{Max}}$). Theses properties are especially good for foams. Figure 2.3 shows the energy absorbed by unit volume of foams and bulk aluminum alloys in regards to their densities. Foams are more efficient than bulk material, even more if the weight is taken in account. If one also considers the Poisson ratio (which has been neglected in this model), it increases the advantage of foams since their lateral expansion is almost null. There is an

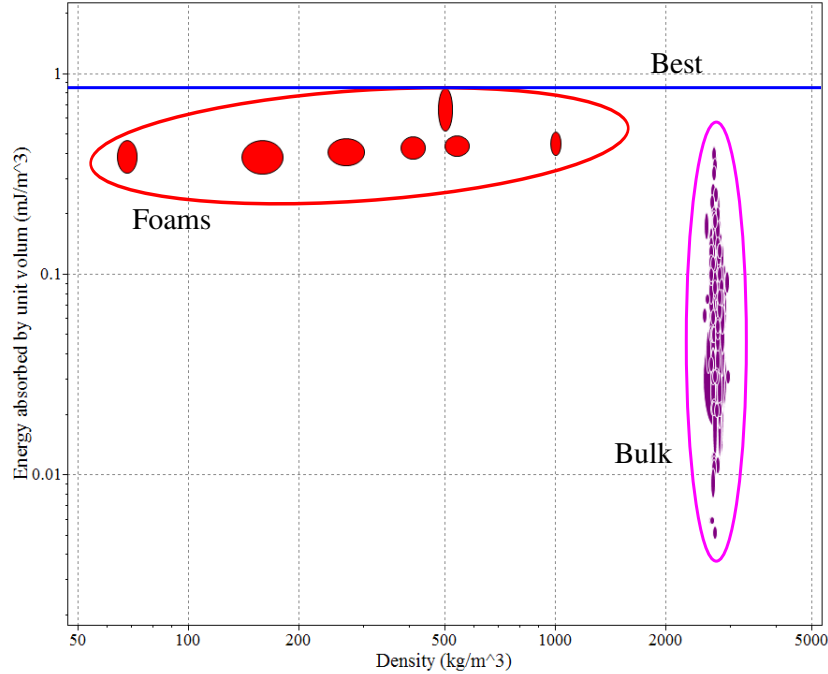


Figure 2.3: Ashby map of energy absorbed \mathcal{E} versus density of aluminum foams and bulk aluminum alloys. Dashed lines indicates iso-values of \mathcal{E}/ρ .

obvious advantage in micro-architecturing matter into foams. The variety of such materials is huge (see Gibson-Ashby for an overview). We will now focus our attention on a special type of micro-architected material.

2.2 Hollow spheres stacking

This PhD focuses on one kind of cellular material : hollow spheres stacking. In this chapter, the structure and the architecture of the material as well as its processing will be presented. Then local deformation mechanisms and macroscopic behavior will be investigated. Finally the material assets and weaknesses will be described.

2.2.1 Structural and architectural parameters

Hollow spheres foams are constituted of hollows spheres of external radius R and of shell thickness t . Spheres are bonded thanks to a neck of radius a that can be approximately be deduced from the geometric indentation h between two spheres⁵). Theses parameters are relative to the structure of the material. The architecture of the material is relative to the organization of the cells. Two parameters

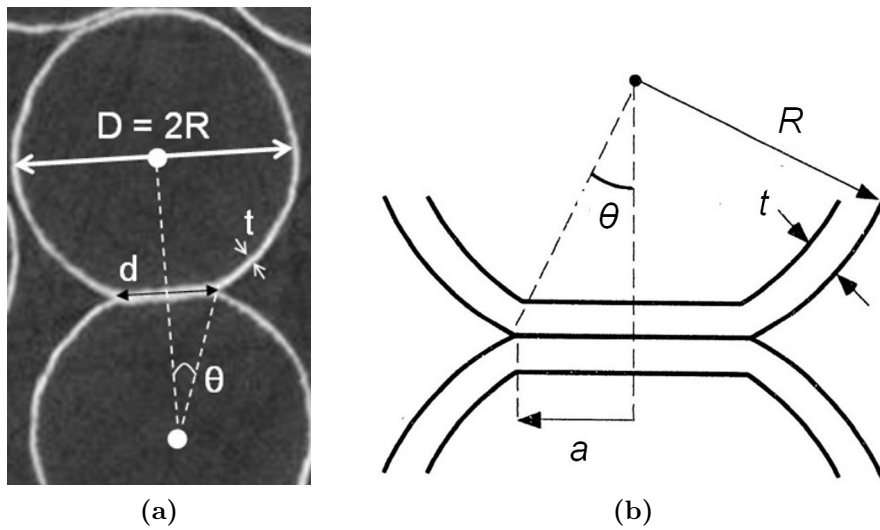


Figure 2.4: Tomography 2D slice and drawing describing the structural parameters of the hollow spheres stacking.

are used to describe the architecture. The first one is the number of contacts between spheres. The number of contacts per sphere is called “coordination number” and is denoted Z . The second one is relative to the orientations of the contact (or to the organization of the spheres). Several indicators of the “crystallinity” of the stacking can be used. The radial distribution function (also called pair-correlation function) describe the distribution of distances between particles [Truskett *et al.*, 1998]. Some distances (such as $\sqrt{2}R$) are indicators of crystallographic organization. Another indicator is the bond-orientational order Q_6 that looks for the mean spherical harmonics [Steinhardt and Ronchetti, 1983].

As any other foams, one might also want to qualify the foam with a single parameter provided the sample can be seen has homogeneous. This parameter is the relative density ρ^* , which is the ratio of the volume occupied by the matter on the total volume. It depends on t , R , a , and on packing compacity. Since this parameter is invariant by similarity, it is more relevant to express it according to adimensional parameters.

Thus stackings will be characterized by:

⁵ h is the variation of distance between the two spheres center in contact. For a punctual contact h is equal to zero.

- t/R : the relative shell thickness
- a/R : the relative neck size
- Z : the coordination number
- ρ^* : the relative density
- a quantitative appreciation of the disordered character

2.2.2 Processing

Several routes exist for the processing of metallic hollow spheres. All of them are described in [Fallet, 2008] (p41). Since all the foams used during this PhD were provided by *PLANSEE* and have been realized with the same process, only one way of processing will be explained. This process has been developed by IFAM (Institut Fertigungstechnik Materialforschung - Dresden). Figure 2.5 gives an overview of the process stages.

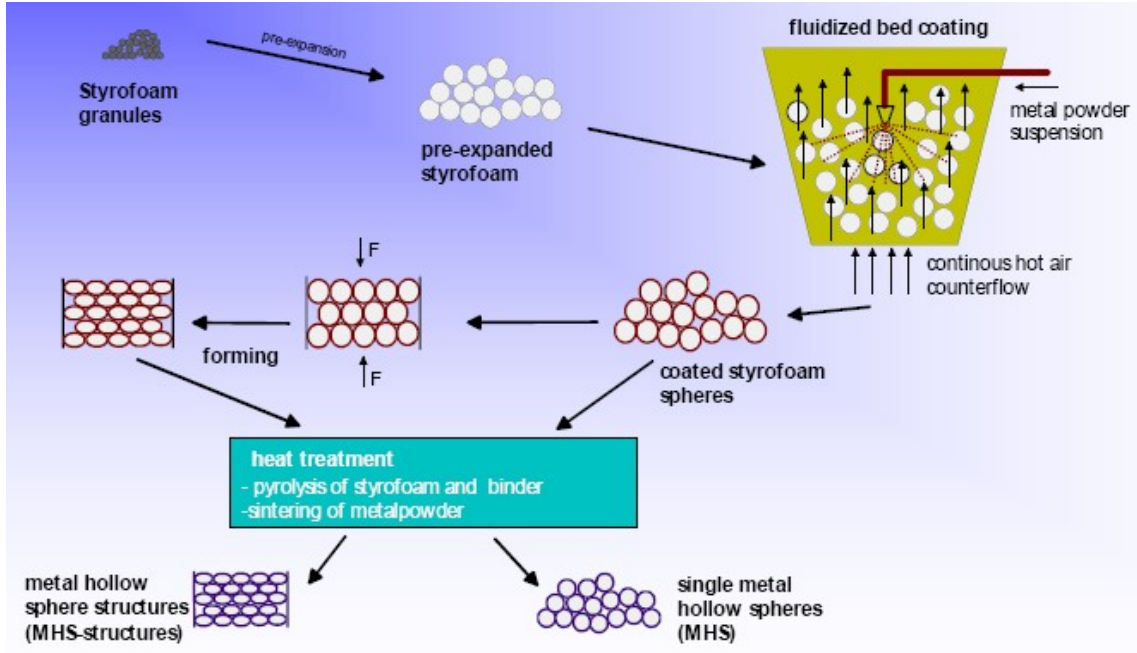


Figure 2.5: Overview of the PLANSEE process for hollow spheres stackings.

The first step consists in the coating of Styrofoam balls with a slurry of mixed metallic powder and organic binding agent. It gives what is called “green spheres”. Then these spheres are randomly packed thanks to gravity. The packing is compressed isostatically, thus creating large contacts between particles. The structure is congealed by debinding. Styrofoam is gaseified and it escapes through the porosity of the shells. Spheres are now hollow. Finally the mechanical properties are conferred to the material thanks to a sintering treatment, ensuring in a single step the cohesion of the shells and of the contacts.

Several remarks can be made about this processing route.

- Since the route chosen is based on powder sintering, it seems that these stacking could be elaborated with any material that can be processed by this technique. It might be interesting to get

such foams with ceramic or super alloys as constitutive material. In this PhD, the hollow spheres are made of stainless steel (314, norm AISI).

- The internal radius of the spheres is imposed by the Styrofoam ball. The dispersion of size of the space holders is directly transposed on the dispersion of size of the foam cells.
- The thickness of the shells is given simultaneously by the thickness of the slurry coating and by the sintering conditions⁶. Due to the surface tension, outer face of the shells are very smooth and regular. On the contrary, the internal face roughness is imposed by the Styrofoam surface roughness, that may reach several tens of micrometers. Thus the shell thickness can locally be very variable (mean thicknesses range from about $50\mu m$ to $100\mu m$). Furthermore, the sintering process often leads to irregular porosity in the shells. These assessments must be kept in mind when using the mean shell thickness value as a structural parameter.

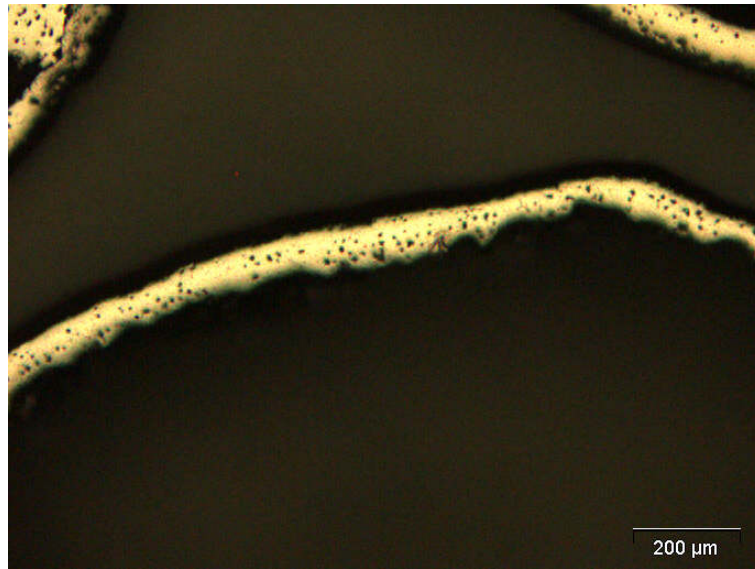


Figure 2.6: A shell observed by optical microscopy. Its porosity and the variation of thickness can be seen.

- The contact size (that will be called “neck size” in the following) is driven by the compression stage. This stage also plays a role on the coordination number. Both parameters (neck size and coordination number) are related through the behavior of Styrofoam balls. One can expect stiff balls to favor reorganization of the packing while soft balls should enlarge the neck size to increase the density.
- Since the Styrofoam balls are first coated and then stacked, the neck thickness must be twice the shell thickness (provided the sintering is homogeneous).

All these observations will be of interest when trying to quantify the structural parameters and then use them for modeling the material behavior.

⁶Depending on the sintering conditions, for a given amount of coating, one can obtain either a thick porous shell, either a thin dense shell.

2.2.3 Local phenomena, macroscopic behavior and scaling laws

When interested in the mechanical properties of hollow spheres stackings, one can look for its behavior at various scales.

2.2.3.1 Local aspect

The local aspect is relative to observations at meso-scale, the scale of a cell. As seen above, spheres are connected via the necks. During deformation, this neck transmit forces from one sphere to another. Under this loading, shells deformation occurs. [Fallet, 2008] showed that deformation mechanisms of the contact is due to plastic hinge (or plastic ring) in the shells. This localized deformation can lead to indentation (the penetration of a sphere in the other) if the plastic ring changes of location in one of the shells. Figure 2.7 shows plastic rings and indentation mechanisms on 2D slices from a volume obtained by tomography. Another local phenomenon that is of importance is the creation of contacts. These

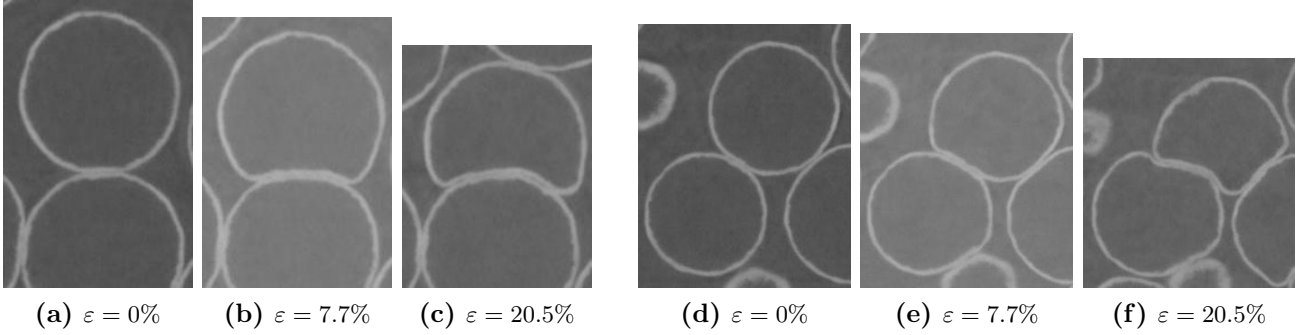


Figure 2.7: *a,b-Formation of a plastic ring in the upper shell under compressive loading. c-The plastic ring location changes and led to an indentation. d,e-Formation of a plastic ring in both shells under shear loading. f-The plastic ring locations do not change and thus symmetry is approximately kept.*

new contacts are unilateral and non permanent. Nevertheless they could play a fundamental role in the strengthening of the material while deformation proceeds. Figure 2.8 illustrates how two spheres can enter in contact thanks to their deformation and/or the deformation of other spheres. Contact can also be created between two parts of the same sphere. It occurs during the sphere crushing. In its final stage, it is also an important strengthening mechanism. Figure 2.9 shows examples of crushed spheres.

2.2.3.2 Macroscopic aspect

The macroscopic mechanical behavior of foams is rather similar. It has been widely investigated for foamed and replicated aluminum foams. Investigations on hollow spheres foams are less numerous, especially for random packing. Thus in this section, the behaviour of various foams will be presented and compared to the behaviour of hollow spheres stackings.

Simple compression The classical compressive behavior is schematically the following. First an elastic domain is encountered. Then comes a plastic domain called “plateau” where the stress is constant or at least the stress strain curve presents a low and constant hardening modulus. And finally comes an important increase in the stress due to densification mechanisms. Figure 2.10 shows strain-stress curves of various foams. Hollow spheres stackings do not have a distinctive behavior except for the smoothness

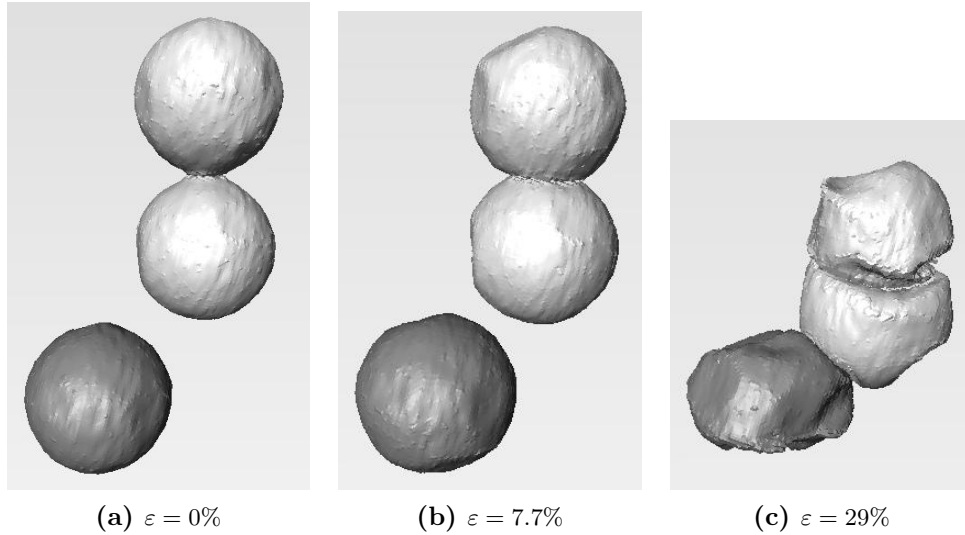


Figure 2.8: 3D visualization of 3 spheres extracted from a tomographic volume. **a,b**-Bright and dark spheres are not in contact. **c**-A contact is created between dark and bright spheres.

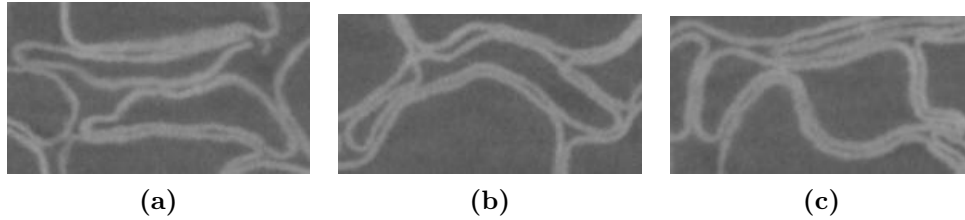


Figure 2.9: Slices of tomographic volume that show various crushed spheres.

of the curves. Actually when observing the strain field at the surface of a classical foam sample undergoing compression, one can often see strain localization in bands. This reflect local instabilities such as buckling of the cell walls. Among all the studies on compression behavior of foams, some get

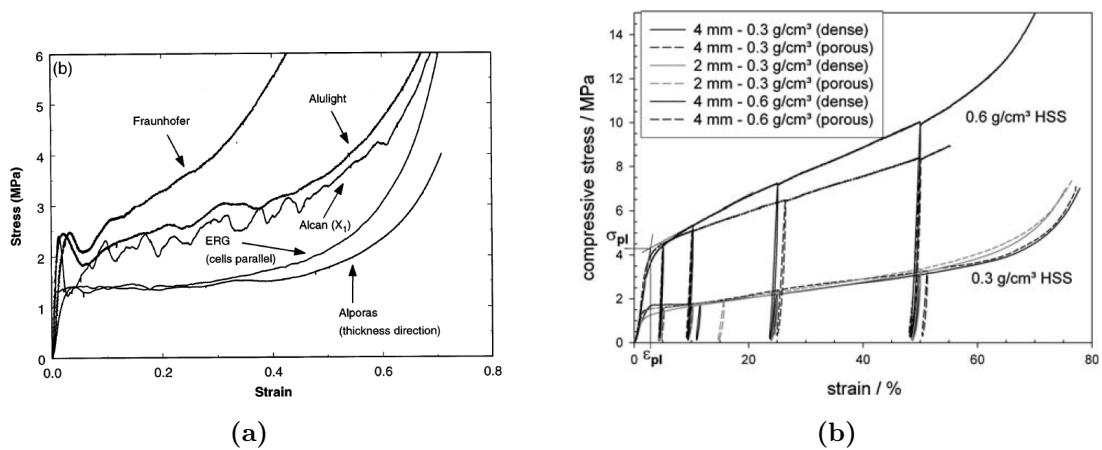


Figure 2.10: **a**-Stress-strain curves of various foams under simple compressive loading [Andrews et al., 1999]. **b**-Stress-strain curves of hollow spheres stackings [Friedl et al., 2008].

also involved in the investigation of the evolution of the stiffness. The stiffness decreases substantially during the first percents of strain, then it can oscillate or remains rather constant, and finally it rise up during densification. Figure 2.11 shows the evolution of the stiffness with strain for various foams.

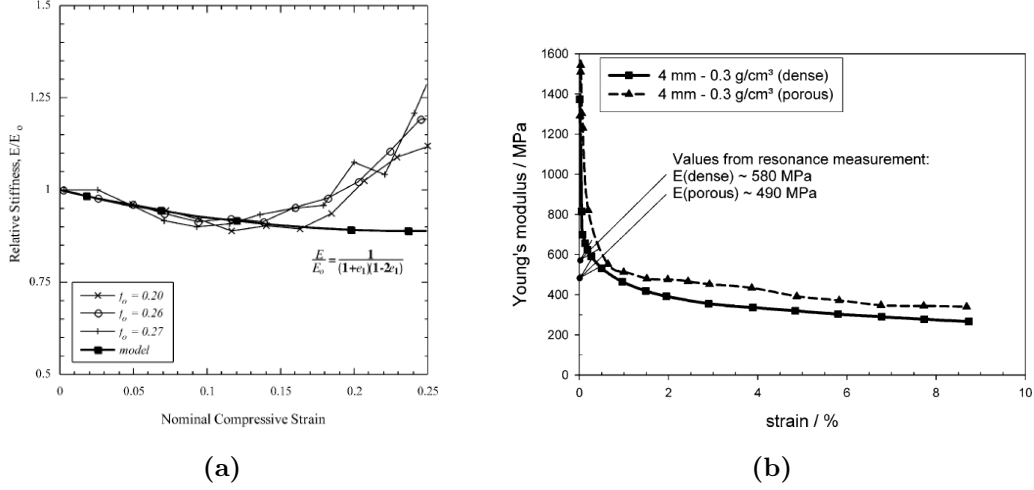


Figure 2.11: **a**-Unloading modulus evolution with strain of aluminum open cells foam under simple compressive loading [Marchi and Mortensen, 2001]. **b**-Same graph for hollow spheres stackings [Friedl et al., 2008].

Tension The tensile behaviour of closed cells foams ([Motz and Pippin, 2001]) and of open cells foams ([Dillard *et al.*, 2005]) have been qualitatively and quantitatively studied. Few studies reports the tensile behavior of hollow spheres stacking. [Motz *et al.*, 2005] investigated the influence of the porosity of the shells on the tensile behavior (figure 2.12). He shows that shell porosity limits the macroscopic elongation but do not significantly changes the stress-strain response. Ultimate elongations were found to range between 1% and 4%.

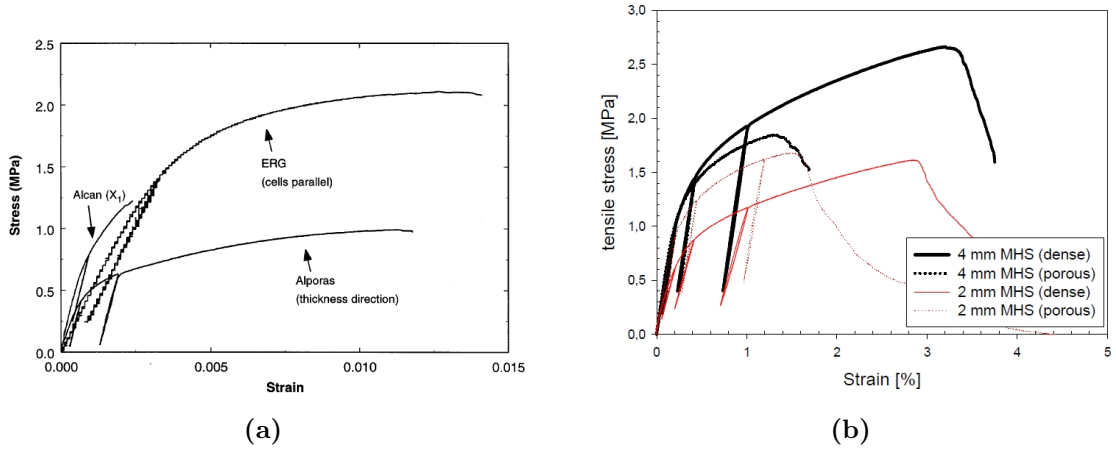


Figure 2.12: **a**-Tensile behavior of various aluminum foams [Andrews et al., 1999] **b**-Stress-strain curves of hollow spheres foams of a given density ($\rho = 340\text{kg/m}^3$) with two spheres radius (2 and 4 mm) and two types of shells (dense or porous) under simple tensile loading [Motz et al., 2005]

Multi-axial compression tests [Deshpande and Fleck, 2000] measured the stress versus strain response of various aluminum foams along several proportional stress paths. The influence of the loading path on aluminum foams behaviour can be seen in figure 2.13a. No experimental results on the behavior of random hollow spheres stackings has been found in the literature. Nevertheless Finite Element simulations have been performed on regular stackings (SC, BCC, and FCC) of hollow spheres

by [Sanders and Gibson, 2003a]. Figure 2.13b shows the yield surface on axes of effective stress versus mean stress for various regular packings of hollow spheres. Multi-axial compression tests on random

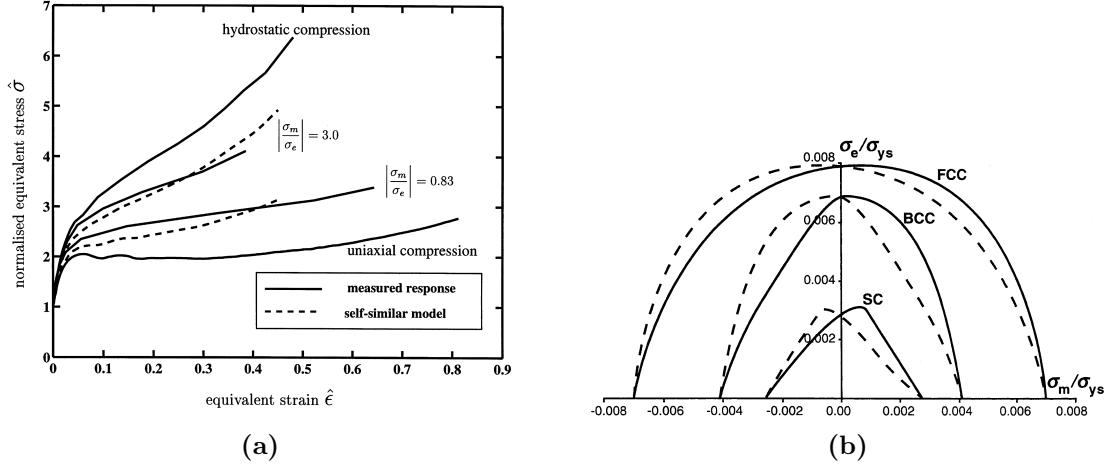


Figure 2.13: *a*-Influence of the loading path on aluminum foams behaviour [Deshpande and Fleck, 2000]. *b*-yield surface on axes of effective stress versus mean stress for various regular packings of hollow spheres [Sanders and Gibson, 2003a].

stackings has also been simulated with Discrete Element Method by [Fallet, 2008] (figure 2.15).

2.2.3.3 Representative Volume Element

Ultimately in this PhD we are interested in sandwich structures with a core of hollow spheres. Therefore the desired modeling is the one of a homogeneous medium in order to apply either beam theory, either finite element modeling, the volume element considered must be several cells size large. In fact the difficulty is to define a Representative Volume Element (R.V.E.), a volume which is large enough to limit dispersion and which leads to the same behaviour that the infinite medium. [Lim *et al.*, 2002] showed that for a sample side of 10 times the spheres diameter the scatter of compressive behavior is low (Fig.2.14). [Andrews *et al.*, 2001] found that from a sample size of 6 or 7 times the cells size, the compressive properties (as in stress as in stiffness) are representative. But it also found that when looking on the shear behavior, the R.V.E. side size can be 2 or 3 times smaller. It is consistent with the fact that the R.V.E. is defined for a physical property measured under a given loading. Techniques to determine the R.V.E. can be either numerical [Kanit *et al.*, 2003] or experimental [Andrews *et al.*, 2001].

2.2.3.4 Equivalent homogeneous medium

Assuming that the R.V.E. is set, modeling of the behavior can proceed. [Deshpande and Fleck, 2000] proposed a plasticity model based on an elliptic criterion with various hardening laws. [Miller, 2000] developed a model based on a Drucker-Prager criterion adjusted thanks to the compressive and tensile yield strengths and to the plastic Poisson ratio. [Hanssen *et al.*, 2002] compared the ability of these models, compared to other models LS-DYNA implemented in ABAQUS, to reproduce the behavior of aluminum foams under various loading conditions. [Badiche *et al.*, 2000] also proposed an elliptical model. [Dillard *et al.*, 2006] improved it by introducing a material length with a micromorphic medium. All these models allows the description of the material behavior under tri-axial loadings, nevertheless

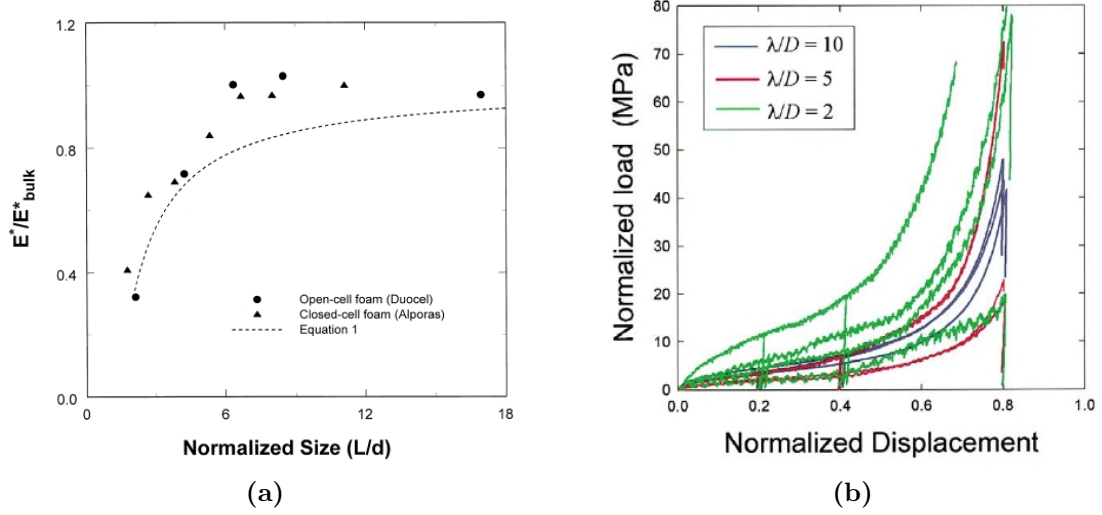


Figure 2.14: *a*-Evolution of the Young's modulus of open and closed foams with the sample size [Andrews et al., 2001]. *b*-Stress-strain curves of hollow spheres foams samples of various sizes under simple compressive loading (λ is the sample side size while D is the spheres diameter) [Lim et al., 2002]

they may require cumbersome fit with numerous experiments. Furthermore no one is able to transcript the evolution of the Young's modulus with strain. Finally one can ask if a plastic multiplier contains enough information on the state of a cellular material. Other internal parameters might be of interest in order to quantify for example the local heterogeneity of spheres deformation, or the damaging of the contacts.

[Fallet, 2008] showed numerically that the Miller criterion seems to fit better the hollow spheres stackings plastic surface than the model of Deshpande & Fleck (Fig. 2.15).

2.2.3.5 Scaling laws

Once a model is chosen and its parameters are evaluated, one would like to predict the behavior for another configuration of the material. The classical characteristic parameter for the behavior of a foam, for given architecture and structure, is the density. Hence for a given configuration, the parameters might be described phenomenologically by a power law of the initial density (Equation 2.6). Theses laws are very useful to perform optimization. Furthermore, the exponent of the power law can be an indication of the local deformation phenomena within the material. For example for a power law for the stiffness, an exponent close to unity is an indicator of compressive/tensile local loading, while an exponent close to two reveals a local dominated loading bending.

$$\frac{P(\rho_2)}{P(\rho_1)} = \left(\frac{\rho_2}{\rho_1} \right)^n \quad (2.6)$$

2.2.4 Assets and weaknesses

Hollow spheres stackings have numerous assets but also some weaknesses.

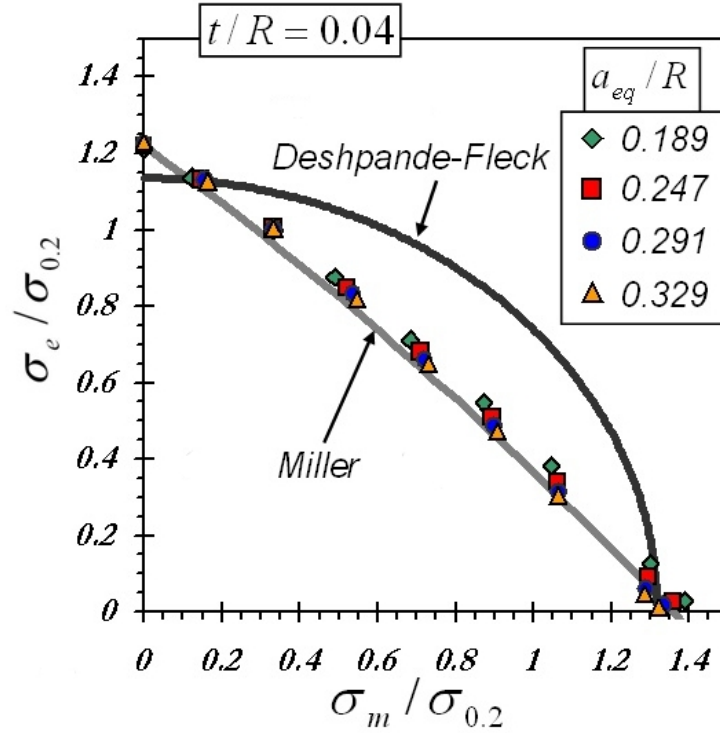


Figure 2.15: Yield surface among normalized mean stress and normalized effective stress for various criterion and for DEM simulations[Fallet, 2008]

2.2.4.1 Assets

Cellular material Hollow sphere foams are cellular materials. It gives them additional degrees of freedom to optimize the material. In our case, one can play as well on the cell size, on the shell thickness, on the number of contact between spheres, but also on the contact size. All these parameters can be approximately chosen independently⁷. Thus this material presents great potential for adaptability to a given set of requirements.

This 3D cellular aspect allows to generate complex macroscopic shapes especially since stacking is random. In addition, this cellular aspect with controlled wall thickness (shell thickness) lead to a very reproducible behavior, this property being uncommon to closed cells foams. The shape of the cells and the architecture induce a soft behavior compared to other foams that tend to buckle.

The architecture of the material could also be modified, either by using multimodals stackings (several spheres sizes), either by using non spherical space holders in order to increase the number of contacts between particles [Donev *et al.*, 2004].

Powder techniques processing The elaboration process provides also a large number of degrees of freedom. First one have in theory a large choice for the constitutive material. It just has to have the ability to be processed by powder metallurgy sintering techniques at temperature superior to the sublimation temperature of the styrofoam. Then changing the powder particles size, one can vary the

⁷This remark is only partially true for the neck size and the coordination number. They are partially linked by the stacking and compaction processes. Nevertheless one can manage to change one without the other. Almost no reorganization and an important compaction of the stacking lead to large necks. A first step of densification by reorganization followed by a densification leading to the same coordination number would rather give small necks.

final grain size within the shell. A multi material shell is also conceivable. Playing on the sintering process parameters, one can also vary the density of the shell.

Open porosity foam Stacking of spheres presents a connected porosity. It can be seen as an open porosity foam. So it contains paths for a fluid to penetrate. The high specific surface is favourable to thermal exchange or dissipation by friction. Thus acoustic absorption properties are good. The size of the paths and their tortuosity can be adapted to absorb a particular wave length range [Gasser *et al.*, 2003].

Close cell foam The fact that spheres are hollow gives a close cell foam aspect to these stackings. The constant shell thickness and the curvature of the cells give it as the "high" mechanical properties of a close cells foam, as well as a soft behavior with regular hardening. Buckling behavior is actually avoided thanks to the spherical shape of the cell with their large number of contacts. It prevents "large" portions of shell to accumulate important elastic compressive stress, which would make it unstable. The income of stress is compensated either by local hardening, either by creation of new contacts.

2.2.4.2 Weaknesses

Hollow spheres stacking presents nevertheless important limitations. First, the processing is expensive. Then machining can only be done by soft techniques such as electro-erosion in order not to damage the material. It also induce an important cost of the material implementation.

The large number of theoretical constitutive material is in practice limited. Up to now, hollow spheres have only been made in iron, steel, titanium and molybdenum by powder metallurgy techniques [Augustin and Hungerbach, 2009]. Other processing routes such as electro deposition have been tested ([Blotti re *et al.*, 1985],[Blotti re *et al.*, 1993]) with nickel, but the scatter of shell thickness is large, thus the macroscopic behaviour is not well controlled and by the fact the processing of such structures has been stopped.

Next come the mechanical limitations. The material can only carry low stresses and it is very sensitive to localized stresses. So its use can only be considered in combination with other materials within a structure.

2.3 Summary on cellular materials

Micro-architected materials are material which are given several further degrees of freedom. It allows them to reach combination of properties that bulk materials cannot reach. Among all the mechanical and general properties they are particularly efficient for the specific properties for stiffness and strength. Their ability to endure large deformation is a key point in the problem of energy absorption. Hollow sphere stackings present particular combination of properties linked to its double type of porosity, such as good acoustic absorption with high isotropic mechanical properties. The regularity of the cell walls (shell thickness), the shape of the cells (spherical), and the type of stacking (random) ensure a regular, homogeneous and very reproducible macroscopic behavior.

Summary

Sandwich structures

Association of two material within a sandwich structure has an important potential to improve the specific ability (in relation to the weight) to carry load. Analytical models describe accurately the behaviour of a sandwich beam while it undergoes only elastic deformation. Analytical models have also been developed to predict the damage mode of theses structures. Maps depending on geometrical dimensions and material properties, can describe either the predominant failure mode, or the location of optimal structures for a given requirement. All theses models are very sensitive to the core material behavior.

Hollow spheres stackings

Among the metallic foams, hollow spheres stacking are of particular interest. A number of controlled and independent degrees of freedom gives them high adaptation abilities. Their potential interest increases for multifunctional set of requirements. Acoustic absorption and energy absorption with maximum prescribed load are potential field of application. State of art on random hollow spheres stacking is limited to local phenomena and early stages of the deformation. The existing modelling tools for their behaviour have to be improved to deal with finite strains.

Part II

Starting point, investigation strategy
and experimental methods

Chapter 1

Starting point : State of the art

Hollow spheres stackings

Structure

Some samples of hollow spheres stackings were available. These samples have been analysed thanks to X-ray tomography and image analysis [Fallet, 2008]. These analysis give information on the structure of the stackings.

⇒ Nevertheless the knowledge of the samples is not sufficient to fully understand the mechanical behaviour (for example, the stiffness is not well predicted). First, the dimensions of shells and necks have been characterized only by their mean values. The roughness and porosity of the shells have not been quantified. Measurements of necks size are also subject to caution especially as far as their scatter is considered. The disordered character of the stacking has not been studied.

Mechanical behaviour

The samples behaviour has been characterized under fatigue loading by O. Caty.

⇒ In collaboration with A.Fallet, we performed an analysis of the response of the material to uniaxial compression loading.

⇒ The behaviour under tensile loading, or under multi-axial loading has not been studied. In addition all previous studies of hollow spheres stackings only focused on low strain response.

Simulation tools

A. Fallet implemented a model for hollow spheres stackings in the Discrete Element Model code dp3D [Martin *et al.*, 2003].

⇒ A number of limitations had to be overcome and an improved code has been developed.

- The contact laws allowed to model only bi-linear elasticity. It was thus impossible to obtain any relevant unloading modulus all along stress-strain curve. The description of the contact law did not take into account the stiffness evolution of the contact with strain.
- The contact between two non bonded sphere was modeled by a Hertz contact of two plain spheres

of approximated Young's modulus. This modeling might generate some unrealistic softening or hardening behaviour.

- The macroscopic loading was limited to periodic boundaries conditions. No law of contact between a hollow sphere and any other object (a plane, a indent ...) had been implemented. Moreover it was not possible to prescribe the motion of a single sphere. So simulations with non-periodic boundaries conditions or with imposed motion of outer particles were not possible.
- Two problems were encountered about the shear loading between particles.
 - The first one deals with a wrong implementation of the shearing law of two particles in the code.
 - The second one is related to the way the code computed global stresses. Elementary shear loads were not taken into account for the computation of the macroscopic stresses. The simulation stress-strain curves present a low hardening slope which is in contradiction to the important hardening of the elementary shear law. The accordance to experimental results is thus fortuitous.

It implies that all the results and observations related to this model in [Fallet, 2008] had to be taken with precaution. Thus the model was limited to predictions up to the initiation of plasticity, with only periodic boundaries conditions.

Sandwich structures

⇒ To our knowledge, no study on the behaviour of hollow spheres stackings integrated in sandwich structures have been performed.

PLANSEE provided us a set of sandwich structures with hollow spheres foam core. The behaviour of the core material was assumed to be known thanks to previous experiments on hollow spheres stackings.

⇒ Nevertheless the core material structure and properties have been changed during the fabrication of the sandwich and this modification has to be taken into account.

Chapter 2

Strategy of this PhD

Based on the above observations, the following investigation strategy has been carried out.

Hollow spheres stackings

Structure

First, an accurate study of the shells and necks structure is performed, based on optical microscopy, scanning electron microscopy and X-ray microtomography in order to quantify the porosity and the roughness of the shells.

Then a precise measurement of the neck size is performed.

Mechanical behaviour

The study on the compressive behaviour of the stackings performed in collaboration with A. Fallet is presented. Then the mechanical behaviour is studied both under tensile loading, and under multi-axial compressive loading.

Discrete Element Modeling

The DEM code is improved. First of all, the local shear loads are better taken into account in the computation of the macroscopic stresses. Then an elasto-plastic behaviour is implemented in the local laws. The local stiffness is varied with the relative motion of the particles. The local law for new contacts is improved. Contact laws with planar objects are also implemented. Comparisons to the experiments are performed and potential improvements are discussed.

Structure evolution and modeling

The evolution of the structure is analysed thanks to X-ray tomography. Local deformation mechanism are related to the macroscopic behaviour. A model for the macroscopic behaviour based on the local mechanisms is set up, calibrated and validated.

Sandwich structures

Structure and mechanical behaviour of the core material

An analysis of the hollow spheres stackings, *after it has been integrated in a sandwich structure*, is performed, both from the structural point of view and from the mechanical point of view. A model of equivalent homogeneous medium is fitted.

Four-point bending

Sandwich beams are tested under four-point bending loading. Results are compared to the prediction of both analytical models and Finite Elements simulations. Special attention was paid to the damage modes.

Plate indentation

The behaviour of sandwich plates under large indentation loading is studied and compared to models.

Chapter 3

Investigations tools for the hollow sphere materials

Contents

3.1	Experimental tools	79
3.1.1	Macroscopic tests	79
3.1.1.1	Simple compression test	79
3.1.1.2	Tensile test	80
3.1.1.3	Multi-axial compression test	81
3.1.2	X-ray tomography and in-situ tests	83
3.1.2.1	Principle of X-ray tomography	83
3.1.2.2	Uni-axial in situ tests	85
3.1.3	Images analysis	85
3.1.3.1	Objectives	85
3.1.3.2	Tools	86
3.1.3.3	Strategy and methods	86
3.2	Simulation tools	86
3.2.1	Discrete Element Method (D.E.M.)	87
3.2.2	Mesoscopic Finite Elements	87
3.2.3	Macroscopic Finite Elements	88

To investigate the behavior and the properties of a material, we have performed a coupled study with experiments and modeling tools. Experiments are the reference behavior. Then either by simple analytical models as in the case of power laws, or by numerical simulations (in one or several steps), the behavior of a variation of the initial material can be predicted. From the types and the outputs of experiments depend the types of simulation tools that can be used and so the scale, the completeness and the accuracy of the prediction.

Thus for experimental tools and for modeling tools, requirements, procedures and outputs are presented.

3.1 Experimental tools

In our case experimental tools provide two types of fields : a displacement field (or strain field if the scale is large enough compared to the cell size) and a stress field. Neither time, neither temperature, nor any other parameter have been investigated nor taken into account since they were assumed to remain approximately constant. Thus two kinds of experiments were investigated. The first ones are called “macroscopic” (in relation to their output) that give relation between the mean stress on the boundaries and the global strain of the samples. They aim at linking both fields through an averaging over a large number of cells. The second ones are in situ tests which might at first sight look like upgraded macroscopic tests. Nevertheless their accuracy at this level is low. They rather enlarge the knowledge of the strain field by giving access to the complete displacement field of the frame of the material. Thus they relate local phenomena to the global strain of the sample.

3.1.1 Macroscopic tests

We focused on three macroscopic tests that in principle should give an homogeneous strain field within the sample : simple compression, tension and multi-axial compression.

3.1.1.1 Simple compression test

Compressive tests are performed on cubic samples of side size ranging from 10 to 30 mm. A macroscopic strain rate is chosen (usually around $10^{-3}s^{-1}$) and various loading-unloading sequences are performed with increasing maximal strain. The machine gives the load and the macroscopic strain at any time. The macroscopic strain can be corrected for machine stiffness thanks to tests performed without samples. The stiffness and especially clearances of the machine are thus appropriately subtracted. This might be of importance for the measures of the stiffness of the samples. Another option is to use a RDP sensor between both compressive plates that records the true length of the sample.

In order to have an idea of the strain repartition within the sample, tests can be registered by a digital camera. Digital image correlation (presented in appendix A.1) allows to obtain the 2D strain field on one of the face of the sample (Figure 3.1). The strain heterogeneity on that face is assumed to be representative of the strain field inside the volume. This measure can also be used to measure the macroscopic strain. So macroscopic tests give access to :

- stress-strain curves assuming that the fields are homogeneous.
- unloading stiffness for each unloading sequence at different stages of straining provided the strain measure during unloading is accurate enough

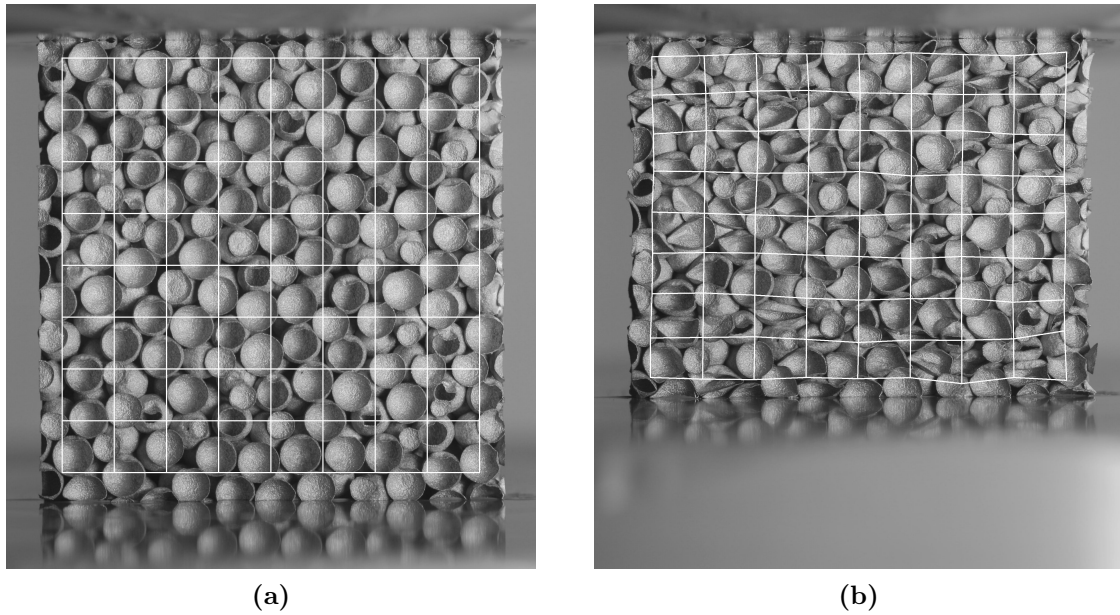


Figure 3.1: 2D strain field obtained by digital image correlation. **a**-Initial sample. **b**-Sample loaded in compression.

- an estimation of the strain field heterogeneity

3.1.1.2 Tensile test

Tensile tests are much more difficult to perform on such material. Actually the thickness of the samples have to be large enough to load a R.V.E. and thus pinching techniques are useless. Various bonding and resin permeating techniques have been tested without any convincing success. The operating tests is done on “dog bone specimens” with double smooth blend. Heads are reinforced with thin steel plates and are permeated with epoxy resin. Specimens are loaded in tension thanks to rollers depressing on the T-branches. Figure 3.2 gives an overview of the samples shapes and of the tensile system. Tensile tests are performed on the same machine that for simple compression nevertheless the system used imply some specificity. Since the system is compliant and since a large useless part of the specimen is deformed in a uncontrolled way precision on the strain is low. No correction method have been used. Therefore the most accurate values of the strain were given by digital image analysis on one face deformation.

Tests are carried up to complete failure of the samples, they allow to study the fracture surface. Theses observations are made by Scanning Electron Microscopy. So tensile tests give access to :

- stress-strain curves
- unloading stiffness for each unloading sequence
- an estimation of the strain field homogeneity
- the fracture surface

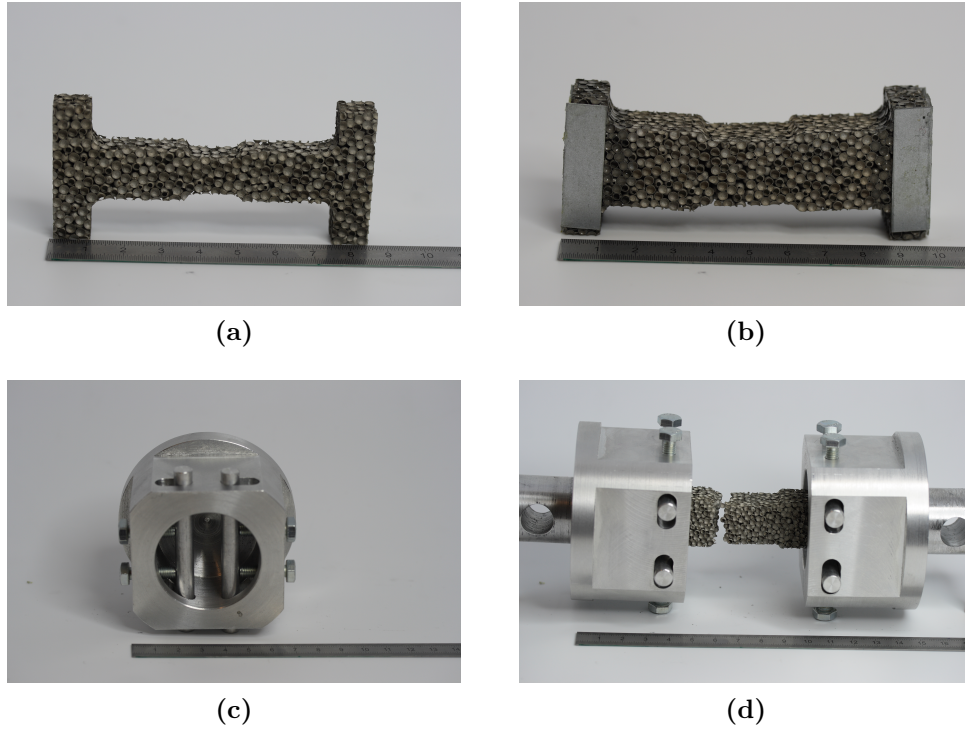


Figure 3.2: *a-Tensile specimen of cubic working volume of 10 mm side size before reinforcement of the heads. b-Tensile specimen of cubic working volume of 20 mm side size after test. c-Top view of one part of the tensile system (Screws are used to fix the rollers span). d-Front view of the tensile system with a specimen after failure.*

3.1.1.3 Multi-axial compression test

Two methods have been used for multi-axial compression tests.

- The first one is based on imposed motion at the boundaries thanks to entangled plates. A testing device has been developed at the École Polytechniques Fédérale de Lausanne (EPFL, Switzerland) to study replicated aluminum foam behavior. This method needs finely shaped specimens. Figure 3.3 shows a specimen and how its is loaded in the machine. In order to have the most uniform fields in the material, the symmetry in relation to the orthogonal plans each of the three axis have to be respected. Thus the system is equipped of 6 motors. Load sensors register the load over each axis. The tests can be driven as well with imposed strain as well with imposed stress. The great difficulty of this system is the control of the motors. Since these tests are often used to draw a surface of plasticity, the strain measurements precision is a crucial point. It has to be remembered that the stiffness of the tested material plays an important role on the accuracy and on the time of response of the actuators. Thus the system is adapted for a range of material properties (stiffness of order of hundred of MPa). If one tests materials out of this range, precision of measures drops significantly and so the quality of the post-mortem analysis.
- The second one originates from the soil mechanics community. Figure 3.5 describes the tri-axial pressure cell. A cylindrical sample is introduced in a neoprene membrane. The stress is imposed by planes over the axis of the cylinder while the stress is imposed on the radial face thanks to a

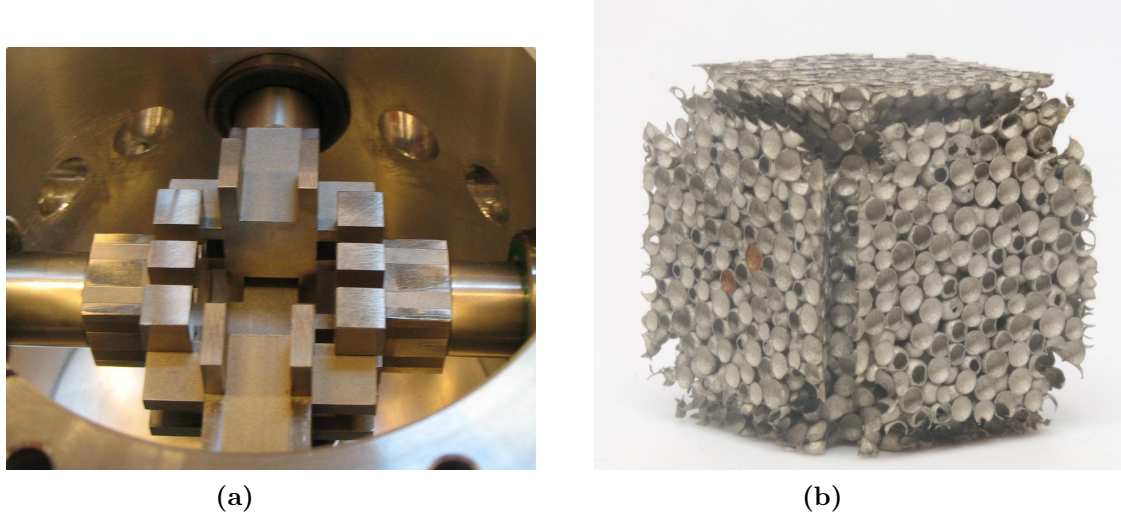


Figure 3.3: *a-Entangled plates of the multiaxial machine of EPFL. Upper plate has been removed for visibility. b-Sample to be tested in the machine.*

fluid under pressure. This technique is thus limited in the path of loading that it can generate. Figure 3.4 describes them. Furthermore, the membrane choice is crucial in the case of soft

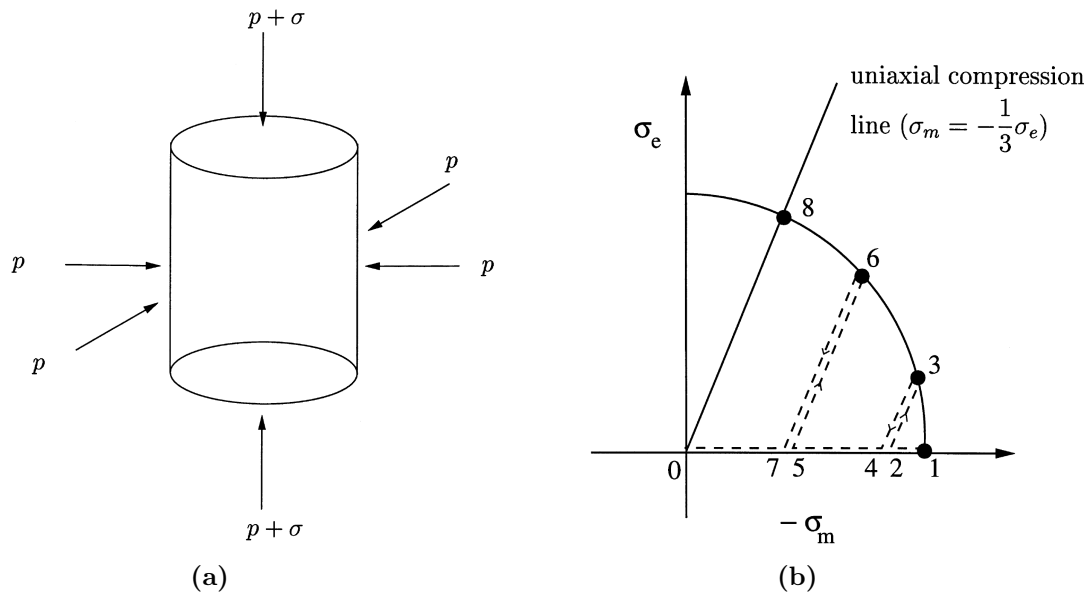


Figure 3.4: *Schematic of the loading state (a) and loading paths drawn on axes of effective stress versus mean stress (b) ($\sigma_m = -(p + \frac{1}{3}\sigma$ and $\sigma_e = -|\sigma|$) [Deshpande and Fleck, 2000].*

materials as are foams. If it is too thin it will scratch, but it should not be too thick in order to keep a low stiffness compared to the one of the tested sample. Moreover the radial deformation of the sample is unknown. Nevertheless this technique has also some interesting strong points. They are due to the fact that there is only one direction among which stress is imposed by contact. Actually, it allows to have a machine that can carry large load without being too large. Then if the constitutive material of the high-pressure chamber is well chosen, and if the system is well designed, one can see the sample during the test (if not by eyes, by X-ray). With a small machine and a visible sample, tomography is directly taken in consideration [Viggiani *et al.*, 2004]. Thus

strain field should be followed during the tests.

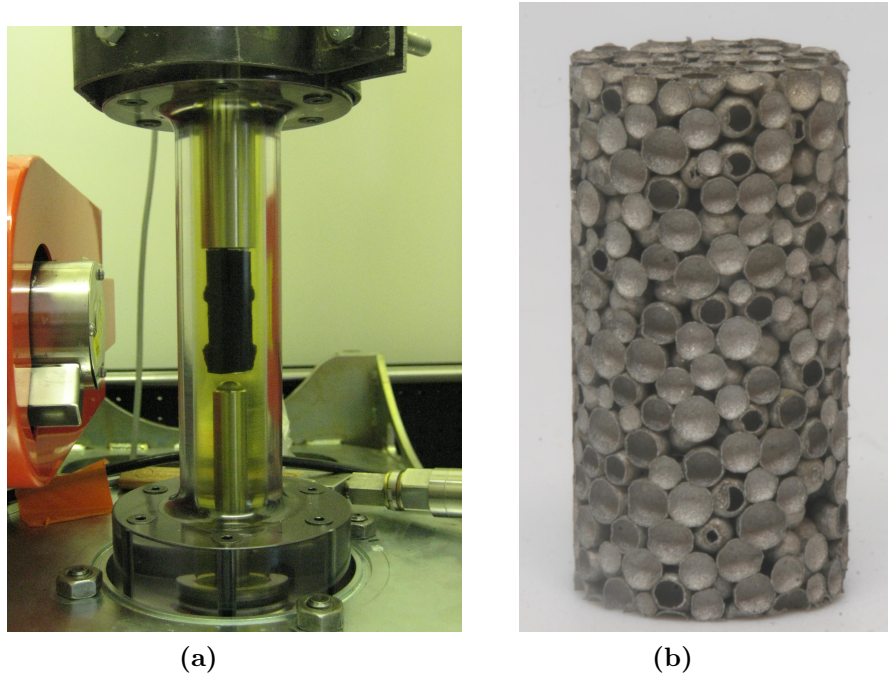


Figure 3.5: *a-Overview of the tri-axial pressure cell. b-Sample to be tested in the machine.*

3.1.2 X-ray tomography and in-situ tests

3.1.2.1 Principle of X-ray tomography

X-ray tomography is a technique based on the different X-ray absorption of the different phases constituting a material that allows to get a 3D digital map of phases spacial distribution. It is similar to a simple radiography of the studied sample, where one obtains a projection of the absorbance within the thickness of the sample. By performing numerous radiographies (also called "projections") each time among a slightly different angle, one has enough information to reconstruct a 3D map of local X-ray absorption coefficient. This reconstruction is never perfect. Refinements depend in theory on the

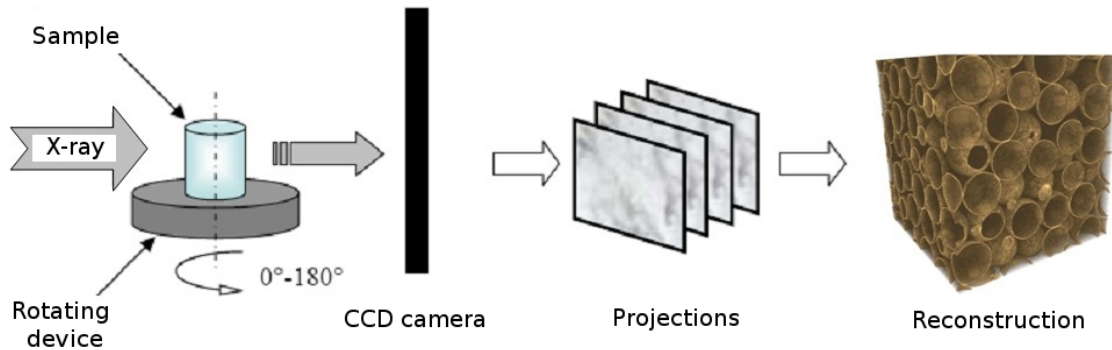


Figure 3.6: *Overview of the principle of X-ray tomography.*

number of projections performed, the global angle of vision and the number of pixels of the detector. But some other perturbations such as the stability of the beam line, the quality of the detector, also

play a role on the final quality of the volume. The theoretical optimal number of scans N_s for a global angle of vision of θ radian with a sensor containing N_p pixels per line is:

$$N_s = \theta N_p \quad (3.1)$$

For a classical observation θ is equal to $\pi/2$ and the sensor contains 1024 pixels per line. So the theoretical optimal number of scans is 1600 but in practice 900 scans is a good compromise. Actually another parameter plays a role : time. When the sample studied does not vary with time the only constrain is the manipulation time. It can be quite large since a standard scans lasts approximately 20-30 minutes, and if one wants to follow the sample evolution under a loading, one would perform a dozen of scans and thus the experiment would take 6-8 hours. It can be a problem when the time on the machine is limited and/or expensive.

Another important aspect is the type of beam line considered. It can be either conical, either parallel, both having strong points and weaknesses.

The conical beam can be obtained on a lab machine and it requires almost no equipment to chose the "voxel" size (the discrete element in 3D, equivalent to what is the pixel in 2D). One just need to change the distance between the sample and the beam source. Thus with this type of beam, the user is rapidly autonomous. Nevertheless the intensity of the beam is rather low and thus the time of exposure has to be long and so are the scans. Moreover the coherency and the stability of the beam are not very good, so the machine is limited to approximately $2\mu\text{m}$ as minimal voxel size⁸. For the considered material, in order to scan sample large enough to be representative, a voxel size of 8 to 20 μm is adequate. Thus this kind of scan has been widely used. The privileged access to the tomograph Phenix at INSA Lyon helped. Another lab tomograph has also been used, the tomograph RX-Solution at 3S-R in Grenoble.

Parallel beams are only obtained on synchrotron. However the access to the beam line is limited in

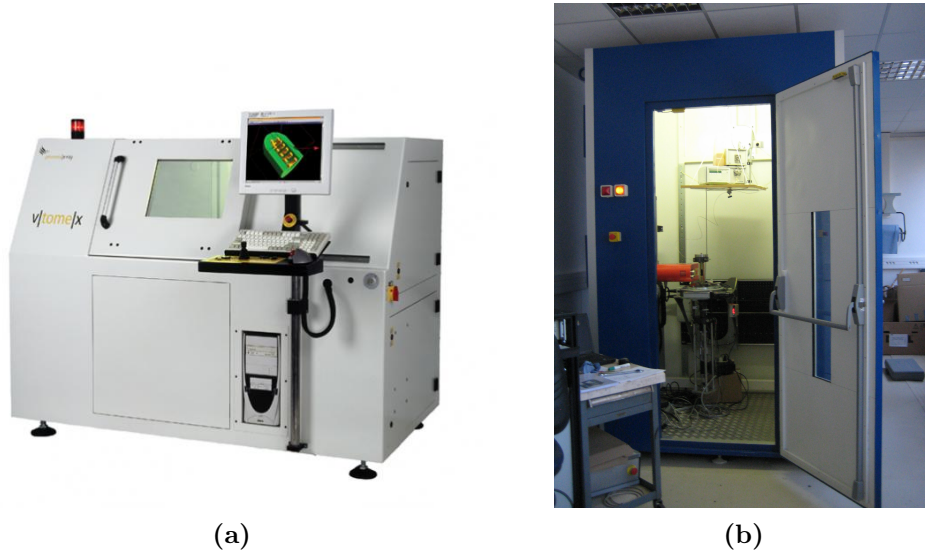


Figure 3.7: Lab tomograph used. **a-**Tomograph Phenix of INSA Lyon. **b-**Tomograph RX-Solution of 3S-Lab.

time, expensive, and has to be planned long before any experiment. Nevertheless these apparatus allow to reach very small voxel sizes and very fast scans. ESRF (European Radiation Synchrotron Facility) in Grenoble can provide such parallel beam. Several scans have been performed on line ID19.

⁸As voxel are cubic, the "voxel size" will refers to the size of the side of the voxel.

Both types of beam can scan simple samples. But if one wants to follow the material during loading, one must have a dedicated machine.

3.1.2.2 Uni-axial in situ tests

INSA Lyon developed a machine dedicated to uni-axial tensile and compressive tests. It can be used both in the lab tomograph at Lyon and at the ESRF. In situ compression can be performed on sample with two flat parallel faces. The width of the sample need to be not too large, in relation to the desired voxel size, in order to remain completely in the field of view for every radiography. Cubic samples of side size equal to 1000 times the voxel size let enough freedom on the position of the sample. For in situ tensile tests, a special device has been developed to pull on dog bone specimens. The T branches of the foam samples have first been reinforced with glued steel plates and then they have been impregnated by epoxy resin. The tricky step in this experiment is to be able to grip both sides of the sample without being able to touch it. Actually, to perform good quality scans, the part of the machine outside of the field of view (that means all the machine) but that are crossed by the X-ray beam, have to be invariant by rotation. In that case, the absorption of the machine is constant, whatever the angle of radiography, and thus it behave as a simple filter. Thus, the part of the machine around the sample is a plexiglas or aluminum hollow cylinder, in order to be transparent to X-rays according to the selected energy. Figure 3.8 presents a picture of this machine that help to understand the previous explanations.

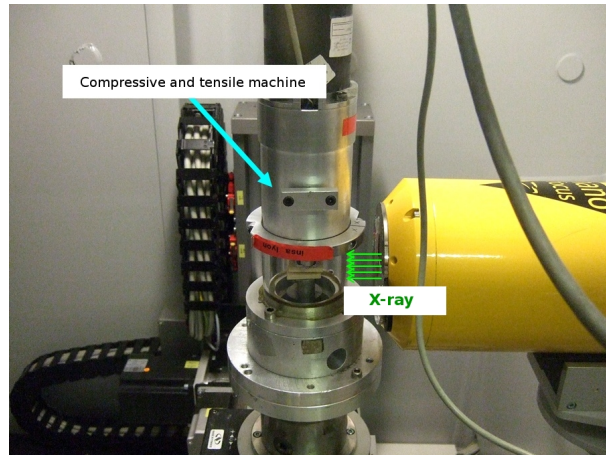


Figure 3.8: *Compressive and tensile machine of INSA Lyon used for in situ tests.*

3.1.3 Images analysis

3.1.3.1 Objectives

X-ray tomography gives 3D gray level images of the material. Without any post treatment these images can only give 2D qualitative information. The out of plane motion may induce inaccurate conclusions. Even for qualitative observations of the structure some treatments are necessary. So the first objective is to be able to visualize the structure in 3 dimensions. But the real interests are on a quantification point of view. It should give access to all the structural and architectural parameters. For in situ tests the evolution of mean parameters should thus be calculated. Furthermore image analysis must give access to the evolution of local parameters (as the distance between the center of to particular spheres).

So each sphere should be identified and recognized from a state to an other.

3.1.3.2 Tools

The software Avizo®(Mercury Computer System) has been used to obtain 3D visualisation outputs. There is hardly a standard quantitative analysis that remains pertinent on all the materials, so one often needs to develop its own set of tools. All the quantification based on image analysis obtained in this PhD were realized thanks to plugins developed on the freeware ImageJ® [Rasband and ImageJ,] which rely under a GNU license. This software is based on Java®language, and thus is portable and easily adaptable.

3.1.3.3 Strategy and methods

The tools being defined, let us have a look on the methods.

The first step is the most critical in image analysis techniques. It consists in being able to differentiate phases and to recognize similar phases. This is realized by the definition of a threshold for the gray level volume. All pixels with gray intensity above the threshold are set white, and all the pixels with a value under the threshold are set black. A little subtlety is introduced in this operation. Since the studied material is made of cells which are interconnected, the threshold is operated with the constraint of connectivity. A pixel that belongs with certitude to the material is chosen as a “seed”. Then this “seed” grows with constraint on the intensity level fixed by the threshold value. This technique erases isolated incorrect pixels that may pollute the further analysis. This operation is done for several threshold values, and the final relative densities inside the sample are compared to the macroscopically measured relative density. When obtained, their agreement gives the best value of threshold to adopt. Another point of comparison, which is furthermore independent of the macroscopic strain, is the thickness of the shells. Since phases have been identified giving binary images, morphological operations and labeling are used to separate and identify the spheres. Then calculation of their properties are computed (position, radius, surface,...). Tracking is operated to recognize any sphere from a state to another. Thus one can follow spheres through all the stage of deformation. Connectivity between spheres is also computed. Then parameters such as mean indentation at any contact are calculated. Theses methods are described in [Fallet, 2008].

3.2 Simulation tools

Simulation tools are useful to quantify the relative influence of various parameters or to predict the behavior of a structure or a material. They have been used several times in this PhD for various purpose and at various scale.

Finite elements method is well adapted to study the influence of shapes or of relative dimensions on structure response. Nevertheless the method is limited in the case of hollow spheres stackings because of the high shape ratio of the shells. So stackings that can be simulated accurately by such method are only constituted of few spheres. In the case of regular stacking, [Sanders and Gibson, 2003b] used small simulation boxes (side size of a few sphere diameters) with periodic boundaries conditions. Nevertheless this method cannot be applied to random stackings. Representative Volume Element would be hard to simulate. How then could one simulate structures with hundreds of spheres? Various

approach exist. [Mamoud, 2007] developed shell elements to simulate hollow spheres stacking. [Coty *et al.*, 2008] modified it to take in account the variation of the shell thickness. A rough simulation is realized on a large number of spheres, then a fine finite element simulation is operated on few spheres with boundaries conditions extracted from the previous computation. If this method has good ability to study with accuracy the damaging mechanisms in fatigue, it is limited to very small macroscopic strain. Actually the model does not take into account the contact creation between shells during deformation. This mechanism is of importance, and might not be neglected. Moreover the potential of this method to simulate large stackings is limited.

Another approach, coupling Finite Element Method (F.E.M.) and Discrete Element Method (D.E.M.), has been chosen.

3.2.1 Discrete Element Method (D.E.M.)

The Discrete Element Method (D.E.M.) has first been developed in the late seventies by Cundall and Strack [Cundall and Strack, 1979]. It is devoted to particles cluster modeling. It relies on the behavior laws of contact between two particles. A D.E.M. code was developed at SIMaP-GPM2 by Christophe Martin, dp3D (Fortan90). Alexandre Fallet implemented during his PhD [Fallet, 2008] the laws of contact between two bonded hollow spheres. A wide range of hollow sphere stacking parameters (shell thickness, neck size) were simulated by Finite Element for two spheres in contact. All the elementary loadings were simulated. Then laws of behavior between two hollow spheres were deduced. The implementation of these laws in dp3D allowed the simulations in periodic conditions of hollow spheres stacking.

This method of modeling allows to simulate the behavior of a large number of particles (easily up to 100000). This advantage on volumetric finite elements is even more important in the case of hollow spheres. Fine meshed Finite Element simulations are only performed for two spheres, and then the fine description is contained in the contact law.

Nevertheless the method has obviously some restriction.

First, the laws are decomposed among the elementary loadings, that means that the global solution is accurate only when superposition of solutions is admissible, i.e. at small strain.

Then the creation of new contacts between particles is based on a spherical shape of the particles. One more time, large strains cannot be investigated. Another point to keep in mind is that the contact laws are elaborated with two semi-spheres in contacts, but inside a packing the mean coordination number ranges from 6 to 12 in our case. There must be an inter-dependence between the contact laws that is not necessarily well captured by the model.

It remains that this method is a good compromise between accuracy and computer intensity to investigate the behavior of an hollow sphere stacking at small strain. Macroscopic behavior for a wide range of properties were obtained by A. Fallet.

Appendix C.1 explains the procedure used to generate the “numerical samples”.

3.2.2 Mesoscopic Finite Elements

The mesoscopic finite elements methods address the behavior of two spheres connected by a neck. The aim of this tool is to give relations between load and relative motion of two spheres considered as discrete elements. A discrete element is, among other things, defined by a point, we assumed the center of the

spheres to be the location of the element. Thus two half-spheres connected by a neck (similar to a diabolo game) are loaded in compression, in tension, in torsion among both principal directions, and in shear. Depending on the symmetry of the loading, either 2D axis-symmetric simulations, either 3D simulations have been performed. Figure 3.9 shows 2D axis-symmetric and 3D meshes. All the methodology of the

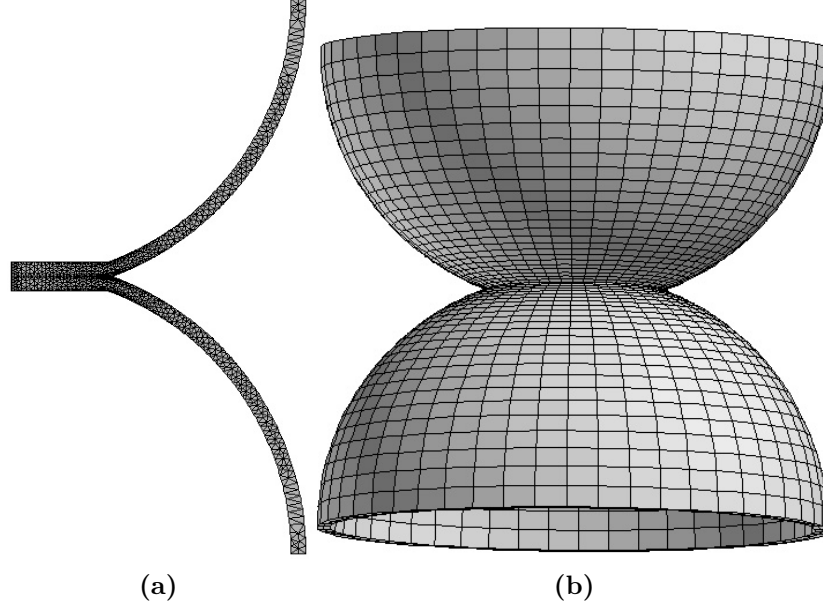


Figure 3.9: Meshes of the simulated bi-spheres. **a**-2D axis-symmetric mesh. **b**-3D mesh.

simulations is thoroughly described in [Fallet, 2008]. All the Finite Element Method simulations in this PhD have been performed thanks to the code *ZeBuLoN*[ZéBuLoN,].

It may just be noticed that 3D mesh have been obtained by sweeping of the 2D mesh. Mesh has been refined at the vicinity of the neck while it has been let coarse elsewhere. A sensitivity of the response to the mesh has been performed by A. Fallet to ensure the validity of the results. During this study, the meso-structure dimensions (t , R , a) has been varied but not the constitutive material. Nevertheless one have to keep in mind that the constitutive material behavior plays a major role in the responses of the model. Thus transitions and/or partition between phenomena that might be observed, even if only due to a dimension variation, are linked with the constitutive material behavior.

A classical load-motion response is shown on figure 3.2.2. The displacement and the load are normed thanks to respectively the radius of the spheres and the square of this radius. Then laws are fitted by bi-linear laws whom three parameters are extracted (K_1 , K_2 and \tilde{u} or $\tilde{\theta}$). A parametric calculation of theses parameters is operated among varied adimensional structural parameters (t/R , a/R) for all the elementary solicitations. Theses parameters will be used as input for the elementary laws for Discrete Element Simulations.

3.2.3 Macroscopic Finite Elements

Macroscopic finite element simulations have been used to simulate the behavior of sandwich structures. A constitutive law based on an elliptic criterion also referred as Green criterion or Deshpande & Fleck model has been used for the foam core, while a Von Mises criterion have been used for the faces. The latter model is easy to compute but it assumes a plasticity at constant volume. The former is more suitable to porous materials by taking into account the influence of the hydrostatic pressure as the com-

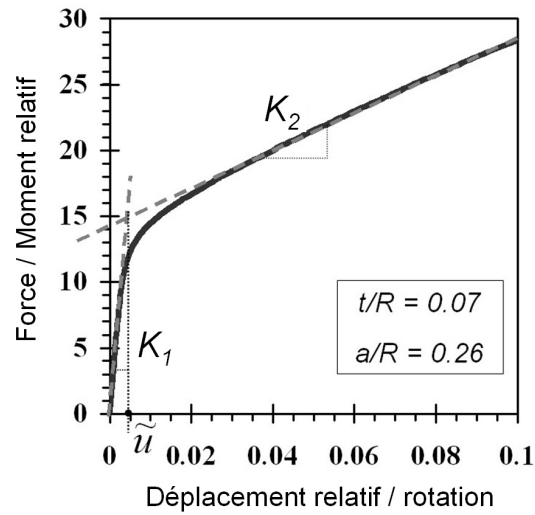


Figure 3.10: *Classical response of the elementary simulations. Parameters of the bi-linear law are noticed.*

pressibility of the material. These phenomena have an important influence on the structure response, and especially on the indentation behavior.

Part III

Hollow spheres stackings

Introduction on hollow spheres stackings

This part deals with the investigations performed on hollow spheres stackings.

First the samples studied and the initial information about them are presented.

Then the structure of the stackings is investigated at various scales. The microstructure of the shell is studied and the necks between spheres are measured. Density is measured over several samples to estimate a representative volume element for this particular macroscopic property. The disordered character of the stacking is also estimated.

After that, improvement of the Discrete Element Model used to describe the behaviour of hollow spheres stackings are presented. The influence of the modifications operated on the original model are studied. Next the macroscopic mechanical behaviour is studied. A complete analyse of the uni-axial compressive behaviour is performed. Both the sample size effect, the sphere size effect and the foam initial density effect are investigated. The compressive behaviour is fully characterized both for the stress-strain curves, and for the evolution of the unloading modulus. Scaling laws of the foam initial density are established. The same study is then performed for uniaxial tensile loading. The behaviour under multi-axial compressive loading is also considered. A systematic comparison with the DEM prediction is performed, and potential improvement of the model are discussed.

Last the deformation mechanism at the scale of the cells are observed and quantified, thanks to in-situ X-ray tomography tests. The local mechanisms are related to the macroscopic behaviour. A phenomenological model, describing the macroscopic behaviour and tacking into account the damage mechanisms, is proposed.

Hollow spheres stackings : presentation of the samples

1 Samples

Origin of the samples The material studied has been obtained thanks to the MAPO⁹ project supported by ONERA and CNRS. Two industrial companies were partners in this project : *ATECA* (Montauban, France) and *PLANSEE* (Reutte, Austria). The last one provided the stainless steel hollow spheres stackings on which the present PhD is focused. This provision of “industrial material” ensures both availability and reproducibility, but left us with little freedom on the “architecture parameters” which are set by the industrial process, which is also, due to industrial intelligence policy requirements kept confidential.

Samples sets Table 1 gives the parameters of the four stackings of hollow spheres provided by *PLANSEE*.

	<i>PLANSEE</i>	<i>PLANSEE</i>	<i>PLANSEE</i>	<i>PLANSEE</i>
	A	B	C	D
Spheres diameter [<i>mm</i>]	3	3	3	1.5
Shell thickness [μm]	45	65	90	45
Density [kg/m^3]	0.4	0.6	0.8	0.8
Material	314 (norm AISI)			

Table 1: Summary of samples properties given by *PLANSEE*.

Samples were provided as parallelepipeds of 100 * 100 * 60 mm and plates of 300 * 300 * 30 mm. These large samples have then been cut thanks to wire electro-erosion. These samples have been analysed by A. Fallet with X-ray tomography and image analysis. The structural parameters obtained are listed in Table 2. These analyses gives information on the structure of the stackings. Nevertheless the knowledge of the structure of the samples is not sufficient to understand the mechanical behaviour. Shells and necks dimensions have been characterized only by their mean values.

⁹POrous MAterials

	<i>PLANSEE A</i>	<i>PLANSEE B</i>	<i>PLANSEE C</i>	<i>PLANSEE D</i>
ρ^*	0.070 ± 0.007	0.092 ± 0.007	0.113 ± 0.007	0.115 ± 0.014
t (μm)	56 ± 8	72 ± 8	88 ± 8	56 ± 8
R (mm)	1.31 ± 0.032	1.31 ± 0.032	1.31 ± 0.032	0.735 ± 0.032
mean a (μm)	418 ± 32	400 ± 32	388 ± 32	233 ± 16
Z_m	7.9	8.2	7.6	7.8
t/R	0.043 ± 0.007	0.054 ± 0.007	0.067 ± 0.007	0.076 ± 0.014
mean a/R	0.319 ± 0.032	0.306 ± 0.032	0.297 ± 0.032	0.324 ± 0.029
mean θ	$18.6^\circ \pm 1.8^\circ$	$17.8^\circ \pm 1.8^\circ$	$17.3^\circ \pm 1.8^\circ$	$18.9^\circ \pm 1.7^\circ$

Table 2: Summary of structural parameters of stackings measured by 3D image analysis ([Fallet et al., 2008]).

Chapter 1

Structural characterization

Contents

1.1	Microscopic scale	97
1.1.1	Experiments	97
	Optical microscope	97
	Scanning Electron Microscope	97
	X-ray micro-tomography	98
1.1.2	Shell thickness	98
1.1.3	Shell porosity	101
1.2	Macroscopic scale	101
1.2.1	Experiments	101
1.2.2	Density	101
1.3	Mesoscopic scale	103
1.3.1	Experiments	103
1.3.2	Results	103
	1.3.2.1 Neck size correction	104
	1.3.2.2 Stacking organisation	105
	Macroscopic Scale	106
	Mesoscopic scale	106
	Microscopic scale	106

The structural characterization of the hollow spheres stackings has been performed at various scales : the macroscopic scale which is the sample scale, the mesoscopic scale which is the cell scale and the microscopic scale which is the constitutive powder scale. At each level, the studied elements had to be large enough to be a Representative Volume Element (R.V.E.) with respect to the parameter of interest. The order of study of the various scales might appear arbitrary, but it is driven by the requirements of input at each scale. Thus the microscopic scale will be investigated first in order to get some information about the shell porosity and the shell thickness distribution. So the density of the "equivalent constitutive material" (the constitutive material when taking into account the shell porosity) will be known. Then the macroscopic study will give information about the macroscopic density. Use of the "equivalent constitutive material" will give access to the relative density. Last the mesoscopic scale is investigated. Actually an accurate knowledge of the relative density and of the shell thickness is required to calibrate the image analysis at this scale. The structure and the architecture of the material will thus be studied.

1.1 Microscopic scale

1.1.1 Experiments

Optical microscope Cubic samples of 10 mm side size were permeated by epoxy resin. Two kinds of coating have been tested. First a hot coating has been performed, at 150°C under 125 bars. The applied pressure was obviously too important for stacking of hollow spheres. Most of the spheres buckled as can be seen on figure 1.1. Nevertheless these samples can be used to qualify the porosity of the shells. The second type of coating was a cold coating under vacuum.

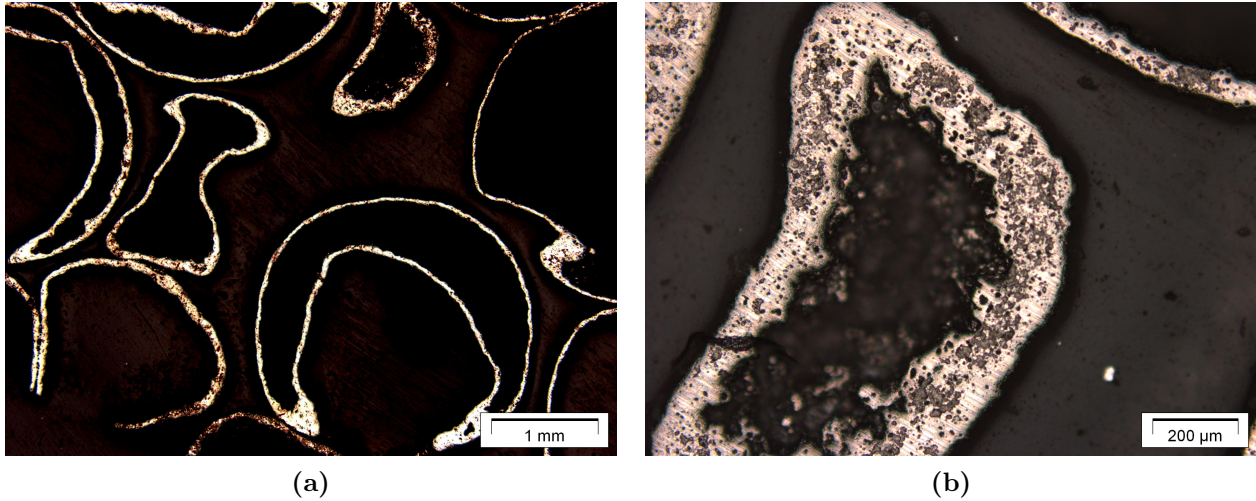


Figure 1.1: *Optical microscope observations of a sample hot coated. a-Pressure made cells to buckle. b-Porosity of the shell is important. The sharp inner surface can be guessed while one can see the rather smooth outer surface.*

Scanning Electron Microscope Observations have also been performed thanks to Scanning Electron Microscope (S.E.M.). They have been used to investigate qualitatively the bondings between spheres. Its use was particularly relevant for the observation of the surface roughness.

X-ray micro-tomography A single specimen has been scanned by X-ray micro-tomography. The observed part is a neck between two spheres with small portions of shells. It has been performed at ESRF on line ID 19 with a voxel size of $1.4\mu m$.

1.1.2 Shell thickness

Figure 1.2 shows various optical microscope images of the samples. Observations show that the shell

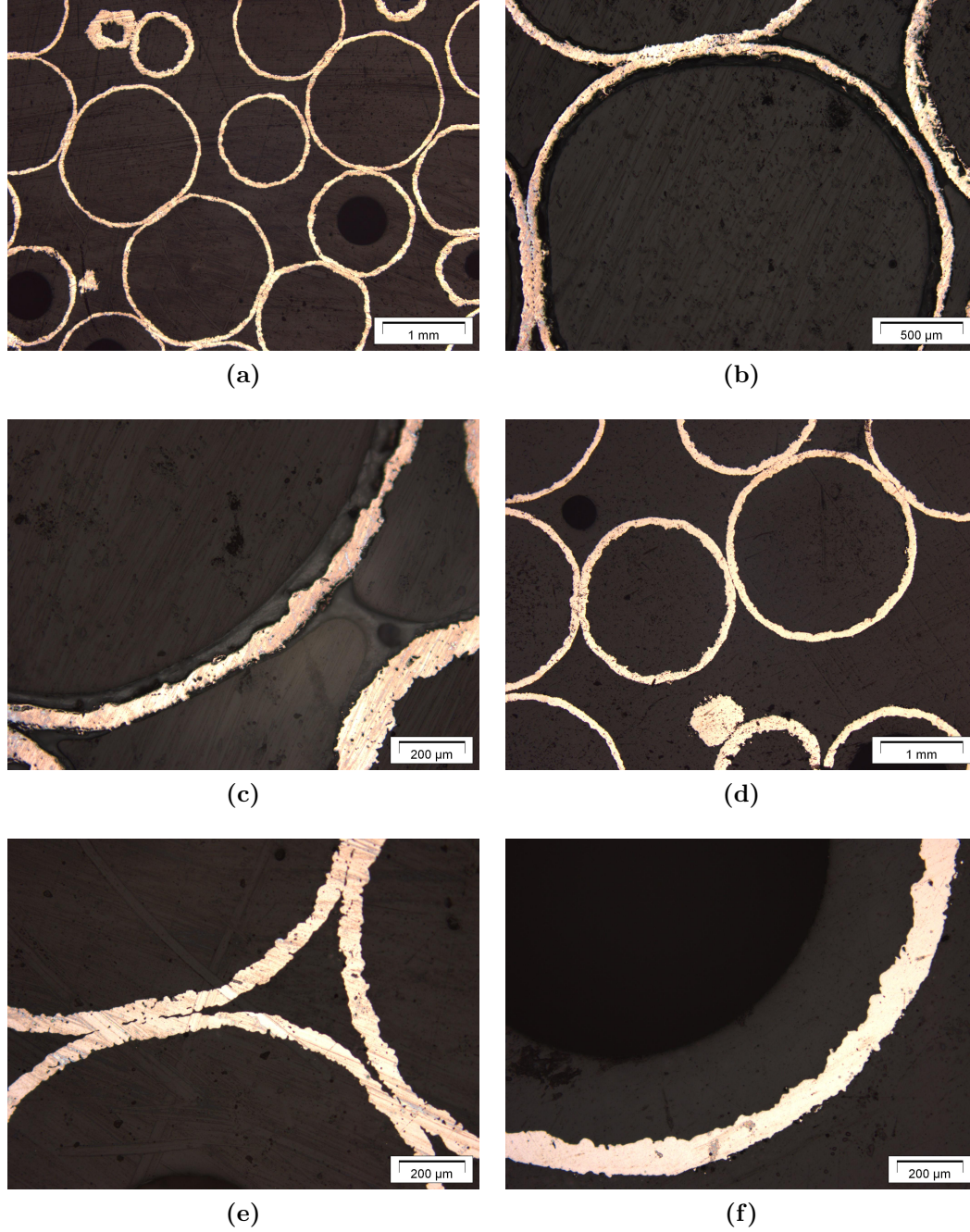


Figure 1.2: Optical microscope observations of samples cold coated. One can see the variation of shell thickness within a single shell. Some severe defects can be observed (b). Mean shell thickness is different between top pictures (a,b,c) and bottom pictures (d, e,f). The roughness of interior surface and the rather smooth outer surface can be seen.

thickness is irregular, even within a single sphere. Length of variation are of the order of the shell thickness, but their amplitude seems independent of the shell thickness. Outer surface of the shells is rather smooth. Shell thickness variation is a consequence of the inner surface roughness. It should be attributed to the processing. Inner surface roughness is almost a negative of the styrofoam balls surface. Outer face benefits of a surface tension of the powder slurry during the fluidized bed coating and also from the higher temperature during sintering that favors this smoothing of irregularities. Thus it is understandable that the roughness is independent of the shell thickness and so the variations of thickness are of same absolute amplitude between samples.

S.E.M. makes easier observations of the faces thanks to its large depth of field. Figure 1.3 shows various S.E.M. images of the samples. One can clearly see pores in the shells. X-ray micro-tomography allows

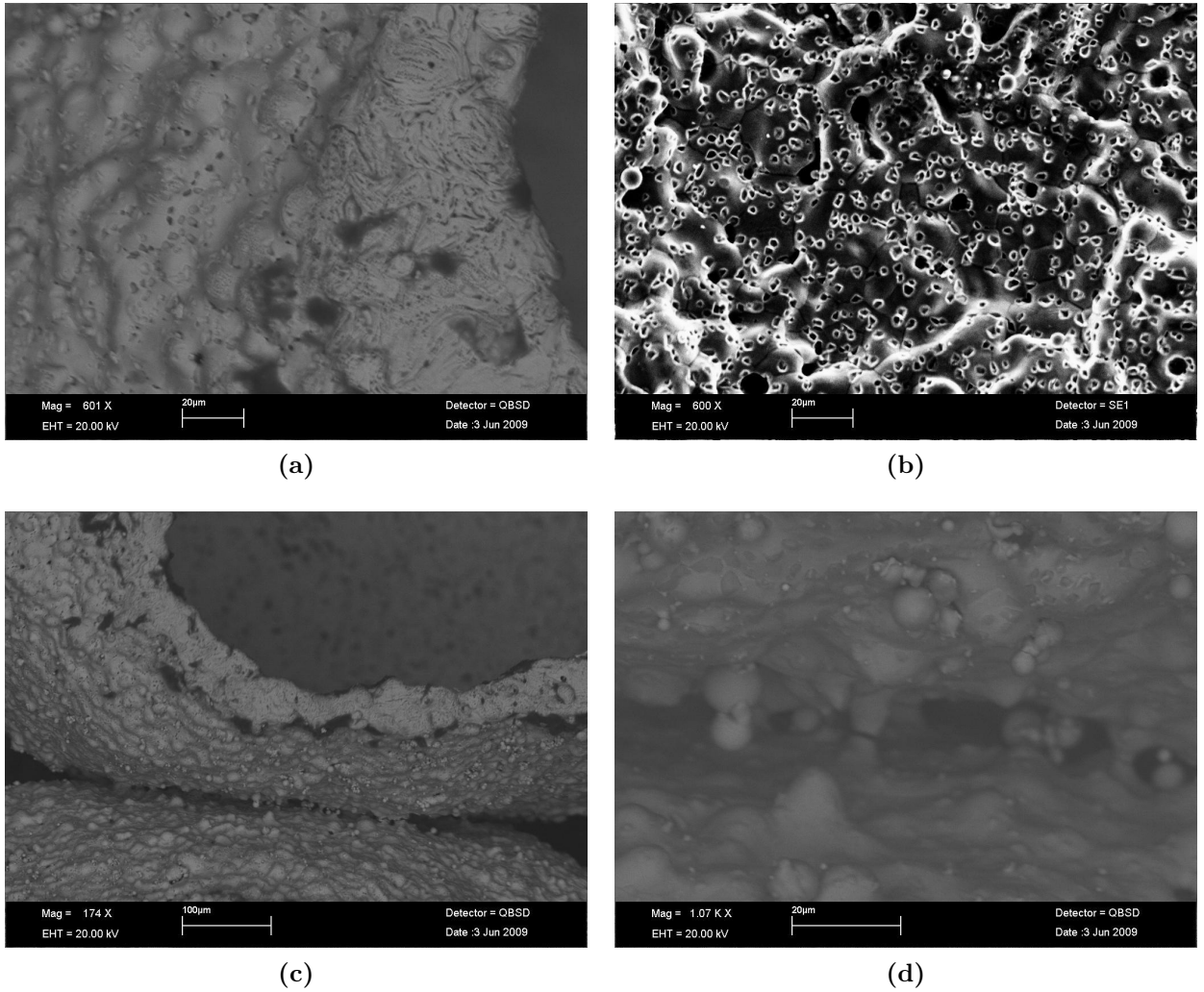


Figure 1.3: *S.E.M. images of the samples either with secondary electrons (b), either with back-scattered electrons (a,c,d). Cross section of the shell and roughness of outer surface can be observed (a). Shell micro-porosity is important (b). Sharp bonding between spheres is seen at various scales (c,d).*

also to make an accurate observation of the various roughness (figure 1.4). Quantitative study of the shell thickness variation have been performed. 2D optical images have been used. In order to avoid

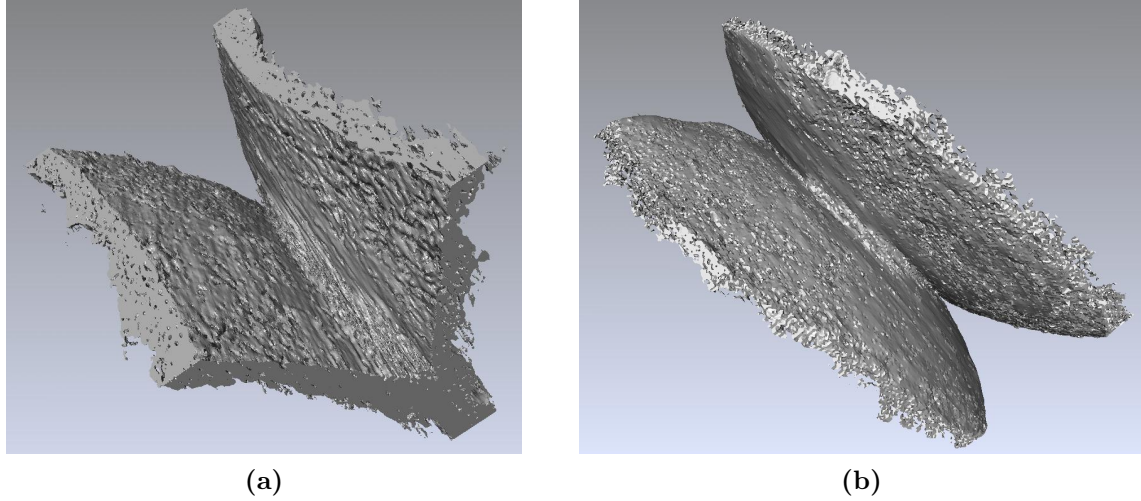


Figure 1.4: *X-ray micro-tomography observation. One can see the roughness of interior surface (a) and the rather smooth outer face (b). Sharp bonding between spheres can be observed (c).*

artifact, the inner radius of the spheres was required¹⁰. Thus the studied shells pertain to spheres that are observed in a plane of symmetry. An appropriate image treatment based on binarization and distance map gives access to the profile of shell thickness along a curvilinear abscissa on the outer surface of the shell. Figure 1.5 shows shell thickness profiles and the mean values of thickness and roughness for the studied samples. The variation of thickness is important. The algebraic roughness

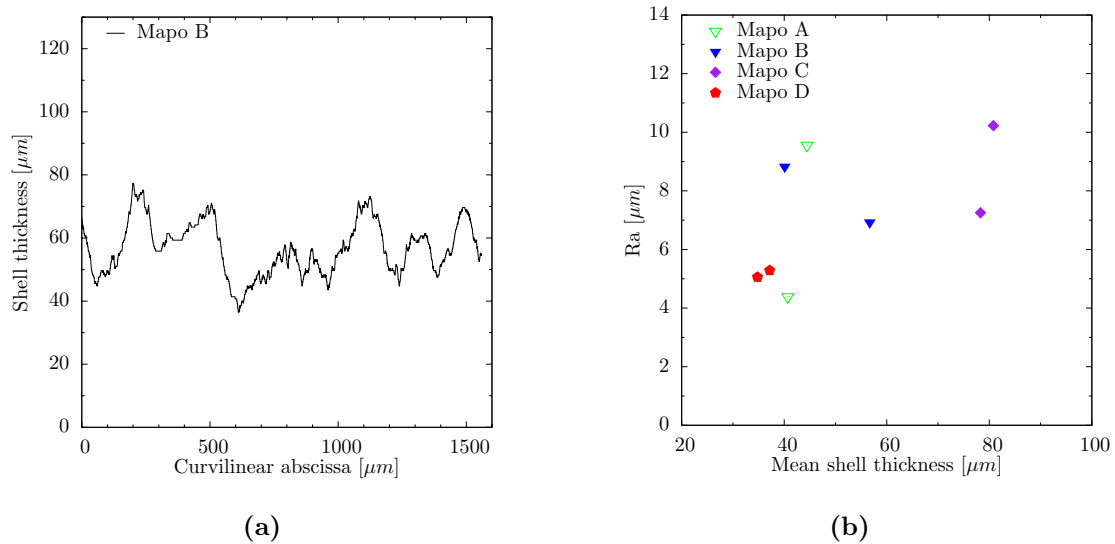


Figure 1.5: *(a)-Shell thickness profiles along a curvilinear abscissa on the outer face of the shell. (b)-Algebraic roughness versus mean thickness for the studied samples.*

ranges between 4 and 10 μm . Nevertheless scatter on the algebraic roughness is too large to conclude on a correlation with the sphere diameter or with the shell thickness.

¹⁰The inner radius has been obtained by tomography analysis with qualitative threshold. This measure is almost non impacted by the threshold level (within the uncertainty range)

1.1.3 Shell porosity

Based on optical microscope observations, an analysis of the shells porosity has been performed. Figure 1.6 presents both the porosity size distribution and the porosity fraction distribution for two portions of shells of the same sample (Plansee D). 80% of the pores have an equivalent radius smaller than $1\mu m$.

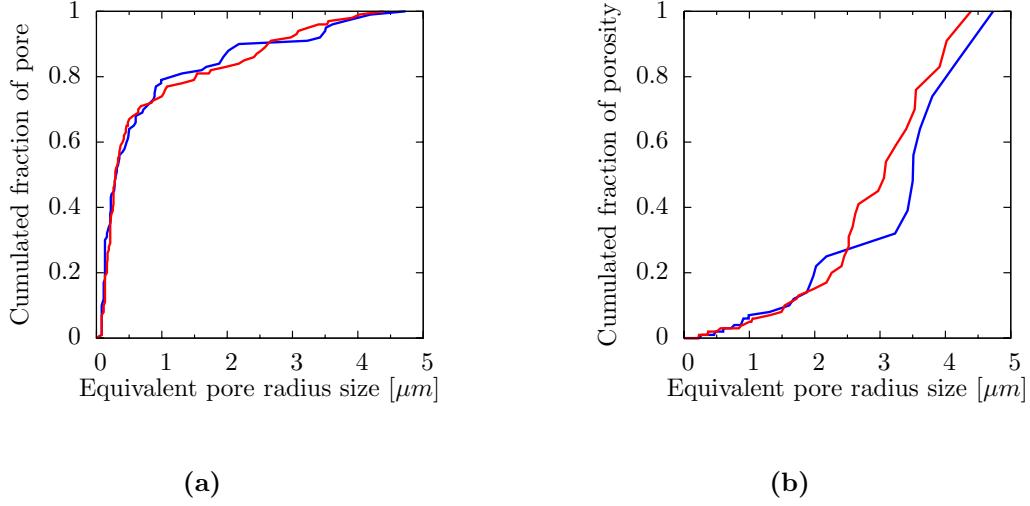


Figure 1.6: (a)-Cumulative pore distribution versus their equivalent radius size. (b)-Cumulative porosity distribution among their equivalent radius size.

But the 20 other percents of the pores accounts for 90% of the porosity. The global porosity of the shells is around 4%.

1.2 Macroscopic scale

1.2.1 Experiments

At a macroscopic scale the easiest parameter to extract for a foam is its density ρ_{foam} . This measure is obtained by the ratio of the mass of a sample to its volume. In order to get an idea of the size of a R.V.E. for the density, it has been measured on each foam on three size classes, each size class containing three samples. The samples were cubic with side sizes of 10, 20 and 30 mm.

1.2.2 Density

The densities of the studied sample ranges from approximately $400g/L$ to $800g/L$. Results are summarized in table 1.1. One can notice the very small scatter of densities whatever the sample size considered and mean values are also the same. Therefore it can be concluded that for the density, the R.E.V. is smaller than a cube of 10 mm side size for the hollow sphere foams studied. Figure 1.7 gives a graphical view of the density evolution and scatter with the sample size. From the density parameter can be extracted a more relevant architectural parameter : the relative density ρ^* given by the ratio between the density of the foam and the density of the constitutive material (that is the "equivalent constitutive material" whose porosity has been studied in the previous paragraph). It gives the volumic fraction of

x	Samples size	PLANSEE A		PLANSEE B		PLANSEE C		PLANSEE D	
		\bar{x}	$\sigma(x)$	\bar{x}	$\sigma(x)$	\bar{x}	$\sigma(x)$	\bar{x}	$\sigma(x)$
ρ [g/cm ³]	10mm	0.468	0.013	0.637	0.010	0.773	0.015	0.736	0.004
	20mm	0.464	0.001	0.612	0.003	0.773	0.008	0.773	0.012
	30mm	0.459	0.005	0.617	0.007	0.775	0.002	0.769	0.014
	all samples	0.464	0.009	0.622	0.013	0.774	0.010	0.762	0.019
ρ^*	all samples	0.067	0.001	0.090	0.002	0.112	0.001	0.110	0.003

Table 1.1: Densities and relative densities of spheres stackings measured on 3 sample sizes. \bar{x} and $\sigma(x)$ are respectively the mean value and the standard deviation of the studied parameter x in each of the size class considered.

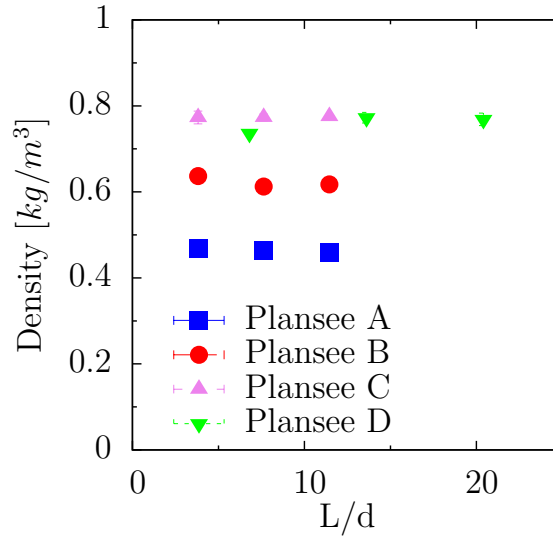


Figure 1.7: Evolution of density with sample size. Scatter is so low that error bars are hidden by the points.

material inside the foam. This parameter is directly related to the material architecture and is independent of the constitutive material. The small dispersion of this parameter is of great importance for the following characterizations. Actually it would have two major roles. The first one is as an input parameter in all the scaling laws that will be set up for mechanical properties. It can nevertheless be noticed that in that case the material density can be used and that an error on the constitutive material density does not change the laws provided the ratio between the density of the real constitutive material and the nominal density remains constant.

The second role of relative density will be to determine the accurate threshold for the tomography image analysis. Because all the analysis are performed on binary images, this step is critical, especially if no quantitative reference is provided. In that case, the constitutive material is the material that is assumed as homogeneous in a voxel¹¹. Thus the microporosity of the shell has to be quantified in order

¹¹approximately a cube of 10 μ m side size.

to correct the density value of the "homogeneous constitutive material".

So the accuracy and constancy of the values of the density and relative density make of these parameters a solid base to rely on for the following characterizations. Once hollow sphere foams structure are characterized macroscopically, one might want to have more information on the organization of the material at a smaller scale.

1.3 Mesoscopic scale

1.3.1 Experiments

The mesoscopic scale of hollow spheres foam is the scale of cells, necks and shells. Thanks to X-ray tomography scans performed at *ESRF* and at *MATEIS*, 3D images of the foams were obtained. 3D image analysis techniques give access to a large set of parameters : spheres diameter, shell thickness, neck size, coordination number ...

The first step consists in tomography acquisition of the samples. A compromise between the samples size (and thus the number of spheres and contacts) and the resolution had to be made. A cubic sample of 10 mm side size has been chosen for each of the four foam types. That represents approximately 60 spheres for samples A, B and C, and 250 for sample D. This sample size allows to reach a resolution of $8\mu m$. The scans have been performed at *MATEIS* on a laboratory tomograph.

1.3.2 Results

The structural parameters obtained are listed in Table 1.2. It can be noticed that samples A, B and C

	<i>PLANSEE A</i>	<i>PLANSEE B</i>	<i>PLANSEE C</i>	<i>PLANSEE D</i>
ρ^*	0.070 ± 0.007	0.092 ± 0.007	0.113 ± 0.007	0.115 ± 0.014
t (μm)	56 ± 8	72 ± 8	88 ± 8	56 ± 8
R (mm)	1.31 ± 0.032	1.31 ± 0.032	1.31 ± 0.032	0.735 ± 0.032
mean a (μm)	418 ± 32	400 ± 32	388 ± 32	233 ± 16
Z_m	7.9	8.2	7.6	7.8
t/R	0.043 ± 0.007	0.054 ± 0.007	0.067 ± 0.007	0.076 ± 0.014
mean a/R	0.319 ± 0.032	0.306 ± 0.032	0.297 ± 0.032	0.324 ± 0.029
mean θ	$18.6^\circ \pm 1.8^\circ$	$17.8^\circ \pm 1.8^\circ$	$17.3^\circ \pm 1.8^\circ$	$18.9^\circ \pm 1.7^\circ$

Table 1.2: Summary of structural parameters of stackings measured by 3D image analysis ([Fallet et al., 2008]).

have the same sphere radius R , and almost the same mean neck size a . They differ only with the variation of the shell thickness t . If far enough of any size effect, the relevant parameters for the structure are the relative neck size a/R and the relative shell thickness t/R . Two foams with the same couple of relative values are just similarities and thus have the same density. It is what we observe for the foams C and D. Thus with these four foams it is possible to investigate the effect of the shell thickness and an hypothetical size effect.

1.3.2.1 Neck size correction

The neck size was measured thanks to the inertia matrix of the neck as detected by A.Fallet. Figure 1.8 shows how the neck were detected. A pattern was centered on each voxel of the shell. When it intercepted two spheres interior, the voxel was labeled with a color relative to the labels of the spheres. The dimensions of the axes of the ellipsoid are calculated thanks to the matrix of inertia of

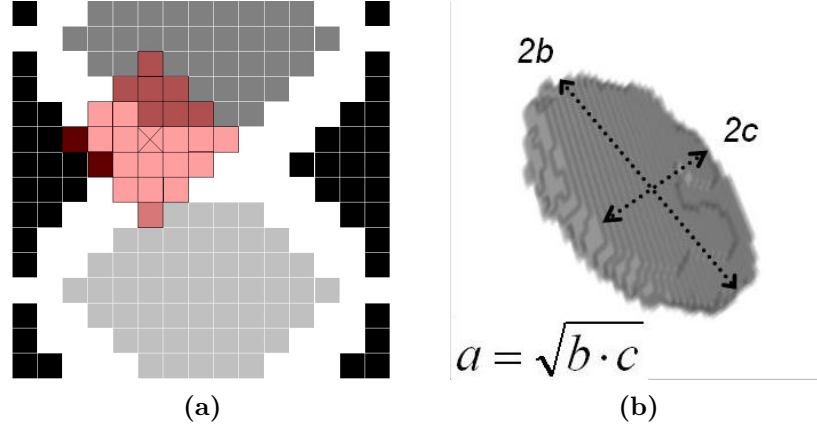


Figure 1.8: Neck detection and measure. **a**-A pattern is moving on the shell. When it intercepts two spheres interior its center is within a neck. **b**-Estimation of the neck diameter based on the two larger axes of an ellipsoid.

the contact. Nevertheless the contact is much more closer to a cylinder with an elliptic base than to a ellipsoid. The computation of the neck size based on this assumption gives sensible differences.

The second parameter that lead to an overestimation of the neck size is due to the voxel size. Actually, in order to obtain closed cells, the threshold used to binarize the images is often increased. A simple geometrical analysis of a neck can give an idea of the error made on its measure. Let's assume that if in the real space a voxel contains some matter it will be full of matter in the discretized space. This assumption is a consequence of the overestimation of the threshold. Thus, based on figure 1.9 the real neck radius a and the apparent radius a^* are linked together thanks to the voxel size p and the sphere radius R by the equation 1.1.

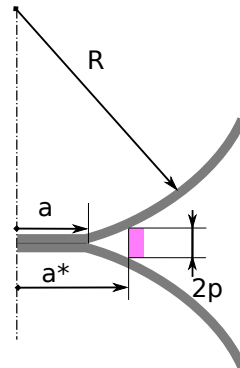


Figure 1.9: Error on neck measure. The distance between two shells has to be of two voxels size to ensure a void voxel.

$$a^{*2} = a^2 + 2 \left(2R - \sqrt{R^2 - a^2} - p/2 \right) d \quad (1.1)$$

Thus it means that for a voxel size of $16\mu m$ the standard parameters of the studied material, the overestimation of the neck size is of about 15%. But the parameter have been estimated on binned¹² images. The voxel size is then of $32\mu m$ and the overestimation of the neck size can reach more than 30 percents. So the mean normalized neck size is certainly closer to 0.25 than to 0.3. This correction only account for the detection of the *perfect* contact between two spheres. Because of the shell roughness the real area of contact is even much smaller.

1.3.2.2 Stacking organisation

Indicators of randomness of stackings can be found in the radial distribution function and in the Q_6 bond orientational order. Figure 1.10 shows these two distributions for the studied samples. Crystalline

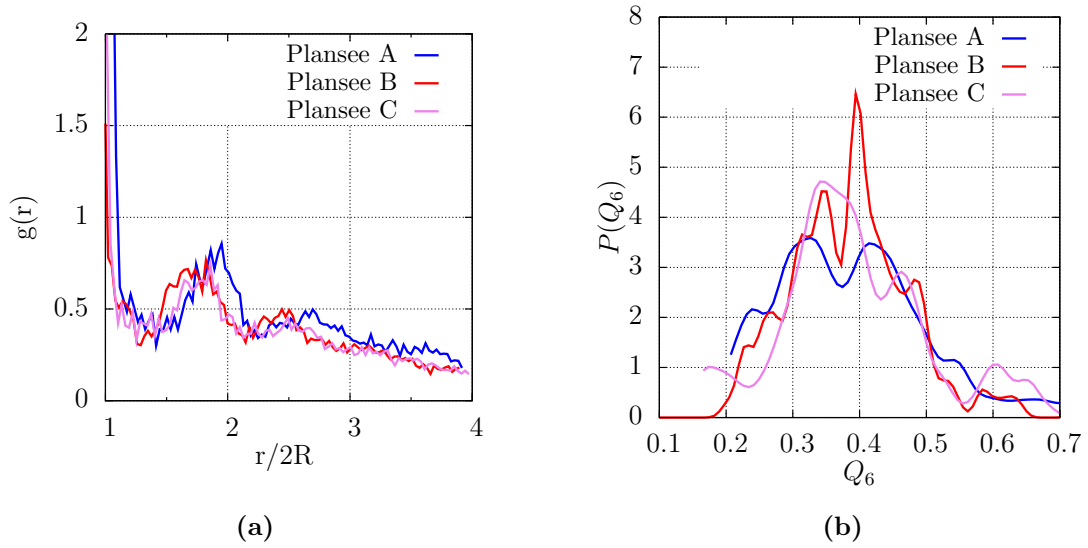


Figure 1.10: Stacking order indicators. **a**-Radial distribution function. **b**- Q_6 bond orientational order.

organization is characterized by peaks of the radial distribution function for particular values. Thus peaks for $\sqrt{2}$ and $\sqrt{5}$ are signature of a regular organisation. In our case, the radial distribution function presents local maxima for values closes to 2 and to 2.5. The stacking can be assumed as random. The Q_6 bond orientational order is rather an indicator of the transition between a disordered medium and an ordered stacking during compaction. Thus a qualification of the stacking based on a single distribution is difficult. It remains that the low values of the peaks (as here around 0.45) are usually associated to disordered stackings.

¹²Binning technique consists in combining voxels in order to decrease the size of the numerical volume.

Summary on the structure at various scales

Hollow spheres stackings structure can be characterized at various scales.

Macroscopic Scale The only structural parameters at macroscopic scale are density or relative density. The R.V.E. for density has been found to have less than 10 mm side size. Thus matter distribution is very homogeneous.

Mesoscopic scale This scale is the scale of the cells. Spheres diameters scatter is very low. Stackings are almost mono-modal. When samples are compared, there is no major differences in the mean neck size, nor in the mean coordination number. This similitude of architecture is a direct consequence of the compaction process which is driven by the styrofoam balls whatever the shell thickness. Nevertheless the measure of the neck size by X-ray tomography was shown to largely overestimate the real contact area (about 30 – 40%). No significant order has been found in the stacking, they can be considered as random.

Microscopic scale Study of the shells showed that the outer surface roughness is of order of the metallic powder size, while the inner surface wave length and amplitude is much more important. This inner roughness is due to the roughness of the styrofoam balls. Thus the absolute variation of the shell thickness is independent of the shell thickness. Porosity is quite important within the shells. It represents roughly 4 percents of porosity for the shells.

Chapter 2

Discrete Element Method applied to hollow spheres stackings

Contents

2.1	Interaction laws for the contact between spheres	109
2.1.1	Compression	110
2.1.1.1	Simulations	110
2.1.1.2	Models	110
2.1.2	Tension	111
2.1.2.1	Simulations	111
2.1.2.2	Models	111
2.1.3	Shear loading	112
2.1.3.1	Simulations	113
2.1.3.2	Models	115
2.1.4	Torsion and rolling	115
2.1.5	Non bonded contacts	115
2.1.5.1	Simulations	115
2.1.5.2	Models	115
2.2	Macroscopic loading on a random stacking of hollow spheres	116
2.2.1	Unloading modulus evolution	117
2.2.2	Influence of the creation of new contacts	117
2.2.3	Influence of the neck size distribution	118
	Interaction laws	120
	Macroscopic behaviour	120

The application of DEM to hollow spheres stackings has been initiated by A. Fallet in his PhD ([Fallet, 2008]). The modeling process is divided into two stages.

The first one is a derivation of the “elementary interaction laws” between two spheres.

The second one deals with the modeling of a stacking of spheres.

Within this chapter, we will describe how the “interaction laws” are obtained, and how they are modeled. Then they are implemented in the DEM code. Several improvements on the stacking simulations have been performed. They are presented and discussed.

2.1 Interaction laws for the contact between spheres

The behaviour of two spheres connected by a neck have been studied under various loadings using a Finite Element Model. It gave “interaction laws” of behaviour for DEM. Loading conditions were compression, tension, shearing, rolling and twisting (figure 2.1). Both shell thickness and neck size

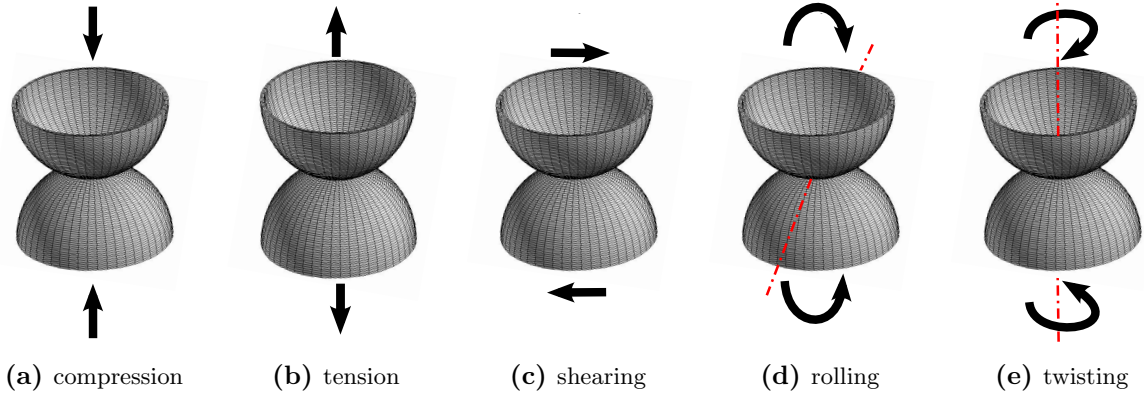


Figure 2.1: Loading conditions of the contact between 2 spheres.

have been varied. An elasto-plastic behaviour with an Hollomon hardening law has been given to the constitutive material. Its properties are the one of 314 stainless steel. *Neither the porosity of the shells, nor their roughness have been taken into account.* Table 2.1 presents the laws describing the behaviour of the constitutive material. Computations have been performed taking into account large strains, using lagrangian elements.

Component of the law	Model	Equations	Parameters
Elastic behaviour	Isotropic elasticity	$\sigma = E\varepsilon_{el}$	$E = 207GPa$ $\nu = 0.3$
Plastic criterion	Von Mises		
Flow rule	Associated plasticity		
Hardening law	Hollomon	$R = R_0 + K\varepsilon_p^n$	$R_0 = 185MPa$ $K = 698$ $n = 0.57$

Table 2.1: Parameters of the law of behaviour of the constitutive material.

2.1.1.1 Compression

2.1.1.1.1 Simulations

The response to compressive loading has been studied thanks to 2D axi-symmetric simulations. For each couple of shell thickness and neck size, a simulation has been performed. Displacements have been imposed at the boundaries. During the compression the state of the structure and its history have been stored in memory in order to perform unloading sequences. Figure 2.2 shows the evolution of the structure geometry from the initial mesh to a deformed mesh, and presents the force/displacement relations, both for loading and modulus, given by the simulations. Load is normalized by the square of the radius size, and motion by the radius size. The decrease of the unloading stiffness is only due to

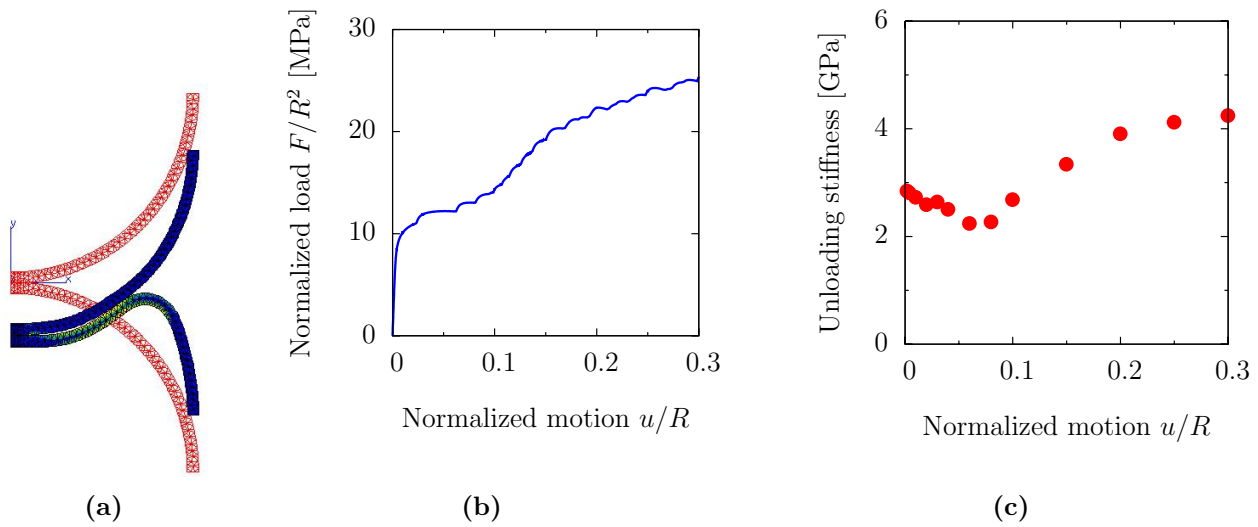


Figure 2.2: Simulations of 2 spheres of normalized shell thickness (t/R) of 0.07 in compression. Axi-symmetric FEM has been used. **a**-Initial mesh (red) and deformed mesh (blue). **b**-Reaction on the upper face versus its motion. **c**-Evolution of the unloading stiffness with motion.

geometrical effect¹³. The final stiffening of the structure stems from the new contact (beside the neck) between spheres which occurs while compression proceeds (at $u/R \simeq 0.1$ in the case of figure 2.2).

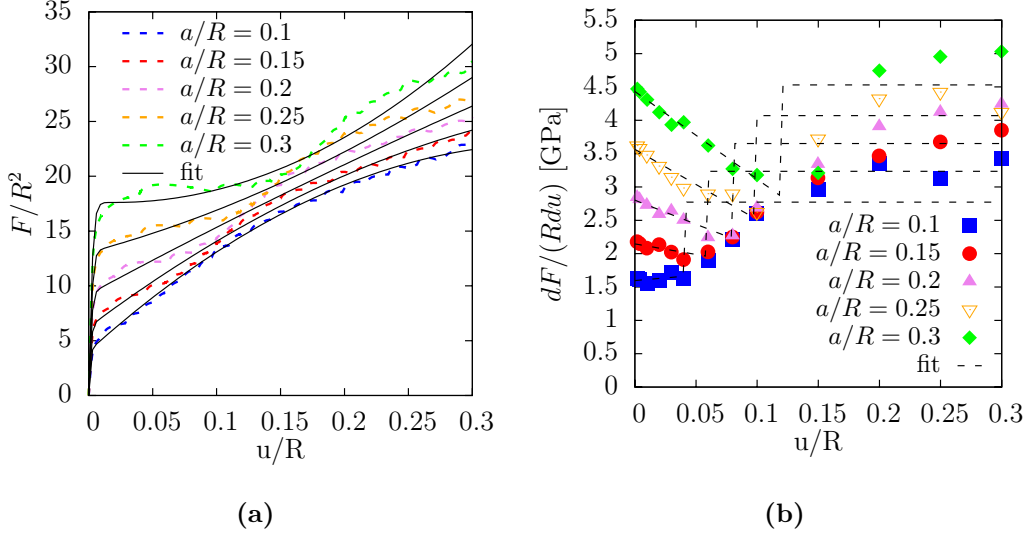
2.1.1.2 Models

For a each shell thickness, the neck size has been varied. Both the normalized load evolution and the stiffness evolution have been fitted. Models used are described in table 2.2. All the parameters are themselves fitted by polynom of order 2 of the normalized neck size. Figure 2.3 presents the results of simulations for various neck sizes and the model associated. The shape of the model laws for the stress has been chosen in order to re-transcript both properly the yield stress and approximately the hardening slope, taking into account the contact event between the shells. The laws are able to capture the softening that appends sometimes in the first stages of the plasticity.

The simplest law that can describe both the initial decrease and the higher values after shells contact

¹³No damage of the constitutive material is ever considered in this model

Normalized Load	$\begin{aligned} &\text{if } \frac{u}{R} < a_1 \text{ then } \frac{F}{R^2} = b_1 \frac{u}{R} \\ &\text{else } \frac{F}{R^2} = b_1 a_1 + \left(c_1 \left(\frac{u}{R} - a_1 \right)^2 + d_1 \left(\frac{u}{R} - a_1 \right) + e_1 \right) \left(1 - e^{-\frac{b_1}{e_1} \left(\frac{u}{R} - a_1 \right)} \right) \end{aligned}$
Stiffness	$\text{if } \frac{u}{R} < a_2 \text{ } E = b_2 \frac{u}{R} + c_2 \text{ else } E = d_2$

Table 2.2: Fit laws for the load and the stiffness evolution with normalized motion (u/R).**Figure 2.3:** Simulations of 2 spheres of normalized shell thickness (t/R) of 0.07 in compression. The size of the bonding (a/R) has been varied. Simulations and corresponding model for the stress-strain curve (a) and for the unloading modulus evolution with strain (b).

for the unloading modulus has been chosen. It obviously induces a large jump of the unloading modulus at the discontinuity.

2.1.2 Tension

The same modeling method as for compressive loading has been applied for tensile loading.

2.1.2.1 Simulations

Figure 2.4 shows the evolution of the structure from the initial mesh to a deformed mesh, and presents responses given by the simulations, both for the load versus motion curve and for the unloading stiffness versus motion curve. Both load and stiffness increase with strain. Because no damage behaviour has been taken into account for the constitutive material, the softening of the structure only appears for a strain of about 25%. It is due to a necking of the shells at the vicinity of the neck.

2.1.2.2 Models

Both the normalized load evolution and the stiffness evolution have been fitted. Models used are described in table 2.3. Figure 2.5 presents the results of simulations for various neck sizes and the model associated.

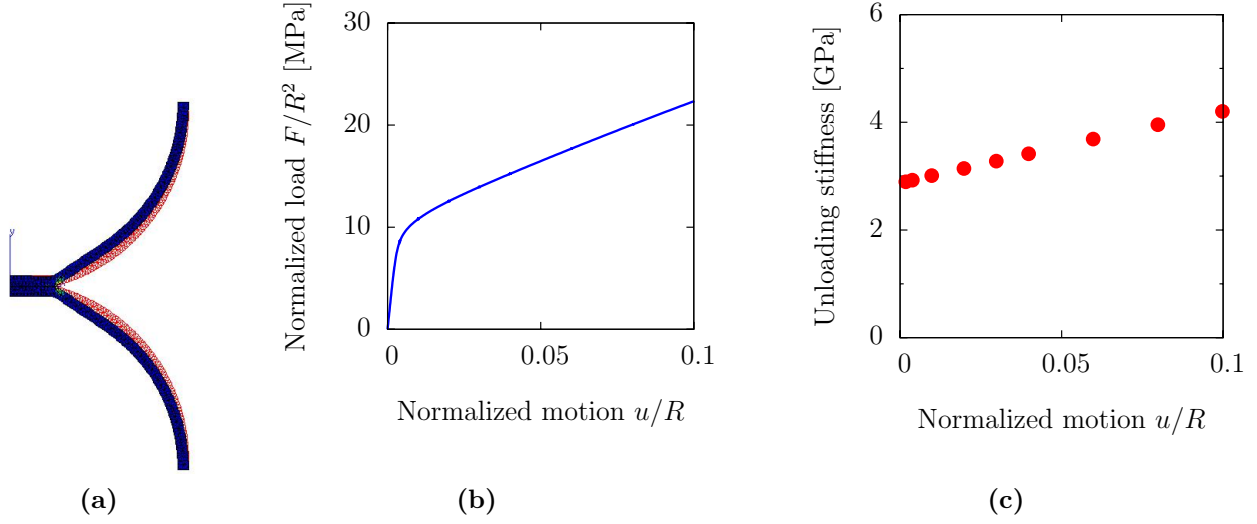


Figure 2.4: Simulations of 2 spheres of normalized shell thickness (t/R) of 0.07 in tension. Axi-symmetric FEM has been used. **a**-Initial mesh (red) and deformed mesh (blue). **b**-Reaction on the upper face versus its motion. **c**-Evolution of the unloading stiffness with motions.

Normalized Load	$\begin{aligned} &\text{if } \frac{u}{R} < a_1 \text{ then } \frac{F}{R^2} = b_1 \frac{u}{R} \\ &\text{else } \frac{F}{R^2} = b_1 a_1 + \left(c_1 \left(\frac{u}{R} - a_1 \right)^2 + d_1 \left(\frac{u}{R} - a_1 \right) + e_1 \right) \left(1 - e^{-\frac{b_1}{e_1} \left(\frac{u}{R} - a_1 \right)} \right) \end{aligned}$
Stiffness	$E = a_2 \frac{u}{R} + c_2$

Table 2.3: Fit laws for the load and the stiffness evolution with normalized motion (u/R).

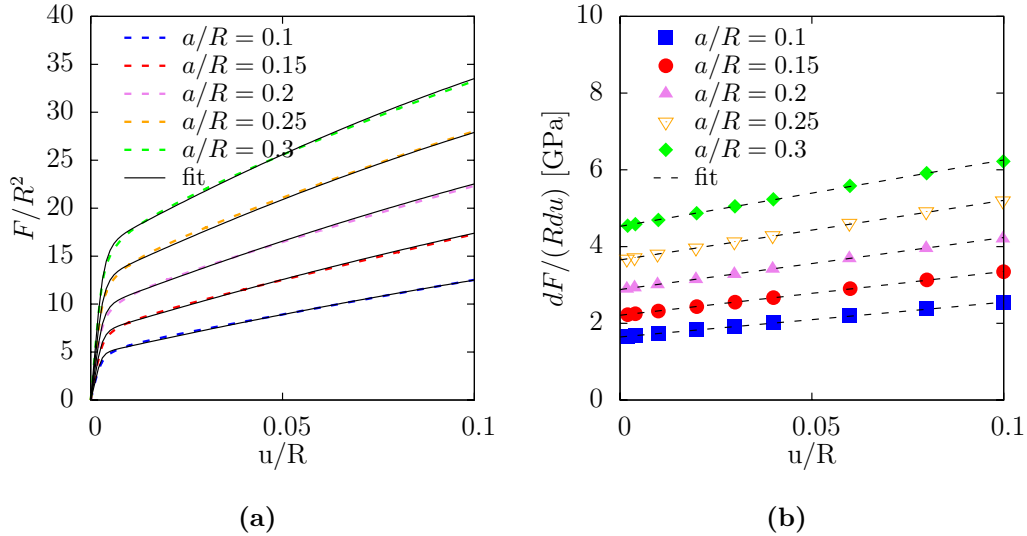


Figure 2.5: Simulations of 2 spheres of normalized shell thickness (t/R) of 0.07 in tension. The size of the bonding (a/R) has been varied. Simulations and corresponding model for the stress-strain curve (**a**) and for the unloading modulus evolution with strain (**b**).

2.1.3 Shear loading

To study the shear loading, 3D FEM had to be performed. These simulations are CPU time consuming. Thus laws obtained by A. Fallet [Fallet, 2008] have been kept. Nevertheless the unloading modulus

evolution and the boundary conditions influence have been quantified thanks to few simulations for particular neck sizes and shell thickness.

2.1.3.1 Simulations

Figure 2.6 presents the mesh used for this modeling. A. Fallet imposed both the full kinematic on the

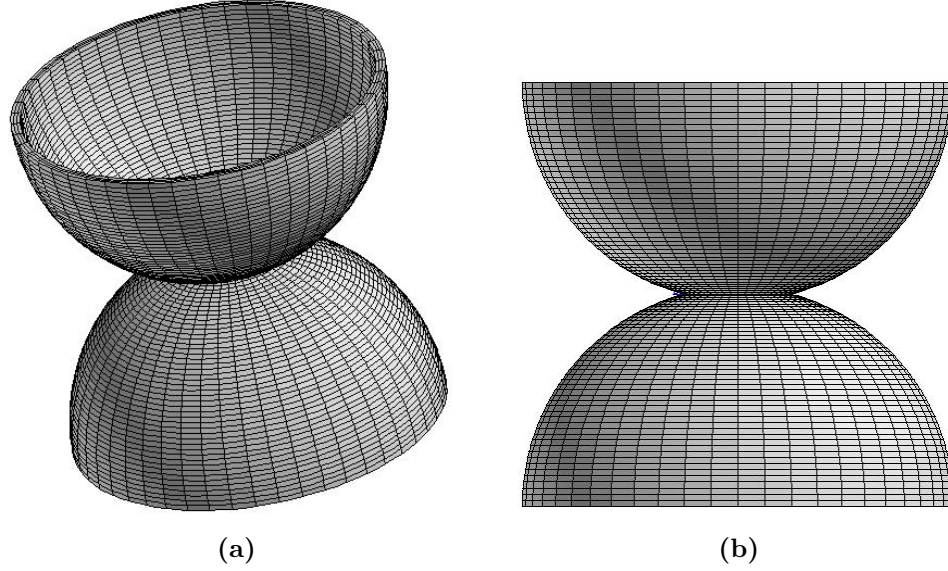


Figure 2.6: Simulations of 2 spheres of normalized shell thickness (t/R) of 0.07 in shear loading. 3D FEM has been used. Mesh used are presented.

upper and lower boundaries of the “diabolo”. Since it gives an overestimation of the stiffness of the structure, the response has been compared to other boundary conditions.

- First mixed boundary conditions have been tested. The axial displacement is imposed to remain null, and a global transverse reaction on the boundaries is increased linearly with time. Figure 2.7 compares the evolution of the normalized load F/R^2 with the normalized displacement u/R for a given shell thickness and for varied neck sizes (normalized radius of 0.1, 0.2 and 0.3) for both boundary conditions models. The influence of the imposed transverse kinematic constraint, which avoids the spheres to become ellipsoids is low. No significant difference on the load is observed. The shape of the deformed mesh is almost the same that the initial mesh after a normalized imposed displacement of 0.05.
- Then all the kinematic constraints have been removed on the upper boundaries. A null global axial reaction and a transverse reaction increasing linearly with the time was imposed on the upper boundary. For the lower boundary, the axial displacement was prescribed on the whole surface, and the transverse displacement was prescribed for a single node.

Figure 2.8 compares the evolution of the normalized load F/R^2 with the normalized displacement u/R for a given shell thickness and for varied neck sizes (normalized radius of 0.1, 0.2 and 0.3) for both mixed and full-reaction¹⁴ boundary conditions models. When no kinematic constraint is imposed on the upper

¹⁴Abusively called so since kinematic conditions are imposed on one side.

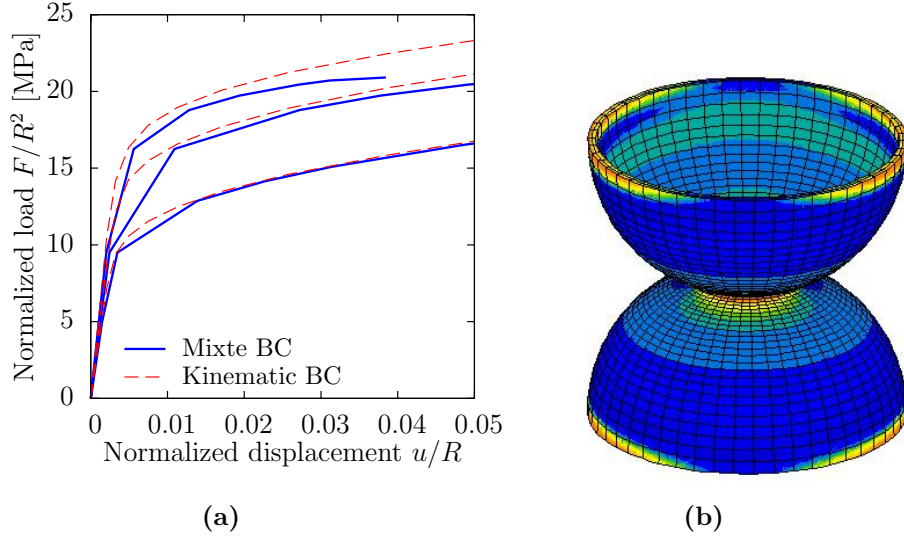


Figure 2.7: Comparison of the evolution of the normalized load F/R^2 with the normalized displacement u/R for the shear loading of 3 necks (of normalized radius 0.1, 0.2 and 0.3) between two spheres of normalized shell thickness of 0.05 for respectively the full kinematic boundary condition and for a mixed kinematic-reaction boundary condition. The shape of the deformed mesh is presented for the model with kinematic-reaction boundary condition for a normalized neck size of 0.2.

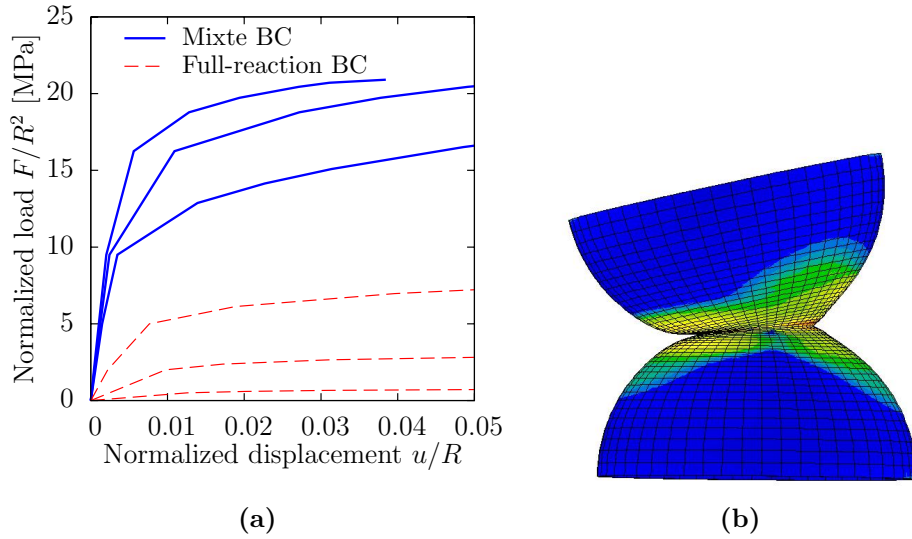


Figure 2.8: Comparison of the evolution of the normalized load F/R^2 with the normalized displacement u/R for the shear loading of 3 necks (of normalized radius 0.1, 0.2 and 0.3) between two spheres of normalized shell thickness of 0.05 for respectively the mixed kinematic-reaction boundary condition and for a full reaction boundary condition. The shape of the deformed mesh for the full-reaction boundary conditions is presented for a normalized neck size of 0.2.

boundary, the deformation mechanism of the structure is preferentially rolling than shearing. The shear load is thus largely lowered. The model with full-reaction boundary conditions may be considered as a lower bound for the shear contact law.

In order to keep coherence between laws, *the initial model, with full-kinematic boundaries conditions,*

has been kept as the reference model.

2.1.3.2 Models

The bi-linear model for the contact law proposed by A.Fallet has been kept unchanged. Table 2.4 recalls the model.

Normalized Load	if $\frac{u/R}{<} a_1$ then $\frac{F}{R^2} = b_1 \theta$ else $\frac{F}{R^2} = b_1 a_1 + c_1(u/R - a_1)$
Stiffness	$E = b_1$

Table 2.4: Fit laws for the load and the stiffness evolution with normalized displacement (u/R) for the shear contact law.

2.1.4 Torsion and rolling

For both torsion and rolling contact laws, the bi-linear models proposed by A.Fallet have been kept unchanged. Table 2.5 recalls the model.

Normalized Load	if $\frac{\theta}{<} a_1$ then $\frac{M}{R^3} = b_1 \theta$ else $\frac{M}{R^3} = b_1 a_1 + c_1(\theta - a_1)$
Stiffness	$E = b_1$

Table 2.5: Fit laws for the load and the stiffness evolution with rotation (θ) for rolling and twisting contact laws.

2.1.5 Non bonded contacts

In order to account for new contacts during loading, local laws for two spheres that are not bonded together have to be set up. In that case the load levels are much more lower than for two bonded spheres. Torsion and even shear loading can be neglected. Thus only laws for local compressive loading have been fitted.

2.1.5.1 Simulations

Figure 2.9 shows the evolution of the structure from the initial mesh to a deformed mesh, and presents responses given by the simulations, both for the load versus motion curve and for the unloading stiffness versus motion curve.

2.1.5.2 Models

Both the normalized load evolution and the stiffness evolution have been fitted. Figure 2.5 presents the results of simulations for various shell thicknesses and the model associated.

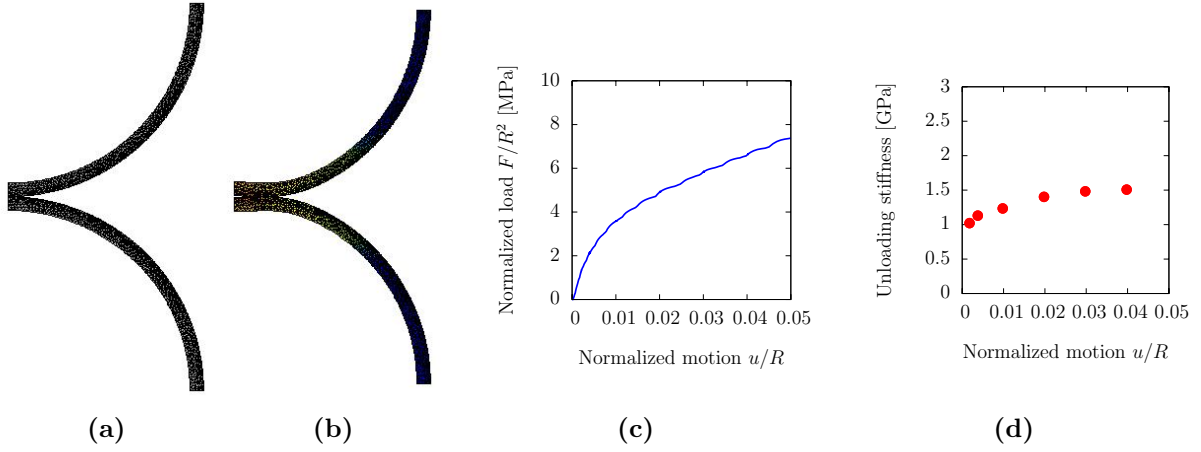


Figure 2.9: Simulations of 2 non connected spheres of normalized shell thickness (t/R) of 0.07 in compression. Axi-symmetric FEM has been used. **a**-Initial mesh. **b**-Deformed mesh. **c**-Reaction on the upper face versus its motion. **d**-Evolution of the unloading stiffness with motions.

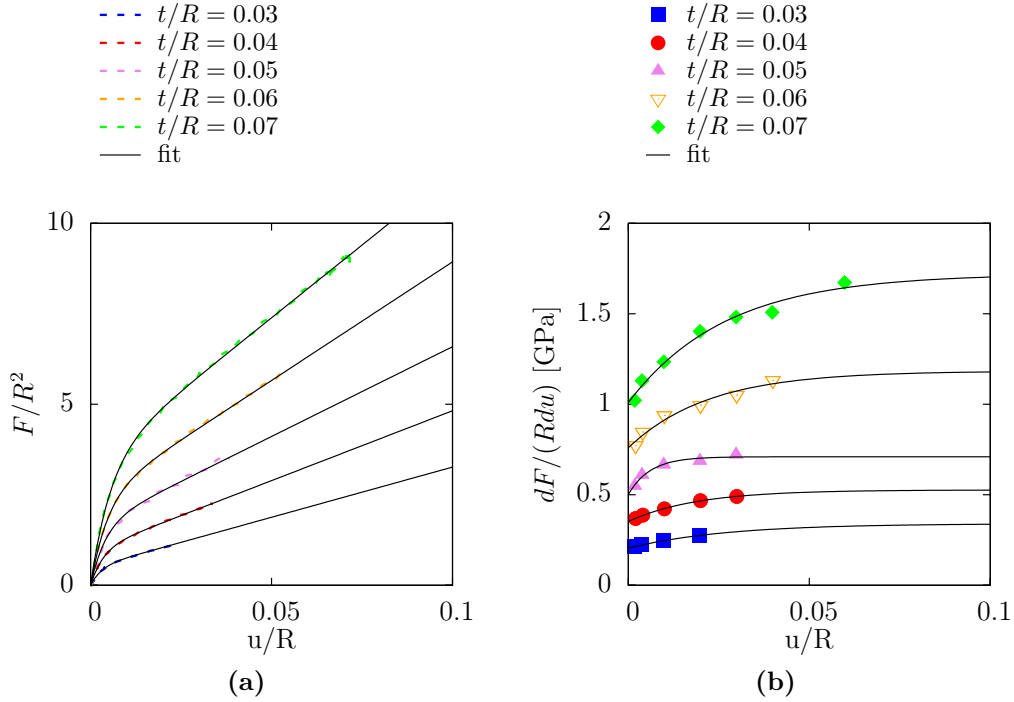


Figure 2.10: Simulations of 2 spheres without neck in compression. The shell thickness (t/R) has been varied. Simulations and corresponding model for the stress-strain curve **(a)** and for the unloading modulus evolution with strain **(b)**.

The behaviour of such contact is almost the same that for bonded contact when the neck size is null.

2.2 Macroscopic loading on a random stacking of hollow spheres

The “interaction laws” presented are implemented in the DEM code dp3D. Several improvements are also implemented in the code. The influence of these modifications in the code will now be discussed.

2.2.1 Unloading modulus evolution

Contacts between spheres are given the ability to unload with an interaction law different from the one followed during loading. Thus the local behaviour can be elasto-plastic and not only elastic. So it allows to measure the real unloading stiffness of a stacking. Without this modification, the stiffness measured was wrong since it would rely on an unphysical unloading tangent modulus.

Moreover, the local stiffness is varied with the local relative motion between particles. In order to quantify this influence, the stiffness of a stacking have been computed twice. Once with an evolution of the local stiffness and once without. Figure 2.11 presents both results. With a constant local stiffness,

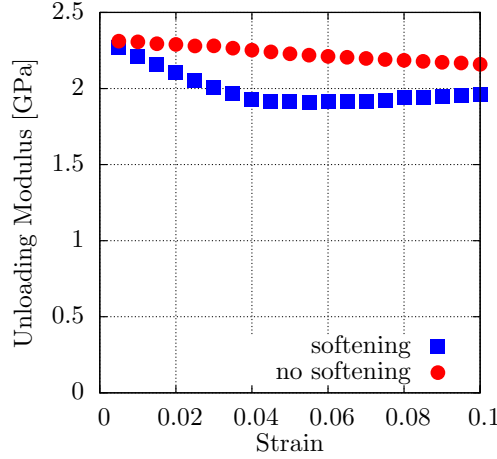


Figure 2.11: Evolution of the unloading modulus of a stacking with the strain. The sample contains 1000 particles and it is loaded in uniaxial compression with periodic boundaries conditions. The macroscopic behaviours with and without a local evolution of the contact stiffness are compared.

the macroscopic unloading modulus is almost constant. The small decrease is due to non linearities. Local stiffness relates load and motions while the macroscopic stiffness links load and true strain. When local stiffness is varied among the evolution observed above, the macroscopic unloading modulus first decreases during the first 5% of strain. Then it is almost constant.

Thus evolution of the stiffness between two particles can lead to a decrease of about 20% of the macroscopic unloading modulus. The unloading modulus is almost constant if the local stiffness is kept constant, even with the creation of new contacts.

This shows the importance of taking into account local softening.

2.2.2 Influence of the creation of new contacts

The new contacts between particles are given a new behaviour under compressive loading as described in 2.1.5. The shear response is driven by the friction coefficient. In order to quantify the influence of the friction coefficient and of the new contacts, simulations have been performed either with varied friction coefficient, either without taking into account any load for contact creation. Figure 2.12 presents the results of these simulations ; the evolution with strain of the mean coordination number, the stress and the unloading modulus. The effect of the friction coefficient is so low that no difference can be observed on the macroscopic response, neither on stress or stiffness level, neither on the reorganization level.

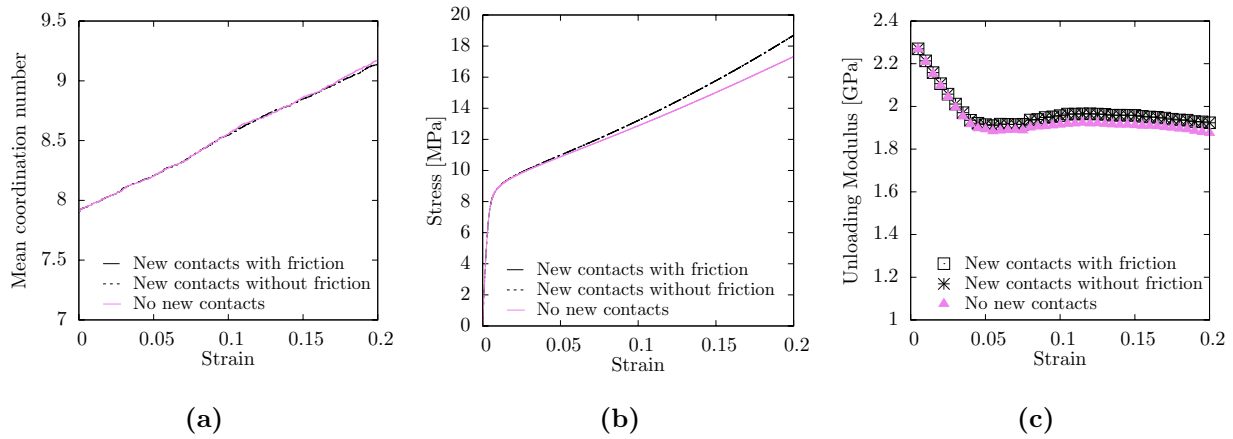


Figure 2.12: Influence of the new contacts and of the friction on mean coordination number, on the stress-strain curve and on the unloading modulus.

New contacts are responsible of a few percents of the hardening. Their influence remains nevertheless very low on the unloading modulus.

Thus all simulations will be performed with a friction coefficient of 0. That means that no shear resistance is generated by non bonded contacts. These new contacts are not responsible for the constant macroscopic stiffness over 5% of strain.

2.2.3 Influence of the neck size distribution

During generation of the stackings, compaction of the styrofoam balls can determine the neck size distribution and the coordination number. Actually these parameters depend both on the initial density before compaction and on final density. A random stacking of spheres of almost 36% of initial open porosity has been densified assuming an elastic behaviour (styrofoam ball behaviour) for the particles. The densification has been performed up to an open porosity f of only 25% but the stacking structure has also been stored in memory several times during this process to measure the evolution of its parameters. Thus the neck size distribution (figure 2.13) and the average coordination number (figure 2.14) can be compared between numerical stackings and the real samples. Figure 2.14 shows that numerical samples of porosity of 25% or 28% have almost the same neck size distribution that the real samples. Mean coordination numbers for numerical samples of porosity of 25% or 28% are also in accordance with the real stacking properties. Nevertheless it seems that a stacking of initial porosity around 38% would have made the numerical structure closer to the real one. It remains that differences are low. Stages of hard particles compaction required to reach the initial density, prior to the styrofoam densification, is CPU time consuming. Based on the above observations, stackings with initial porosity of 36%, already generated by A. Fallet, have been used. The numerical styrofoam compaction was performed up to a porosity of 28%.

A. Fallet observed that the mean quadratic value of the neck radius size can be applied to all the necks, instead of the size distribution, without any change in the macroscopic response. It has been checked that the shear contribution does not change this conclusion. The mean neck size and the mean quadratic neck size have been compared to the initial distribution. Figure 2.15 presents the cumulative neck size distribution that have been compared and the responses obtained for the stress-strain curve

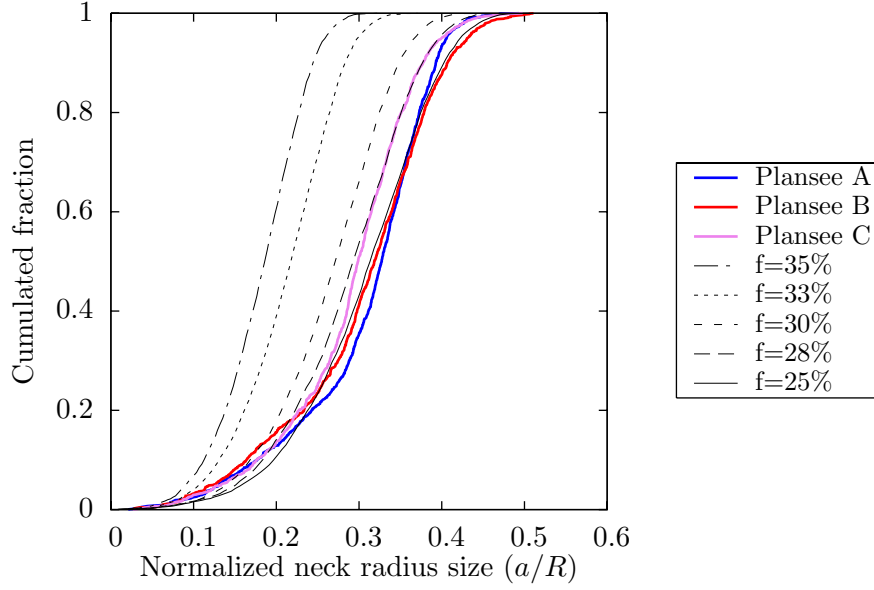


Figure 2.13: Comparison of the neck size distribution in the real and numerical samples of varied open porosity f generated thanks to a stacking of 36% of initial open porosity.

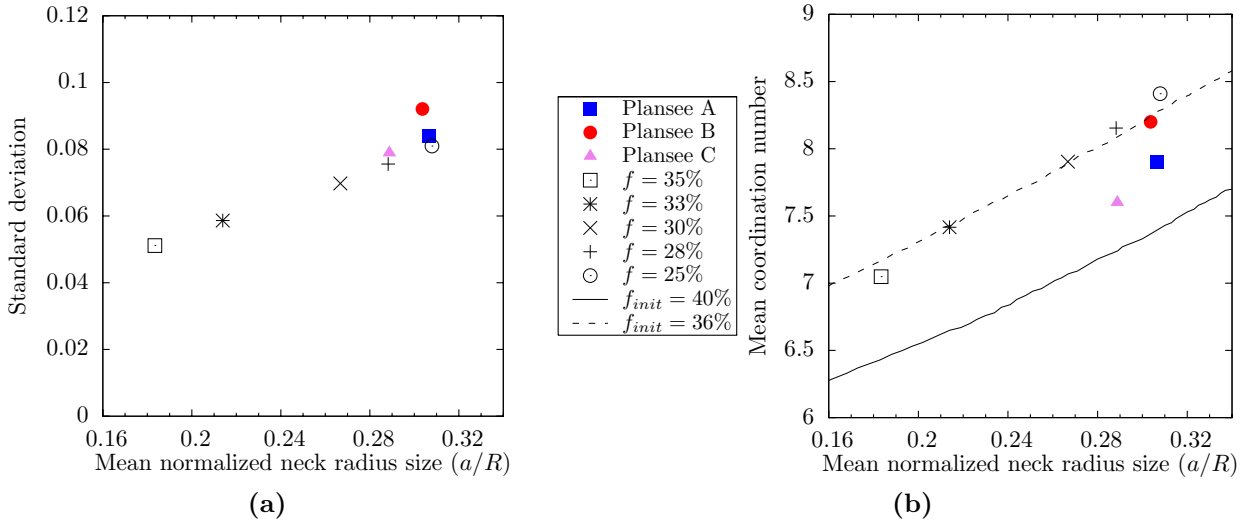


Figure 2.14: Comparison of the neck size scatter **(a)** and of the relation between the mean neck size and the mean coordination number **(b)**, in the real and numerical samples. The mean coordination evolution with mean neck size is described both for samples of initial porosity f_{init} of 40% and 36%.

and for the unloading modulus. Thus, in order to set up scaling laws, the mean quadratic neck size can be used to characterize the stacking behaviour (all other structural parameters remaining unchanged).

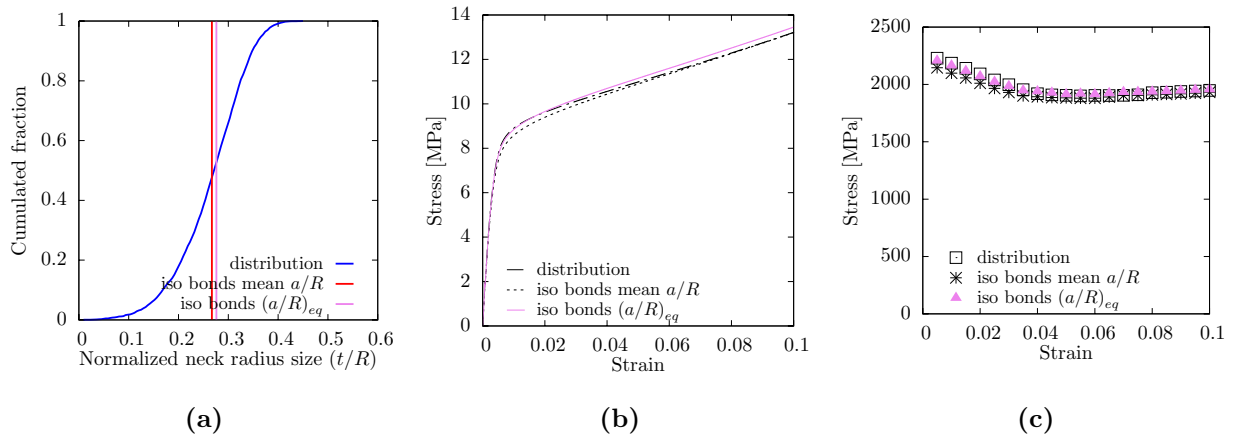


Figure 2.15: Comparison of the neck size distribution (a) and of its influence on the stress-strain curve (b) and on the unloading modulus (c).

Summary on DEM applied to hollow spheres stacking

Interaction laws Elementary laws have been given an elasto-plastic behaviour with a stiffness that is evolving with strain. Compression lead to a decrease of the local stiffness within the first percents of strain. All other elementary loadings are hardening. New contacts have also been given a new behaviour law.

Macroscopic behaviour The evolution of the local stiffness is responsible for a decrease of 20% of the macroscopic unloading modulus within the first 5% of strain.

New contacts lead to a small increase of the hardening, but they are not responsible for the evolution of the macroscopic unloading modulus. Friction was shown to have almost no effect on the hollow spheres stackings behaviour.

Initial density of the stackings, prior to the styrofoam densification process, plays a role on the structure properties. A stacking of initial porosity of 36%, compacted up to 28% of porosity, presents structural properties close to the real samples. The neck size distribution was shown to have little influence on the macroscopic behaviour since the mean quadratic neck size is kept constant.

Chapter 3

Macroscopic behavior

Contents

3.1	Uni-axial compressive tests	123
3.1.1	Experiments	123
3.1.2	Representative Volume Element	123
3.1.3	Sphere size effect	125
3.1.4	Density effect	126
3.1.5	Comparison of experiments and simulations	128
3.1.5.1	Direct confrontation	128
3.1.5.2	Model improvement	129
	Neck size correction	129
	Elementary shear law enhancement	130
3.1.5.3	Combination of corrections	130
3.2	Uni-axial tensile tests	132
3.2.1	Experiments	132
3.2.2	Representative Volume Element	132
3.2.3	Density effect	132
3.2.4	X-rays tomography in situ tests	136
	Shell tearing	136
	Neck debonding	137
	Correlation with the macroscopic behaviour	137
3.2.5	Comparison of experiments and simulations	137
3.3	Multi-axial compressive tests	138
3.3.1	Experiments	138
3.3.2	Boundary conditions with imposed motion	139
3.3.2.1	Limitation of the method	139
3.3.2.2	RVE	139
3.3.2.3	Density influence	139
3.3.3	Boundaries with imposed pressure	140
3.3.4	Comparison of experiments and simulations	141

Uniaxial compressive behaviour	143
Uniaxial tensile behaviour	143
Multi-axial compressive behaviour	143
DEM modeling	143

3.1 Uni-axial compressive tests

3.1.1 Experiments

Simple compression tests have been performed on cubic samples of various sizes. Cubes with a side size of 10, 20 and 30 mm have been investigated. A constant displacement rate of 0.05mm/s has been imposed for all the samples. It gives initial strain rates ranging from $1.7 \cdot 10^{-3}$ to $5 \cdot 10^{-3}\text{s}^{-1}$. Numerous loading-unloading sequences have been performed in order to get the evolution of Young's modulus with strain. Relative motion of the plateau has been recorded by a RDP sensor. Figure 3.1 presents a sample and its stress-strain curves.

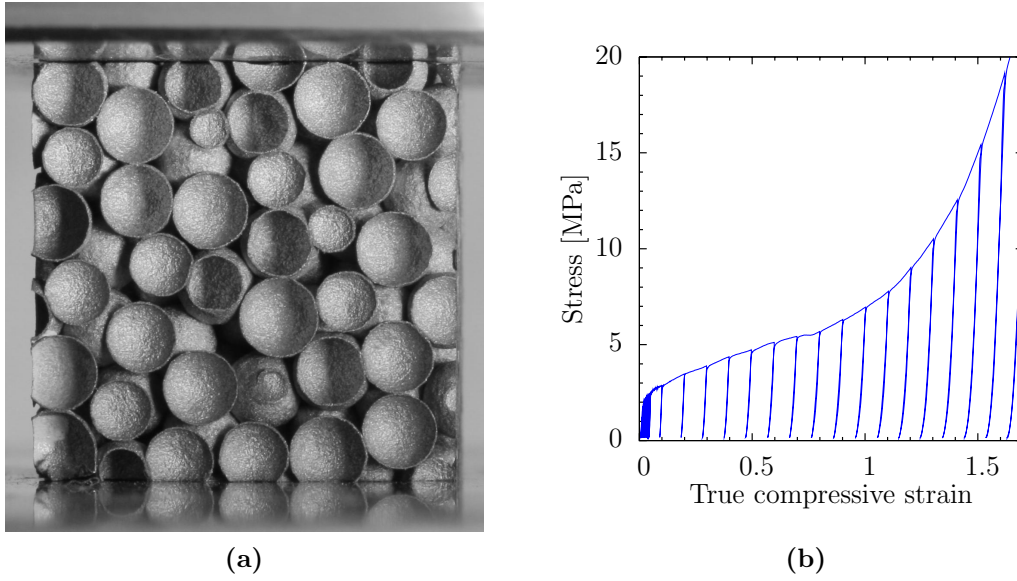


Figure 3.1: *a-A sample before uniaxial compressive loading. b-Stress-strain curve with unloading sequences.*

Complementary experiments have been performed to check the non dependence of the responses on the strain rate, and on the numerous unloading sequences. Reported in Appendix B, these experiments conclude that neither a variation of the strain rate, nor unloading sequences, have any influence on the overall response of the materials considered.

From the experiment, several outputs are obtained. First stress-strain curves can be plotted, without the unloading sequences. Unloading moduli can be calculated at each unloading sequence, and thus its evolution with strain can also be visualized. Then from these two main data sets are extracted several properties. Figure 3.2 shows the parameters extracted while table 3.1 explains how they are obtained. The stress-strain curve can be described thanks to a bi-linear-law. The plastic behaviour is defined by the mean plateau hardening modulus H and by the yield stress σ^* .

3.1.2 Representative Volume Element

Stress-strain curves do not show any major sensitivity to the specimen size. When looking at the shapes of the curves, scatter seems to be relatively low (Figure 3.3a). Nevertheless, when properties extracted from the curves are compared, one can see some “slight” influence of the sample size. Figure 3.3b shows the evolution of two properties (Initial unloading modulus and strain at 50% of strain) with the sample size (that is the ratio of the sample size L by the sphere diameter d). The mean stress value

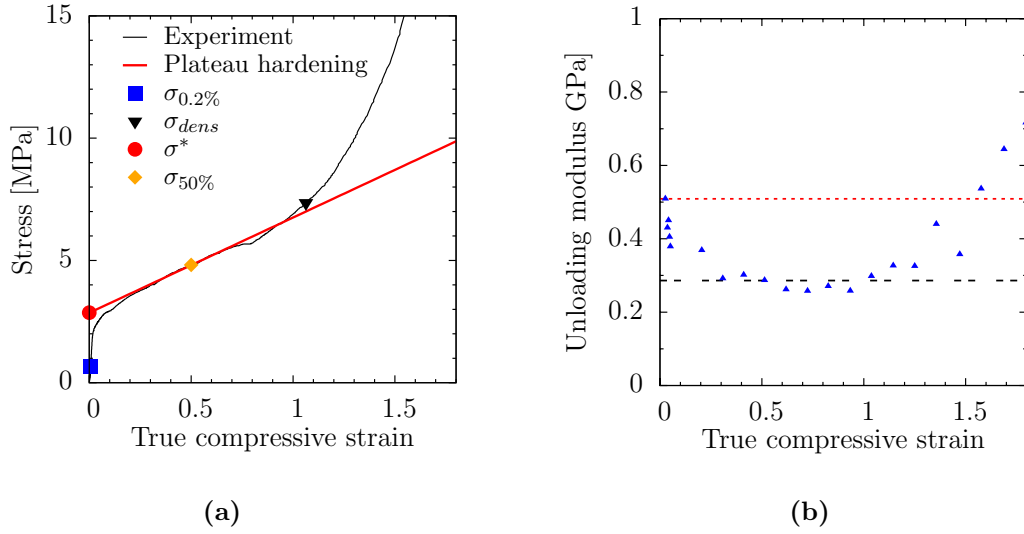


Figure 3.2: Compressive loading response. **a**-Parameters extracted from the stress-strain curve. **b**-Parameters extracted from the unloading modulus evolution with strain.

Table 3.1: Procedure of extraction of parameters for compressive tests.

Parameter	Sign	Particular procedure
Stress at $\varepsilon = 0.25$	$\sigma_{25\%}$	Slope of the stress-strain curve for $0.2 < \varepsilon < 0.8$
Stress at $\varepsilon = 0.50$	$\sigma_{50\%}$	
Mean plateau hardening modulus	H	
Unloading modulus	$E(\varepsilon_i)$	Slope of the unloading stress-strain curve for $0.2 * \sigma(\varepsilon_i) < \sigma < \sigma(\varepsilon_i)$
Initial unloading modulus	E_{init}	Maximum of E for $\varepsilon < 0.05$
Mean “plateau” unloading modulus	E_{mean}	Mean value of E for $0.2 < \varepsilon < 0.8$
Stress at densification	σ_{dens}	Stress for $\sigma(\varepsilon) = 1.05 * H * (\varepsilon - 0.5)$
Strain at densification	ε_{dens}	Strain for $\sigma = \sigma_{dens}$
Energy absorbed at densification	W_{dens}	$\int_0^{\varepsilon_{dens}} \sigma(\varepsilon) d\varepsilon$

evolves slightly and the scattering almost vanish when the sample ratio size (L/d) goes from 4 to 12. Concerning the unloading moduli, things are less clear since the accuracy of the measurements is rather low. It remains that one should expect the R.V.E. to be larger for the stiffness that for a stress level at large deformation. Figure 3.4 shows the evolution of the mean standard deviation of several properties with the ratio L/d . For sample size ratio superior to 7, the standard deviation of the stress levels is lower than 5%. Thus a sample size ratio of 7 can define a R.V.E. for stress level at large deformation. Dealing with the unloading modulus, the sample ratio has to be at least of 10. In that case, relative deviation remains about 10%.

So for a simple compressive state about 350 particles are required to define a R.V.E. for stress level at large deformation, while 1000 can define a R.V.E. for the initial unloading modulus.

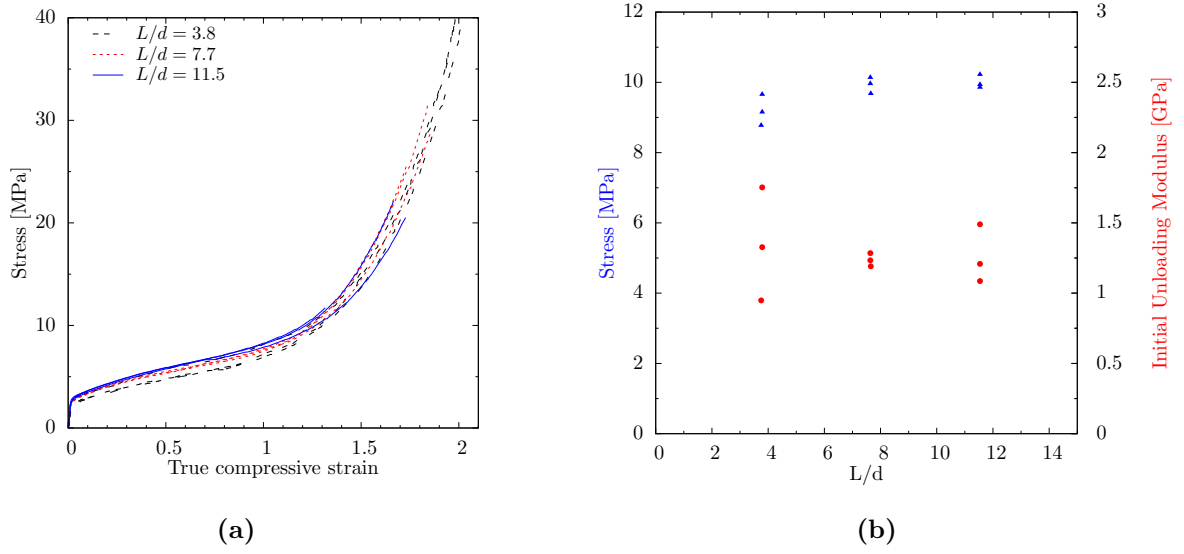


Figure 3.3: Influence of sample size. **a**-Comparison of strain-stress curves. **b**-Comparison of extracted properties : stress at $\varepsilon = 50\%$ (upper points, blue triangles, with scale on the left hand side axis) and initial unloading modulus (lower points, red circles, with scale on the right hand side axis).

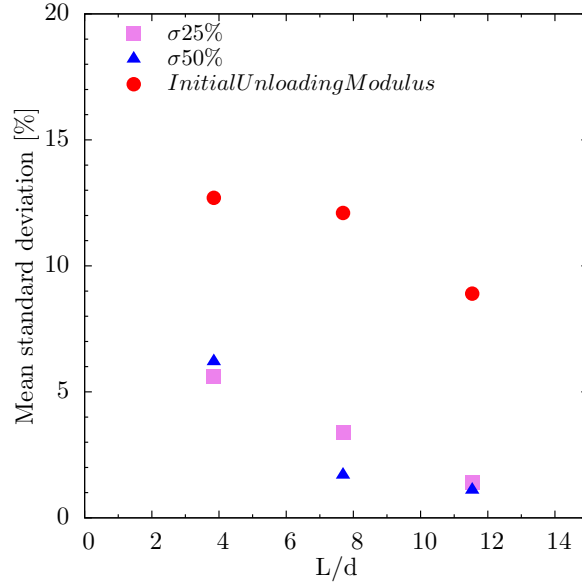


Figure 3.4: Mean standard deviation evolution with the ratio L/d for stresses at $\varepsilon = 25\%$ and $\varepsilon = 50\%$ and for initial unloading modulus.

3.1.3 Sphere size effect

Figure 3.5a shows stress-strain curves of two foams with two different spheres size but with same density, while figure 3.5b compares unloading moduli and stresses at 50% of strain for both sphere radius. First one can observe that the small spheres seems to present a larger scatter while the sample size is the same. That would imply that the R.V.E. is larger (in relation to the sphere diameter) for small spheres. Nevertheless the global shape of the stress-strain curves is the same, and no general trends can be seen

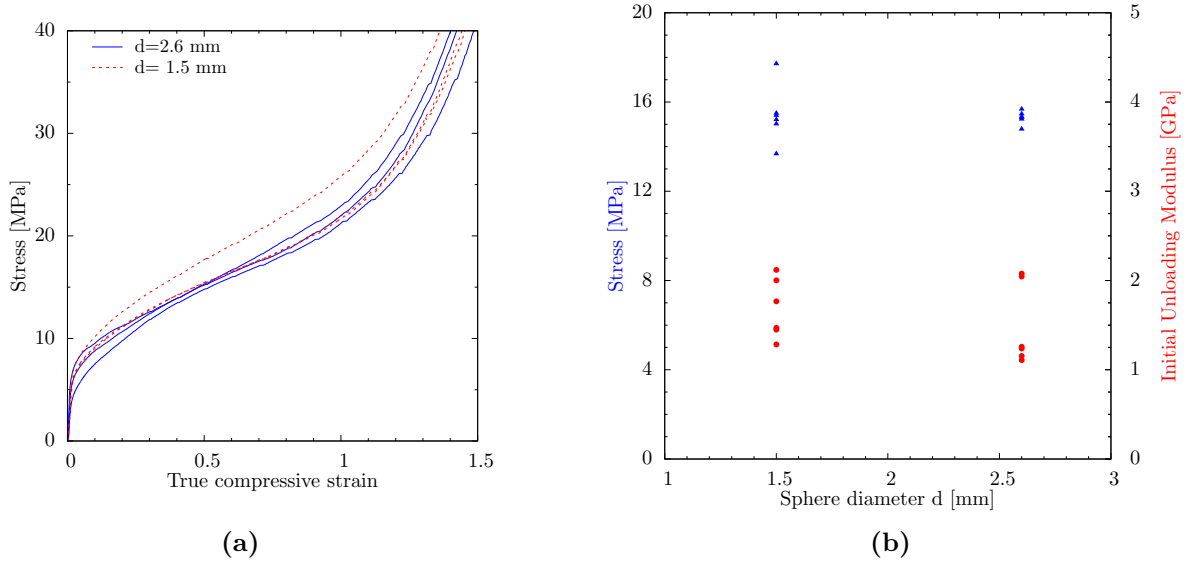


Figure 3.5: Influence of sphere size. **a**-Comparison of strain-stress curves. **b**-Comparison of extracted properties : stress at $\varepsilon = 50\%$ (upper points, blue triangles, with scale on the left hand side axis) and initial unloading modulus (lower points, red circles, with scale on the right hand side axis).

in relation to the sphere diameter. Thus the behaviour is assumed to be independent of the sphere size. A larger scatter can be attributed to smaller spheres.

3.1.4 Density effect

In order to allow easy comparisons with other foams, the input parameter chosen is the density.

Figure 3.6 shows the simple compressive response of hollow sphere stackings of various density. Both stress-strain curves and unloading moduli evolution are plotted. It is clear that there is no major

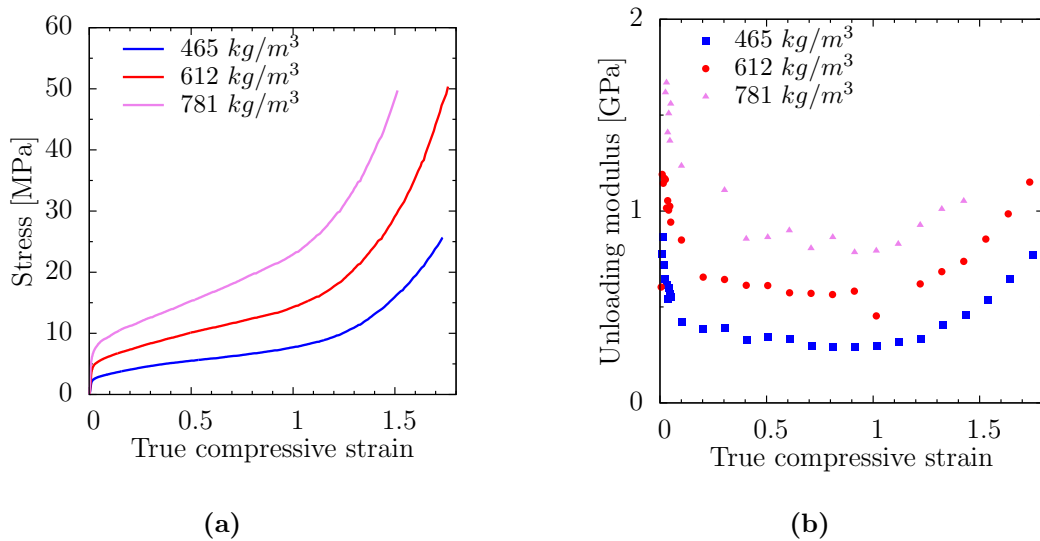


Figure 3.6: Influence of foam density. **a**-Comparison of strain-stress curves. **b**-Comparison of unloading modulus evolution with strain.

differences in the shapes of the curves and that, as expected, all the stress and stiffness levels are enhanced with a denser foam. Nevertheless no variation on the strain scale is observed. All the transition strains between the different domains (elastic area, plateau, and densification area) seem independent of the foams initial densities (figure 3.7).

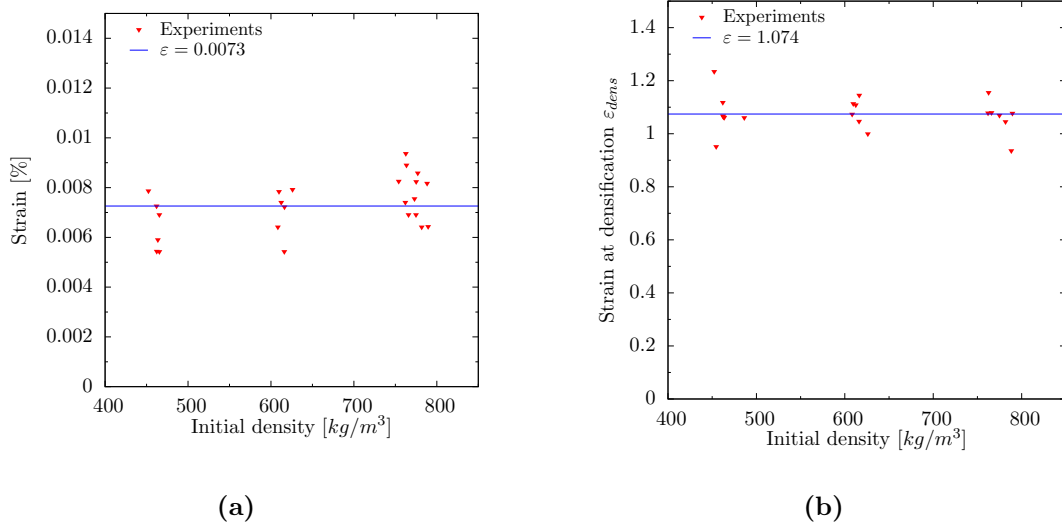


Figure 3.7: Influence of foam density on elastic strain (a) and on densification strain (b).

Thus all the curves can be described with the same law, provided the coefficients of the law are dependent on the density. The bi-linear law previously chosen can therefore be fitted for several stackings. The law of evolution of the parameters P with density is usually a power law for foams. It can be either a power law of the foam initial density (Eq.3.1), or a power law of the initial relative density (Eq.3.2). n is obviously the same for both laws.

$$P(\rho) = K\rho^n \quad (3.1)$$

$$P(\rho) = K^*(\rho^*)^n \text{ with } \rho^* = \frac{\rho}{\rho_s} \quad (3.2)$$

Figure 3.8 describes the evolution of various stress levels and of unloading moduli with the foam initial density. Table 3.2 sums up the exponent of the power laws of the parameters.

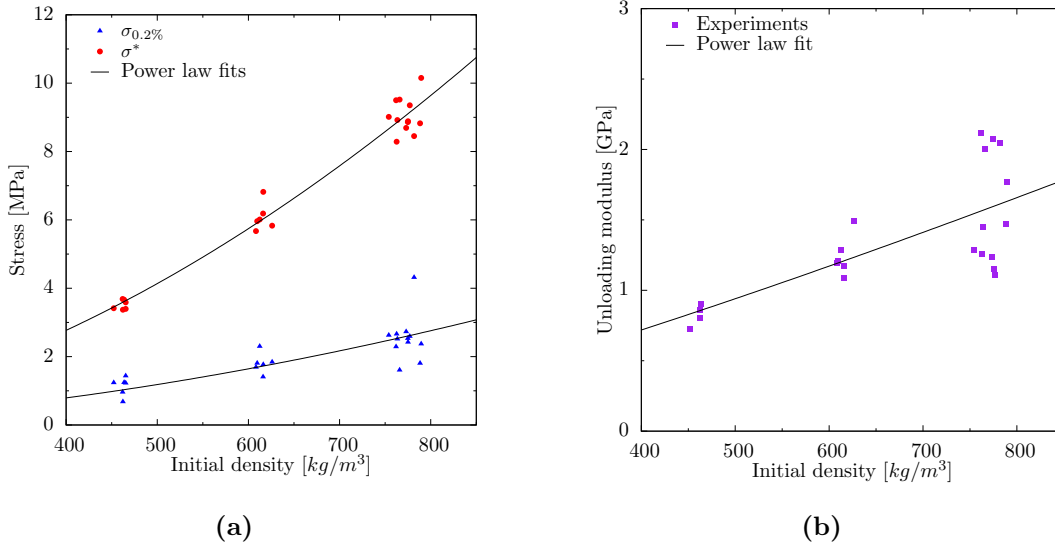


Figure 3.8: Power law of the initial density for various parameters. *a*-Elastic limit σ^* and stress at $\varepsilon = 50\%$. *b*-Initial unloading modulus.

Table 3.2: Power laws for compressive behavior parameters. K is relative to the power law of the initial density (Eq.3.1) while K^* is relative to the power law of the initial relative density (Eq.3.2). n is the same for both laws.

Parameter	unit	K	n	Standard deviation	K^*
$\sigma_{25\%}$	MPa	$7.42 \cdot 10^{-05}$	1.80	$4.88 \cdot 10^{-01}$	$6.03 \cdot 10^{+02}$
$\sigma_{50\%}$	MPa	$4.39 \cdot 10^{-05}$	1.92	$6.88 \cdot 10^{-01}$	$1.02 \cdot 10^{+03}$
$\sigma_{0.2\%}$	MPa	$8.92 \cdot 10^{-05}$	1.54	$4.99 \cdot 10^{-01}$	$7.45 \cdot 10^{+01}$
σ^*	MPa	$5.91 \cdot 10^{-05}$	1.79	$4.26 \cdot 10^{-01}$	$4.40 \cdot 10^{+02}$
ε_{el}	$7.30 \cdot 10^{-03}$		$1.10 \cdot 10^{-03}$	$7.30 \cdot 10^{-03}$	
ε_{dens}	$1.07 \cdot 10^{+00}$		$6.65 \cdot 10^{-02}$	$1.07 \cdot 10^{+00}$	
E_{init}	GPa	$5.19 \cdot 10^{-04}$	1.21	$3.00 \cdot 10^{-01}$	$2.23 \cdot 10^{+01}$
E_{mean}	GPa	$5.06 \cdot 10^{-06}$	1.82	$8.58 \cdot 10^{-02}$	$4.87 \cdot 10^{+01}$
H	MPa	$1.51 \cdot 10^{-05}$	2.05	$1.00 \cdot 10^{+00}$	$1.11 \cdot 10^{+02}$

3.1.5 Comparison of experiments and simulations

Simple compressive tests have been simulated by DEM. Periodic boundaries conditions with $\sigma_{xx} = \sigma_{yy} = 0$ and imposed $\dot{\varepsilon}_z$ have been applied to a reference cubic sample of 1000 particles. The shell thickness has been varied.

3.1.5.1 Direct confrontation

Strain-stress curves and unloading modulus evolution with strain for DEM simulations and for experiments are compared in figure 3.9. Both shapes of the curves and shift with density are similar between experiments and simulations. Nevertheless the level of stress and stiffness predicted are obviously too high.

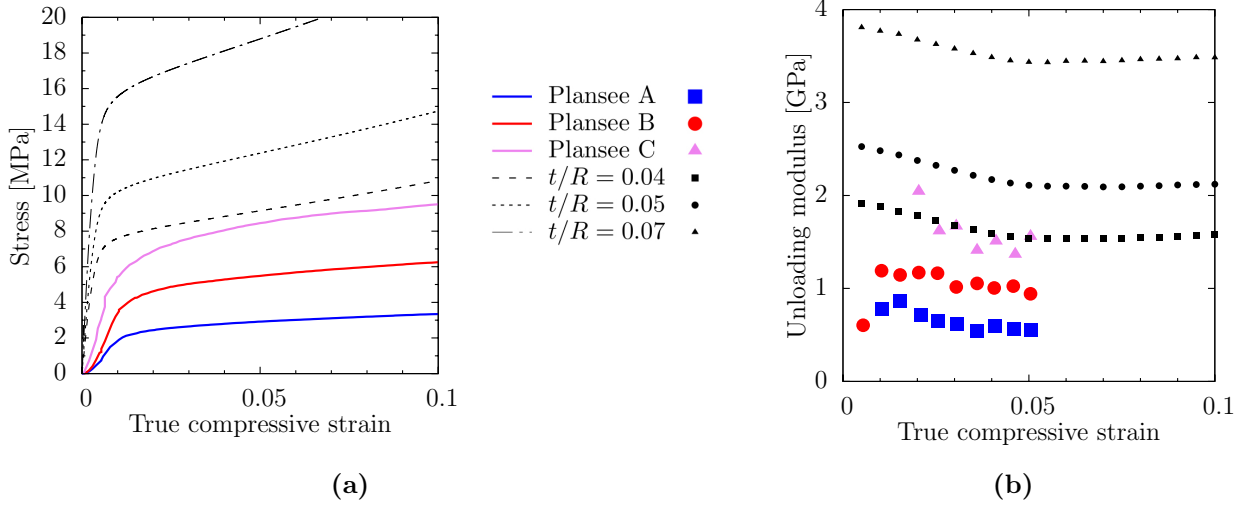


Figure 3.9: Confrontation of experiments and model for the stress-strain curves (a) and for the unloading modulus (b) under uniaxial compression.

3.1.5.2 Model improvement

Several possibilities have been investigated in order to have a better simulation of the mechanical properties of the stackings.

Neck size correction In order to account for the overestimation of the neck size, as described in 1.3.2.1, a stacking with a smaller mean neck size has been used. The stacking presents an initial open porosity of 25% and an average normalized neck size of 0.18. Figure 3.10 compares the stress-strain curves and the unloading modulus evolution of the experiments with the DEM simulations with neck size correction. The model predictions are consistent with the experiments for the highest foam

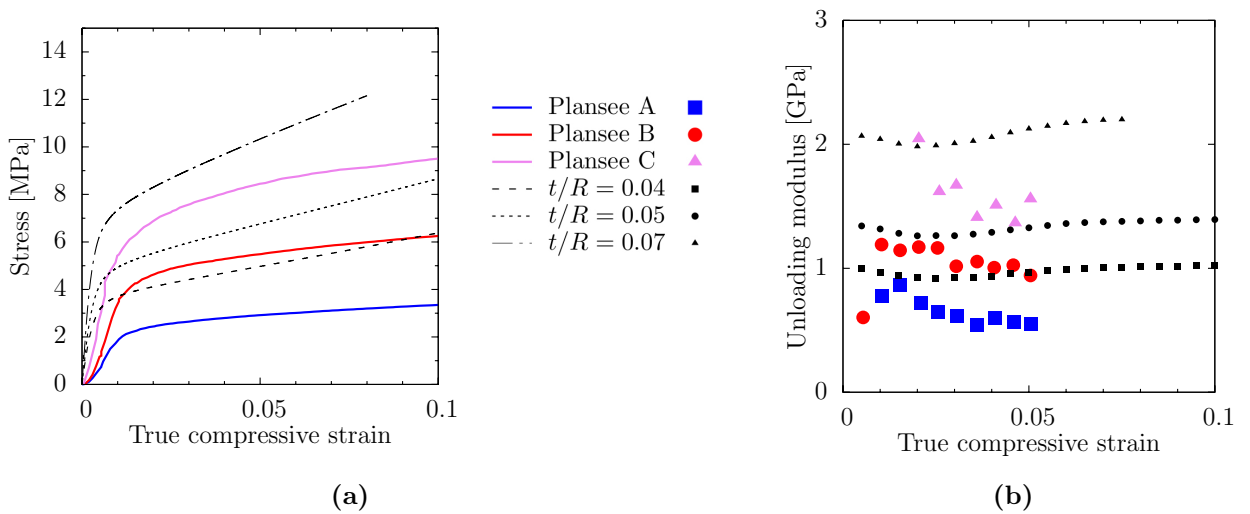


Figure 3.10: Confrontation of experiments and model for the stress-strain curves (a) and for the unloading modulus (b) under uniaxial compression with correction of the neck size.

densities. The yield stress and the initial unloading modulus are well described. Nevertheless the model

still overestimates the mechanical properties of the foam with the lowest density. The fact that the normalized shell roughness is larger on these samples might explain the difference, since the modeling considers only perfect shells. Next the model does not predict any sensible evolution of the unloading modulus when necks are small. The role of damage in the shell has been neglected in the model. It seems that its influence is larger than expected. The geometrical effect cannot account for all the unloading modulus evolution. Same observations can be made about the overestimated hardening slope.

Elementary shear law enhancement Another potential improvement deals with the local contact shear law. Actually when decreasing the neck size, the shape of the contact is varied and thus the compressive contact law is also modified. Now, if the shape of the contact is assumed fixed (and so the contact size), taking into account for the surface roughness, would just change the shear contact law. We cannot quantify this effect, but in order to estimate its influence, the shear contact law reaction has been divided by an arbitrary factor of 4. Figure 3.11 presents the stress-strain curve and the unloading modulus evolution for a stacking taking into account for this correction. The decrease of

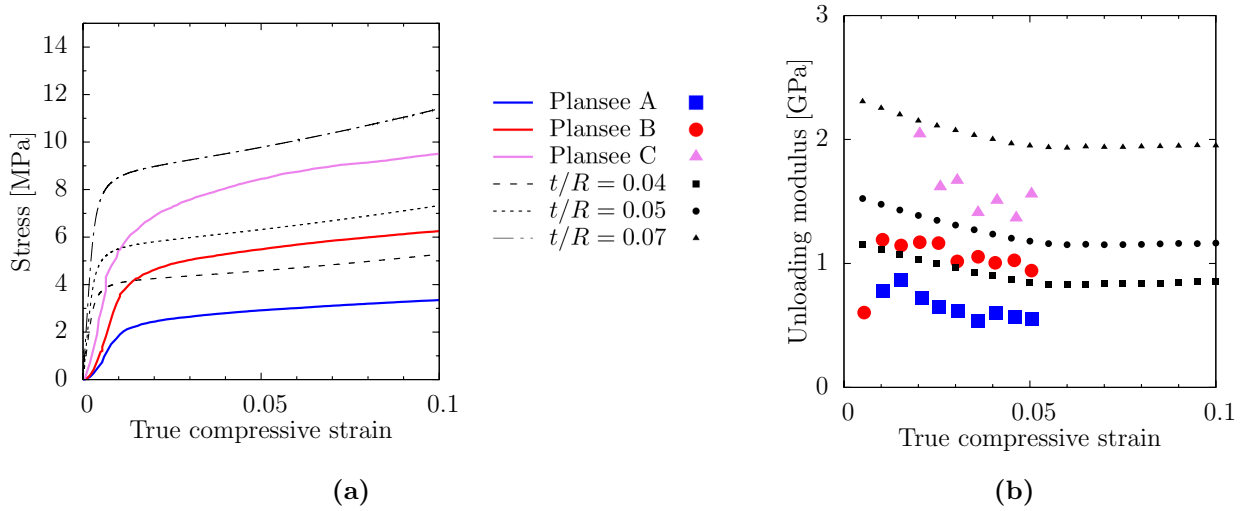


Figure 3.11: Confrontation of experiments and model for the stress-strain curves (a) and for the unloading modulus (b) under uniaxial compression with correction of the shear contact law.

the contact shear law response impacts significantly the stress level on the macroscopic scale. The stress-strain curves are almost well described for higher density foams, even for larger strains. The unloading modulus evolution is also well described, nevertheless it remains overestimated.

3.1.5.3 Combination of corrections

The combination of correction of both the neck size and the shear contact law lead to a good description of the mechanical behaviour of stackings of medium density (Plansee B, 600g/L) under uni-axial compressive loading (figure 3.12). Nevertheless, since both the scatter on the mean shell thickness per sphere and the roughness of the surfaces are not taken into account, the first slope of the stress-strain curve is predicted steeper than on the real samples. The roughness of the faces have much more influence on thin shells and might be responsible for the overestimation of the lightest foam (Plansee A). For a mean normalized neck size of 0.265 and a shear contact law reaction decreased by a factor 4,

both the stress-strain curve and the unloading modulus evolution with strain are well described for the medium density foam. (figure 3.12).

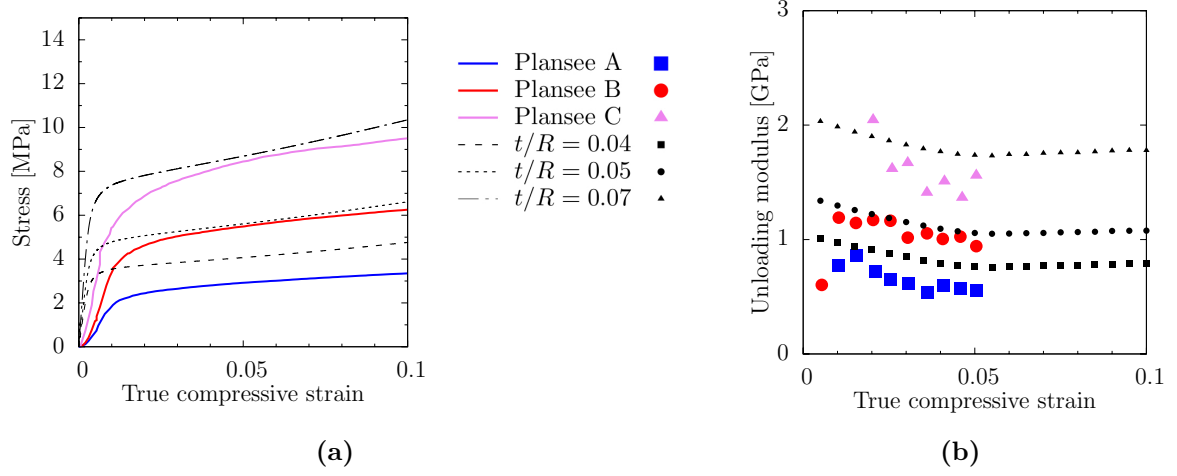


Figure 3.12: Confrontation of experiments and model for the stress-strain curves (a) and for the unloading modulus (b) under uniaxial compression with correction of both the shear contact law and the neck size.

- A sample can be considered as representative of the material if its size ratio is respectively of 7 for the stress at large deformation, and of 10 for the unloading modulus.
- No sensible influence of the spheres diameter can be observed on both the stress and on the unloading modulus of samples with the same initial density, if not on the scatter which is larger for small spheres when the same sample size is considered.
- Both the stress-strain curve and the unloading modulus evolution with strain depends on the initial foam density. The mechanical properties of the foam evolve as a power law of the initial density with an exponent ranging between 1.2 and 2.1.
- The stress-strain curve can be described by DEM provided the neck size is corrected and the shear contact law reaction decreased (a correction of 10% on the neck size and a factor 4 for the shear contact law give good correlation with the medium density foam). With the same correction, the unloading modulus evolution with strain is somehow captured, but the geometrical effect that DEM describes cannot account for the overall decrease with strain.

3.2 Uni-axial tensile tests

3.2.1 Experiments

The investigation of the tensile behavior of the foams was performed with the same approach than in compression. Two sample sizes were used in order to quantify a size effect and to evaluate the size of a Representative Volume Element (R.V.E.). Tests were performed on “dog bone” specimens. The working volumes chosen were the same than in compression : cubic volumes of respectively 10 mm and 20 mm side size. Figure 3.13 shows two samples. The strain field within the sample was measured by digital image correlation technique.

Unloading sequences give access to the evolution of the unloading modulus with strain. From the strain-stress curves and from the unloading modulus curve are extracted the stress and the strain at failure, the initial unloading modulus and the energy absorbed at complete failure.

3.2.2 Representative Volume Element

Stress-strain curves show a major sensitivity to the specimen size (figure 3.14a). These observations are confirmed by the study of the evolution of the failure stress with the sample size (figure 3.14b). Scatter is very large for samples of 10 mm side size and the failure often occurs at lower stress. The low scatter on the failure stress for 20 mm side size specimen, allows considering that these samples are representative. Thus a cubic working volume of 20 mm side size is a RVE in uniaxial tension. Following results only rely on these large samples.

3.2.3 Density effect

Figure 3.15 shows the simple tensile response of hollow sphere stackings of various densities. Both stress-strain curves and unloading moduli evolution are plotted. All curves have a similar shape. Two

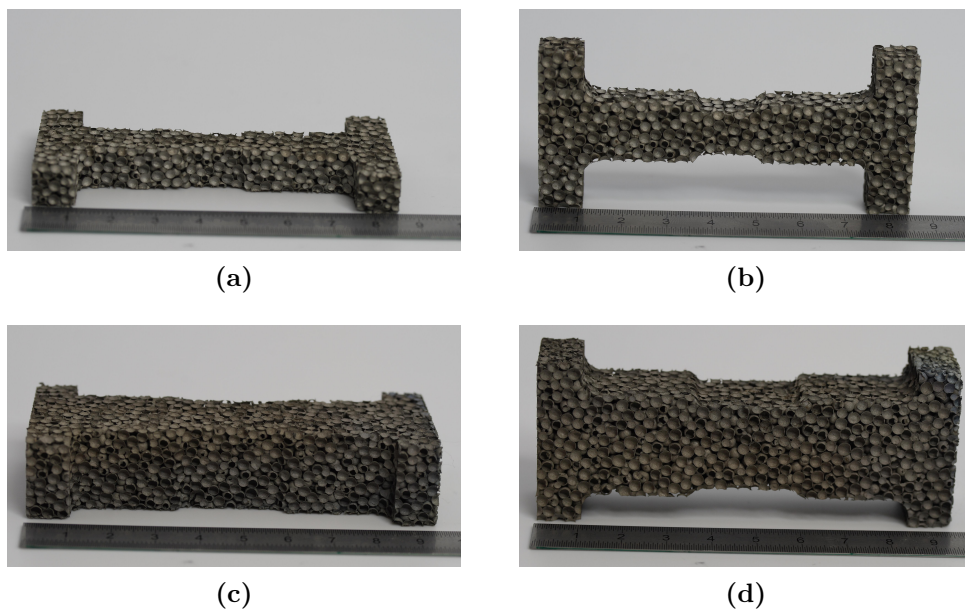


Figure 3.13: *Tensile samples before strengthening procedure. Samples have respectively a side size cubic working volume of 10mm (a,b) and 20 mm (c,d).*

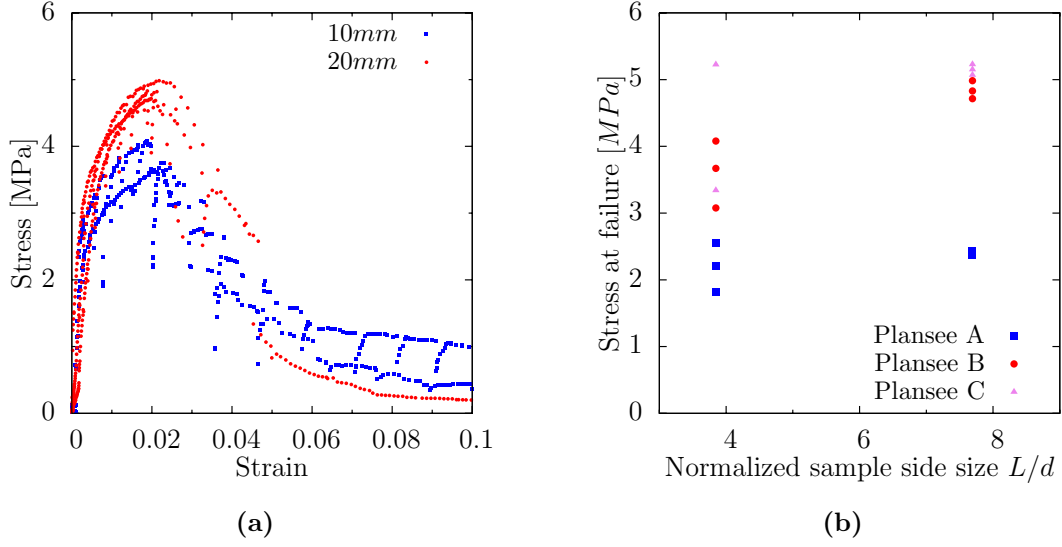


Figure 3.14: Influence of sample size. **a**-Comparison of strain-stress curves. **b**-Comparison of failure stresses.

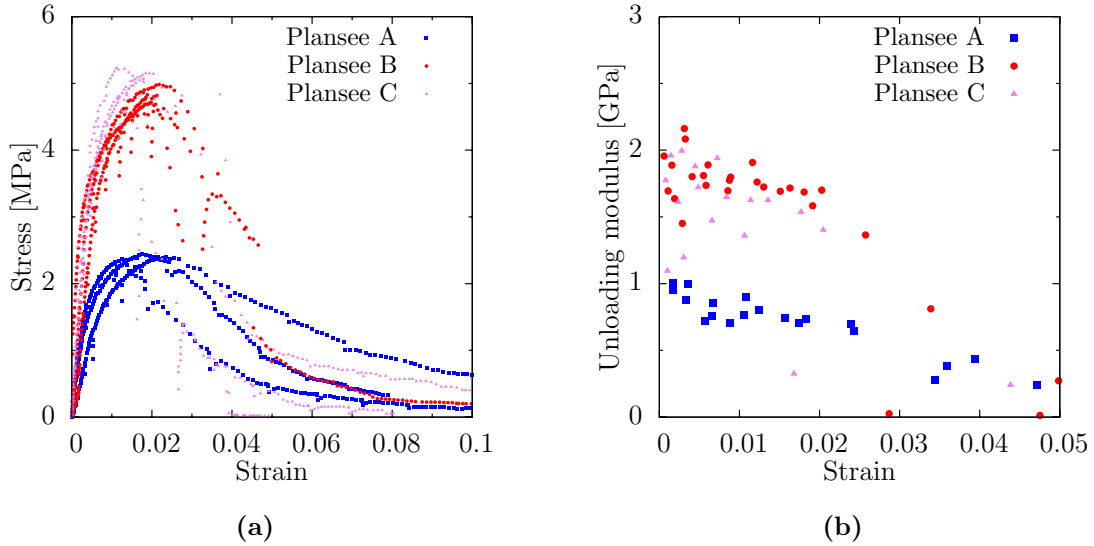


Figure 3.15: Influence of foam density. **a**-Comparison of strain-stress curves. **b**-Comparison of unloading modulus evolution with strain.

main classes of behaviour are observed.

For low density samples (Plansee A), the stress reaches a maximum of about 2.5 MPa, and then slowly decreases with strain. The unloading modulus decreases with strain from about 1 GPa at initial state to 200 MPa at 5% of strain.

For higher density samples (Plansee B and Pansee C), the behaviour is less dependent on the density. Both foams present a maximal stress of about 5 MPa. This failure stress is followed by a decrease in the stress-strain curves. The denser the foam, the steeper is this decrease. No difference can be seen on the unloading moduli, neither on their value, nor on their evolution with strain.

Figure 3.16 presents the evolutions of failure stresses and initial unloading moduli with the initial density of the hollow spheres stackings. The evolution of the stress at failure with density indicates a transition

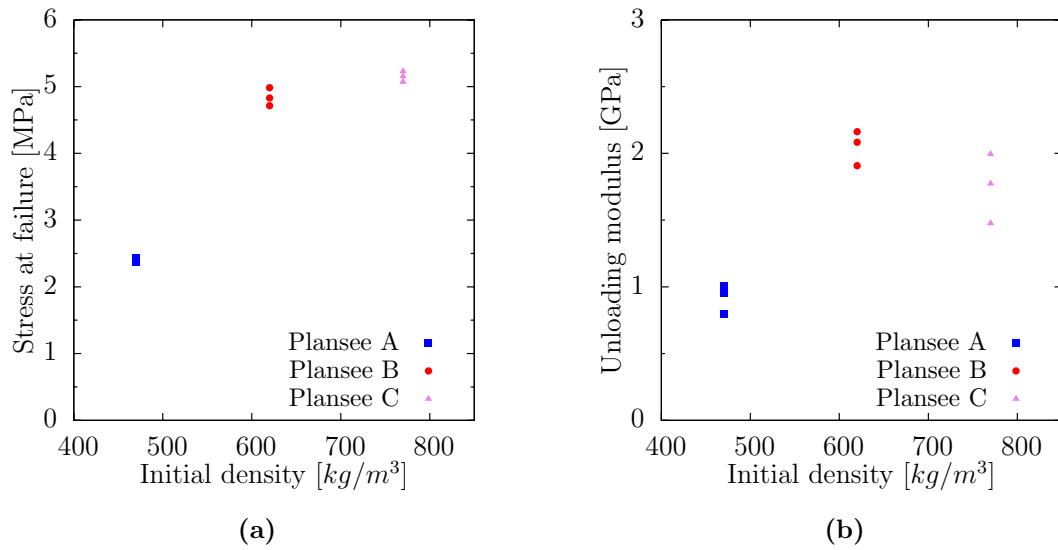


Figure 3.16: Influence of foam density. **a**-Stress at failure (maximal stress). **b**-Initial unloading modulus.

between two mechanisms. For hollow spheres with thin shell the failure stress increase with the shell thickness. But for spheres with thicker shells the failure stress is constant. Same observations are made on unloading moduli. Post mortem observations of the failure by SEM give information on these mechanisms. Tensile loading lead to failure of the necks between spheres. When the shell thickness is

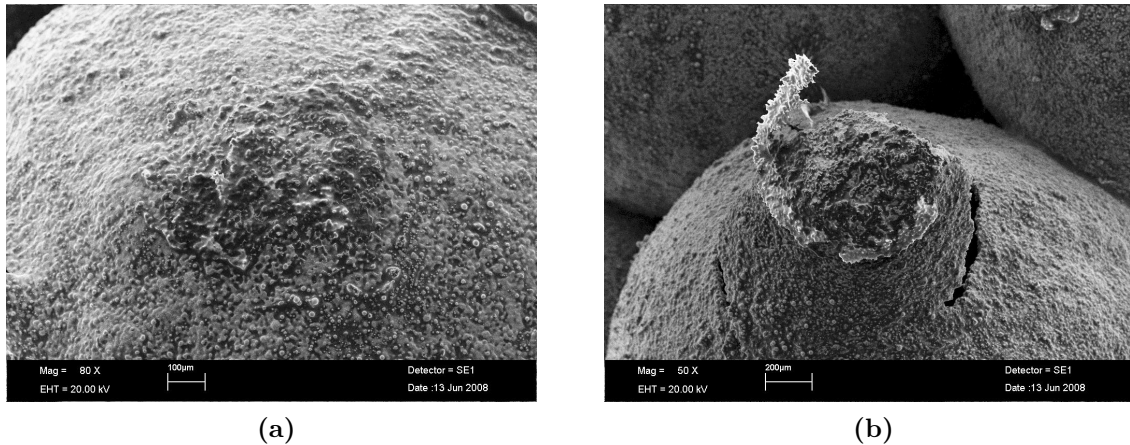


Figure 3.17: Scanning Electron Micrographies of spheres at the vicinity of the neck. **a**-Failure by debonding between two spheres. **b**-Failure by tearing of the shell.

large, the weakest point is the neck and thus the bonding fails by rupture of the neck (Figure 3.17a). But when the shells are thin, the higher stresses take place in the shells at the vicinity of the neck and thus the shells fail by tearing (Figure 3.17b). So for thick shells, tensile properties of hollow sphere stackings are mainly driven by the neck properties and independent of shell thickness while for lower thicknesses the shell itself fails and does so at a smaller stress when the shell thickness is smaller. Simultaneous observation of the fracture profiles on the three foams clearly shows a transition. For the lower density foam, all the failures occur in the shell (figure 3.18a). For the higher density foam, all the failures occur in the neck without any damage of the shells (figure 3.18c) For the foam with

intermediate density, there is a partition between both failure mechanisms (figure 3.18b). Strain at

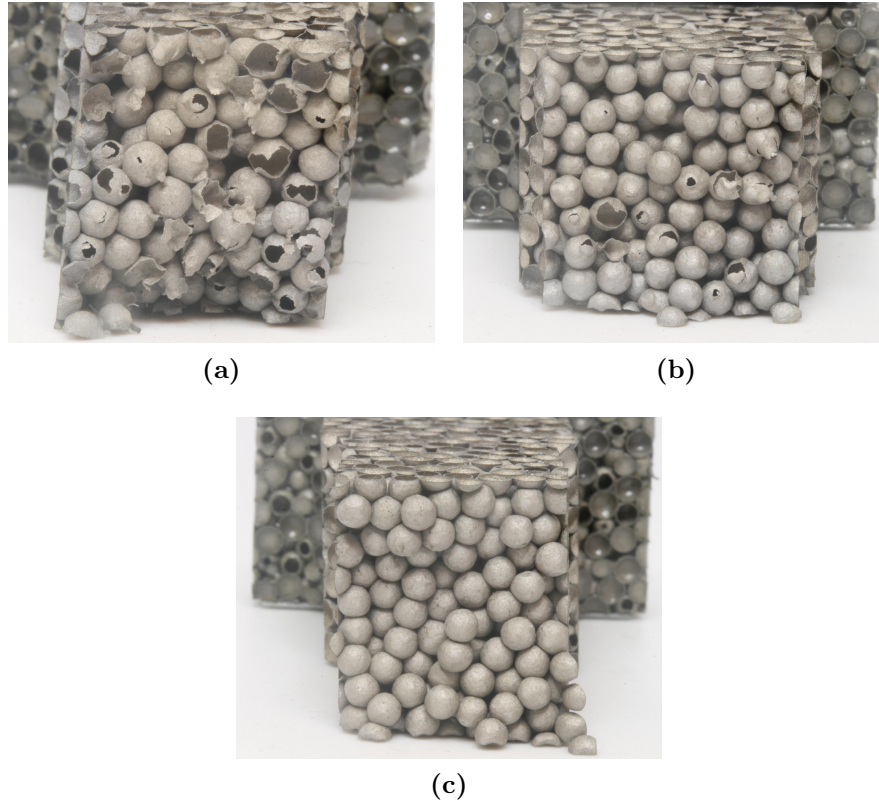


Figure 3.18: *Influence of foam density. a-For thin shells, failure occurs in the shell. b-For medium shell thickness, there is a partition between the failure in the neck and in the shells. c-For thick shells, failure occurs in the neck without any damage for the shells.*

failure is independent of the shell thickness (figure 3.19a). Observations based on the energy absorbed up to complete failure (figure 3.19b) and on the shape of the stress-strain curves, indicate an evolution from a “ductile” failure mechanism for thin shells to a “brittle” failure for thick shells. The low failure stress of thin shells is balanced by a failure mechanism that keep cohesion of the material up to large deformations. With increasing thickness of the shells, spheres become stiffer and stresses concentration increases in the necks.

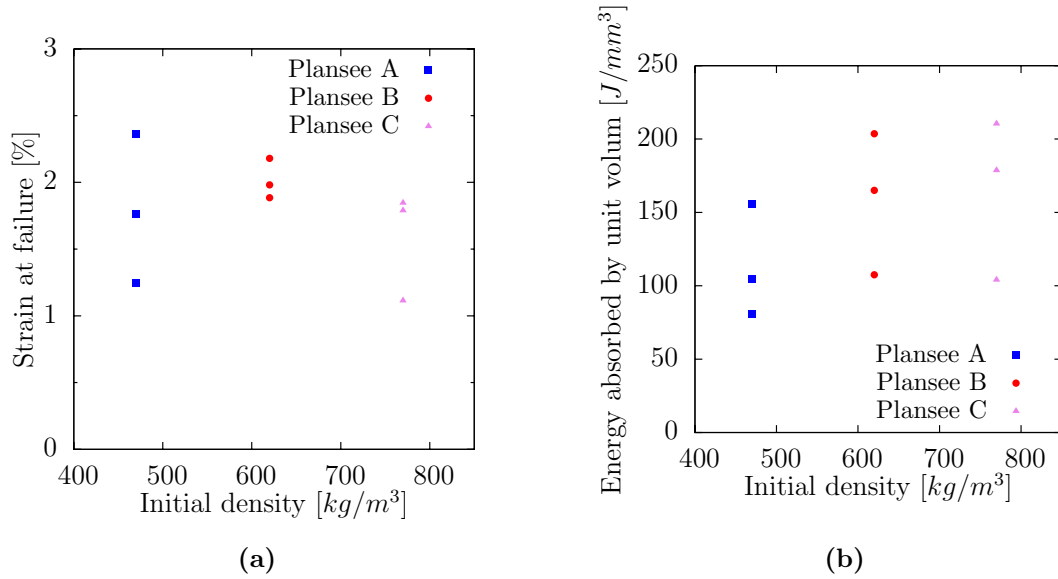


Figure 3.19: Influence of foam density. **a**-Strain at failure (strain at maximal stress). **b**-Volumic energy absorbed up to complete failure.

3.2.4 X-rays tomography in situ tests

In situ tensile tests have been performed on the three foams with large spheres at *MATEIS*. Both shell tearing and neck failure have been observed.

Shell tearing Shell tearing has been observed for spheres with thin shell thickness. The mechanism is easily observed on 2D slices as presented in figure 3.20. Shell tearing makes quantitative image analysis

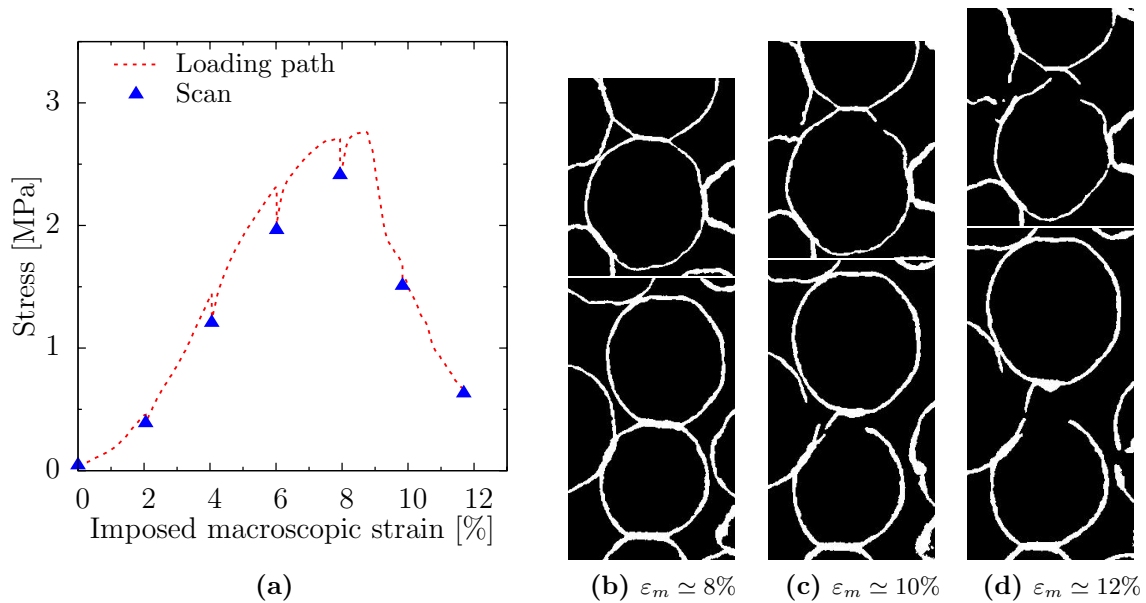


Figure 3.20: **a**-Position of the scans in a stress-strain map. **b,c,d**-With strain, damage increase by tearing of the shells. The strain ϵ_m presented is the macroscopic strain imposed by the machine, without any correction for the high compliance of the machine. The real average strain within the sample is almost 3 or 4 times smaller.

more difficult. It becomes almost impossible to follow particles as it can be done when the cells remain close. Even the quantification of the number of shell scratching is difficult because of the thin thickness of the shell with respect to the accuracy of the measurements. If by eyes, one can easily make the difference between a scratched shell and a defect in the image, an automatic analyse is discriminant. Thus this mechanism has not been quantified.

Neck debonding When stackings of hollow spheres with thick shells endure a sufficient tensile loading, failure occurs in the necks. Two spheres connected via a neck are separated *without any damage of the shell*. Figure 3.21 presents 2D images of a stacking for various tensile strains.

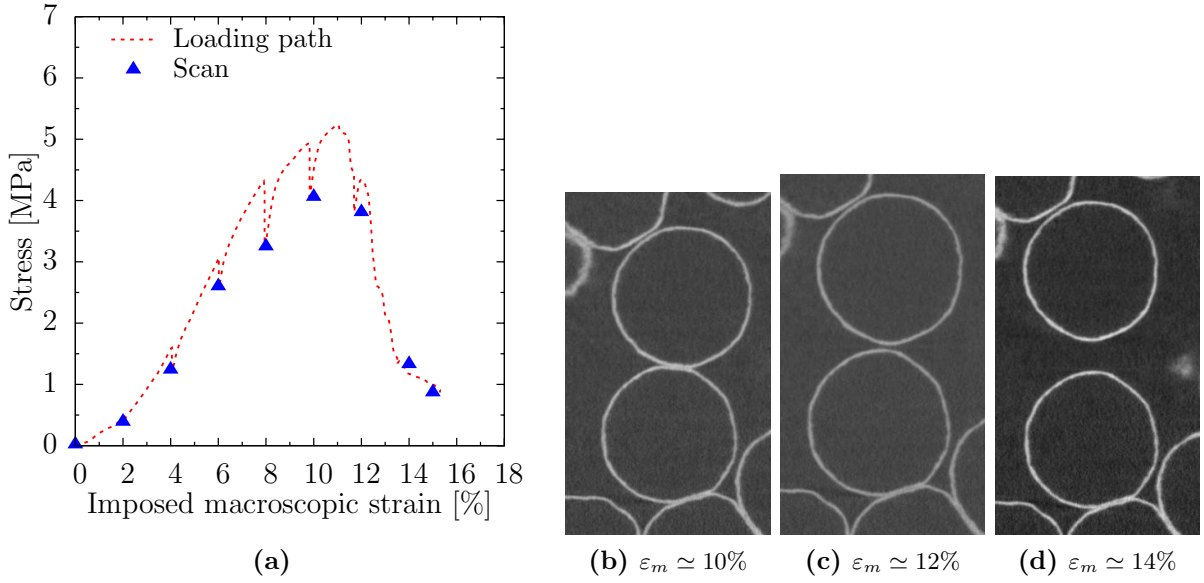


Figure 3.21: *a*-Position of the scans in a stress-strain map. *b,c,d*-With strain, the neck fails without damage for the shells. The strain ε_m presented is the macroscopic strain imposed by the machine, without any correction for the high compliance of the machine. The real average strain within the sample is almost 3 or 4 times smaller.

Correlation with the macroscopic behaviour Whatever the shell thickness, no shell failure has been observed within the first stages of deformation. Nevertheless the initial decrease of the unloading modulus is due to damage (since this decrease cannot be impacted to any geometrical effect, see 2.1.2.1). Damaging of the shells by coalescence of cavities or failure of portion of the necks, must be responsible for this decrease, but they cannot be observed at this scale.

3.2.5 Comparison of experiments and simulations

Simple tensile tests have been simulated by DEM. Periodic boundaries conditions with $\sigma_{xx} = \sigma_{yy} = 0$ and imposed ε_z have been applied to a reference cubic sample of 1000 particles. The shell thickness has been varied.

Strain-stress curves and unloading modulus evolution with strain for DEM simulations and for experiments are compared in figure 3.22. As for compressive loading, the initial model overestimates largely the level both for the stress and the stiffness. But other imperfections are clearly seen for the

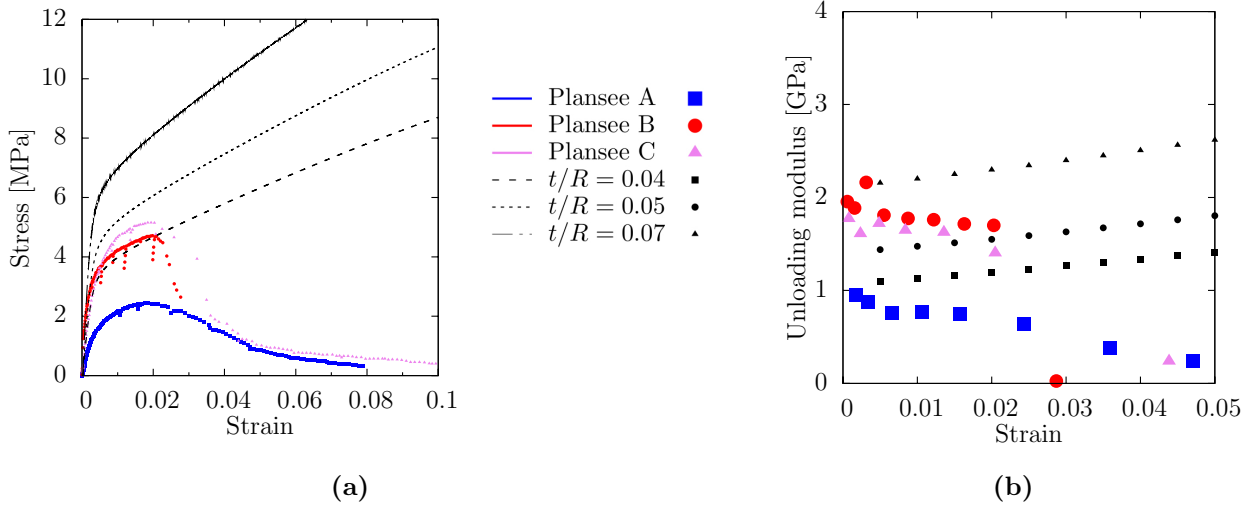


Figure 3.22: Confrontation of experiments and model for the stress-strain curves (a) and for the unloading modulus (b) under uniaxial tensile loading.

tensile loading. The model cannot describe neither the softening due to the progressive failure, nor the similar behaviour for high density foams. The tensile contact laws, for which damaging has not been taken into account, are responsible for this limitation. A failure criterion, depending both on the neck size and the shell thickness, for the contact law might allow to describe both the damage evolution with strain and the threshold imposed by the neck properties. Thus, in the present state, the model cannot describe the behaviour under macroscopic tensile loading.

3.3 Multi-axial compressive tests

3.3.1 Experiments

Multi-axial compressive tests have been performed using different techniques.

- The first one is based on imposed motion at the boundaries thanks to entangled plates. Specimens are cubes with notches among each line. The side size of the cubes were of 20 mm, but the working volume had a smaller side size. Thanks to varied notch depth and width, two working volumes have been considered. Theses volumes are equivalent to cubic specimens of 10 and 13 mm side size respectively. Specimens were loaded with varied strain rate ratio between the principal directions. Reference was the z direction. Strain rate relation is given by :

$$\dot{\varepsilon}_{xx} = \dot{\varepsilon}_{yy} = \frac{\dot{\varepsilon}_{zz}}{\alpha} \quad (3.3)$$

α have been varied between 1 and 100. Loading rates were approximately of $5\mu\text{m}/\text{s}$ for the master axis (z). Numerous unloading sequences have been performed and the plastic strain was registered after each sequence. Theses experiments have been performed on the four kinds of foams.

- The second technique used, is based on imposed pressure at the boundaries with an unilateral motion condition on the master axis. The cylindrical samples of 20 mm length and 10 mm diameter

have been wrapped up in three neoprene membranes of 0.4 mm thickness. Two cylindrical plates have been added on the z boundaries of the samples. The overall assembly is introduced in a confining cell. Pressure is applied on all the boundaries thanks to oil. A spherical indent imposes the compressive strain on the master axis. Pressure in the cell were recorded punctually, while motion and reaction on the master axis were recorded every 5 seconds. The imposed strain rate was of about $4\mu\text{m/s}$ on the master axis. All the tests have been performed in an X-ray tomograph, so scans of the structure have been performed at several loading stages. Four tests have been performed. For three of them a pressure p_{init} has been imposed and then a deviatoric loading have been imposed parallel to the master axis. For two samples, the pressure has been increased by stages. After each increment of pressure, the strain on the master axis was measured by detection of contact with the spherical indent. Theses tests have been performed on the “Plansee D” foam.

3.3.2 Boundary conditions with imposed motion

The results of tests performed on the cubic samples are unfortunately suspect. Actually, several observations reveal that the accuracy of the results is doubtfull. Nevertheless qualitative trends can be established from theses results, and so they will presented.

3.3.2.1 Limitation of the method

Several techniques to estimate the yield stress have been used.

The first one is based on the plastic strain. After each unloading sequences, the plastic strain has been recorded. Nevertheless due to the looseness of the mechanism, this measure was shown to be completely inaccurate.

The second one is based on the loading stiffness. The loading stiffness is estimated from the stress strain curve, and then a plastic strain offset of 0.2% determines the yield stress. This is the technique used. It remains that the stress-strain curves are completely modified when taking into account the stiffness of the machine. The correction is hard to determine and varies from a sample to another. Thus, because of the non-linearity of the machine, the accuracy of this technique is also reduced. Nevertheless this is the only technique available for theses samples.

3.3.2.2 RVE

Figure 3.23a presents the yield stress versus various deviatoric paths for foams with various sample size. The foam used has spheres of 1.3mm of diameter. Figure 3.23b presents two trends for the yield surface. The scatter is large. When all the samples are considered, the shape of the yield surface seems elliptic, but when one considers only the larger samples a straight line might be more convenient.

3.3.2.3 Density influence

Figure 3.24 presents the yield stress versus various deviatoric paths for foams with various densities. The shape of the yield surface is proposed. The foam initial density does not seem to modify the shape of the yield surface, if not for the size which increases with the initial density. Nevertheless the yield surface shape is hard to define since both proposed shapes seem convenient. Moreover, the number of

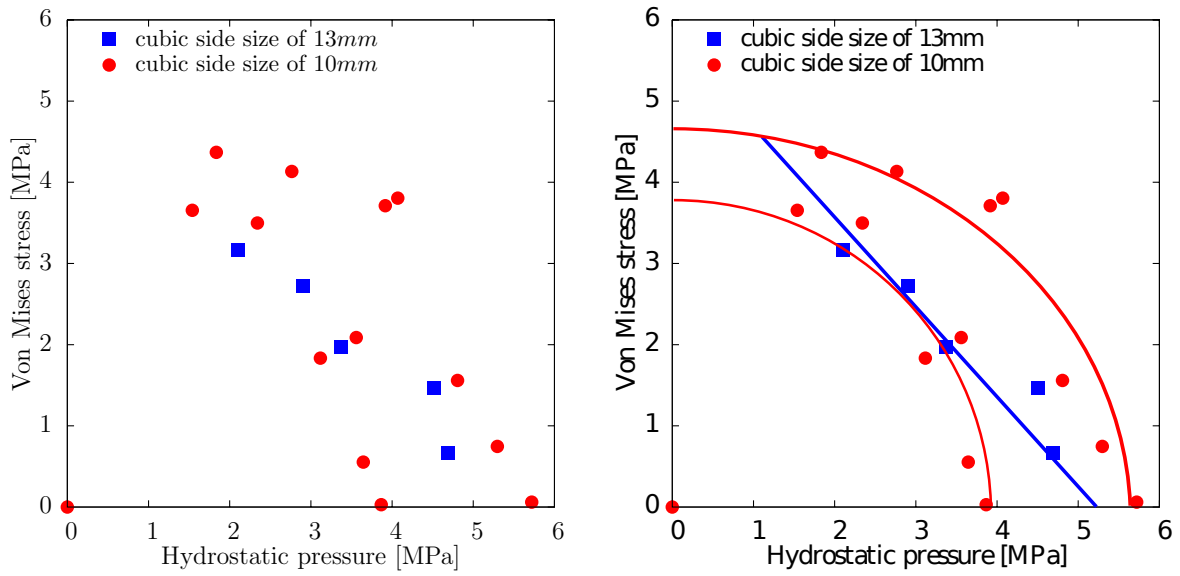


Figure 3.23: *Von Mises stress versus hydrostatic pressure elastic surface for samples with varied size. Models for the yield surface are proposed*

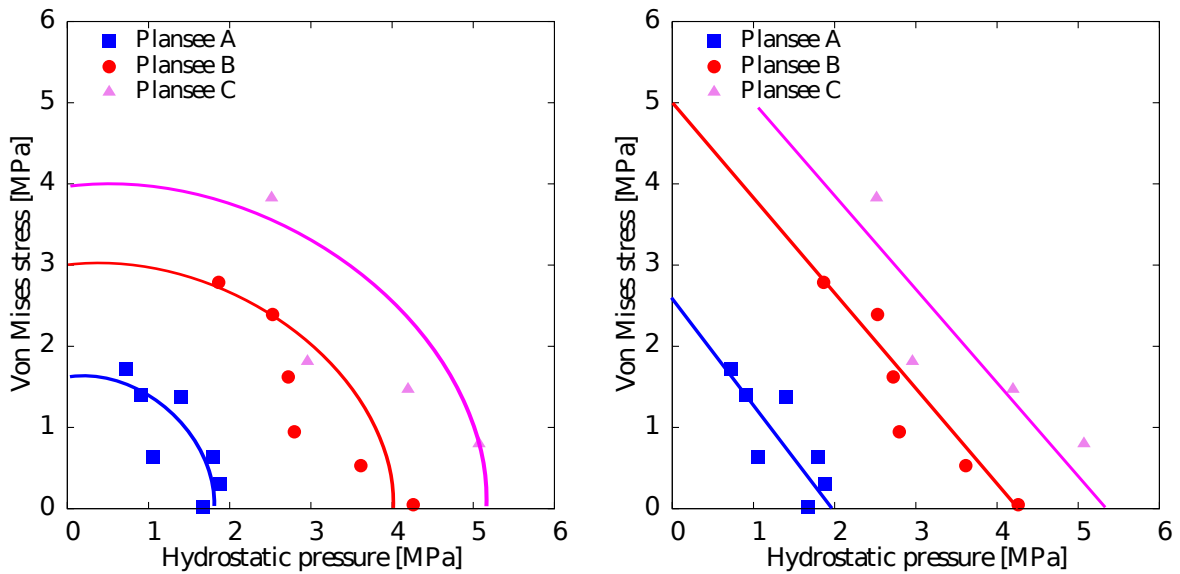


Figure 3.24: *Von Mises stress versus hydrostatic pressure elastic surface for samples with varied density. The shape of the yield surface is proposed.*

particles per samples is lower than that for the small samples in the case of figure 3.23a. The large scatter must be kept in mind since on figure 3.24 there is only one point per loading direction.

3.3.3 Boundaries with imposed pressure

After an initial isotropic loading, a deviatoric loading is applied parallel to the master axis. The shape ratio of the samples (ratio of 2) and the particular boundary condition (punctual loading on one face) favored buckling of the samples. Moreover, the small sample diameter compared to the spheres

diameter (about 7 times) enhance localisation phenomena. Thus the probability to observe geometric instabilities is large. Figure 3.25 presents portions of samples at different stages of loading along a deviatoric direction. Figure 3.26a presents the influence of the hydrostatic pressure on the stress-strain

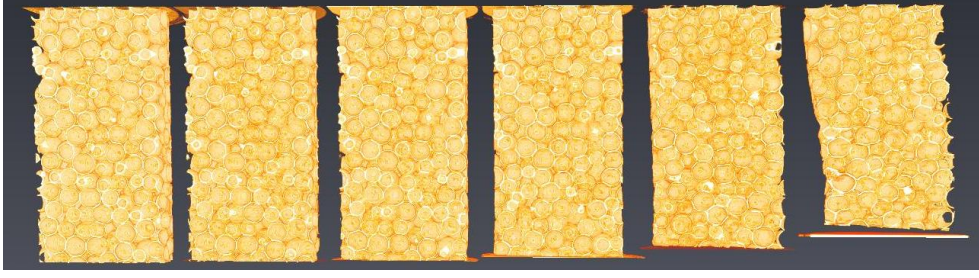


Figure 3.25: Sample loaded in compression parallel the cylinder axis with a confinement pressure of 1 MPa. The section shows how buckling is initiated by strain localization (on the left side, a third of the height approximately).

curve. Figure 3.26b plots the various yield stress versus the two first invariants of the stress tensor.

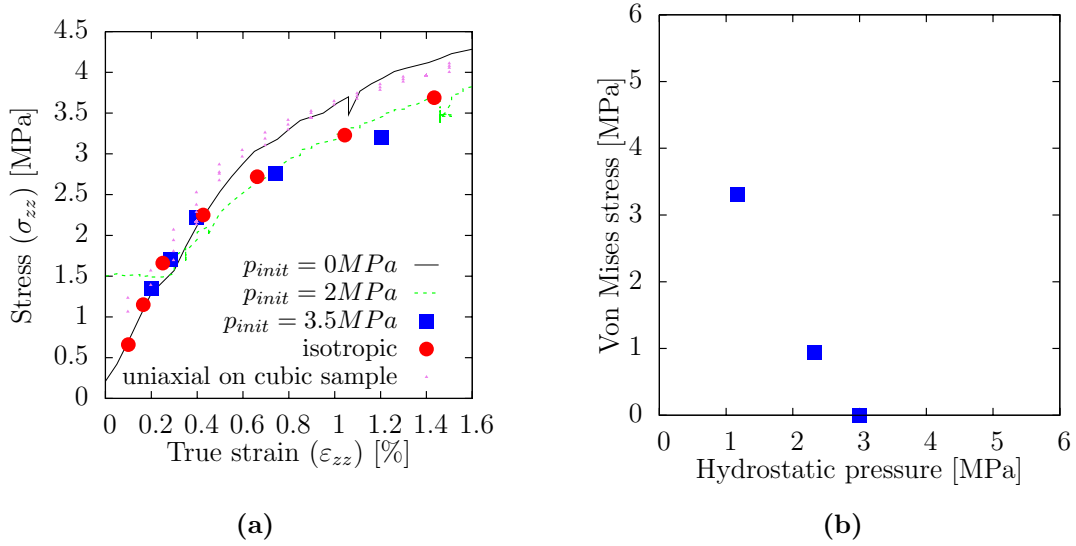


Figure 3.26: **a**-Stress-strain curve (parallel to master axis) for various initial pressure p_{init} . Responses are compared to an uniaxial test performed on a cubic sample. **b**-Yield stress versus the mean stress and the effective stress for various mean stresses.

3.3.4 Comparison of experiments and simulations

Simulations of periodic cubes of 1000 particles have been performed for various loading paths. The yield surface has been computed for several shell thicknesses. Figure 3.27 presents the yield surface for three shell thicknesses for samples with already corrected neck sizes. The elongated shape of the elliptic model of Deshpande-Fleck that is used to fit is the sign of a small plastic Poisson ratio. The shear stress is much more important than the isotropic yield stress. It is consistent with the local ratio between shear and compressive load of the elementary laws. The shape of these numerical yield surfaces is obviously not the same that the one obtained on the real material. The contact shear laws are responsible for this

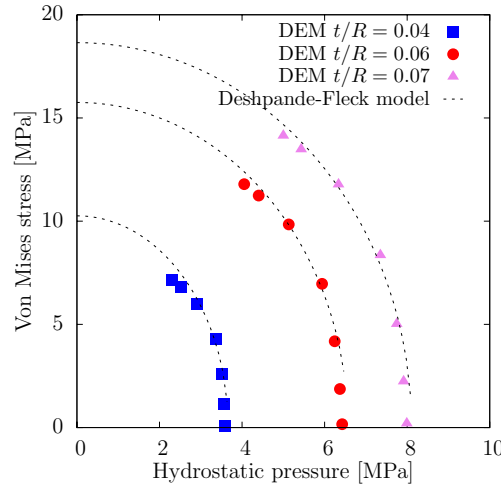


Figure 3.27: Yield surface obtained by DEM for three normalized shell thicknesses t/R for two stackings with corrected neck size.

elongated shape. If the same correction that the one used for compressive tests is applied on the model (a softening of the shear law by a ratio of 4), the shape evolves to an ellipse closer to the experimental surface. Figure 3.28 presents both the evolution of the surface with the correction of the model on the shear contact law, and the comparison between the corrected model and experiments. When both the

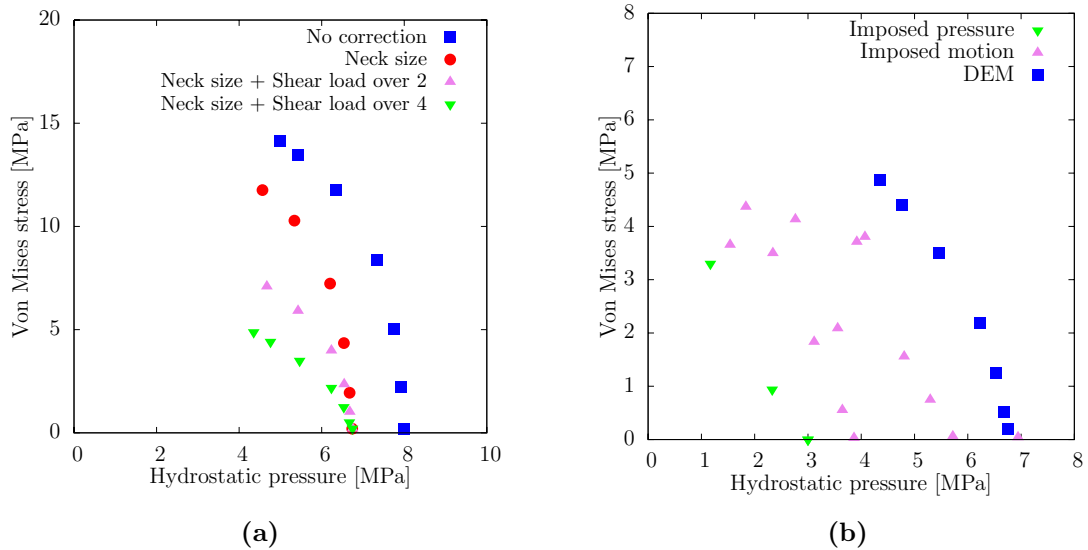


Figure 3.28: **a-** Yield surface obtained by DEM with ponderation of the shear contact law. **b-** Comparison between experiments and corrected DEM simulations for the yield surface.

neck size and the shear contact law are corrected, DEM better describes the hollow spheres behaviour. The model predicts a shape for the yield surface similar to the one obtained on the experiments. The size of the yield surface is slightly overestimated, but this deviation could be in accordance with the decrease of the properties due to the small experimental sample size.

Summary on the macroscopic behavior

Uniaxial compressive behaviour The mechanical behaviour of hollow spheres stacking enduring compressive loading was shown to present a low scatter provided the sample contains respectively about 350 spheres and 1000 spheres if the concerned property is a stress or a stiffness. The mechanical properties evolves as power laws of the foam initial density with exponents ranging from 1.2 to 2.1. No softening is observed on the stress-strain curve.

Uniaxial tensile behaviour Two main classes of damage mechanism are encountered when tensile loading is considered. If shells are thin, a progressive macroscopic softening occurs. On the cell scales, the shells fails by scratching at the vicinity of the neck. If shells are thick, the macroscopic stress-strain curve presents a steep decrease at failure. The necks fails without damaging the shells. When the shell is thick enough to observe this damage mechanism, increasing the thickness does not change the mechanical properties.

Multi-axial compressive behaviour The yield surface of hollow spheres stacking seems to be elliptic in the space of the two first invariant of the stress. Nevertheless the scatter, of both on the measurement and on the behaviour of the small samples, is too large to enable a definitive statement since a linear surface could also be a good fit.

DEM modeling Discrete Element Method applied to hollow spheres stackings can describe the foam macroscopic behaviour provided that there is no major tensile nor shearing strain and that the neck size and the contact shear law are corrected. This method gives good estimation of the initial material properties both for stress and stiffness. However the yield surface is overestimated though it seems that DEM can catch experimental trends.

Chapter 4

Phenomenological modeling

Contents

4.1	Experiments	147
4.2	Damaging	147
4.2.1	Description of the mechanisms	147
	Indentation	147
	Neck shearing	148
4.2.2	Quantification of damaging	148
4.3	Densification	151
4.4	Equivalent homogeneous medium by phenomenological approach . . .	152
4.4.1	The model and its parameters	152
	4.4.1.1 Extrapolation to other densities	153
4.4.2	Validation of the model	154
4.5	Summary on the mesoscopic metamorphism	155
	Damage	155
	Densification	155
	Phenomenological model	155

The macroscopic tests has shown the existence of various domain in compression (elastic area, plateau, and densification area) and of several tensile behaviors. In situ experiments allow to follow the material structure and architecture during the tests and thus to link the local mechanisms to the macroscopic behavior. This is what we will try to do in this chapter. Within a first step the various mesoscopic mechanisms encountered are described, and then they are put in relation to the macroscopic behavior.

4.1 Experiments

Experiments have been performed in compression on cubic samples of 15 mm side size. The voxel size is of 16 μm . The four kind of foams has been tested in simple compression and in tension. About 10 scans have been performed for each sample. For multi-axial compressive tests, the single foam with small spheres has been tested. This choice has been driven by the size of the sample that could be tested : cylinders of diameter 10 mm and 20 mm length. Three deviatoric paths have been tested and for each of them between 3 and 8 scans have been performed.

4.2 Damaging

4.2.1 Description of the mechanisms

Based on tomography images observations several majors damaging mechanisms has been taken in account.

Indentation The first one is the indentation of a sphere by another (figure 4.1). It corresponds to a compressive loading. A small asymmetry makes that a sphere undergoes most of the deformation while the other remains almost spherical. This mode has also been observed numerically by A. Fallet when simulating the elementary laws between two spheres (figure 4.2). The important shape ratio R/t allows to obtain such high deformation mechanisms with low strains in the shell.

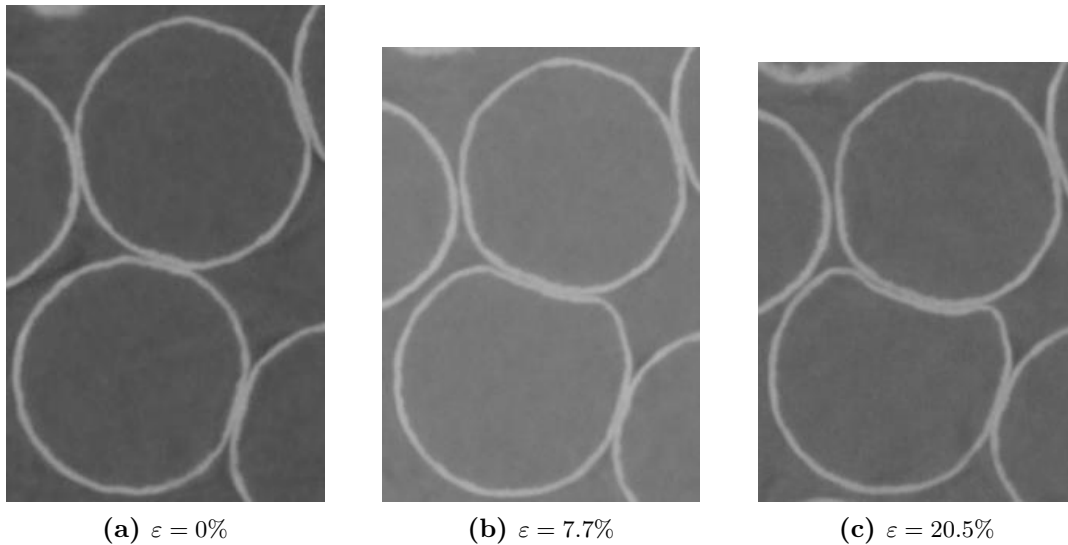


Figure 4.1: Indentation mechanism on hollow spheres observed thanks to X-ray tomography.

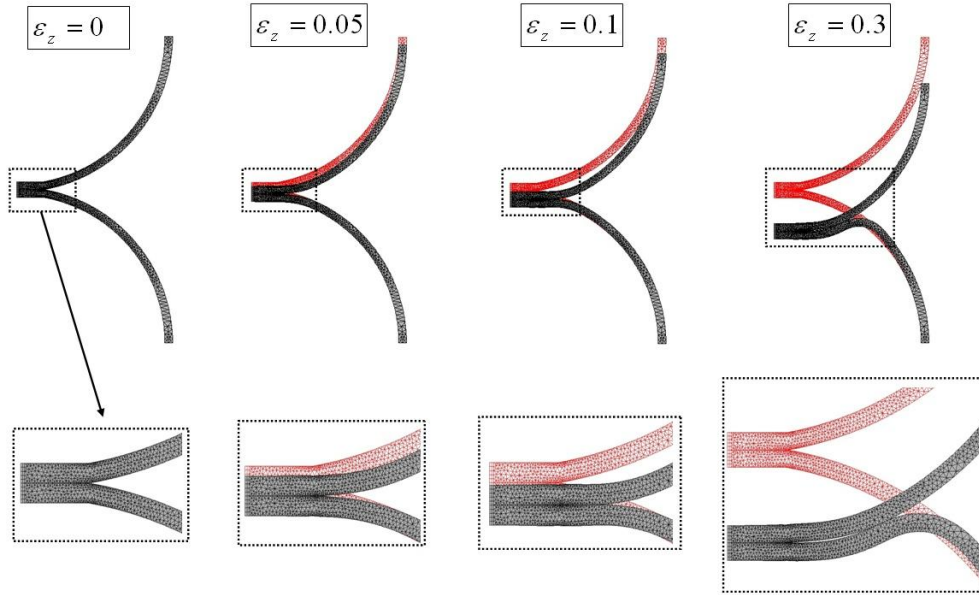


Figure 4.2: *Indentation mechanism observed on finite element simulations.*

Neck shearing The second mechanism is relative to a shear loading of the neck. It implies the formation of two plastic rings at the vicinity of the neck. Figure 4.3 presents 2D observations of the mechanism.

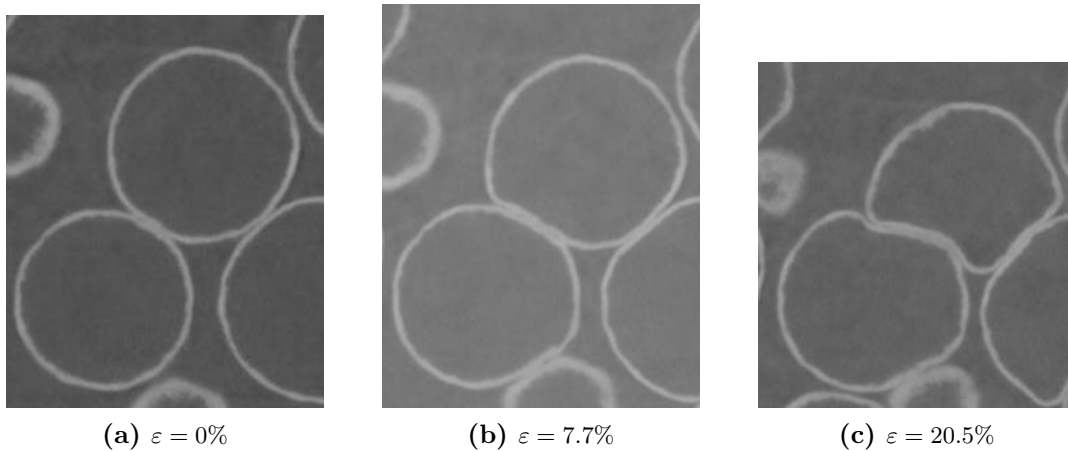


Figure 4.3: *Neck shearing mechanism on hollow spheres observed thanks to X-ray tomography.*

4.2.2 Quantification of damaging

Two ways can be investigated to qualify the damaging of the material. One can consider either the damaging of the spheres, either the damaging of the necks.

In the case where spheres are considered, one can look at the integrity of the shell or at the variation of volume of the spheres. Nevertheless both measurements do not give information on the damaging at early stages. The variation of volume of a sphere is low even for an important indentation. While looking on the shells, the tearing only occurs at large strain. Furthermore, the integrity of the shell is sometimes "virtually" spoiled because of the numerical volume reconstruction. So a quantification of

the damaging based on the spheres does not seem adapted to deal with the damaging that occurs at low macroscopic strain. These parameters will be rather used to quantify ultimate damaging such as densification or tensile failure.

If focused on the necks, the easiest way to take into account indentation or any other loading of these necks, is to compute the relative motion of the spheres. Actually both mechanisms involved in the compression tests (indentation and shearing) lead to variation of the distance between spheres (figure 4.4). Thus a criterion based on it allows to quantify damaged necks. An equivalent engineering

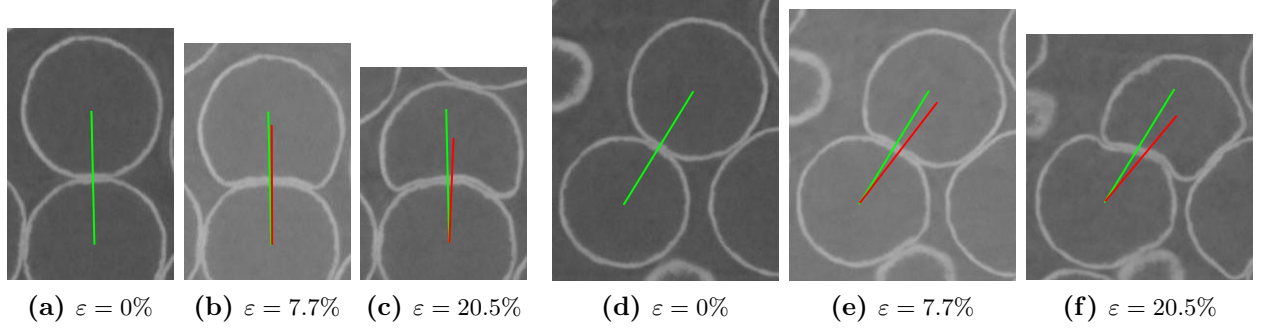


Figure 4.4: *a,b,c*-Indentation mechanism involve diminution of spheres center of mass distance. *d,e,f*-Shear loading of the neck does the same.

strain is defined for the neck based on the evolution δL of distance L between centers of mass of both spheres in contact through this neck (Eq 4.1 and figure 4.5).

$$\varepsilon_{neck} = \frac{\delta L}{L} \quad (4.1)$$

By computing, over a whole sample, for each deformation stage, for each bonded neck, this deformation,

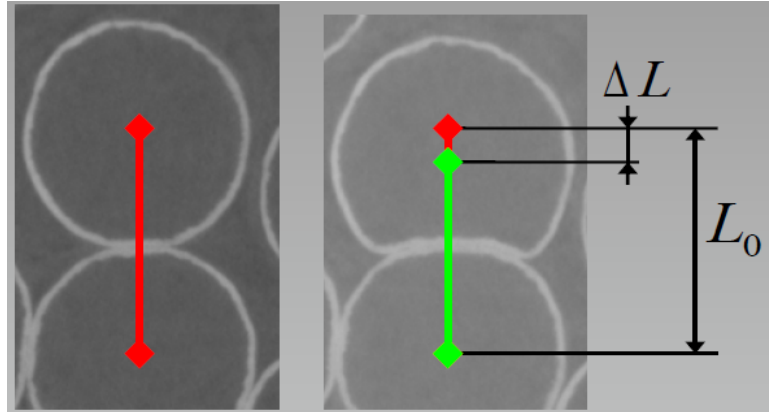


Figure 4.5: *Equivalent engineering neck strain.*

one obtains the distribution of equivalent strain on the necks. Figure 4.6a shows, for all the macroscopic deformation stages, the fraction of spheres that overpass a given neck strain. A threshold defining a damage neck is operated on the equivalent strain of the neck. If the equivalent strain is higher than the threshold, the neck is assumed as damaged, else it is still safe. This threshold is hard to define, that is why we will try several ones. Figure 4.6b shows the evolution of the fraction of damaged necks with the macroscopic strain for 3 thresholds.

It can be noticed that whatever the threshold chosen, the fraction of spheres damaged increase steadily

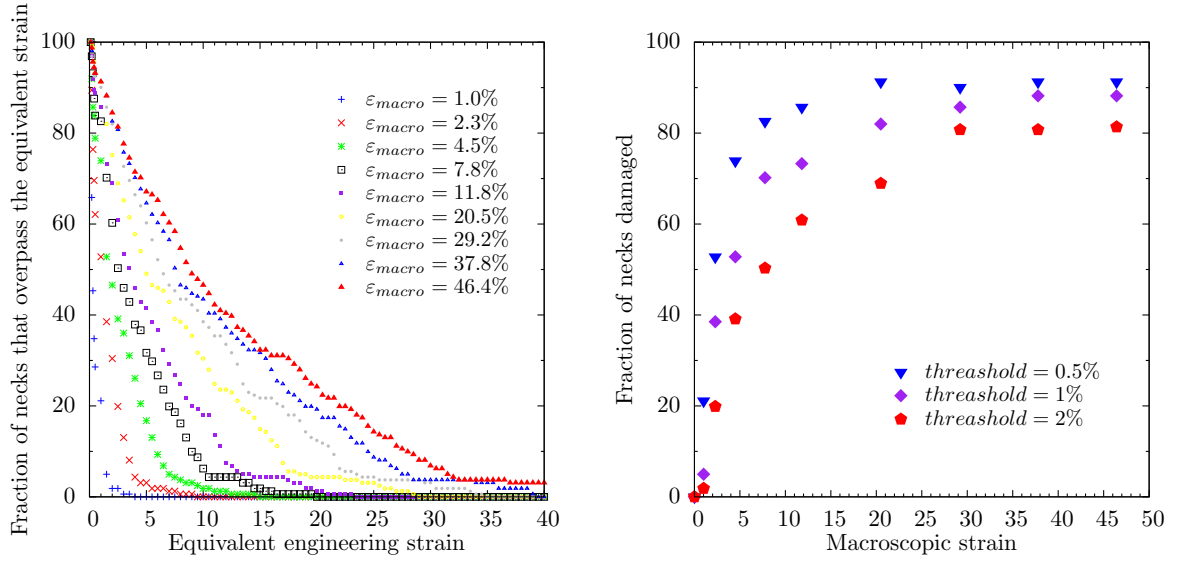


Figure 4.6: **a**-Fraction of neck overpassing a given equivalent strain. For a given an equivalent strain ϵ_{given} of 15%, at a macroscopic strain ϵ_{macro} of 11.8% only 5% of the necks have an equivalent strain higher than ϵ_{given} , while at a macroscopic strain ϵ_{macro} of 46.4% more than 35% of the necks have an equivalent strain higher than ϵ_{given} . **b**-Evolution of the fraction of damaged necks with the macroscopic strain for various thresholds.

during the first percents of macroscopic strain. That implies that most of the necks are deformed during the early stages of macroscopic deformation and that this deformation is rather homogeneous. We are not in presence of few spheres that are undergoing the whole deformation.

This criterion is based on the local deformation of the neck, it clearly shows that the macroscopic deformation results in a homogeneous deformation at the cell scale. But one can ask "What is the link with damaging?". Answer has to be found on the numerical experiment side. Actually if real experiments observations give access to local deformation mechanisms, load paths are much more difficult to see. When simulating the loading of a neck in compression as used for the establishment of D.E.M. elementary laws, if one performs unloading sequences at various strain to obtain the stiffness of the structure, one will observe an important decrease of this unloading modulus at low strain. Figure 4.7 plots the evolution of the normalized stiffness ($\frac{F/R^2}{u/2R}$) with the equivalent engineering strain ($u/2R$). The stiffness level is very high, but one must think that this is a particular orientation and that both spheres are perfect. The interesting thing is that within 10% of strain, the stiffness is divided by two. This is a clear signature of a softening of the structure within the first percents of deformation.

Thus it has been shown that most of the necks are deformed during the early stages of macroscopic deformation and that small equivalent strain in the neck leads to a drop of its stiffness. So it can be concluded that this mechanism is responsible of the damaging of the material, which macroscopically results in an important decrease of the unloading modulus.

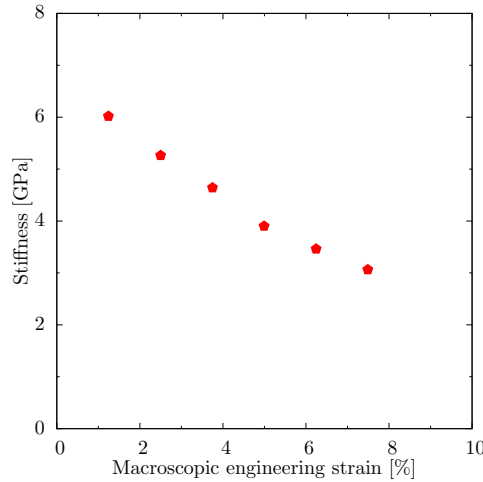


Figure 4.7: *Evolution of the stiffness of a neck with the local equivalent strain.*

4.3 Densification

Densification corresponds to a decrease of the porosity. Nevertheless, this decrease occurs since the early stages of any compressive test. Thus we define the densification as the mechanism responsible of the important hardening of the material in the late stages of the stress-strain curves. This mechanism is also responsible of the large increase of the unloading modulus.

During the compression of a stacking, there are local mechanisms that induce deformation of the spheres. Theses mechanisms can be hardening or softening as seen above. But their are also creation of new contacts between the spheres. Theses new contacts can obviously only harden the material. Nevertheless the number of contacts evolves more or less in a linear way with the stacking compacity (figure 4.8a). This hardening mechanism is thus balanced with softening and damaging in the necks and/or the shells. It can be noticed that the mean coordination number evolution could somehow be described by the Artz model (for full spheres) up to values of about ten. The densification mechanism has to be found in the evolution of the two types of porosity : open porosity and closed porosity. Within the first hundred percents of compressive strain, most of the strain is due to the evolution of the open porosity (figure 4.8b). Both re-organisation and shells small deformations have a great impact on the open porosity, but their influence on the close porosity is small. Thus, as it can be seen on figure 4.9, within a first stage, the open porosity is filled up, the close porosity does not evolve so much. The structure remains soft. But when all the open porosity has disappeared, cells have to crush, with hardening boundaries conditions. Thus at densification, global porosity remains important (about 60%) but it is now only closed porosity.

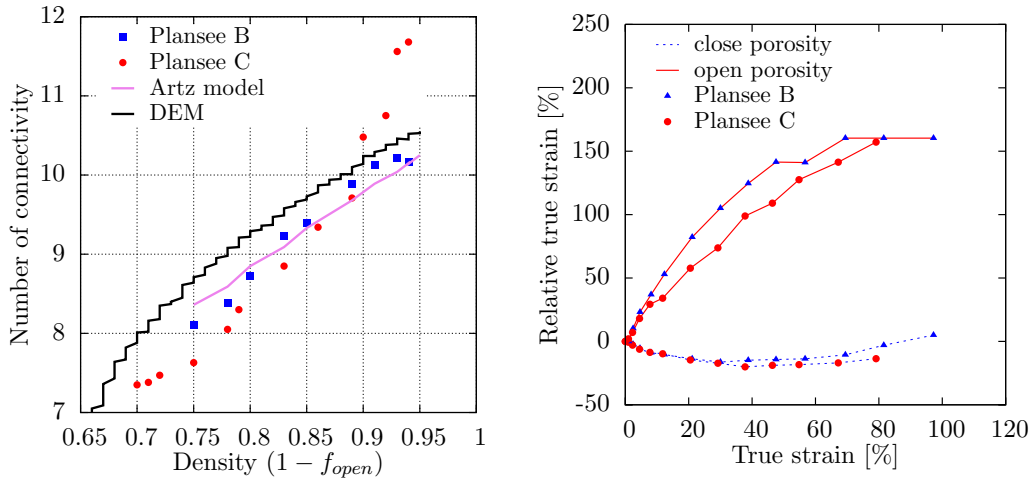


Figure 4.8: *a*-Evolution of the mean coordination number with the packing density. Artz model describes the re-organisation behaviour up to a mean coordination number of 10. *b*-Relative strain of open and closed porosity compared to the macroscopic strain. Most of the macroscopic strain is due to the open porosity.

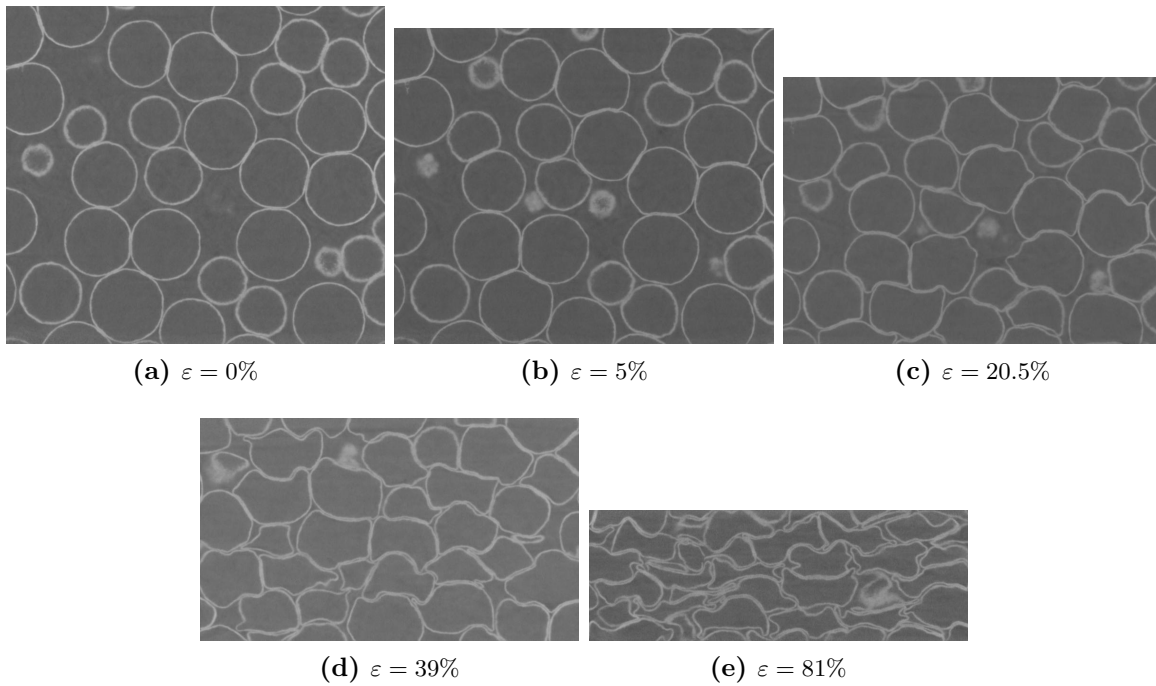


Figure 4.9: Tomography observation of a stacking during compression.

4.4 Equivalent homogeneous medium by phenomenological approach

4.4.1 The model and its parameters

Relying on the previous observations, a simple approach is proposed to develop a phenomenological description of the stress strain behaviour, along the lines of “damage plasticity”. The integration of damaging and densification in a “uniaxial” simulating model was done by considering the foam as a multi-phase material corresponding to different stages in the damage process. It consists in a healthy

phase (He), a damaged phase (Da) corresponding to the formation of plastic hinges or indentations, and a densified phase (De). Each phase is described by an elastic-plastic behaviour with a linear work hardening H . Healthy phase and damaged phase are assumed to be loaded “in parallel” while the densified phase is loaded “in serie” (figure 4.10). The transition from a phase to another is driven by a probabilistic law of evolution with strain, such as equation 4.2 given by the tomography analysis.

$$P(\varepsilon) = 1 - e^{-\frac{\varepsilon}{\varepsilon_u}} \quad (4.2)$$

The model does not explicitly account for the new contacts between spheres. This effect is captured

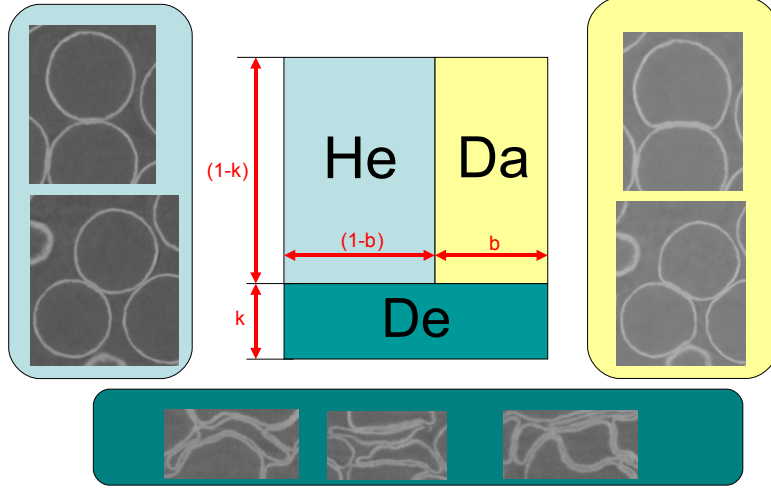


Figure 4.10: *Presentation of the model.*

by a progressive densification of the material since the early stages of deformation.

The Young modulus of the healthy phase (E_{He}) was taken equal to the initial unloading modulus, and the others parameters were adjusted to fit the experimental results obtained for the highest density foam (specimen C). The response of the model is shown in figure 4.11 and describes well both the stress-strain curve and unloading modulus evolution with strain.

4.4.1.1 Extrapolation to other densities

The input parameters of the model depend on the material initial relative density. Based on the density effect analysis of chapter 3.1.4, this dependence was described by a simple power law. Young moduli of the three phases and hardening moduli followed :

$$\frac{E_2}{E_1} = \frac{H_2}{H_1} = \left(\frac{\rho_2}{\rho_1} \right)^{1.8} \quad (4.3)$$

The other parameter of the model, namely the mean strain ε_u of equation 4.2, is also expected to depend on the initial relative density. Hence it were described by a linear dependence (Eq. 4.4).

$$\frac{\varepsilon_2}{\varepsilon_1} = \frac{1.37 - \rho_1}{1.37 - \rho_2} \quad (4.4)$$

Strains for damage initiation ε_0 and densification were every time taken as null value obtained from the tomography analysis (Eq. 4.5).

$$\varepsilon_0 = 0 = \varepsilon_0^{PlanseeC} \quad (4.5)$$

Table 4.1 summarizes the input parameters of the model for the three samples

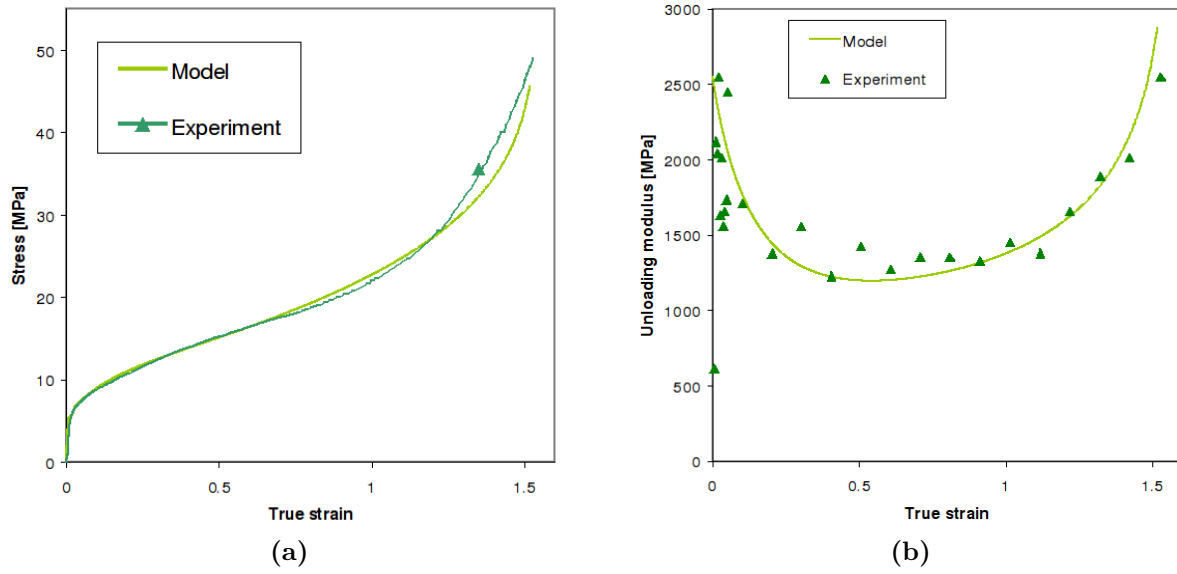


Figure 4.11: Model response for the stress-strain curve (a) and for the unloading modulus evolution with strain (b).

	Properties	Plansee A	Plansee B	Plansee C
Healthy phase	E_{He} [MPa]	819	1549	2550
	H_{He} [MPa]	10.9	20.7	34
Damaged phase	E_{Da} [MPa]	321	603	1000
	H_{Da} [MPa]	5.5	10.3	17
Densified phase	E_{De} [MPa]	1285	2430	4000
Damaging law	Weibull exponent n	0.75	0.75	0.75
	Mean strain ε_u [%]	0.09	0.075	0.06
	Initial strain ε_0 [%]	0	0	0
Densification law	Weibull exponent n	0.75	0.75	0.75
	Mean strain ε_u [%]	1.8	1.5	1.2
	Initial strain ε_0 [%]	0	0	0

Table 4.1: Input parameters for the model.

4.4.2 Validation of the model

Figure 4.12 shows the comparison between responses of the model and experimental results for two densities corresponding to specimens A and B, for both the stress-strain curve and unloading modulus evolution with strain. Stresses are well predicted up to strain of 1.2 and unloading moduli up to densification.

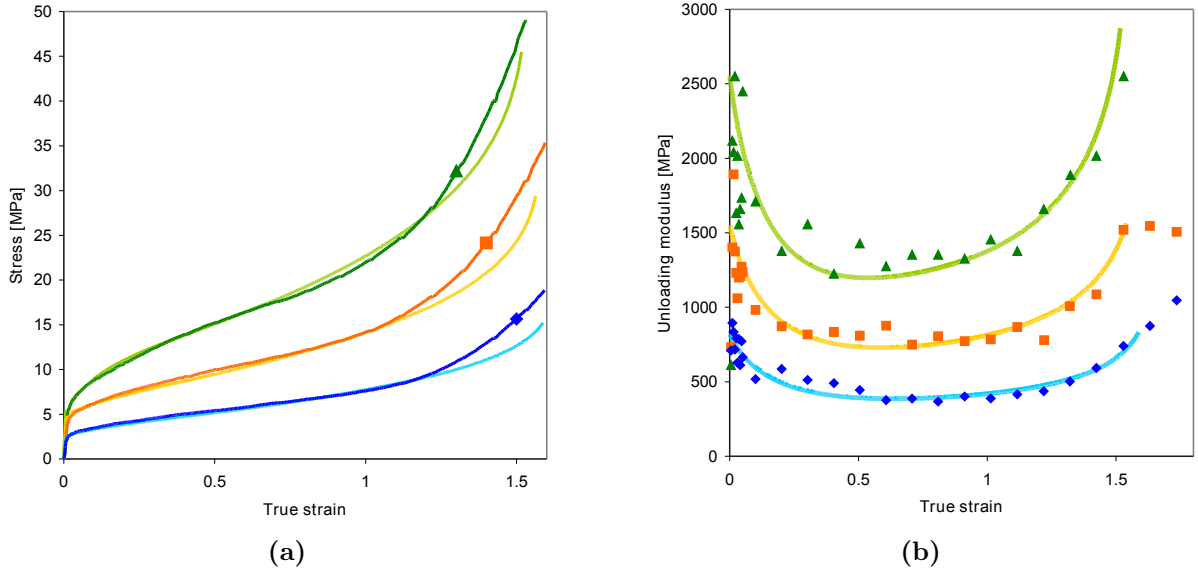


Figure 4.12: Comparison of the model to experiments

4.5 Summary on the mesoscopic metamorphism

Damage Four mechanisms are responsible for the damage of the material at the mesoscopic scale. Two of them are consequences of the localisation of the strain into plastic hinges (or plastic ring) : indentation and neck shearing. Both other mechanism are induced by local tensile loading. It can be either a tearing of the shell, or a failure of the neck.

Densification Creation of news contacts occurs all along the compression of the stacking. Nevertheless theses new contacts are not responsible for the important strengthening of the material for large compressive strains. Most of the compressive macroscopic strain is endured by the open porosity up to the transition to the densification mechanism. When all the open porosity have been “consummed”, the sphere are constrained on their whole boundary, and become thus stiffer.

Phenomenological model A phenomenological model, based on a partition of the material in a healthy phase, a damaged phase and a densified phase, can describe both the stress-strain curves and the evolution of the unloading modulus with strain. Thanks to scaling laws, the predictions are also accurate for a varied foam initial density.

Summary on hollow spheres stacking

Hollow spheres stackings have been studied from three different viewpoints. First the structure have been fully characterized. Then the macroscopic mechanical behaviour has been investigated. Last the deformation mechanisms at the scale of the cell have been studied and linked to the macroscopic behaviour. Various model have been set up to describe the material properties and mechanical behaviour.

Structures

Hollow spheres stackings structure have been characterized at various scales.

Macroscopic Scale The only structural parameters at macroscopic scale are density or relative density. the R.V.E. for density has been found to have less than 10 mm side size. Thus matter distribution is very homogeneous.

Mesosopic scale This is the scale of the cells. Spheres diameters scatter is very low. Stackings are almost mono-modal. When samples are compared, their is no major differences in the neck size, nor in the mean coordination number. This similitude of architecture is a direct consequence of the compaction process which is driven by the styrofoam balls whatever the shell thickness. Nevertheless the measure of the neck size by X-ray tomography was shown to largely overestimate the real contact area. No significant ordering has been found in the stacking, they can be considered as random.

Microscopic scale Study of the shells shown that the outer surface roughness is of order of the metallic powder size, while the inner surface wave length and amplitude is much more important. This inner roughness is due to the roughness of the styrofoam balls. Thus the absolute variation of the shell thickness is independent of the shell thickness. Porosity is quite important within the shells, roughly 4 percents.

Macroscopic Behaviour

The macroscopic mechanical behaviour have been characterized for various loading conditions.

Uniaxial compressive behaviour The mechanical behaviour of hollow spheres stacking enduring compressive loading was shown to present a low scatter provided the sample contains respectively about 350 spheres and 1000 spheres if the concerned property is a stress or a stiffness. The mechanical

properties evolves as power laws of the foam initial density with exponents ranging from 1.2 to 2.1. No softening is observed on the stress-strain curve.

Uniaxial tensile behaviour Two main classes of damage mechanism are encountered when tensile loading is considered. If shells are thin, a progressive macroscopic softening occurs. On the cell scales, the shells fails by scratching at the vicinity of the neck. If shells are thick, the macroscopic stress-strain curve presents a steep decrease at failure. The necks fails without damaging the shells. When the shell is thick enough to observe this damage mechanism, increasing the thickness does not change the mechanical properties.

Multi-axial compressive behaviour The yield surface of hollow spheres stacking seems to be elliptic in the space of the two first invariant of the stress. Nevertheless the scatter, of both on the measurement and on the behaviour of the small samples, is too large to enable a definitive statement since a linear surface could also be a good fit.

DEM modeling Discrete Element Method applied to hollow spheres stackings can describe the foam macroscopic behaviour provided that there is no major tensile nor shearing strain and that the neck size and the contact shear law are corrected. This method gives good estimation of the initial material properties both for stress and stiffness. However the yield surface is overestimated though it seems that DEM can catch experimental trends.

Mesoscopic mechanisms

Deformation mechanisms at the mesoscopic scale have been studied and connected to the macroscopic behaviour.

Damage Four mechanisms are responsible for the damage of the material at the mesoscopic scale. Two of them are consequences of the localisation of the strain into plastic hinges (or plastic ring) : indentation and neck shearing. Both other mechanism are induced by local tensile loading. It can be either a scratching of the shell, or a failure of the neck.

Densification Creation of news contacts occurs all along the compression of the stacking. Nevertheless theses new contacts are not responsible for the important strengthening of the material for large compressive strains. Most of the compressive macroscopic strain is endured by the open porosity up to the transition to the densification mechanism. When all the open porosity have been “consummed”, the sphere are constrained on their whole boundary, and become thus “stiffer” much before the classical densification occurs.

Phenomenological model A phenomenological model, based on a partition of the material in a healthy phase, a damaged phase and a densified phase, can describe both the stress-strain curves and the evolution of the unloading modulus with strain. Thanks to scaling laws, the predictions are also accurate for a range of foam initial density.

Part IV

Sandwich structures

Introduction on sandwich structures

This section is concerned with the behaviour of sandwich structures with a hollow sphere foam core. First the sample set is described. Observations of the bonding between core and faces are performed. Then the core material is studied. Actually, the process of integration in the sandwich structure modifies the core material structure. Thus analyses, based either on microscopy, either on X-ray tomography, are performed on the shells microstructure and on the necks size and shape. The compressive behaviour of the core material is also studied. A model of homogeneous equivalent medium is fitted. Next the behaviour of sandwich structure beam under four-points bending loading is investigated. The properties of the structures are quantified. The damage mechanisms of the sandwich structures are described and their relative importance depending on the structure dimensions is discussed. The results are systematically compared with both classical analytical models and Finite Element modeling. Finally the behaviour of sandwich structure plates under indentation loading is performed and compared to predictions of the models.

Sandwich structure : presentation of the samples

Origin of the samples A set of sandwich structures with hollow spheres foam core has been provided by *PLANSEE* (Reutte, Austria) Plansee.

Samples set It consists in 12 square sandwich plates of 300 mm side size, with a core of 400g/L density steel hollow sphere core and with 314 stainless steel symmetrical faces. Faces are brazed to the core. The set is composed of 3 face thicknesses (0.4, 1 and 1.5 mm) and 4 core thicknesses (approximately 14, 19, 24, and 28 mm). Figure 1 and 2 are pictures of the plane cut of the structures. These plates

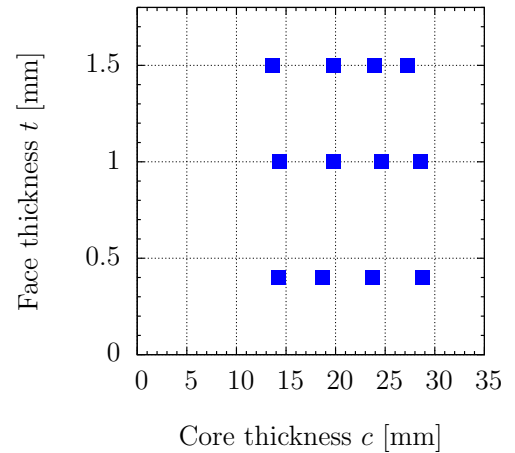


Figure 1: Overview of the set of sandwich structures. **a**-Cross section of the structures are aligned. **b**-The samples dimensions are described in a map of the face thickness t versus the core thickness c .

will be loaded either in 4 points bending as beams, or in indentation as plates. In each plate, sandwich beams of 50 mm width and 300mm length have been cut. Wire electro-erosion machining have been used to perform it. They were loaded in four point bending with 210 mm of outer span and 100 mm of inner span. The lengths were chosen in order to observe various failure mode, depending on sandwich dimensions : indentation, core shear and face yield. Figure 3 presents the sandwich beams in a map of the weight and of the core thickness. *PLANSEE* provided an analysis of the quality of the bonding between core and faces. For each sandwich structure, two maps of ultrasonic analysis of the bonding were available. It allowed us to avoid the use of areas where the bonding was poor or even completely

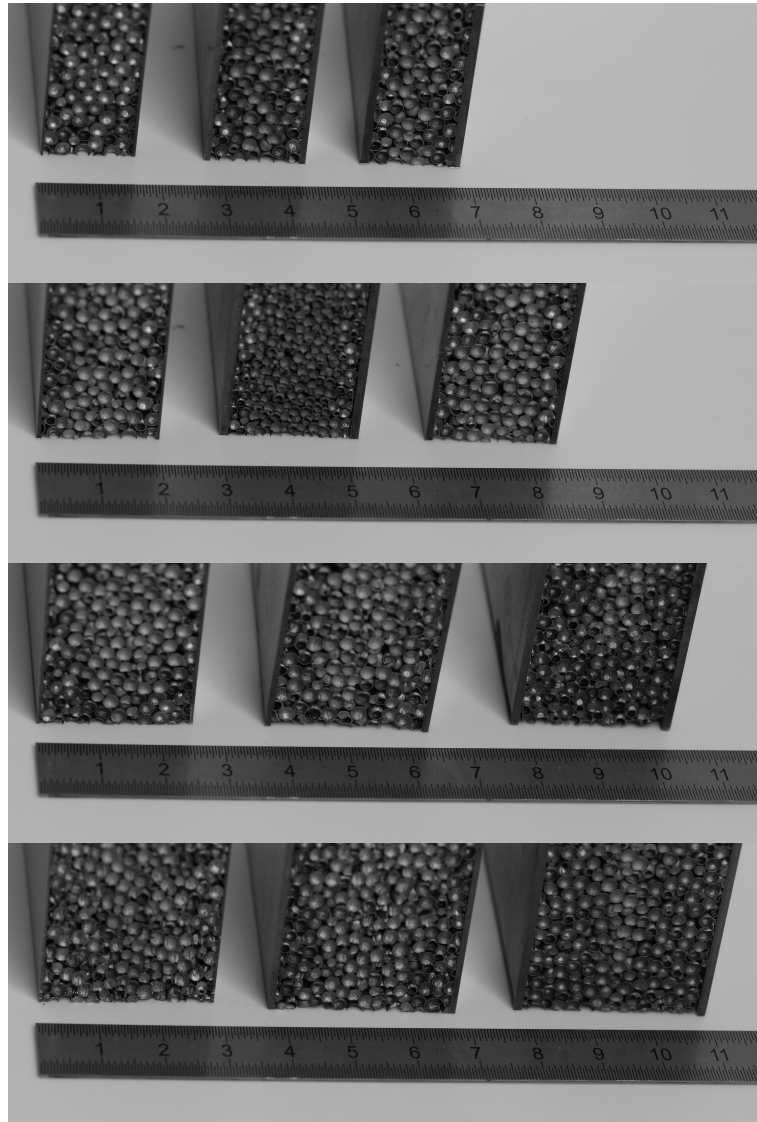


Figure 2: *Decomposition of the set of sandwich structure in 4 core thickness families with 3 face thicknesses. One can notice that one of the sandwich core is a stacking of smaller hollow spheres.*

failed.

The bonding has been observed thanks to S.E.M.. Figure 4 shows the geometrical quality of this bonding. The composition of the brazing element has not been determined. No difference between spheres, faces and brazing element could have been seen with back scattered electrons.

During these observations, the hollow spheres stackings in the middle of the core have also been studied. Large differences to the initial hollow spheres stackings have been observed, both on the shells and on the necks. It is clear that the core material has been changed due to the brazing processing. An analysis of the core material, in the sandwich structure, has to be performed.

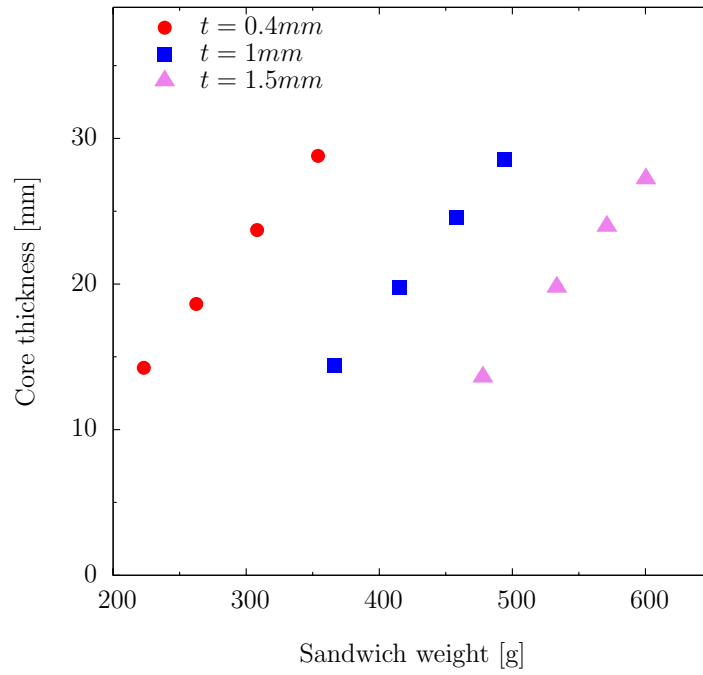


Figure 3: Description of the sandwich beams in a map of the core thickness and of the weight of the structure.

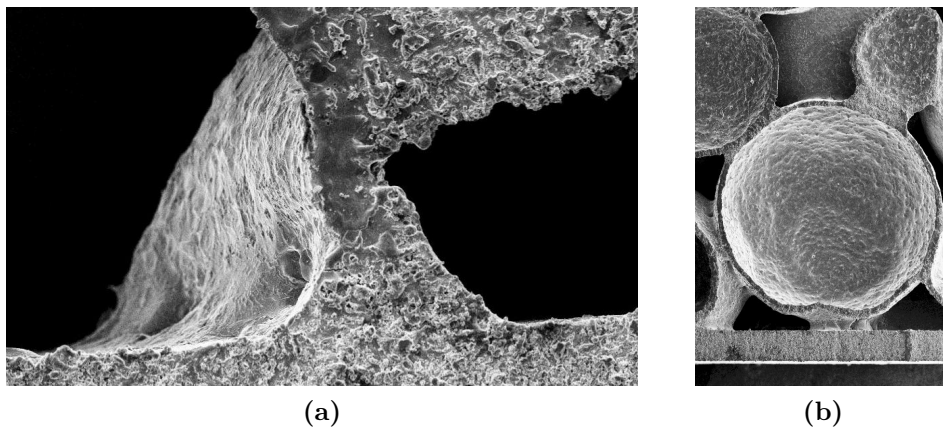


Figure 4: Overview of the brazing bonding with SEM. On the bottom of each picture can be seen a portion of a face of the sandwich structure. Scale have been varied, spheres have a radius size of 1.3 mm and shells a thickness of approximately 60 μm

Chapter 1

Analysis of hollow spheres stacking in sandwich structures

Contents

1.1	Structural characterization	167
1.1.1	Microscopic scale	167
1.1.1.1	Experiments	167
	Optical microscope	167
	Scanning Electron Microscope	167
1.1.1.2	Shell thickness and porosity	167
1.1.1.3	Neck shape	168
1.1.2	Macroscopic scale	168
1.1.2.1	Experiments	168
1.1.2.2	Density	169
1.1.3	Mesoscopic scale	170
1.1.3.1	Experiments	170
1.1.3.2	Results	170
	Qualitative observation	170
1.2	Macroscopic behavior	171
1.2.1	Experiments	171
1.2.2	Results	172
1.2.3	Modeling	173
	Microscopic scale	174
	Mesoscopic scale	174
	Macroscopic scale	174

1.1 Structural characterization

The structural characterization of the hollow spheres stackings in sandwich structures has been performed at various dimensional scales : the macroscopic scale which is the sample scale, the mesoscopic scale which is the cell scale and the microscopic scale which is the constitutive powder scale.

1.1.1 Microscopic scale

1.1.1.1 Experiments

Optical microscope Slices of sandwich structures, of about 1 mm thickness, have been cut by wire electro-erosion. These pieces have been permeated by epoxy resin at room temperature under vacuum. And then faces have been polished.

Scanning Electron Microscope Observations have also been performed thanks to Scanning Electron Microscope (S.E.M.). They have been used to investigate qualitatively the necks between spheres, the diffusion of the brazing element, and the bondings between the structure faces and the spheres. Its use was particularly relevant for the observation of the faces roughness.

1.1.1.2 Shell thickness and porosity

Optical microscope observations of the shell clearly showed that the material is different at this scale. Figure 1.1 compares a portion of shell in a sandwich structure with a portion of shell of the initial material. The first shell presents a low porosity and a regular surface. Opposite, the second shell is

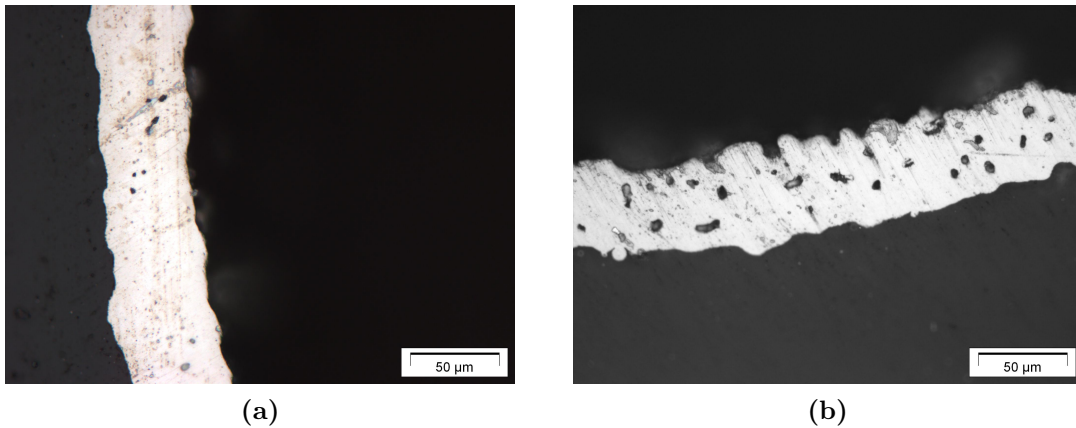


Figure 1.1: *Optical microscope observations of portions of shells. (a)-Shell of sandwich structure core material. The porosity is low and the characteristic length of surfaces roughness is large. (b)-Shell of a sphere that have not been integrated in a structure. Porosity is important and the surface is irregular.*

rough and porous. The heat treatment required to integrate the material in a structure decreases the irregularities of the shells.

SEM observation of the shells (figure 1.2) clearly shows an evolution of the microstructure.

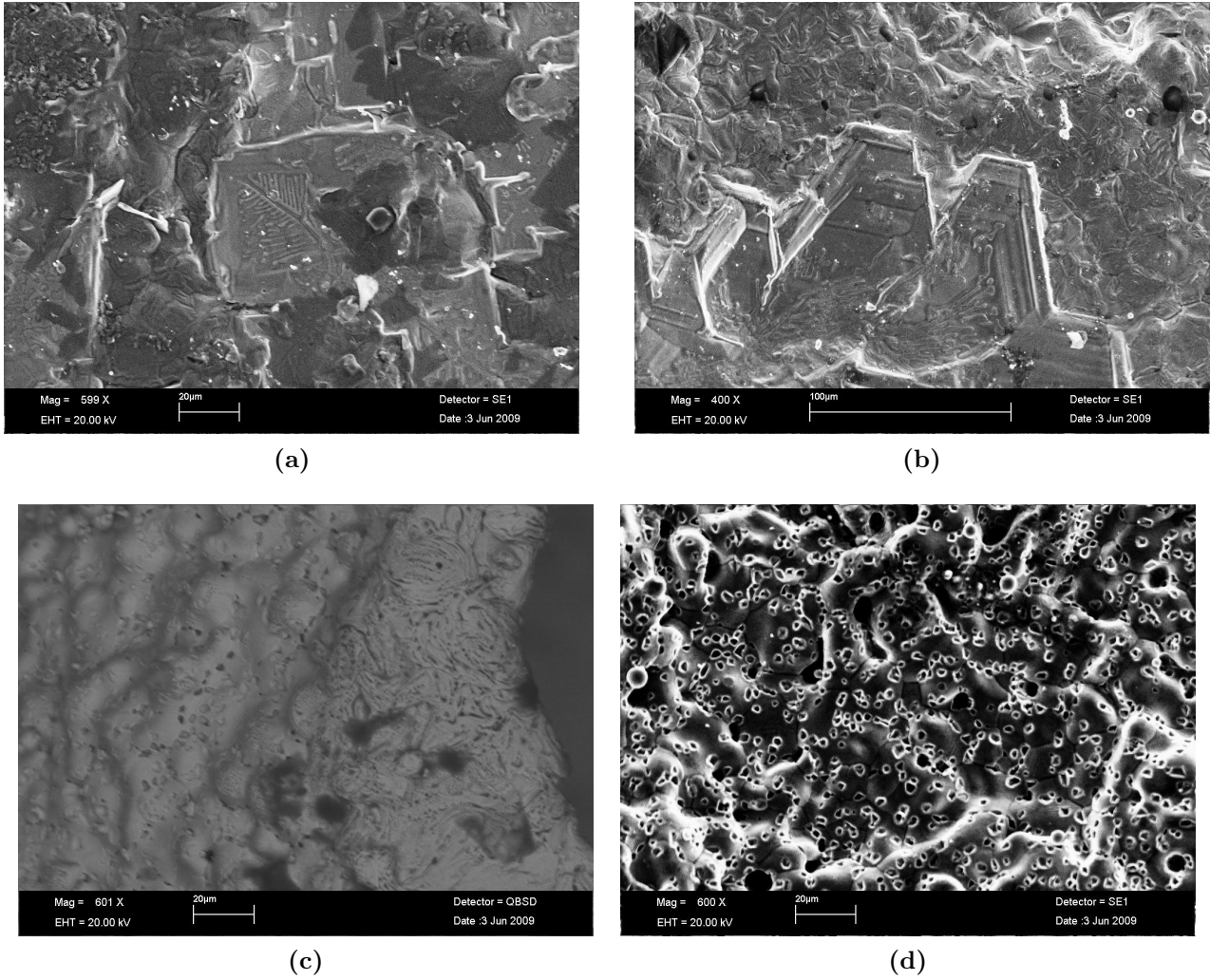


Figure 1.2: *S.E.M. images of the samples. Sandwich core material (a,b) can be compared to hollow spheres stackings that have not been integrated within a structure (c and d). Scatter of surfaces roughness is decreased but they are sharper. The microstructure of the constitutive material also seems to be changed.*

1.1.1.3 Neck shape

Matter diffusion that occurs during the heat treatment also induces evolution of the neck shape. Figure 1.3 compares the necks before and after integration into a sandwich structure. The shape of the necks clearly changes with the process of integration. The sharp necks become smooth. They also seem to be larger.

1.1.2 Macroscopic scale

1.1.2.1 Experiments

Two sandwich structures core materials have been studied. Core thicknesses were of about 14 and 26 mm. For both structures, two cylinders with square bases of 25 mm side size were cut with wire electro-erosion. These had their faces removed by wire electro-erosion about 0.5 mm from the face. The core material was assumed to have a density of about $400g/L$.

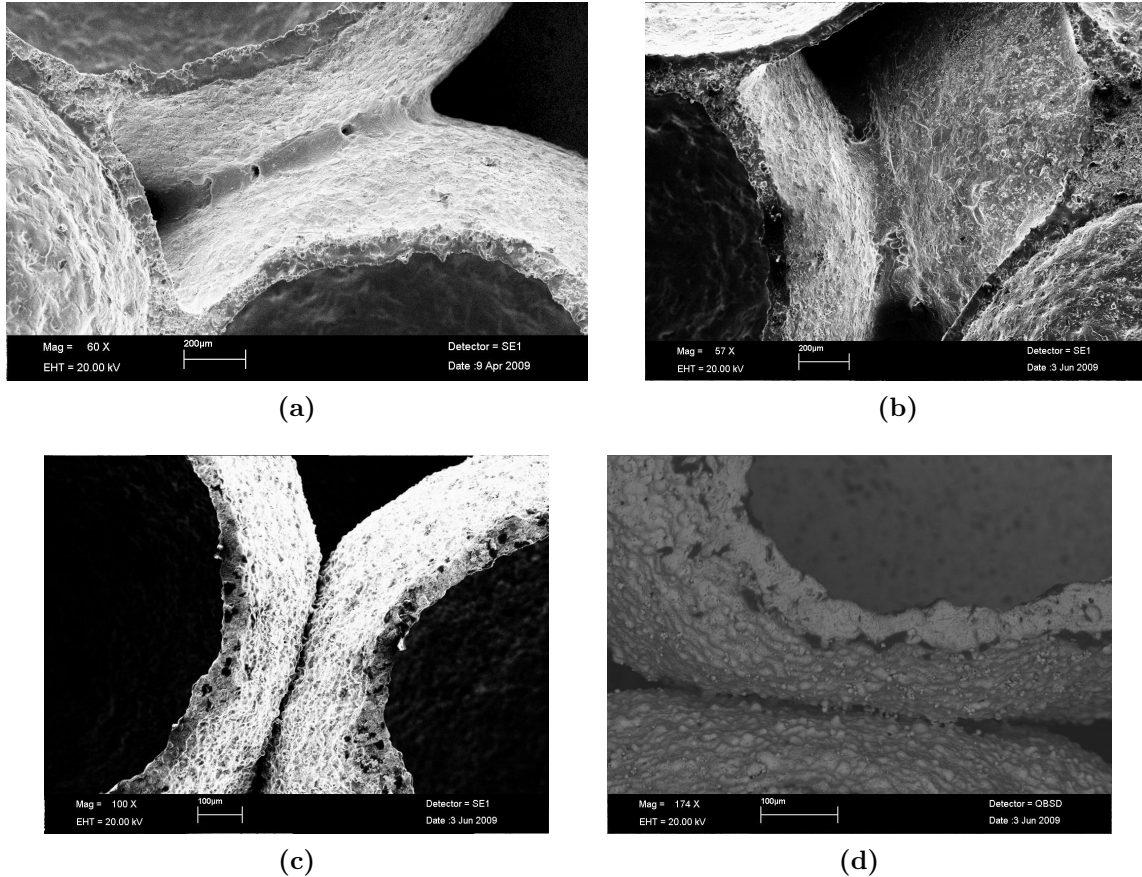


Figure 1.3: *S.E.M. images of the samples. Sandwich core material (a,b) can be compared to hollow spheres stackings that have not been integrated within a structure (c and d). Shapes of the necks are different.*

1.1.2.2 Density

The measured density was of approximately 600g/L and not of 400g/L as announced by *PLANSEE*. Table 1.1 presents the measures of density on the various samples. The scatter is large between the

Samples	Sandwich 1	Sandwich 2
core thickness	13.9mm	26.8mm
Mean density ρ	$0.65 \pm 0.04/\text{cm}^3$	$0.61 \pm 0.05\text{g}/\text{cm}^3$
Relative density ρ^*	0.082 ± 0.006	0.077 ± 0.005

Table 1.1: *Densities and relative densities of spheres stackings measured on two samples for each sandwich structure. Relative density is computed assuming a density of $7.9\text{g}/\text{cm}^3$ for the constitutive material since porosity is almost null.*

structures, and even within a single structure. Concerning the scatter between the structures, observations show that shell thickness varies from one sample to another. That clearly means that the foam used as core material was initially different from one structure to another. Then the scatter within a single structure might be due to the brazing element distribution. Actually, the amount of this element is not negligible. As seen on figure 1.4, the brazing element can spread within the structure. The length of propagation can be several spheres size.

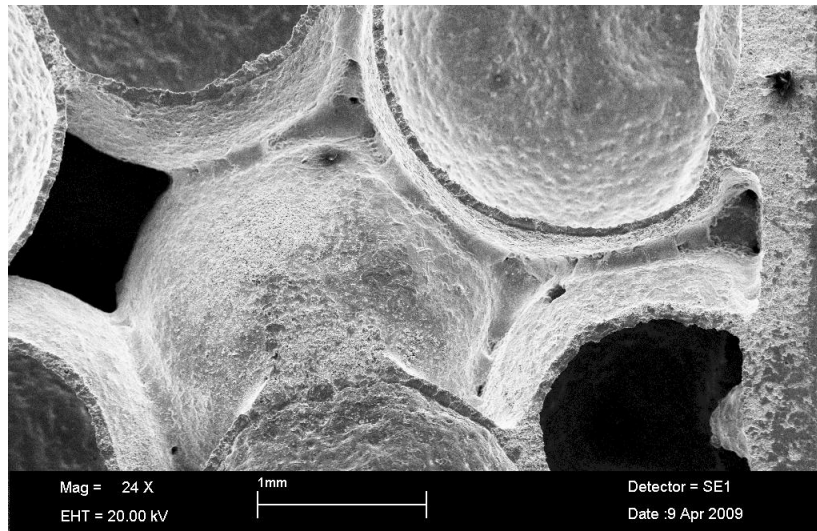


Figure 1.4: SEM observation of the core material at the vicinity of the sandwich structure face. On the right hand side, the face of the sandwich structure is visible. The brazing element spreads within the core over a length of several spheres diameters.

1.1.3 Mesoscopic scale

1.1.3.1 Experiments

Cylinders with circular base of 15mm diameter have been cut by wire electro-erosion in sandwich structures of several thicknesses and with varied face thicknesses. Thanks to X-ray tomography scans performed at *ESRF*, 3D images of the sandwich structures were obtained. The voxel size was $7.5\mu\text{m}$. Optical microscope observations were also performed at this scale.

1.1.3.2 Results

Qualitative observation Figure 1.5 shows various optical microscopy micrographs of the samples. Sandwich core material can be compared to hollow spheres stackings that have not been integrated within a structure. The process of integration into a structure makes the shell thickness more regular, decreases the constitutive material porosity and smooths the necks between spheres. It generates also some severe defects such as initial indentation of some spheres or such as failure of some shells.

The observation performed on the various samples have shown that for sandwich structures with thick core, spheres are damaged. Figure 1.6 shows reconstructed volumes of two structures. For the thin core, particles are spherical. For the thick structure, some damaged spheres can be observed, both by straining and tearing of the shells. It is thus obvious that the mechanical macroscopic behaviour will no be the same.

The core material evolution can be seen when observing a cross section of a thick sandwich structure (figure 1.7). One can see differences in the core depending on its distance to the faces.

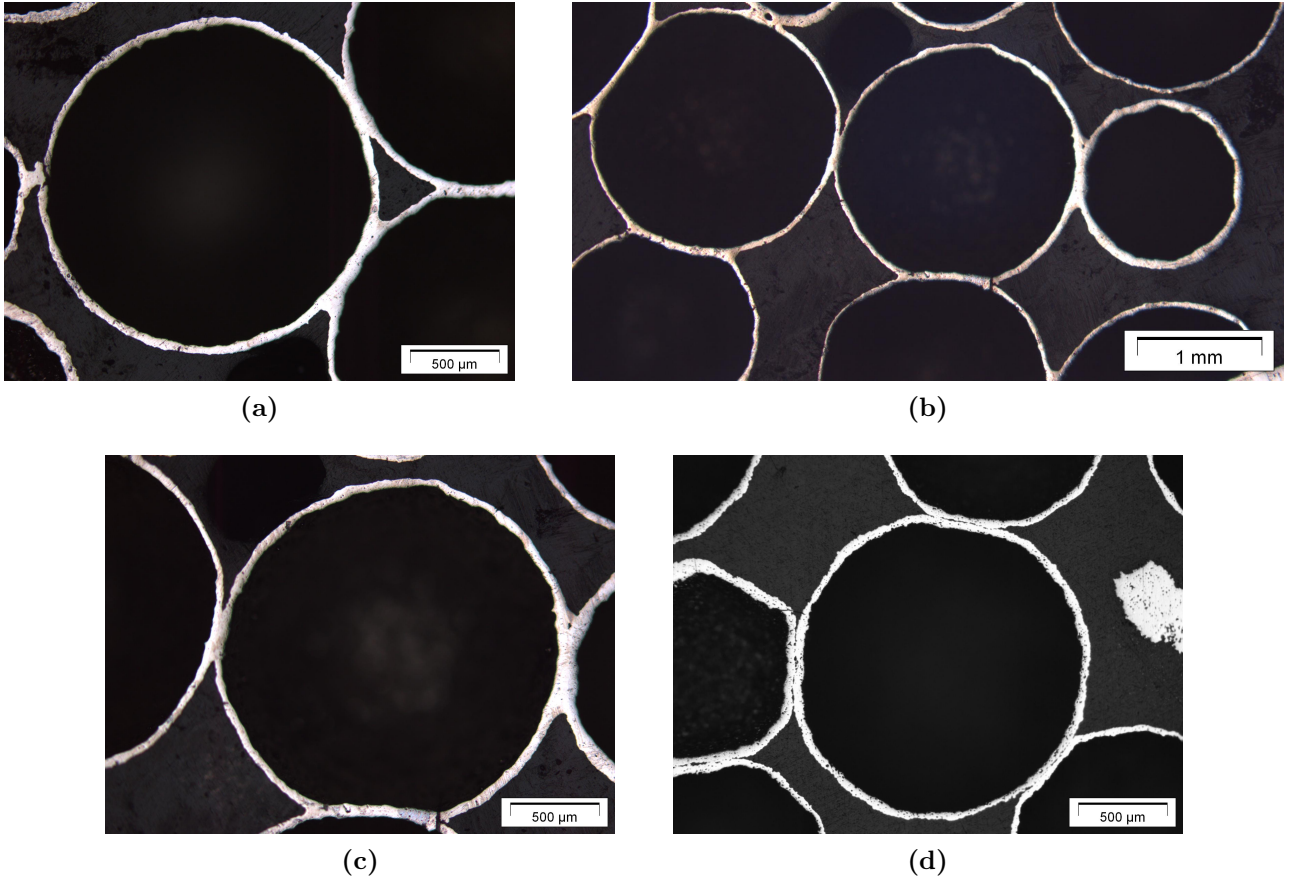


Figure 1.5: *Optical microscope observations of the hollow spheres stackings. Sandwich core material (a,b and c) can be compared to hollow spheres stackings that have not been integrated within a structure (d). One can see the regularity of shell thickness, its low porosity (a), and the smooth connection between spheres thanks to a reinforced neck. Some severe defects can be observed such as an initial indentation of spheres (bottom contacts of (b) and (c)) or such as a failure of the shell (left hand side of (a)).*

1.2 Macroscopic behavior

1.2.1 Experiments

For both structures, four cylinders with square bases of 25 mm side size were cut with wire electro-erosion. For each sandwich structure, two pieces had their faces removed by wire electro-erosion about 0.5 mm from the face. Uniaxial compressive tests, in a direction perpendicular to the faces, have been performed on samples both with and without faces. A constant strain rate of $0.001s^{-1}$ has been imposed for all the samples. Numerous loading-unloading sequences have been performed. Relative motion of the plateau has been recorded by a RDP sensor.

From the experiment, several outputs can be obtained. First stress-strain curves can be plotted, without the unloading sequences. Unloading moduli can be calculated at each unloading sequence, and thus its evolution with strain can also be visualized.

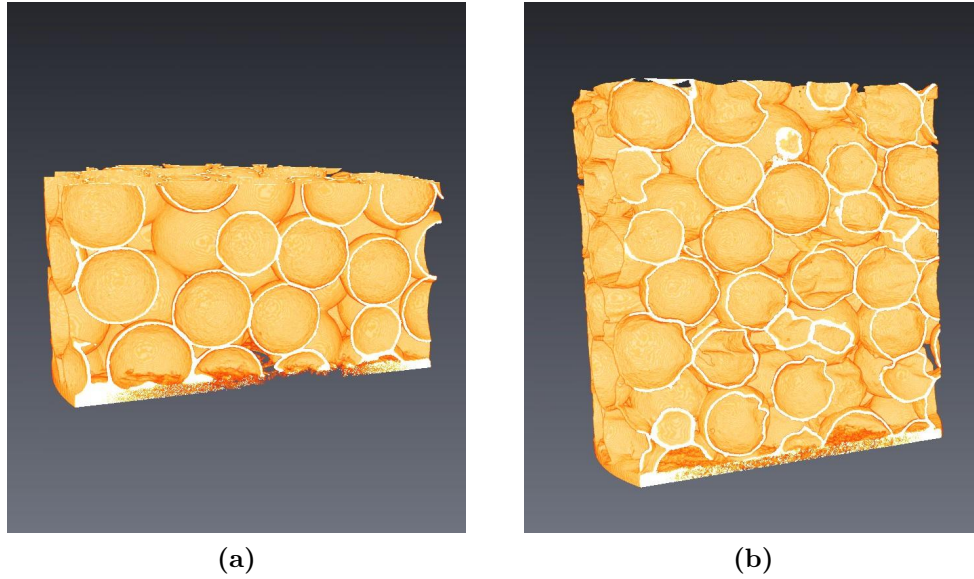


Figure 1.6: 3D visualisations of half sandwich structures with respectively thin core (a) and thick core (b). On the bottom, sandwich structure faces can be seen.



Figure 1.7: Cross section of a sandwich structure. The core varies depending on its distance to the faces

1.2.2 Results

Figure 1.8 shows the stress-strain curves obtained with these tests and also reminds the stress-strain curves obtained for the initial foams of various densities. Figure 1.9 does the same for the unloading modulus evolution with strain. The mechanical behaviour has been changed with the integration into sandwich structures. First, the stress-strain curves can present softening. This is a clear signature of local instabilities. The shells might not endure large strains. It seems that they are more brittle. The macroscopic behaviour becomes closer to classical closed cells foams, maybe also because of the stiffening role of the rounded necks. Then the scatter is large within a single sample type in regard to the (large) size of the samples. The stiffened meso-structure makes the material much more sensitive to defects. Next the unloading modulus only slowly decreases with strain. It means that the materials has

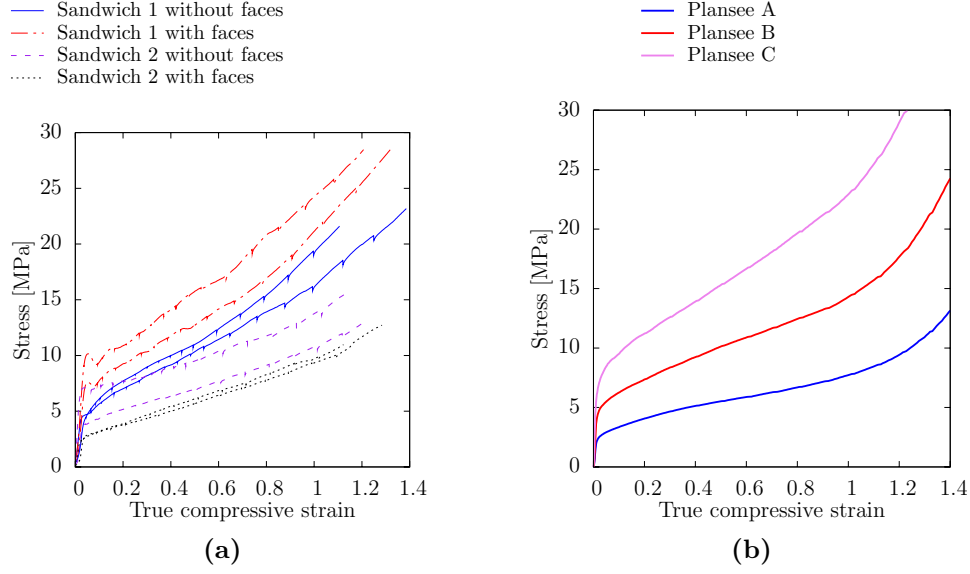


Figure 1.8: *Compressive loading response. a-Stress-strain curves of the core material both with and without the sandwich structure faces. b-Stress-strain curves of the initial hollow spheres stackings of various densities.*

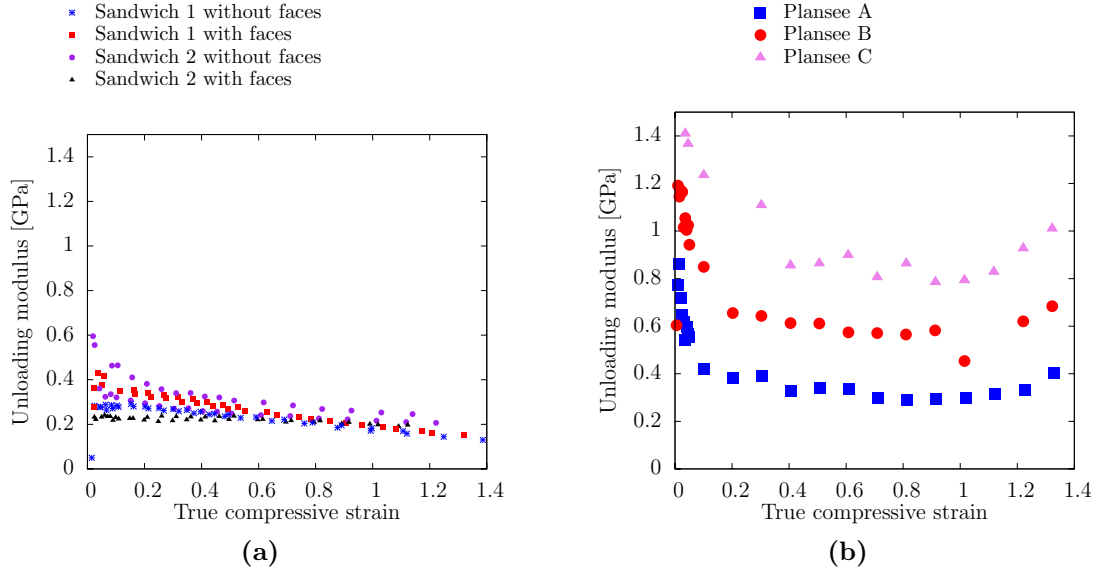


Figure 1.9: *Compressive loading response. a-Unloading modulus evolution with strain for the core material both with and without the sandwich structure faces. b-Unloading modulus evolution with strain for the initial hollow spheres stackings of various densities.*

already been damaged. It is in accordance with optical microscope and X-ray tomography observations.

1.2.3 Modeling

A modeling of the hollow spheres stackings thanks to a homogeneous equivalent medium gives access to Finite Element simulations of sandwich structures. By the time of this modeling the yield surface of the core material was not known. The model can thus only rely on the compressive and tensile behaviour. The similarity with other metallic foams made us to choose an associated elliptic criterion

to model the plastic behaviour. The parameter of this model, called Green criterion, elliptic criterion or Deshpande-Fleck model, have been kept constant with the foam density. A linear isotropic hardening was used to describe the evolution of stress level. The yield stress and the hardening coefficient were fitted to a compressive stress-strain curve. The parameters of the model are presented in table 1.2.

Core thickness [mm]	E_c	σ_y^c	H_c
$c < 21$	500 MPa	6.3 MPa	13.4 MPa
$c > 21$	500 MPa	3.5 MPa	7.5 MPa

Table 1.2: Fit laws for the stress-strain curves in compression depending on the core thickness.

Figure 1.10 compares the model with the experiments.

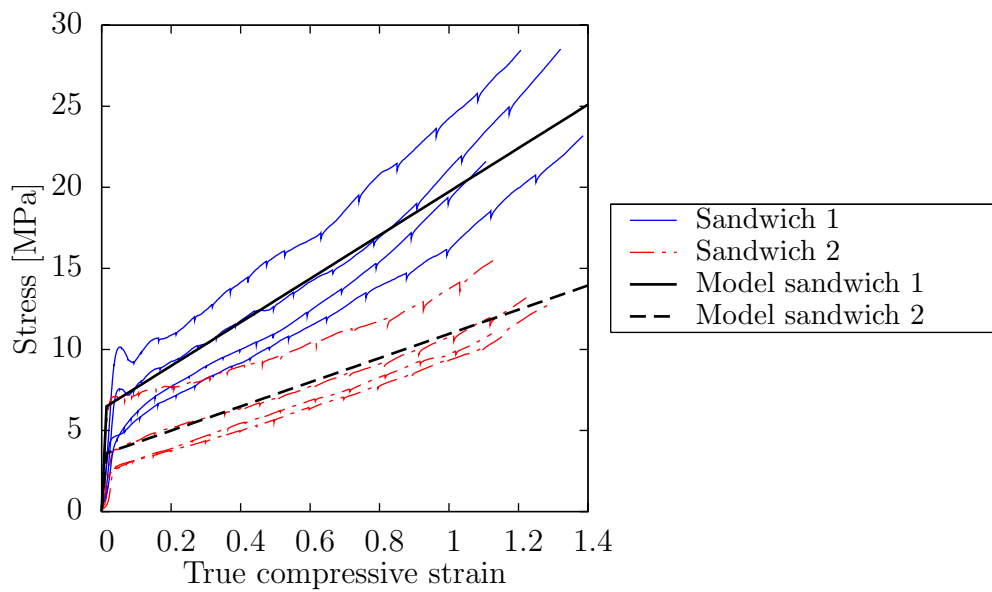


Figure 1.10: Compressive loading response and corresponding model. Depending on the core thickness c the model is varied.

Summary on the hollow spheres stacking in a sandwich structure

The integration of hollow spheres stackings into sandwich structures induces changes of the material. Micro-structure and meso-structure are affected as well as the mechanical macroscopic behaviour.

Microscopic scale The heat treatment lead to an evolution of the microstructure. The porosity is highly decreased, as well as the roughness of the surfaces. The shell seems to become less ductile.

Mesoscopic scale Diffusion of the constitutive material modifies the neck shape. It becomes soft. During the process of implementation in the structure the spheres have been damaged. The thicker is the core, the larger seems to be this effect.

Macroscopic scale The mechanical behaviour changes with the process.

Chapter 2

Four-point bending

Contents

2.1	Experiments	177
2.2	Results	177
2.2.1	Stiffness	177
2.2.2	Characteristic loads and associated deflections	178
2.2.3	Energy absorbed	179
2.2.4	Damaging modes	179
2.2.4.1	Detection of the damaging mode	179
	Core shear	183
	Face yield	183
	Indentation	184
2.2.4.2	Failure map	184
2.3	Numerical simulations	184
2.4	Comparison of experiments and models	186
2.4.1	Description of the damaging modes	186
2.4.1.1	Core shear	186
2.4.1.2	Face yield	187
2.4.1.3	Indentation	187
2.4.2	Failure map	188
2.4.3	Optimal structures	190
2.4.3.1	Service condition	190
2.4.3.2	Ultimate condition	192
	Sandwich behaviour	193
	Models for the sandwich behaviour	193

2.1 Experiments

Sandwich plates presented in IV were cut in beams of 50 mm width and 300mm length. They were loaded in four point bending with 210 mm of outer span and 100 mm of inner span. The lengths were chosen in order to observe various failure mode, depending on sandwich dimensions : indentation, core shear and face yield. During the tests, the load and the motion of the rollers were recorded by the machine, while a RDP sensor recorded the motion of the central point of the lower face of the sandwich. A digital camera has also been used. Numerous unloading sequences have been performed during the tests to obtain the evolution of the stiffness of the beams with the deflection. Figure 2.1 recalls the various dimensions, and also the records of the tests which are *the load F , the deflection d and the thickness diminution e (also called thickness parameter in the following)*.

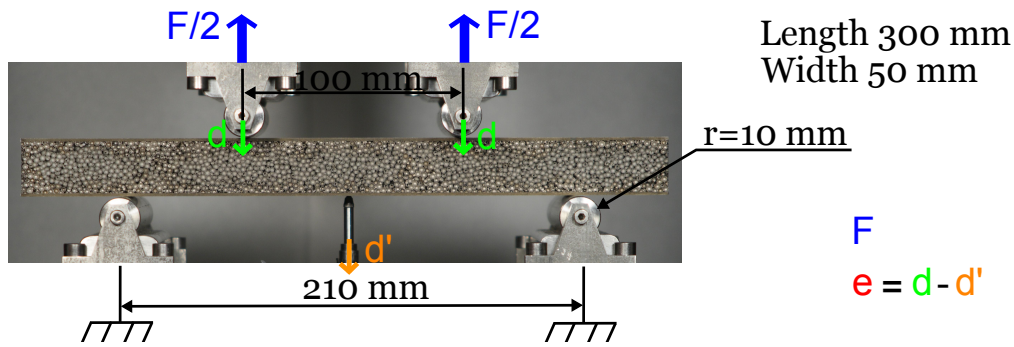


Figure 2.1: Dimensions and records of the four-points bending tests.

2.2 Results

From these tests, common properties, such as initial stiffness, damaging load and ultimate load, can be compared. Then a more detailed analysis has to be performed to identify the various damaging modes.

2.2.1 Stiffness

Two values for the stiffness have been extracted from the load-deflection curves.

The first one is the value of the loading slope. In order to obtain a relevant comparison value, the slopes have been measured from the portion where load was between 1 and 2 kN. The lower bound has been chosen to avoid the initial portion of the loading curve that presents a non linear response due to the positioning and the alignment of the rollers. The upper bound is low enough to be less than the initiation of non linearity due to damaging.

The second one is the maximum value of the unloading stiffness within the elastic domain. The unloading stiffness has been fitted on the first 1kN of each unloading sequence. Figure 2.2 shows both values of the stiffness plotted as function of the weight of the sandwich structure. Because of the low density of the core material compared to the face material, the abscissa axis can be divided in three regions, each one corresponding to a given face thickness. For each group, the sandwich structures are ranked by increasing thickness (as seen on figure 3).

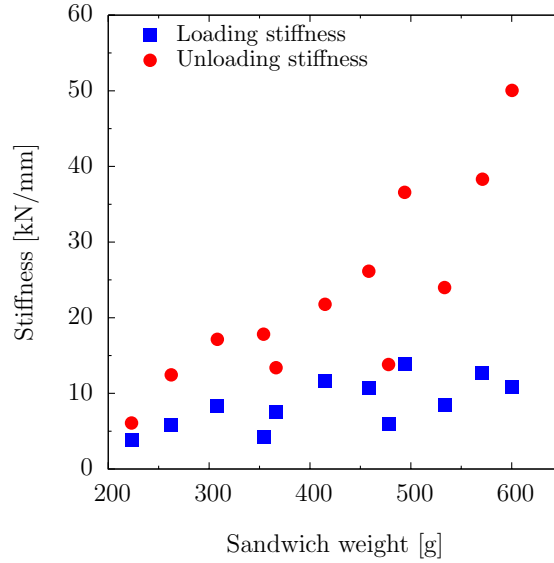


Figure 2.2: *Stiffness versus weight for the set of sandwich structures. Both loading and unloading (within the elastic domain) values are presented.*

2.2.2 Characteristic loads and associated deflections

Two characteristic loads have been identified : the damaging load and the ultimate load. The damaging load corresponds to the initiation of a non linear behaviour in the load versus deflection curve. It is detected by a deviation of 0.2 mm from the linear behaviour. The ultimate load is the maximum load that the structure can carry within the first 30 mm of deflection. Figure 2.3a shows the damaging deflection of the sandwich structures plotted as a function of their weight. Figure 2.3b shows the deflections associated to these characteristic loads plotted versus the weight of the sandwich structures. Both the damaging load and the ultimate load increase with the face thickness and the core thickness,

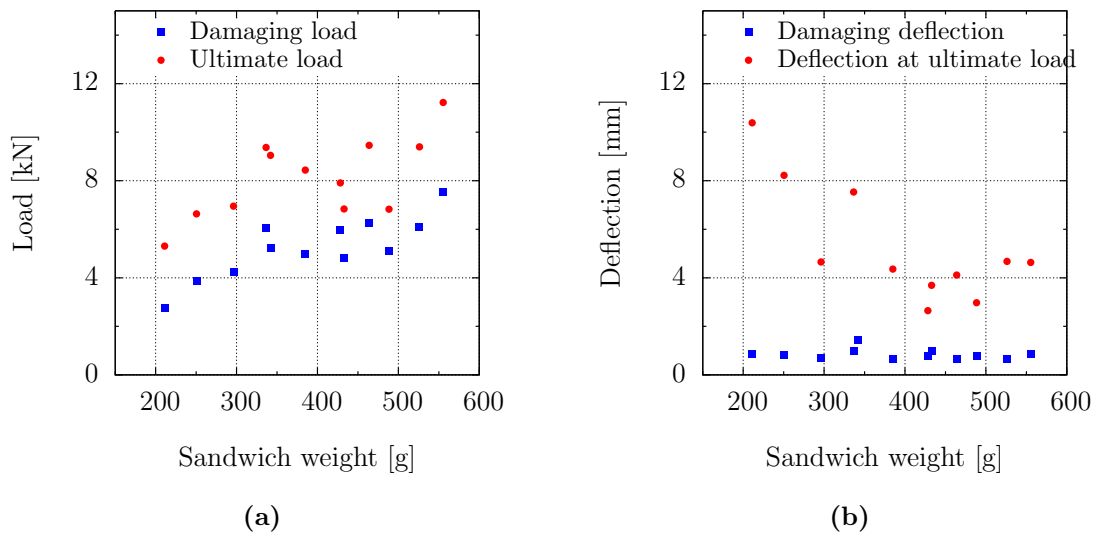


Figure 2.3: *Characteristic loads (a) and associated deflections (b) plotted versus the weight of the sandwich structures.*

but not every time with the weight of the sandwich beam. A somehow constant offset seems to be observed between the two characteristic loads.

The deflection at ultimate load is large for the light weight structures and follows a decreasing trend. For heavier structures, the deflection at ultimate load is almost constant and is of about 4 mm. The damaging deflection is almost the same whatever the core and face thicknesses and it is of about 1mm.

2.2.3 Energy absorbed

An important property of these sandwich structures is their ability to absorb energy. The total energy absorbed by the structure at 30 mm of deflection have been quantified. Figure 2.4 shows the energy absorbed for a prescribed displacement of 30 mm for the sandwich structures plotted versus their weight. The energy absorbed ranges between 100 and 250 J for beams of 50 mm width.

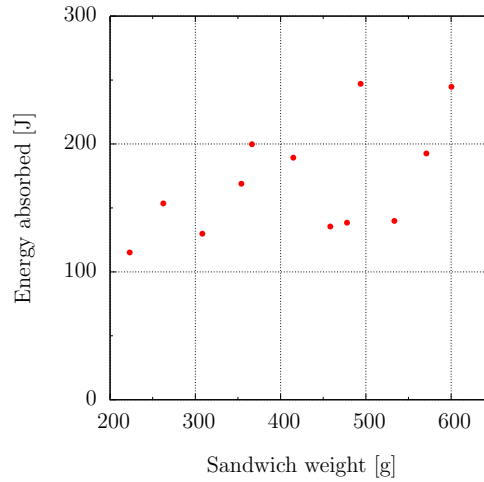


Figure 2.4: *Energy absorbed for a deflection of 30 mm versus weight for the set of sandwich structures.*

2.2.4 Damaging modes

2.2.4.1 Detection of the damaging mode

From the experiments three failure modes have been observed. A simultaneous analysis of both the digital image analysis and the load and motion records, allows to identify the signatures of these damaging modes. Actually, the single observation of the final shape of the structure is not sufficient to determine the damaging mode. A particular mode can initiate the damage but then the structure can fail via another mode. Load, thickness reduction and stiffness evolutions with the motion of the rollers have been used. The thickness reduction of the sandwich is obtained thanks to the difference between displacements registered by the RDP sensor and the displacement imposed by the machine corrected by its stiffness. This parameter contains simultaneously the information of indentation and of curvature of the central part of the beam. Figure 2.5, figure 2.6 and figure 2.7 show the evolution with the deflection of the shape of structures that fail respectively by core shear, face yield and indentation.

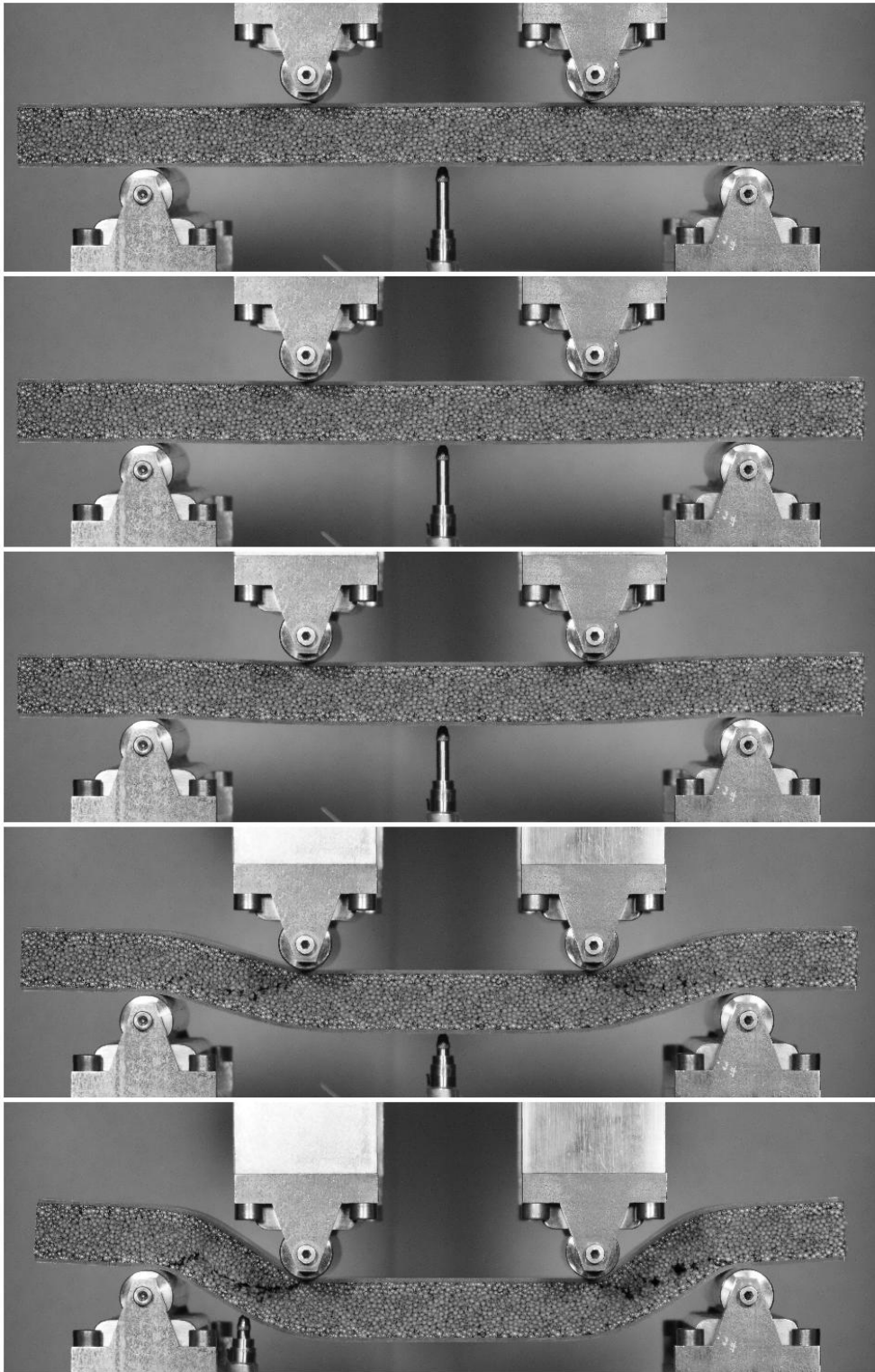


Figure 2.5: Sandwich loaded in four points bending. The sandwich fails by core shear. Pictures were taken at deflection of 0mm, 2mm, 4mm, 16mm and 30mm.

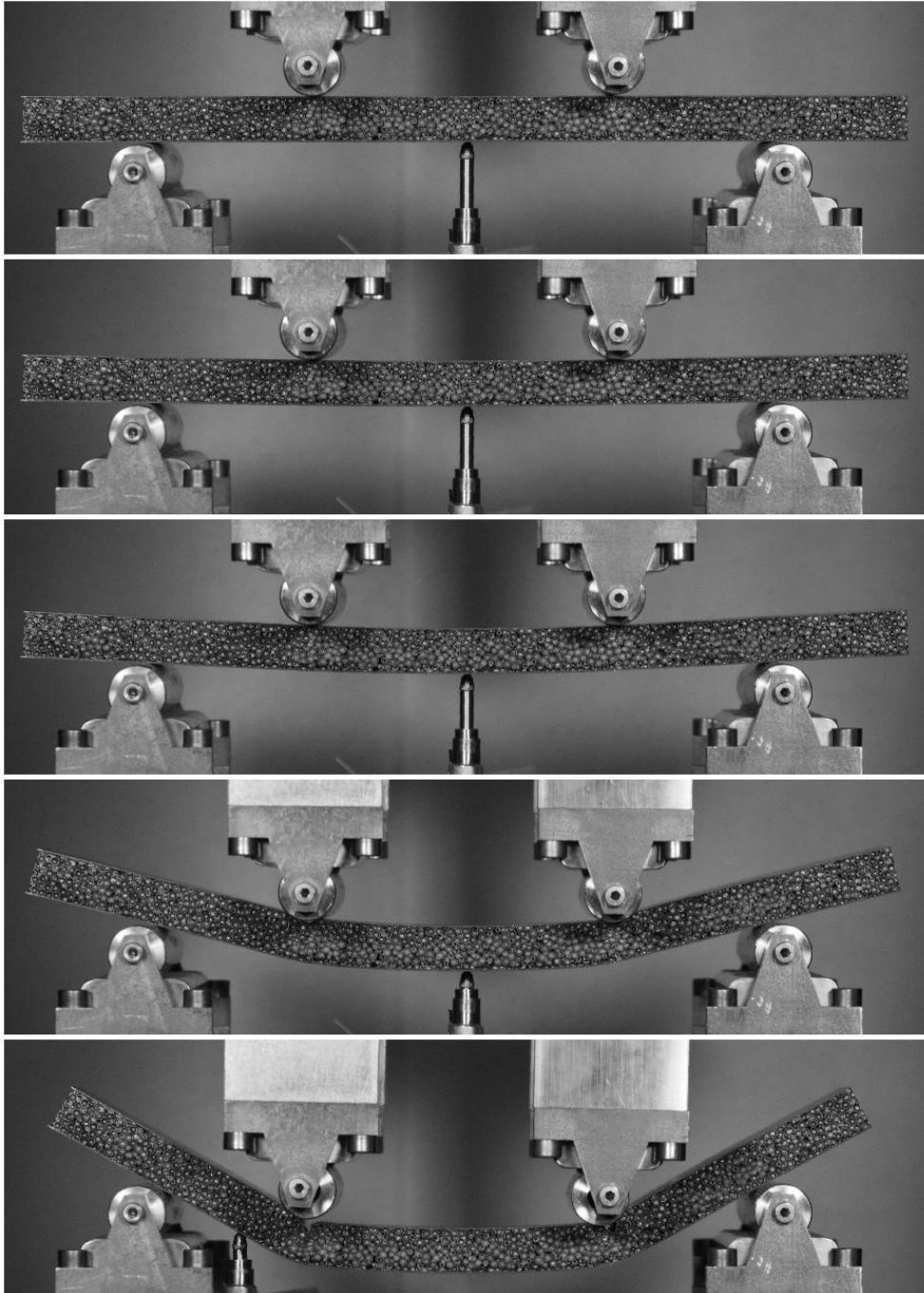


Figure 2.6: Sandwich loaded in four points bending. The sandwich fails by face yield. Pictures were taken at deflection of 0mm, 2mm, 4mm, 16mm and 30mm.

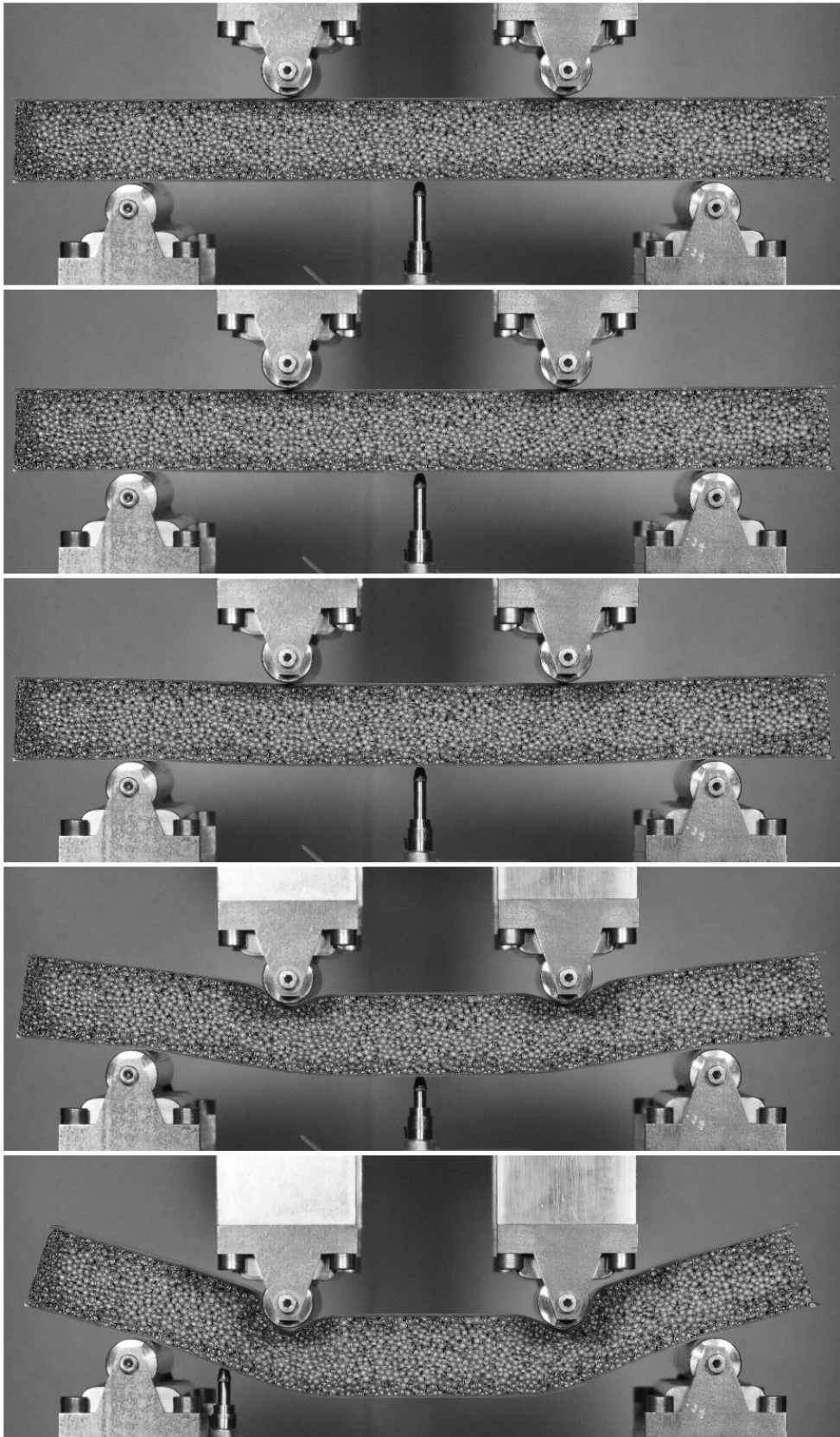


Figure 2.7: Sandwich loaded in four points bending. The sandwich fails by indentation. Pictures were taken at deflection of 0mm, 2mm, 4mm, 16mm and 30mm.

Core shear Figure 2.8 presents the load, the thickness reduction and the stiffness evolutions with deflection characteristic of that failure mode. A deformed grid, obtained by image correlation techniques, reveals the strain fields within the core. Core shear induces formations of plastic hinges at the vicinity

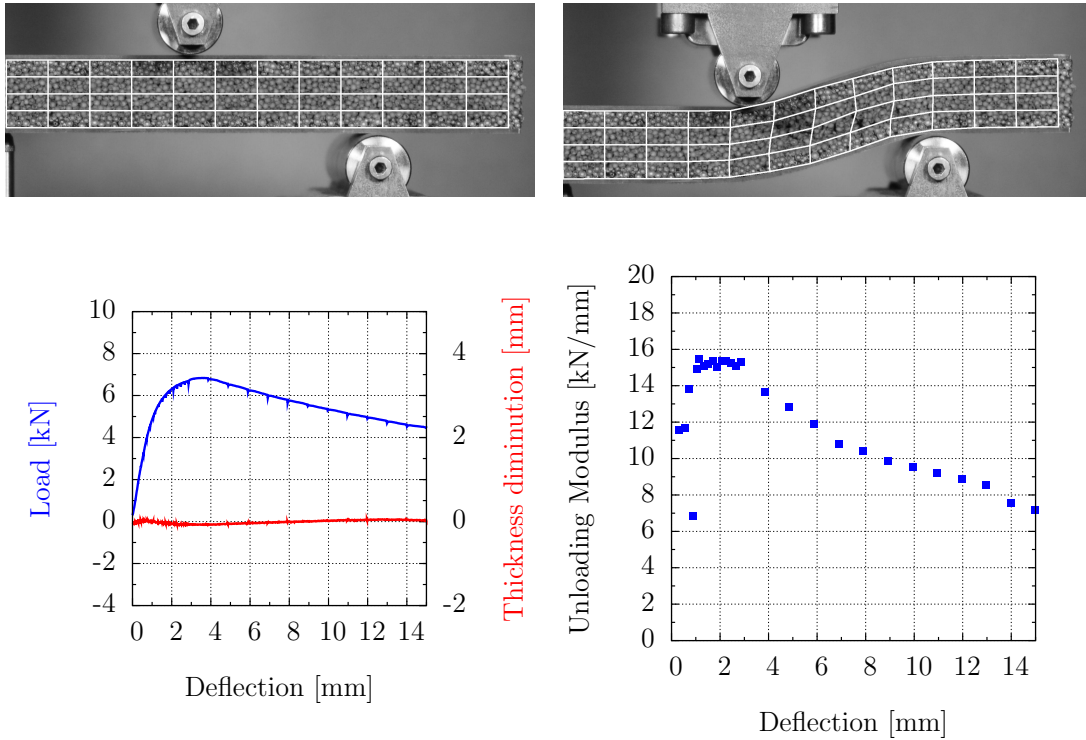


Figure 2.8: Digital image correlation of a part of a sandwich structures loaded in four points bending failing by core shear. Pictures were taken at deflection of 0mm, 2mm, 4mm, 8mm and 16mm. The grid points out the strain field within the core.

of the rollers, a mechanism which gives at the macroscopic scale a flat central part and no indentation. Core shear is therefore characterized by a constant sandwich thickness. The load response was shown to reach its maximum at low deflection and then the structure undergoes a softening stage.

In our case the core depth is important, therefore the critical overhang of transition between the two core shear failure modes (Equation 1.8) is very small (less than 1.2 mm). The consequence is that the core shear failure mode that might occur would necessarily be the B mode, in which the core overhang is not loaded.

Face yield Figure 2.9 presents the load, the thickness reduction and the stiffness evolutions with deflection characteristic of that failure mode. A deformed grid, obtained by image correlation techniques, reveals the strain fields within the core. Face yield is the signature of an important flexural deformation of the structure, thus the central deflection is more important than the imposed displacement. The thickness increases. The load-deflection curve shows a long hardening stage where faces are yielding. At maximal load the change of behaviour is more abrupt than for other failure modes. It is simply the results of instabilities that led to a localisation of the rotations of the sections of the beam. The shape of the structure at the end of the tests could be misinterpreted as an indentation failure, but the hardening stage clearly excludes this hypothesis.

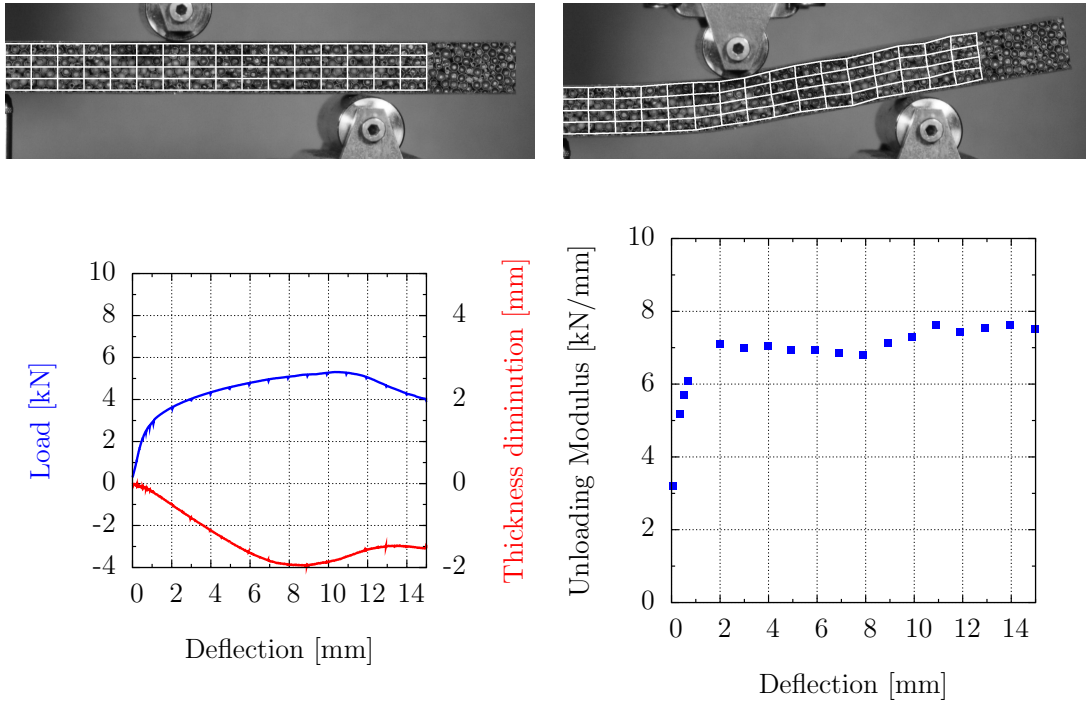


Figure 2.9: Digital image correlation of a part of a sandwich structures loaded in four points bending failing by face yield. Pictures were taken at deflection of 0mm, 2mm, 4mm, 8mm and 16mm. The grid points out the strain field within the core.

Indentation Figure 2.10 presents the load, the thickness reduction and the stiffness evolutions with deflection characteristic of that failure mode. A deformed grid, obtained by image correlation techniques, reveals the strain fields within the core. Indentation mode is characterized by a limited displacement of the lower face while upper rollers penetrates the upper face of the structure. The thickness decreases. Maximal load can be reached at low deflection or at large deflection but whatever the case, the load remains relatively close to the maximal load during a large deflection stage.

2.2.4.2 Failure map

Based on the above description of the damaging modes, the various structure failure mode have been determined. For some of them the classification was not obvious. It happens sometimes that two failure modes coexist on a single structure. Figure 2.11 shows the locations of the tested structures in a failure map, where axis represents the ration c/L (core thickness over outer span) and t/c (face thickness over core thickness). There is a clear partition of the map between the various damaging modes.

2.3 Numerical simulations

The experiments have been simulated by finite elements. The core was given an elasto-plastic behaviour with a linear hardening as described in 1.2.3. A porous criterion was used to ensure compressibility of the core. Simulation have been carried out in 2D assuming a plane-strain state on half a structure. Figure 2.12 presents the mesh of a simulated structure. The mesh has been refined in the faces. Triangular elements with 6 nodes have been used. Depending on the dimensions of the structure,

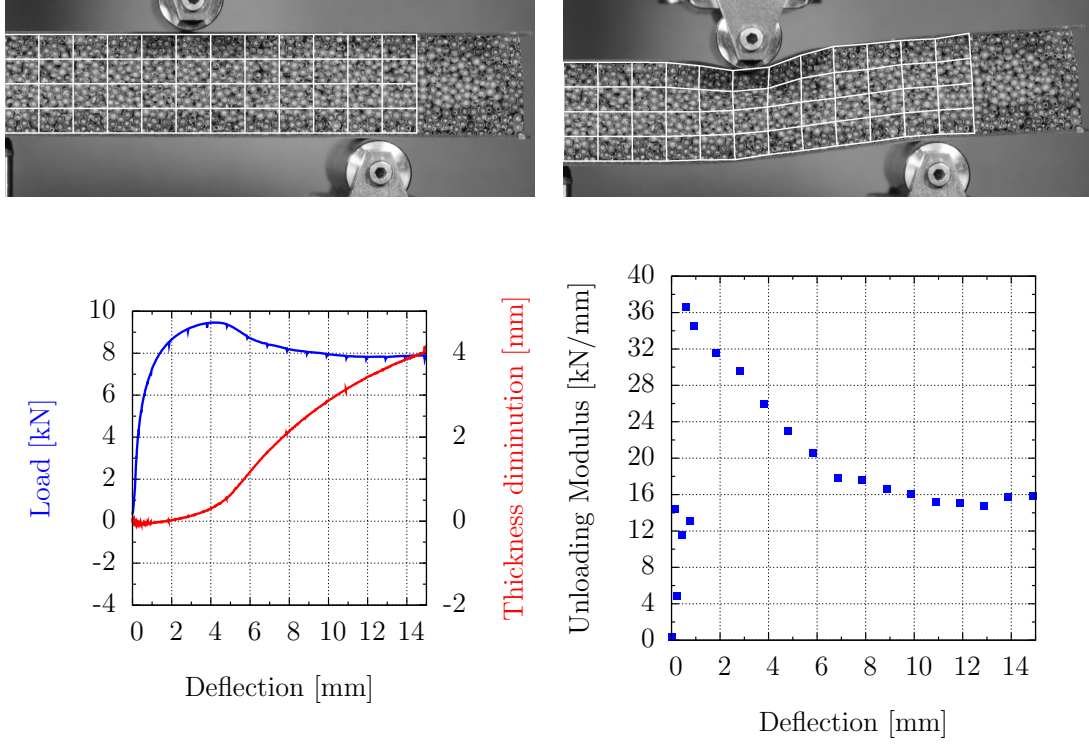


Figure 2.10: Digital image correlation of a part of a sandwich structures loaded in four points bending failing by indentation. Pictures were taken at deflection of 0mm, 2mm, 4mm, 8mm and 16mm. The grid points out the strain field within the core.

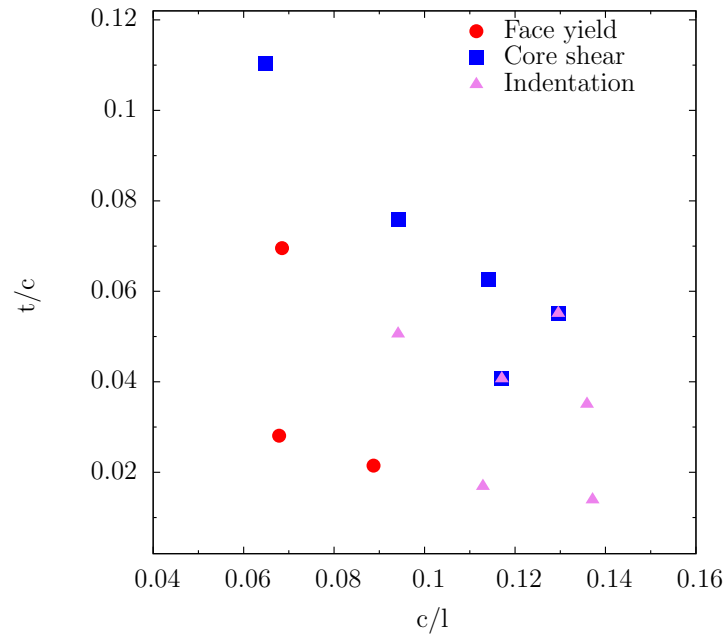


Figure 2.11: Failure map. Sandwich structures are placed in the t/c - c/l map.

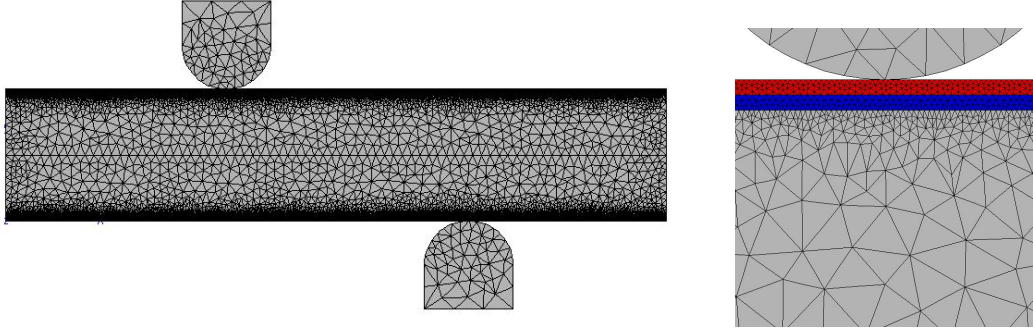


Figure 2.12: Mesh of a simulated structure. **a**-Half the structure has been simulated. **b**-A fine mesh has been applied to the faces .

meshes contained between 12,000 and 22,000 elements, between 26,000 and 42,000 nodes and had between 50,000 and 10,000 degrees of freedom.

Among all the information given by the simulations we focused on the data recorded for real experiments. Thus the motion of the center of the lower face, the motion of the moving rollers and the global reaction of the structure on the rollers were recorded.

2.4 Comparison of experiments and models

2.4.1 Description of the damaging modes

Analytical models (see 1.2.1.3), FE simulations and experiments are compared through their description of each damage mode.

2.4.1.1 Core shear

Figure 2.4.1.1 presents the evolution of the load and of the thickness parameter with the deflection of a structure failing by core shear.

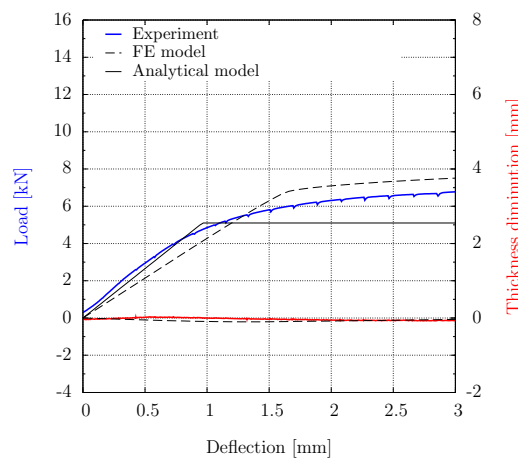


Figure 2.13: Comparison of experiments, analytical models and FE simulations of a sandwich structures loaded in four points bending failing by core shear.

The analytical model describe a damaging load that correspond to the initiation of the non linearity

on the load-deflection curve of the real experiment. FE modeling gives some more information. The thickness parameter remains almost null as it does for the experiment. The load-deflection curve is well described up to the critical load. The model does not take into account the damage of the core which is responsible for the softening of the structure.

2.4.1.2 Face yield

Figure 2.4.1.2 presents the evolution of the load and of the thickness parameter with the deflection of a structure failing by face yield. Both the analytical model and the FE simulations underestimate

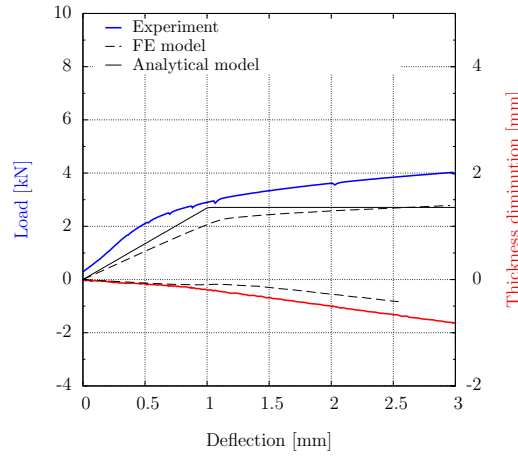


Figure 2.14: Comparison of experiments and FE simulations of a sandwich structures loaded in four points bending failing by face yield.

slightly the first loading slope. Nevertheless the analytical model predicts a damage load that correspond to the initiation of no-linearity on the load-deflection curve of experiments. The FE simulations accurately describe the damaging load. It remains that the hardening behaviour is reproduced similarly to the experiments and that the important curvature of the structure is well described by the thickness parameter.

2.4.1.3 Indentation

Figure 2.4.1.3 presents the evolution of the load and of the thickness parameter with the deflection of a structure failing by indentation. The analytical model slightly underestimates the damaging load. FE simulations perfectly describes the load evolution with deflection. The diminution of thickness is also predicted by the FE model but it initiates at larger deflection on the experiments.

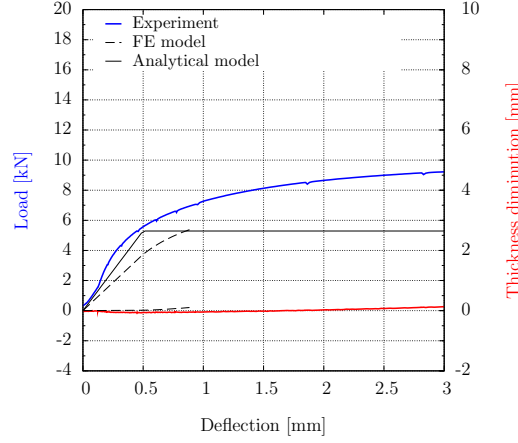


Figure 2.15: Comparison of experiments and FE simulations of a sandwich structures loaded in four points bending failing by indentation.

2.4.2 Failure map

From the above description of the failure modes, it is clear that all the failure modes can be predicted by the models. For FE simulations, their signature on the macroscopic parameters is the same as for experiments. Thus the predictions of both the FE simulations (figure 2.16a) and the analytical models (figure 2.16b) can be compared to experiments (figure 2.16c) in a failure map of the normalized structure dimensions. The axis are the ratio of the face thickness over the core thickness t/c and the ratio of the core thickness over the outer span c/L .

The global partition of the map in three areas is consistent between models and experiments. Nevertheless models predictions and experiments differ for structure close to the border between failure mechanisms. It is obvious that differences will occur on the border, moreover that the partition between failure modes is progressive. There are large portions of the map where several failure maps coexists. Thus, in addition to the determination of the failure mode, the distance between the expected one and the other failure mode can be determined by a “safety factor” determined by :

$$S_f = \frac{F_{2^{nd} failuremode} - F_{1^{st} failuremode}}{F_{1^{st} failuremode}} \quad (2.1)$$

When this safety factor is less than 20%, the accuracy of the analytical models is not sufficient to discriminate what will be the failure mode. Iso safety factor lines are plotted on figure 2.17. Since the core properties have been varied discretely with the core thickness, two maps have to be plotted (one for each core material), and then combined together. Enhanced with these iso safety factor lines, the predictions of the analytical models seems much closer to the experiments. All of the structures whose failure mode has been wrongly predicted to be core shear instead of indentation are located within the area of safety factor lower than 20%. Even if located within the area of safety factor lower than 50% , the structures that have failed by core shear show that the analytical model prediction for the damaging load associated to this failure mode is overestimated in relation to the other failure modes. The hardening of the faces, that has not been taken into account for the modeling, would make the plastic hinges to generate higher bending moments and thus would increase the critical load predicted by both the core shear and the indentation models.

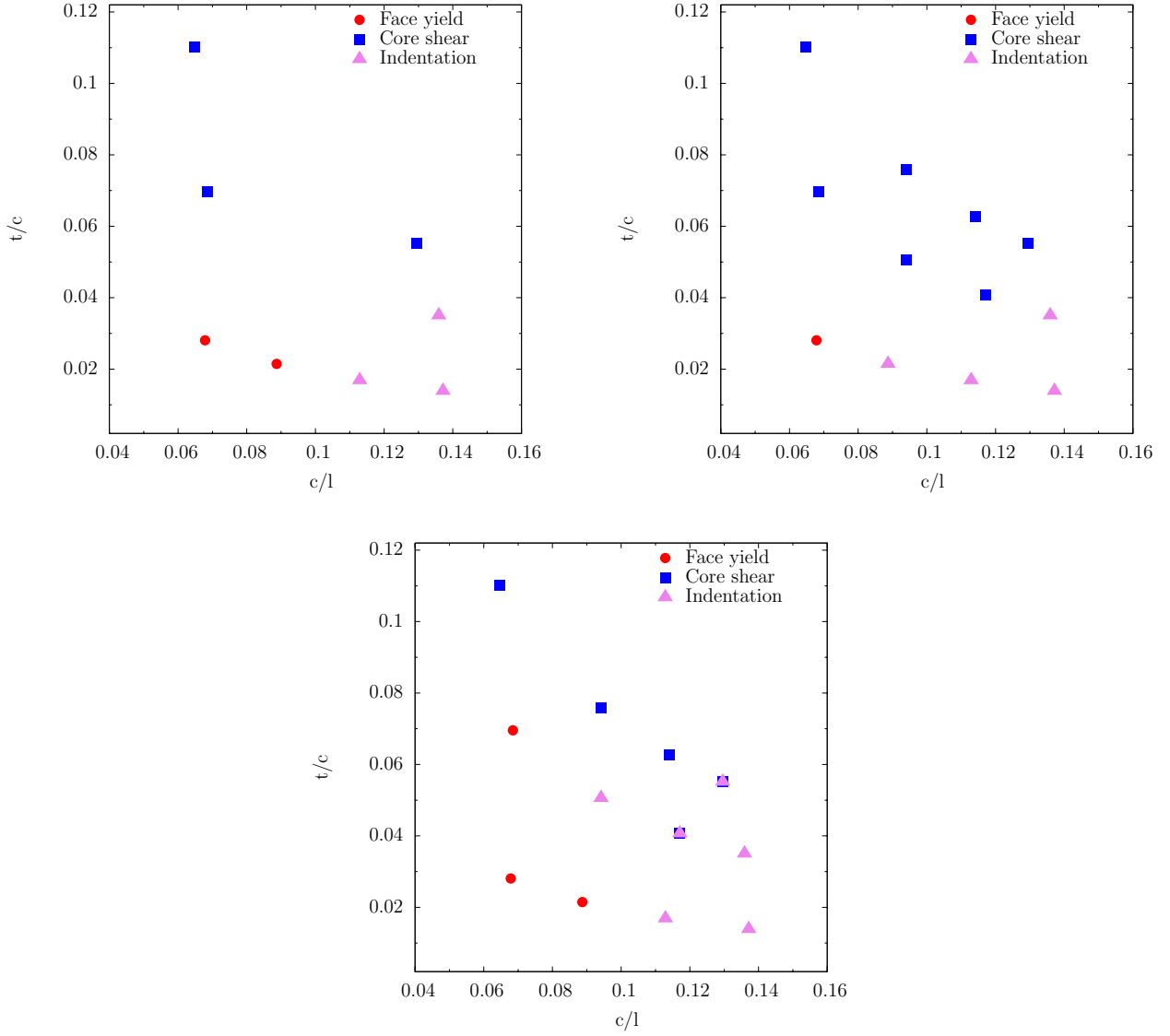


Figure 2.16: Failure maps of the normalized structure dimensions t/c and c/L for FE simulations (a), analytical models (b) and experiments (c).

So it is of interest to study the damaging load for the various models. Depending on the sandwich weight, the critical load predicted by FE models (figure 2.18a) and by analytical models (figure 2.18b) can be compared to experiments (figure 2.18c). FE simulations description of the damaging load for sandwich structures with thin face is perfectly in accordance to the experiments. For thicker faces, the predictions are also close, even if slightly overestimated, to the experiments, except for two structures of medium core thickness (about 20mm), presumably because they have been given wrongly a “strong” core material.

The analytical estimation for the indentation failure load is underestimated for thin face. It is responsible for the almost systematic prediction of this mode for the structures with thin faces. Nevertheless for thicker faces this model is not dominant. It means that the face hardening is not responsible for the wrong prediction.

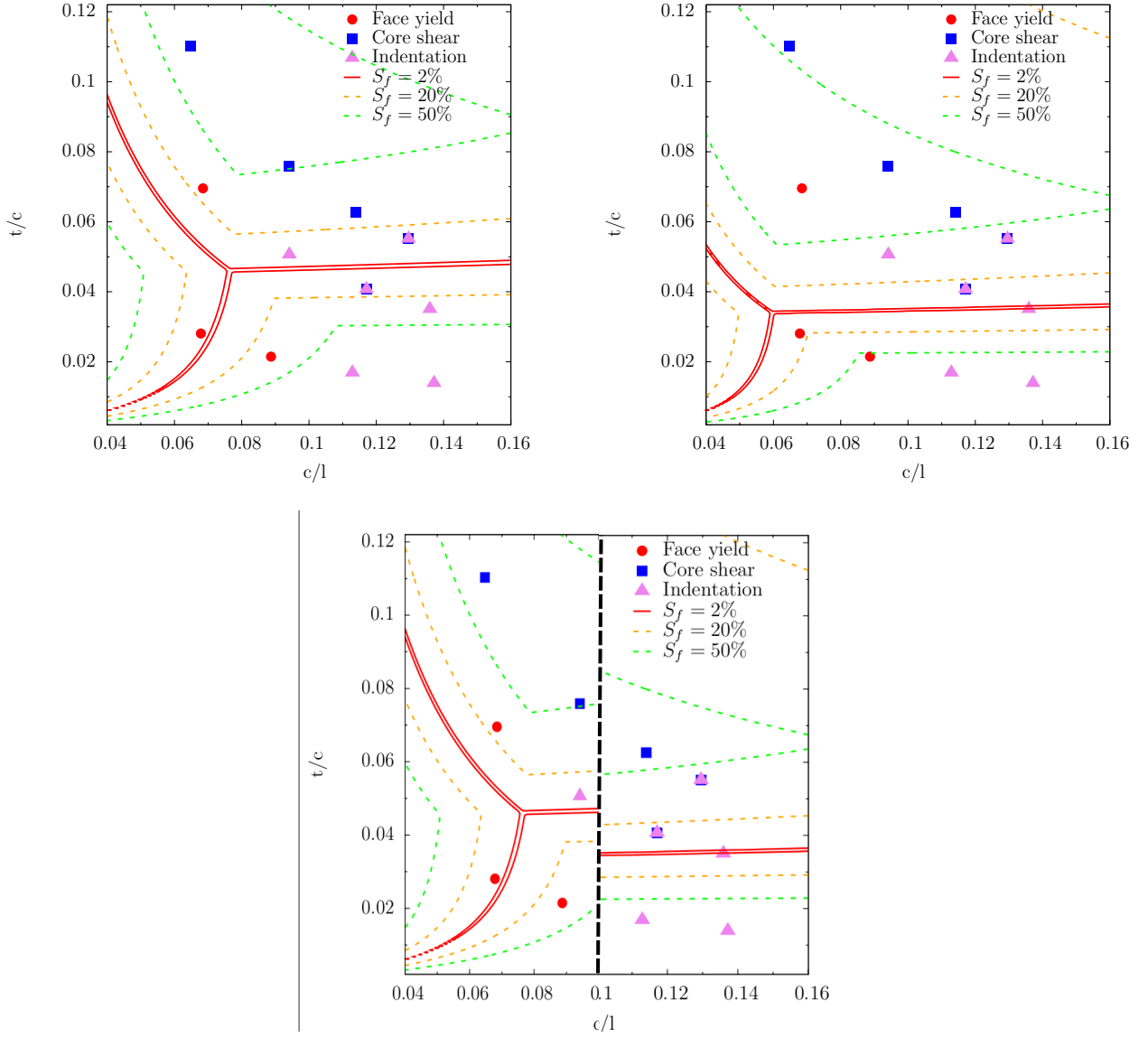


Figure 2.17: Failure maps of the normalized structure dimensions t/c and c/L for analytical models and experiments. **a**-The core is given an "high" yield stress (valid for thin cores). **b**-The core is given an "low" yield stress (valid for thick cores). **c**-Both previous map are combined in accordance to the relevant core thickness and core properties.

2.4.3 Optimal structures

2.4.3.1 Service condition

If a set of requirements address to the mechanical properties of the sandwich structures in service condition, the relevant properties to look at are the stiffness and the damaging load. Figure 2.19 presents the unloading stiffness and the damaging load, both normalized by the weight of the beam for sandwich structures with varied core and face thicknesses. The specific stiffness (ie the stiffness normalized by the weight) increases with the core thickness. For thin core, the specific stiffness is not impacted by the face thickness. For larger core thickness, the specific stiffness increases with the face thickness. The lower stiffness observed for the sandwich with thin faces and thick core can be put into relation with

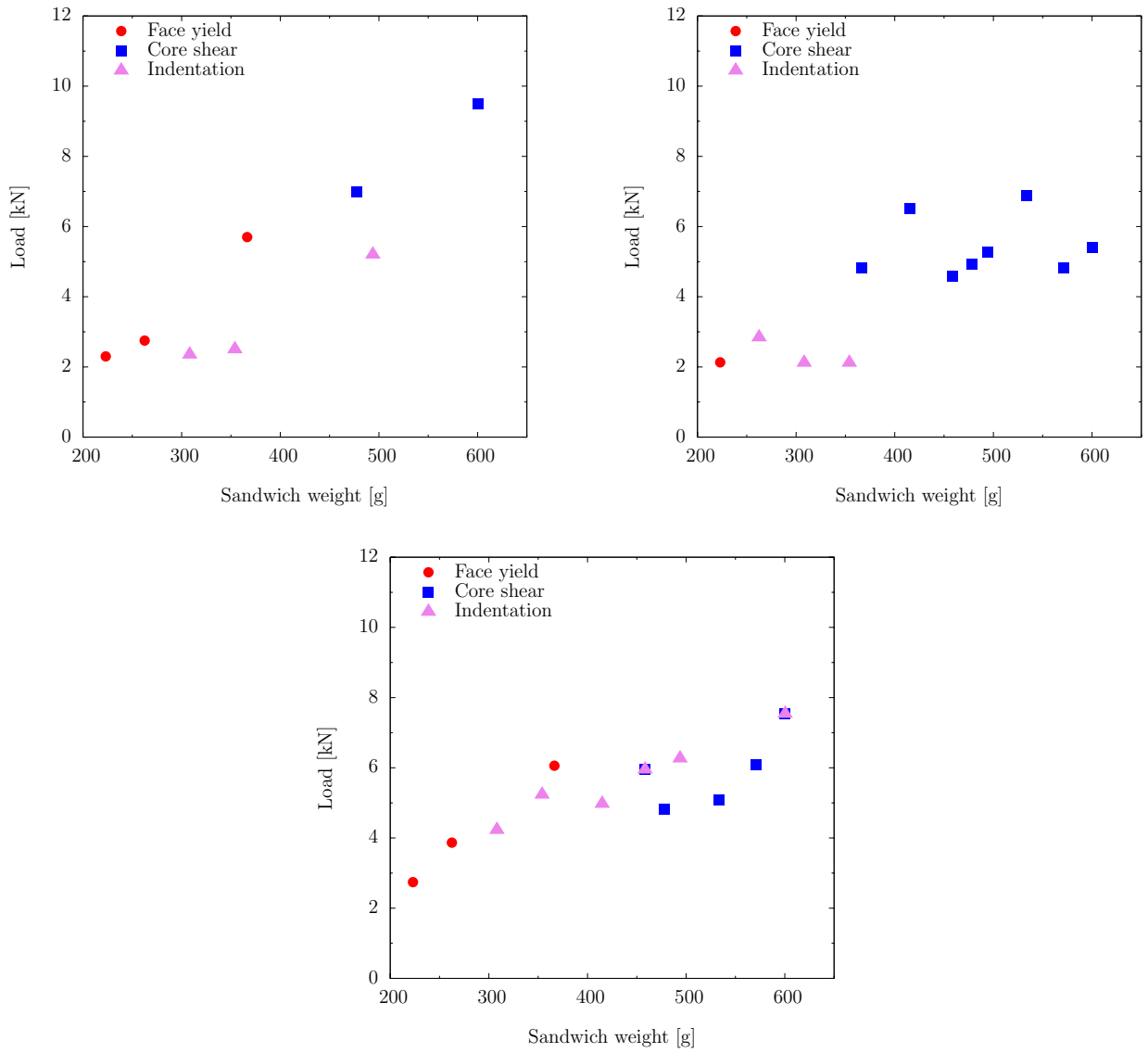


Figure 2.18: Damaging load and associated failure mode are plotted versus the weight of the sandwich beam for FE simulations (a), analytical models (b) and experiments (c).

the damaging mode of these structures. These structures are damaged by indentation, and it might be that strain localization under the rollers are responsible for this decrease.

The specific damaging load is somehow constant for the structures with thin faces. When the faces are thick, the specific damaging load increases with the core thickness.

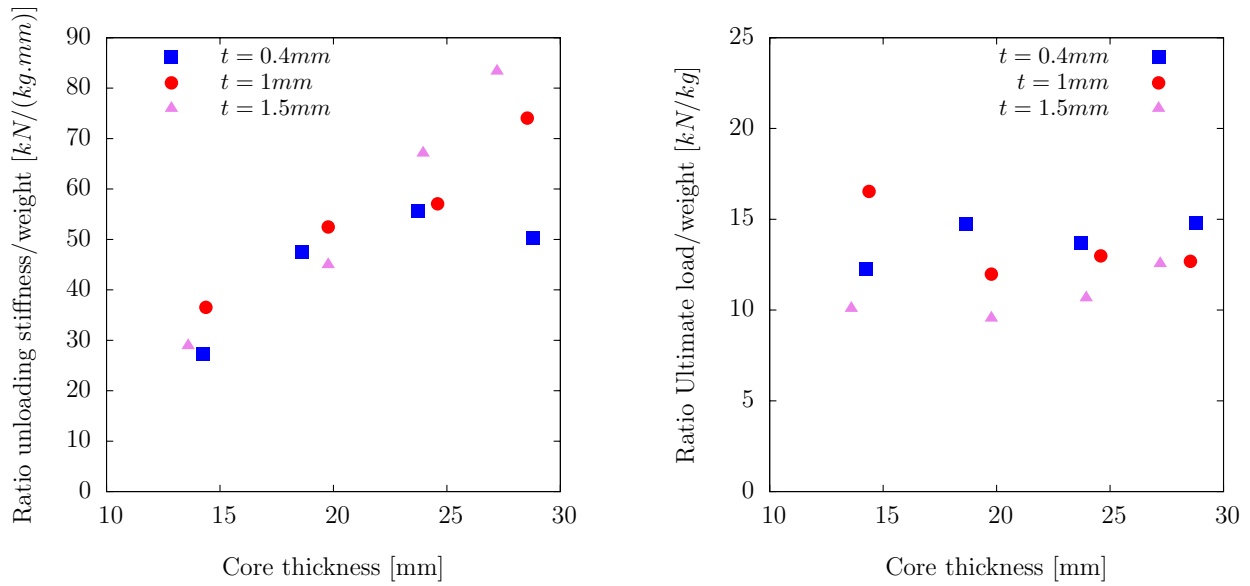


Figure 2.19: Unloading stiffness (a) and damaging load (b), both normalized by the weight of the beam for sandwich structures with varied core and face thicknesses.

When both considerations are put in regards, the design advices can be proposed as following :

- If, because of design constrains, one has to use a thin structure, the optimal specific properties have to be found on the side of thin faces. With thin faces, one obtains almost the same specific stiffness that with larger faces, but a larger specific damaging load.
- If, thick core can be used, the specific stiffness will be highly enhanced, especially if the faces are thick. The specific damaging load will remain optimal whatever the face thickness chosen. In that case, thick faces present thus a better combination of properties.

2.4.3.2 Ultimate condition

Now if the set of requirements deals with the mechanical properties of the structure under ultimate conditions, the relevant properties to look at can be the ultimate load and the energy absorbed by the structure for a prescribed deflection. Figure 2.20 presents the ultimate load and the energy absorbed for a deflection of 30 mm, both normalized by the weight of the beam for sandwich structures with varied core and face thicknesses. Sandwich structures with thin faces presents a constant specific ultimate load that is also an upper bound for the studied structures. The specific ultimate load for sandwich structures with thick faces are especially lower when the core is thin.

The specific energy absorbed by the structure for a prescribed deflection is similarly impacted by the face thickness.

Thus the thinnest face thickness is the best choice in the case of energy absorption. Nevertheless these observations are only relevant for the given indent (here a cylinder of radius 10mm). We will see in the next part that thin faces choice depends on the set of requirements.

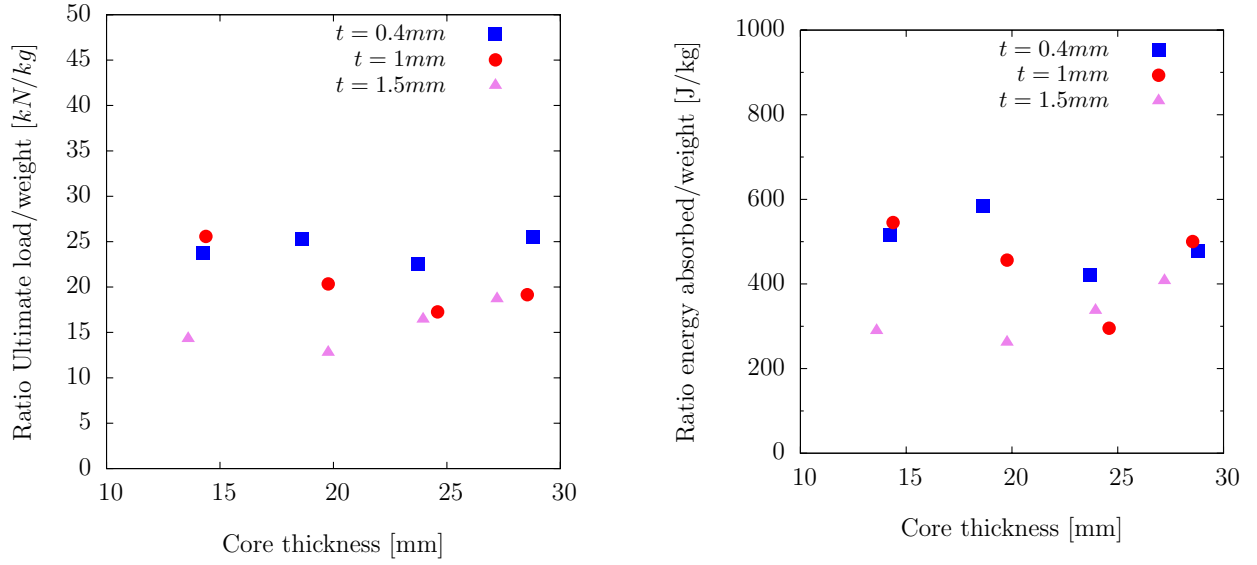


Figure 2.20: Ultimate load (a) and energy absorbed for a deflection of 30 mm (b), both normalized by the weight of the beam for sandwich structures with varied core and face thicknesses.

Summary on the behavior of sandwich structures in four-points bending

Sandwich behaviour When loaded under four-points bending, at least three failure modes can be observed : core shear, face yield and indentation. The macroscopic responses of the structure allow to determine the failure mode before it can be done by eyes. The sign of each failure mode can be found in the evolution of a thickness parameter tacking in account both the thickness of the structure and its curvature.

Models for the sandwich behaviour The macroscopic response of hollow spheres sandwich structures can be described thanks to classical analytical models. The prediction of the transition between core shear and indentation is in agreement to the experiments, provided a safety factor of 20% to the other mode is used. Nevertheless the damaging load associated to these modes is underestimated. Thus the face yield failure mode is underpredicted.

Finite Element simulations have good potential to describe both the macroscopic response and the failure mode of hollow spheres sandwich structures.

Chapter 3

Behavior under indentation loading

Contents

3.1	Experiments	197
3.2	Load-indentation responses	197
3.2.1	Results	197
3.2.2	Transition between plate and membrane behaviour	198
3.2.3	Elastic membrane behaviour	199
3.2.4	Perfectly plastic membrane behaviour	199
3.2.5	Indent size effect	200
3.2.6	Core size effect	201
3.3	Energy absorbed	203

3.1 Experiments

Sandwich plates presented in IV were cut in squares of 250 mm side size. A grid has been drawn on the upper face of the plate previous to the experiments in order to determine the strain of the face. Plates were loaded first by a spherical indent of diameter size of 30 mm in the middle of the plate up to a load of $19kN$. This load is just below the load sensor capacity ($20kN$). Loading has been performed with a constant velocity of the indent of $0.05mm/s$. The reaction on the indent and the motion were recorded. Then the apparent damage area have been measured thanks to the use of talk powder and a rule. It has been defined as the area where sandwich thickness has decreased. Then, since the plates were large enough, another indent test have been performed but with an indent diameter of $16mm$. Figure 3.1 shows a plate in testing configuration.

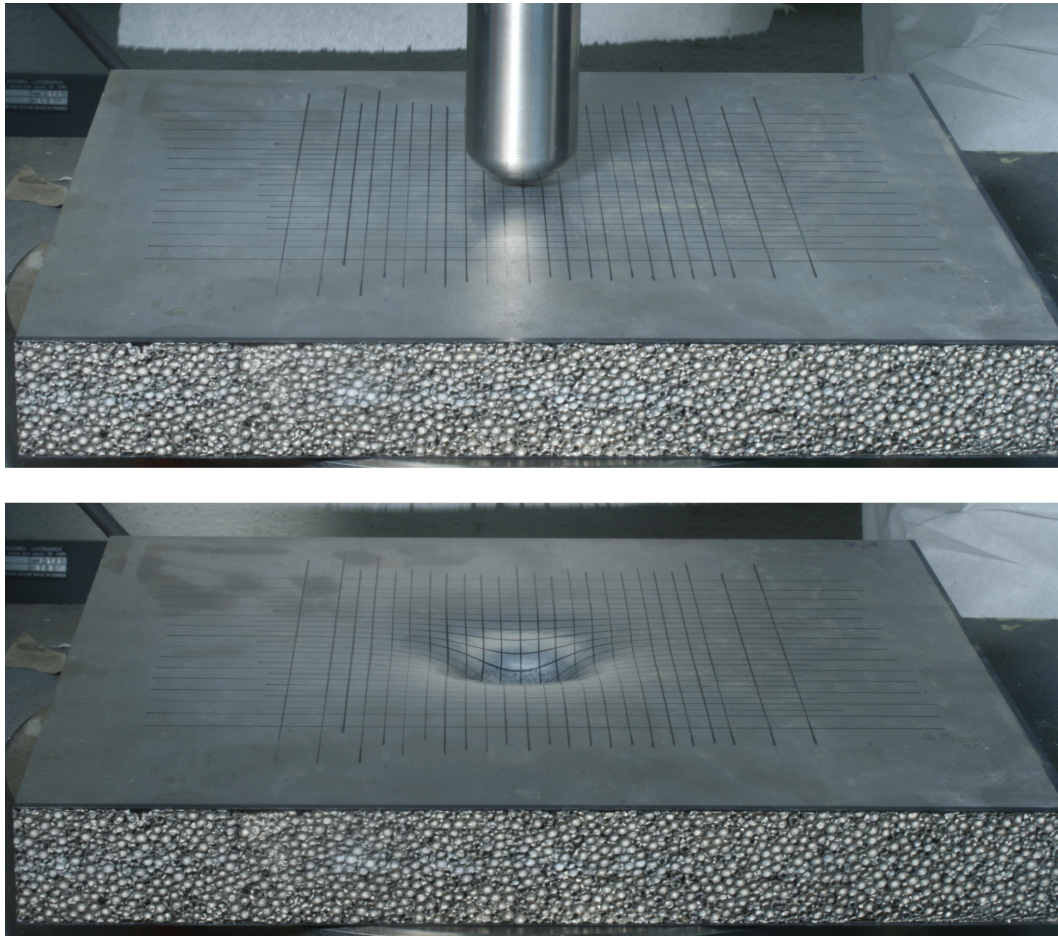


Figure 3.1: Sandwich plate just after an indent test. The indent has a diameter of 30mm.

3.2 Load-indentation responses

3.2.1 Results

Figure 3.2 presents the load-indentation curves for various core thicknesses and various face thicknesses. The common sense would make the load at given indentation depth increasing with the face thickness. It is in agreement with the experiments when the core is thick. Nevertheless, when the core is thin ($14mm$)

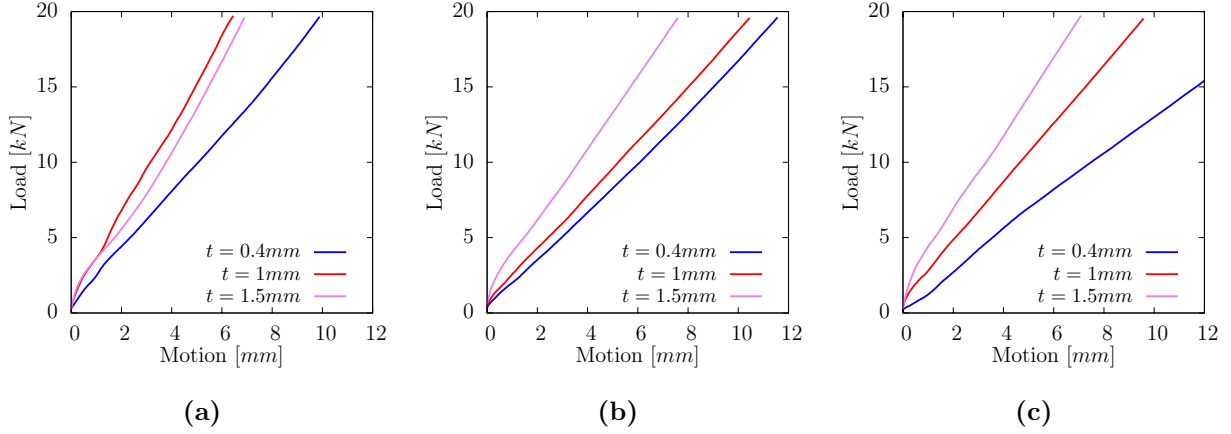


Figure 3.2: Load-indentation curves for varied core thicknesses and face thicknesses. Core thicknesses are respectively of 14 mm (a), of 24 mm (b) and of 28 mm (c).

this trend is not anymore observed.

3.2.2 Transition between plate and membrane behaviour

The load-indentation curves are almost linear for large indentation depth. Nevertheless one can see that the first stages of indentation are not so. The transition between the the deformation of an elastic plate resting on a elastic foundation and an elastic plate resting on a plastic foundation occurs for indentation depths of ε_y^c ([Fatt and Park, 2001]). This transition occurs for indentation depth lower than 0.1 mm in our case. Thus it cannot be observed with the present experimental set. The second transition between two deformation mechanisms (plate on a plastic foundation and membrane on a plastic foundation) is quantified (figure 3.3). The indentation depth that corresponds to the transition

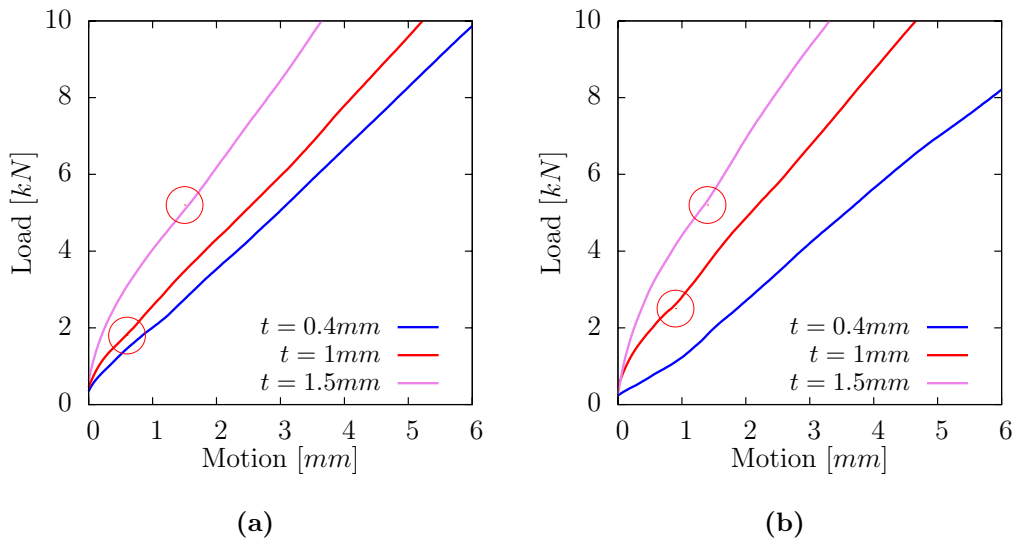


Figure 3.3: Transition between the plate and the membrane behaviour for sandwich thickness of respectively 24 mm (a) and 28 mm (b) for varied face thicknesses.

is of the order of size of the face thickness. It is in accordance to the observations of [Fatt and Park,

2001]. Since we will focus on large deflection, the face can be modeled by a membrane.

3.2.3 Elastic membrane behaviour

First the membrane is assumed as elastic. The model proposed by [Türk and Fatt, 1999] is compared to the experiments load-indentation curves in figure 3.4. The model overestimates largely the load-

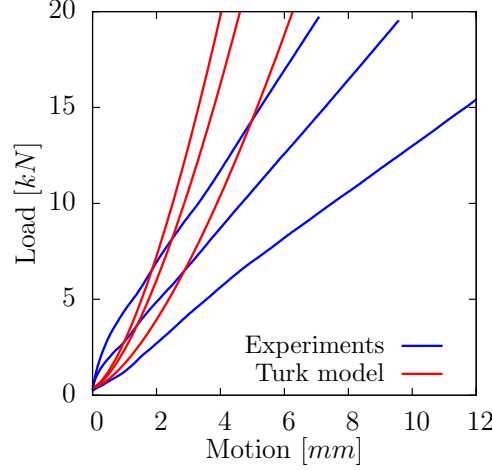


Figure 3.4: Comparison of the modeling of an elastic membrane resting on a rigid-plastic foundation [Türk and Fatt, 1999] and the experiments for a sandwich thickness of 28 mm and for varied face thickness.

indentation curve for large indentation. The assumption of an elastic membrane is responsible of that.

3.2.4 Perfectly plastic membrane behaviour

The size of the final indented area¹⁵ is plotted versus the final deflection¹⁶ in figure 3.5. No significant

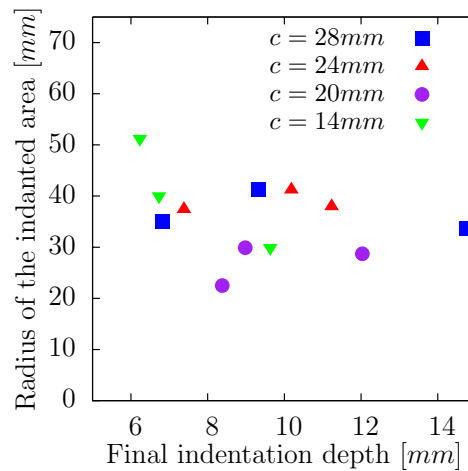


Figure 3.5: Radius of the final indented area as a function of the final deflection for sandwich structures with varied face and core thicknesses.

¹⁵The area where the upper face moved vertically of a few tenth of millimeters

¹⁶The final deflection is the deflection that correspond to an indentation load of 20 kN.

variation of the size the indented area can be observed. The radius of this area is roughly of 35 mm. Another way to describe the behaviour of the indented sandwich is to consider separately the core crushing and the face indentation. The model of indentation of a clamped membrane proposed by [Simonsen and Lauridsen, 2000] is applied to the tested structures (figure 3.6) with a given clamping radius of 35 mm. The model assumes a perfectly plastic behaviour for the membrane and it also does

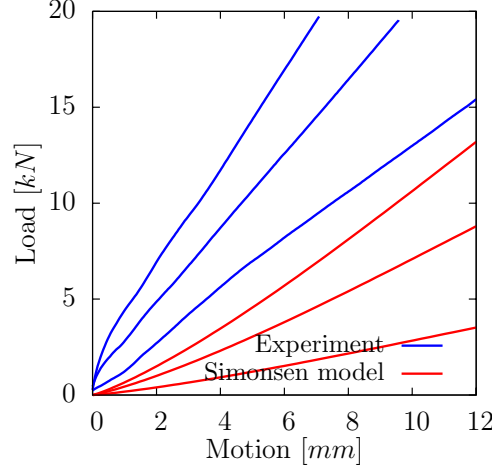


Figure 3.6: Comparison of the modeling of an perfectly-plastic membrane clamped on a circle of 35mm of radius [Simonsen and Lauridsen, 2000] and the experiments for a sandwich thickness of 28 mm and for varied face thickness.

not take into account for the core material contribution. It is thus not surprising that it underestimates the loads.

The contribution P_{core} of the core to the indentation load can be modeled by a perfectly plastic cylinder of yield stress σ_y^c of radius the radius R of the indent loaded in compression (equation 3.1).

$$P_{core} = \pi R^2 \sigma_y^c \quad (3.1)$$

The hardening of the face is taken into account by correction on the yield stress σ_y^f assuming a new yield stress σ_y^{f*} (equation 3.2) as proposed by [Simonsen and Lauridsen, 2000].

$$\sigma_y^{f*} = \frac{\sigma_y^f + \sigma_u^f}{2} \quad (3.2)$$

With the contribution of the core, which is responsible for the initial offset, and with the mean equivalent yield stress, the experiments are better described at large indentation depth (figure 3.7).

There are models that properly account for the hardening of the face but they imply a numerical resolution. In the case computations are required, it would be more relevant to model the indentation test thanks to Finite Elements. The coupling between the face and the core would be in that case fully taken into account.

3.2.5 Indent size effect

Up to now, we have only considered the indentation of the plates with a spherical indent of radius 15 mm. Tests have also been performed with a spherical indent of radius 8 mm. Figure 3.8 presents

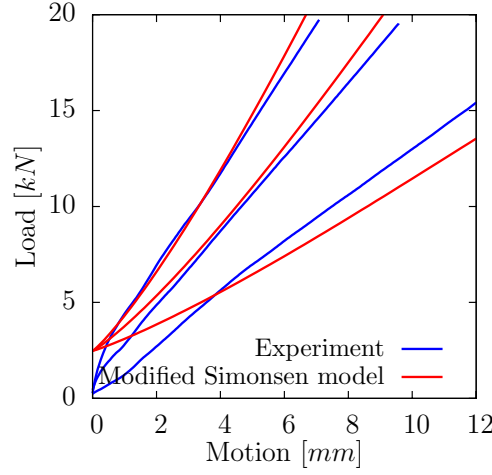


Figure 3.7: Comparison of the modeling of an perfectly-plastic membrane with modified yield stress clamped on a circle of 35mm of radius [Simonsen and Lauridsen, 2000] with contribution of the core and the experiments for a sandwich thickness of 28 mm and for varied face thickness.

pictures of the indented area for both the large and the small indenter. A grid had been drawn on the faces before the indentation loading. Tests have been performed up to a load of 19kN except for the sandwich plates that failed by perforation. Actually, in the later case, the load drop down as soon as the face tears. Figure 3.9 shows the influence of the indent size on the load-motion curves for two sandwich structures with varied face thickness (and same core thickness of 28 mm). [Simonsen and Lauridsen, 2000] proposed an empirical law for the indentation failure of a strain hardening membrane clamped on a circle. The depth of indentation at failure is given by :

$$\delta_f = 1.41n^{0.33}R_b^{0.48}R^{0.52} \quad (3.3)$$

The model explicitly accounts for the indent radius, and it predicts that the larger is the indent the larger is the indentation depth required for the failure of the face. Nevertheless the model cannot describe accurately the depth of indentation at failure of the face for the whole set of tested structures.

3.2.6 Core size effect

First observations on the load-indentation curves have shown that the core thickness impacts the indentation response. Figure 3.11 presents load-indentation curves for structures with faces of respectively 0.4, 1 and 1.5 mm with varied core thicknesses. For thin faces, the thicker the core the lower is the indentation load for a given indentation depth. The core thickness has a large impact on the indentation response in that case. But when the face is thick, the core thickness do not impact at all the load-indentation curve.

The indentation of two structures with a face thickness of 1 mm and with core thicknesses of respectively 14 mm and 28 mm have been simulated by FE. The core has been assumed to follow the same law that for bending loading simulations, if not that within a first time the two structures are given

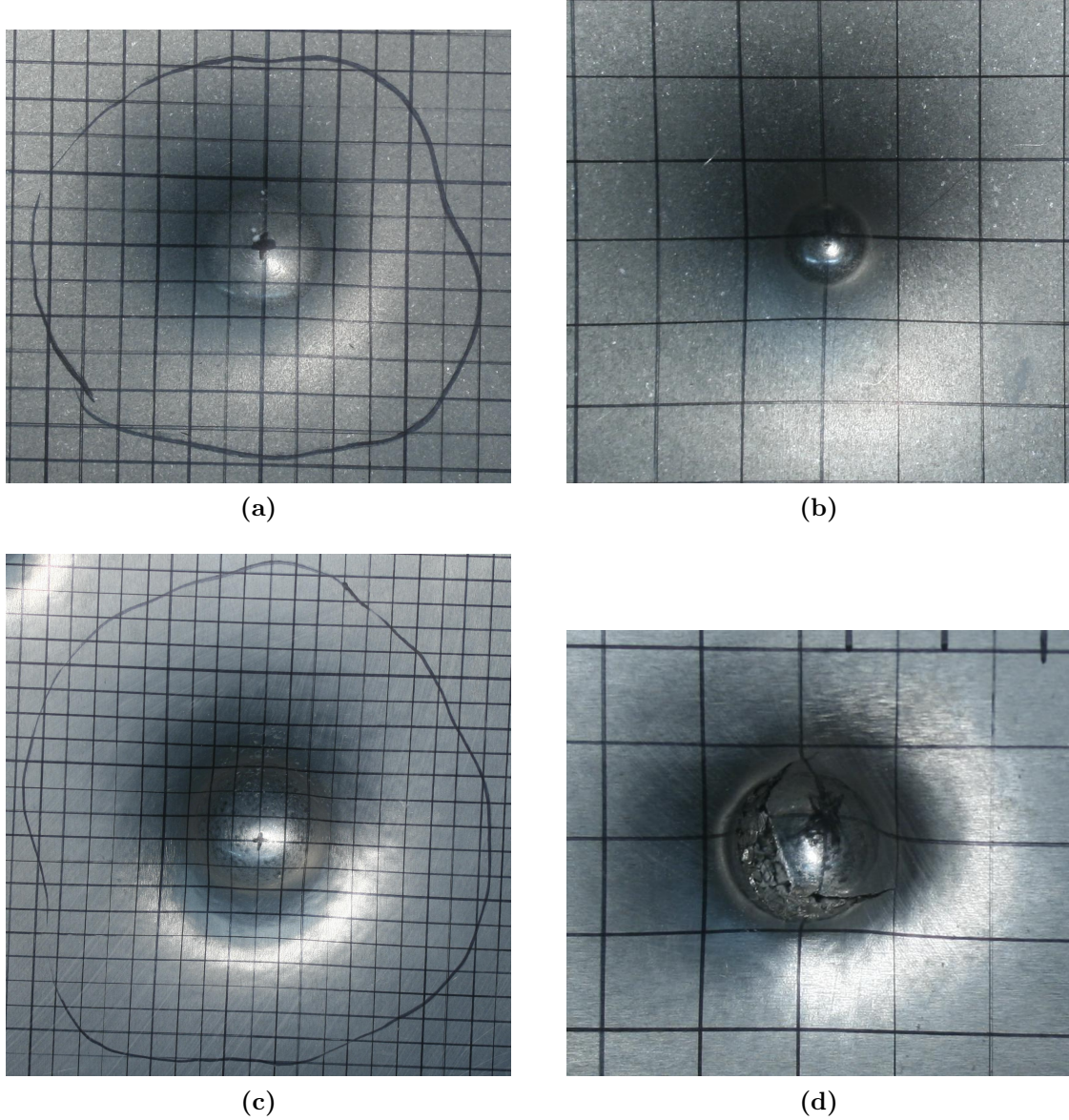


Figure 3.8: *Indent prints for two face thicknesses t and two indenter size (radius a). **a**- $t = 1\text{mm}$, $a = 15\text{mm}$. **b**- $t = 1\text{mm}$, $a = 8\text{mm}$. **c**- $t = 0.4\text{mm}$, $a = 15\text{mm}$. **d**- $t = 0.4\text{mm}$, $a = 8\text{mm}$. The latter structure is perforated by the indenter. The face failed by excessive tensile strain. The grid is not consistent between the various plates.*

the same core properties¹⁷. Figure 3.12a presents the load-indentation curves for the two structures. The responses are not impacted by the core thickness. Thus the variation of core material properties must be responsible for this “core thickness effect”. Figure 3.12a presents the load-indentation curves for two identical structures if not for the properties of the core material that can be either “soft” or “hard” (as described in part 1.2.3). The load-indentation curve is impacted by this change. When these simulations are compared to the experiments (figure 3.13) a good correlation is observed. There is an initial offset but the slope of the curves are very similar. This offset might be due to face yield stress which was kept at 185MPa. The “core thickness effect” is completely captured by this model. Thus the

¹⁷In part 1.2.3, we assumed that the properties of the core are not independent of the core thickness, and that depending on the core thickness the core was given a “hard” behaviour ($c < 20$) or a “soft” behaviour ($c > 20$).

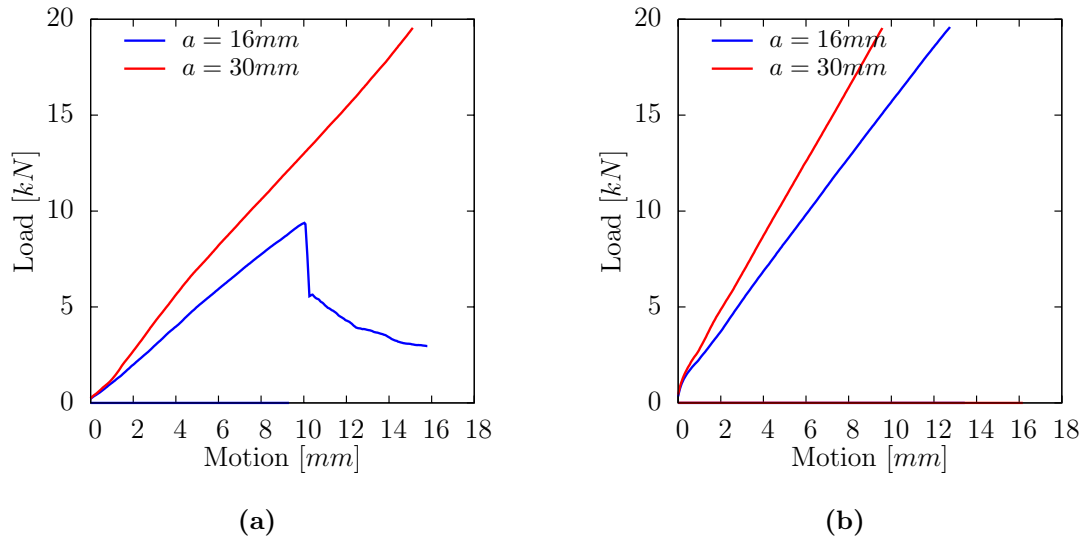


Figure 3.9: Load versus motion for two sandwich structures and for two indent sizes. **a-** Sandwich structure with face of 1 mm thickness. The indent prints are similar with both indent sizes. The larger the indent the smaller is the motion required to reach the maximal load. **b-** Sandwich structure with face thickness of 0.4 mm. With the small indent, the face fails by tearing, and thus the structure is perforated. The maximal load is never reached.

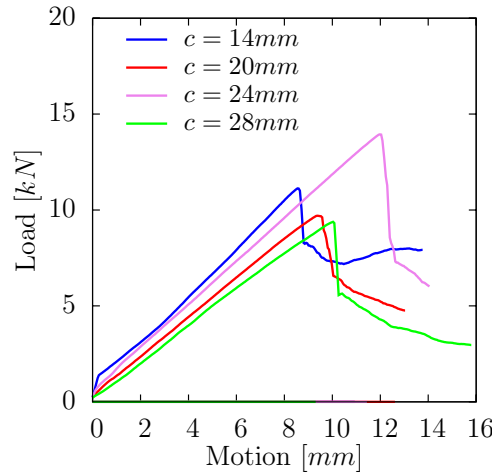


Figure 3.10: Load-indentation curves for sandwich structures with a face thickness of 0.4mm loaded with an indent of radius of 8mm. The fall down of the curves correspond to the perforation of the face.

observed effect of the core thickness is in fact an effect of the core material properties.

3.3 Energy absorbed

The energy absorbed by each structure for a load of 19kN have been measured. Figure 3.14 presents this energy for all the sandwich structure tested for both indent sizes. For a large indent, thin faces are optimal to absorbed at given load. But when the indent is smaller, theses later faces fails by tearing and the structure is perforated, leading to a low absorbed energy. For all other structure, the smaller

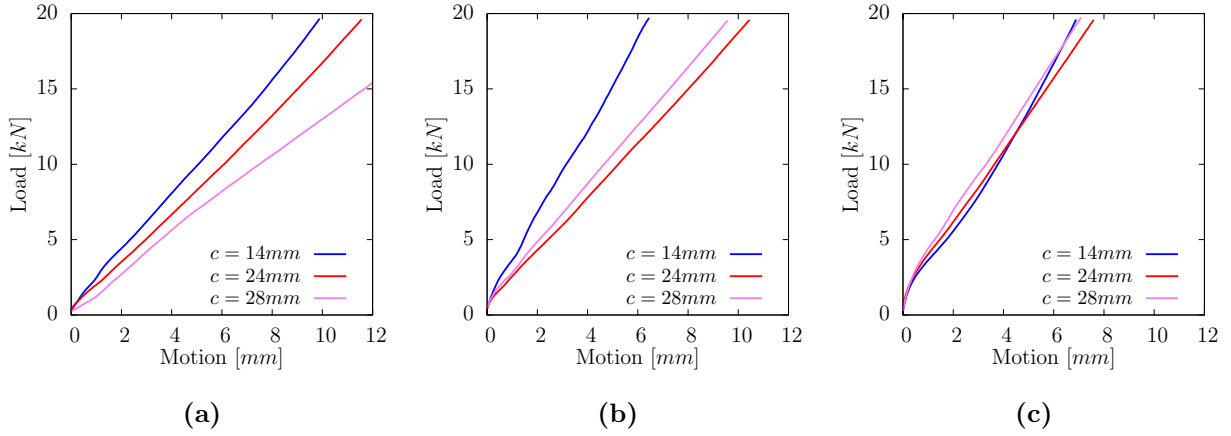


Figure 3.11: Load-indentation curves for varied core thicknesses and face thicknesses. Face thicknesses are respectively of 0.4 mm (a), of 1 mm (b) and of 1.5 mm (c).

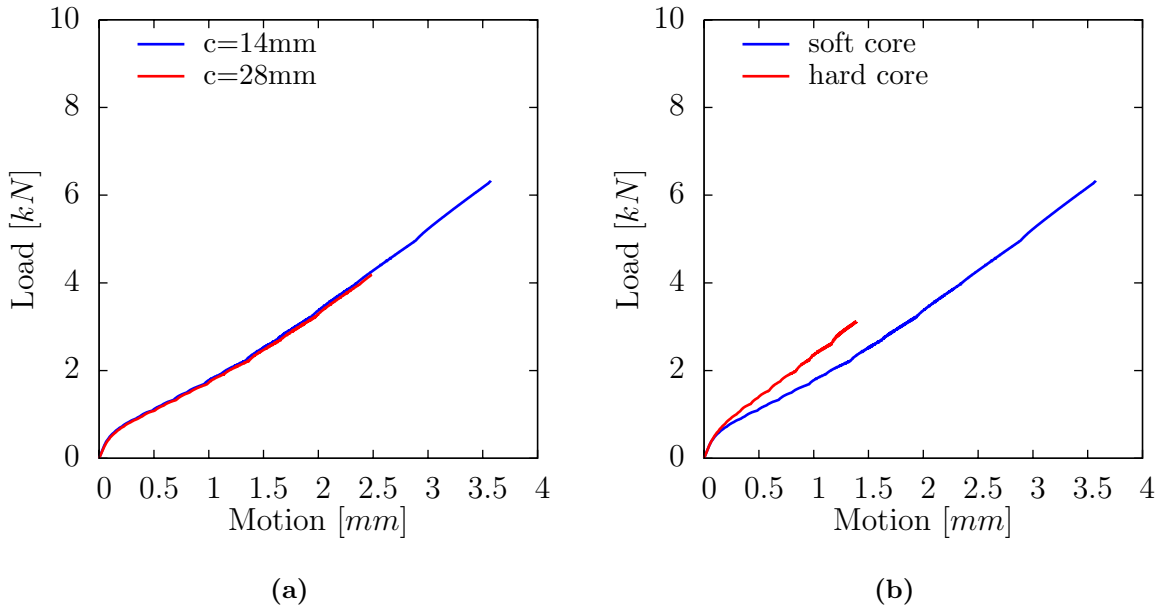


Figure 3.12: a-Load-indentation curves of FE models for two identical structures if not for the core thickness that is respectively of 14 mm and 28 mm. b-Load-indentation curves of FE models for two identical structures if not for the core material that is either hard or soft.

is the indent the larger is the energy absorbed at given load. The core thickness has various influences depending on the face thickness. For thin faces, the thicker is the core, the more energy is absorbed. But when faces are too thick (1.5mm), there is no longer benefit to have a thick core. Thus depending on the set of requirements, and especially of the size of the impactor, the thin faces are the best choice or they fail by perforation.

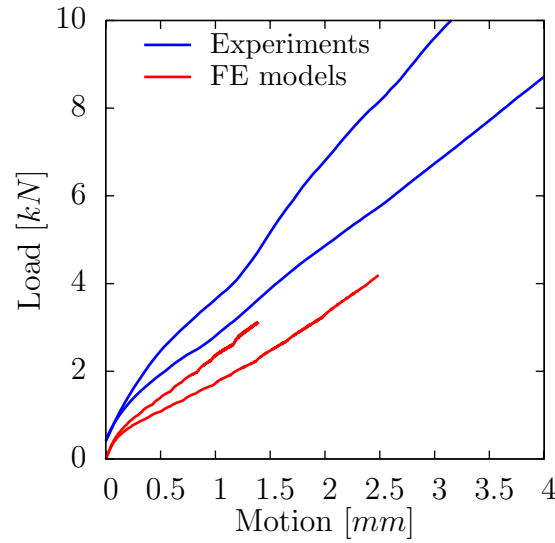


Figure 3.13: Comparison of the load-indentation curves for FE models and for experiments for two structures with faces of thickness 1 mm of core thickness of respectively 14 mm and 28 mm.

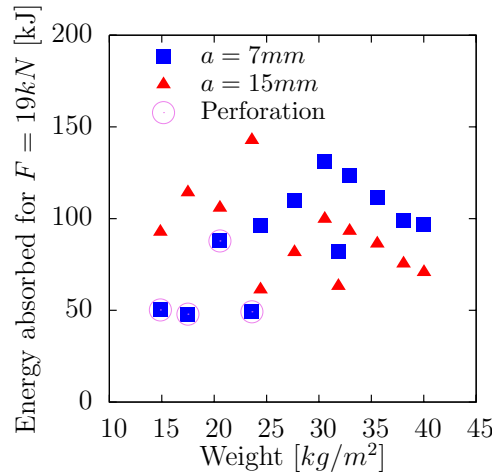


Figure 3.14: Energy absorbed for a load of 19 kN among the surfacic weight of the structures. Energies for both indent sizes are presented. Marks of sandwich structures that failed by perforation are circled.

3.4 Summary on the behavior of sandwich structures under indentation loading

Indentation of sandwich structures with hollow spheres foam core is mainly controlled by the membrane effect of the face. Decoupled models of the face and the core behaviour under indentation can almost describe the load-indentation curve. Such models can also capture the influence of the indent size, nevertheless their are not discriminant enough in regards to the experiments to predict accurately the perforation of the upper face.

Summary on sandwich structures

The potential applications of hollow spheres stackings have been studied in the case of sandwich structures. First, hollow spheres stackings, as a core material, have been characterized. Then sandwich structures with hollow spheres foam core have been loaded both in four-points bending and in indentation loading.

Hollow spheres in sandwich structures

The integration of hollow spheres stackings into sandwich structures induces changes of the material. Micro-structure and meso-structure are affected as well as the mechanical macroscopic behaviour.

Microscopic scale The heat treatment lead to an evolution of the microstructure. The porosity is highly decreased, as well as the roughness of the surfaces. The shell seems to become less ductile.

Mesosopic scale Diffusion of the constitutive material modifies the neck shape. It becomes soft. During the process of implementation in the structure the spheres have been damaged. The thicker is the core, the larger seems to be this effect.

Macroscopic scale The mechanical behaviour changes with the process.

Four-points bending loading

Sandwich behaviour When loaded under four-points bending, at least three failure modes can be observed : core shear, face yield and indentation. The macroscopic responses of the structure allow to determine the failure mode before it can be done by eyes. The sign of each failure mode can be found in the evolution of a thickness parameter taking in account both the thickness of the structure and its curvature.

Models for the sandwich behaviour The macroscopic response of hollow spheres sandwich structures can be described thanks to classical analytical models. The prediction of the transition between core shear and indentation is in agreement to the experiments, provided a safety factor of 20% to the other mode is used. Nevertheless the damaging load associated to theses modes is underestimated. Thus the face yield failure mode is underpredicted.

Finite Element simulations have good potential to describe both the macroscopic response and the

failure mode of hollow spheres sandwich structures.

Indentation loading

Indentation of sandwich structures with hollow spheres foam core is mainly controlled by the membrane effect of the face. Decoupled models of the face and the core behaviour under indentation can almost describe the load-indentation curve. Such models can also capture the influence of the indent size, nevertheless their are not discriminant enough in regards to the experiments to predict accurately the perforation of the upper face.

Conclusions and perspectives

Conclusions

Aim and strategy

The aim of this PhD was to characterize the mechanical behaviour of hollow spheres stackings, and to validate models describing their behaviour, in order to be able to predict the mechanical properties of structures with a hollow spheres foam core. The problem has been tackled, with increasing dimensional scales, with a combination of experiments, observations and modeling.

The characterization of the material structure, thanks to image analysis techniques both in 2 dimensions and in 3 dimensions, gave the required information to model the contact law between two spheres. Then these laws have been implemented in a Discrete Element Code in order to model stackings. The mechanical behaviour of hollow spheres stackings has been studied for the main classes of loading (except shearing). Both Discrete Element Method models and analytical models have been calibrated to ensure a good description of the material behaviour. Within the same time, an investigation of the material with in situ X-ray tomography tests, allowed to understand the relation between the local deformation mechanisms and the macroscopic behaviour.

Then sandwich structures with hollow sphere foam core have been loaded both in four-point bending and in indentation. The structures have been modeled both with Finite Elements and with analytical models, and the constitutive law of the core have been varied.

Main results

Hollow spheres stackings

- The hollow spheres stackings structure have been fully characterized from the scale of the roughness and porosity of the shells up to the scale of a Representative Volume Element for the initial density.
- The behaviour of hollow spheres stackings has been studied for uni-axial tensile and compressive loading and for multi-axial compressive loading. The large number of tests performed with varied foam initial density and with varied sample size constitutes a reliable database for the description of the hollow spheres stackings.
 - For uni-axial compression loading, both the stress-strain curves and the unloading modulus evolution with strain are well described for low strains thanks to the combination of observations of the shell and neck microstructure, with Discrete Element Method modeling. Large strain behaviour is captured thanks to a phenomenological model that rely on mesoscopic observations with x-ray tomography coupled with 3D image analysis.
 - For uni-axial tensile loading, microscopic and mesoscopic mechanisms responsible for the macroscopic behaviour have been identified up to large strains. The DEM that does not take into account the damaging of the constitutive material cannot capture them. The improvements required for a better description of the tensile behaviour with this model have been pointed out.
 - Two techniques have been used for multi-axial compressive tests. Due to scatter between experiments it is difficult to conclude with certainty if the surface of the criterion is elliptical

or linear. The shape of the yield surface can somehow be described by DEM provided the shear contact law between spheres is softened. Nevertheless more experiments are required to decrease the scatter on the results and allow to select a relevant yield criterion.

Sandwich structures

- The evolution of the structure with the process of integration in sandwich structures have been qualified. This process of implementation into a structure modify considerably the hollow spheres stackings structure.
- Sandwich structures with hollow spheres foam core with a range of core thickness and face thickness have been tested both as beams loaded in four-points bending and as plates loaded in indentation.
 - A failure map of the structure dimensions have been obtained for bending tests. FE models described the same partition between the failure modes. Analytical models can also describe it but with a lower accuracy. Indentation modeling is especially responsible for this.
 - The data required for the optimization of a sandwich structure both in service condition and in case of energy absorption requirements have been obtained from the bending tests.
 - The load-indentation curve of a sandwich plate can be somehow described by a plastic membrane model with a decoupled contribution of the core on the load. The model captures the influence of the shell thickness, the core thickness and the indenter size, but it does not describe accurately the failure. FE modeling gives good results provided that face material properties are well known.

Perspectives

The observations and experiments performed during this PhD allow us to suggest various follow up to this study, which can be achieved either at short term, or at longer term.

Short term follow up

Improvement of the Discrete Element Method applied to hollow spheres stackings

The key point to improve the description of hollow spheres stackings with DEM is contained in the contact laws. These contact laws must capture the damaging of the constitutive material with strain. The use of either a model for the material that account for damage, or particular elements (such as cohesive elements), for the Finite Element modeling of the contact between two spheres, should allow that. Micro-tomography observations of the necks would give information for a better description of the neck shape and especially for the real contact area. If one can access to the processing of the spheres, loadings of real necks would be of great interest to quantify the ratio of the stiffness for the various loading. These experiments would be hard to perform without a processing device since the machining required to isolate two spheres would undoubtedly damage them.

Another technique would consist in a calibration of the contacts laws by correlation with tomography in-situ tests. Since the connection between tomography observations and DEM already exists, it would

“only” remains to implement an optimization routine in the DEM code.

The definition, “a priori” of a threshold, depending on the neck size and the shell thickness, for the failure of the connection between two spheres is also of potential interest. It has the advantage to keep unchanged, if not for the failure criterion, the contact laws. It “only” requires to connect appropriately some routines of the DEM code, since this behaviour already exist for other types of particles.

Description of the mechanical properties

Several simple tests would allow a better description of the mechanical behaviour of hollow spheres stackings.

- Tests for several loading on the hollow spheres stackings after is as been integrated into a sandwich structure would allow to better understand the influence of the various structural parameter.
- Multiaxial compressive tests on larger samples, with imposed pressure boundaries conditions, would improve the description of the yield surface. The evolution of the yield surface for large strains will be of interest to model the indentation behaviour of structures with such a core.
- High strain rates compressive tests would give more information on the potential interest of the material as core for protecting structures.

Sandwich structures

- FE simulations of indentation with varied yield criteria for the core would quantify its impact on the structure reaction. The coupling between face and core, as well as the core thickness influence would be clarified.
- High-velocity impact tests would experiment the ability of such structures to be used as shield as the plane radom act for birds impact.
- The study of the initial scratching mechanism would help to select the face material during design stages.

Long term follow up

Material structure modification

The variation of the structure of hollow spheres stackings should be achieved with various aims.

The generation of stackings with small necks (and thus with a large open porosity) could increase the densification strain of the material. But if the strength level has to be improved, multi-modal stackings or stackings with hollow ellipsoids might be of interest.

In order to improve the acoustic absorption properties of the material, one might try to generate holes through the shells.

Sandwich structures

Still concerned with the concept of sandwich structure three main directions are suggested.

- Sandwich structures with hollow spheres stackings processed “all in one”, if possible, could solve some of the problems encountered in this PhD. First it would not require any machining of the stacking before it is implemented in the structure, and would reduce the number of thermal treatments. Next, the increased contact area between the stacking and the faces, thank to the compaction stage, might allow to decrease the intensity of brazing thermal treatment. It could allow to obtain a structure with more controlled mechanical properties. The process could be applied to curvated structures. Sandwich structures with corrugated faces could thus easily be obtained.
- Sandwich structures with grid faces might allow to combine both the acoustic properties of hollow spheres stackings by connecting its open porosity to the outer space, and the mechanical properties of a sandwich structure.
- Generation of structures with one more intermediate scale of architecture could be achieved to tackle problems such as shaping or assembly. An example of such core architecturing is described in appendix D.

Appendices

Appendix A

Experimental techniques

A.1 Digital image correlation

The 2D image correlation technique was developed in order to obtain strain fields on the sample scanned. It is based on the tracking of patterns on gray level images through the assumption of a rigid translation motion. The tracking of patterns is itself based on image intensity correlation.

In order to limit the problem of “uncontrollable” patterns, a selection of the most textured patterns is first operated, and after the calculation of the motion of these patterns, an interpolation is operated on an initially regular grid (which obviously is deformed during the test). A sub pixel motion correlation is also used thanks to image inter pixels interpolation.

All the previously cited points will be explained in the following sections.

A.1.1 Pattern tracking

The aim is to calculate the motion of a point from the initial image to the destination image.

A region around that point is considered. It consists in the ensemble of pixels that are contained within a square centered on the followed point. The intensity of the pixels at point $P(x, y)$ is $I_0(E(x), E(y))$ for the initial image and $I_1(E(x), E(y))$ for the final image with $E(x)$ being the integer part of x . A maximal displacement d_{max} is set, limiting thus the number of admissible displacement. This value has to be at least equal to the maximum local displacement from an image to the following, nevertheless a too large value is highly time consuming and can lead to instability due to the increase of probability to encounter another area of the image very similar. The maximum of a normalized scalar product of pattern intensities (Equation A.1) is search within all the admissible translation vectors $U_{ad} = \{(u_{ad}, v_{ad})\}$. The real displacement (u, v) is given by this maximum (Equation A.2).

$$Correlation(u^*, v^*) = \frac{\int \int_{Pattern} I_0(x, y) I_1(x + u^*, y + v^*)}{\int \int_{Pattern} I_0(x, y) \int \int_{Pattern} I_1(x + u^*, y + v^*)} \quad (A.1)$$

$$Correlation(u, v) = \max_{(u^*, v^*) \in U_{ad}} Correlation(u^*, v^*) \quad (A.2)$$

This normalized scalar product have two important advantages over an intensity difference method. First it is insensitive to a variation of a local (nor global) mean gray value. Then it gives a correlation value which ranges between 0 (no correlation) and 1 (perfect correlation) and thus returns an indicator of the quality of the correlation. In case of low value of correlation, an other tracking may be performed by enlarging the size of the pattern for example. Figure A.1 shows an example of the tracking of a pattern between two images.

The obtained displacement is an integer value of pixel size. To reach a subpixel resolution, the region of interest is scaled by interpolation. Then the same procedure than previously is applied. A scale factor of 8 is commonly used. The precision can therefore rise up to 1/8 of pixel.

A.1.2 Selection of points to follow

Within the region of interest a certain number of points is decided to be followed. The choice of these points is not random, nor based on a regular grid. Such definition of points to follow would lead to large errors because the pattern would often contain no sufficient texture to ensure a good tracking. This selection is therefore realized by the method of detection of corners of Harris. It relies on the gradients

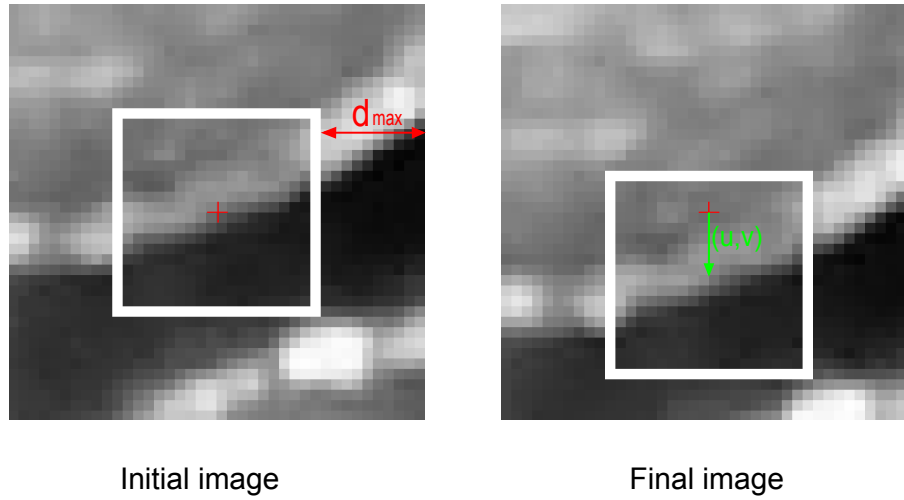


Figure A.1: Motion of a pattern between two images.

of intensity. Selected points are the centers of patterns where the minimum eigenvalue of gradient mean are maximal (A.3).

$$Selectedpoint = \max_{M \in R.O.I.} \min eigenvalue \left(\begin{bmatrix} \sum_{Pattern} I_{,x} I_{,x} & \sum_{Pattern} I_{,x} I_{,y} \\ \sum_{Pattern} I_{,y} I_{,x} & \sum_{Pattern} I_{,y} I_{,y} \end{bmatrix} \right) \quad (A.3)$$

The points are selected by decreasing value of the lowest eigenvalue with the constrain not to be too close from an already selected point in order to avoid an over concentration of points in an area that necessary induce an under concentration in some areas of the image.

A.1.3 Interpolation of fields

Because the tracked points repartition is not regular, an interpolation of the fields are realized at the nodes of a initially regular grid. The interpolation method is based on center of mass weighted by the invert of distance to the considered point. The only points taken in account are those located in the neighborhood of the interpolation position. The interpolation is realized in the deformed configuration. Once the displacement fields known at the nodes of the grid, strain fields are calculated for each element. The size of the initial grid have a great influence on the localization events that can be observed. A too large grid will homogenize the fields, while a too fine mesh may give unrealistic strain because the description of the strain by a field does not become relevant at that scale. Furthermore the finest is the mesh the largest is the number of points to be tracked.

A.2 Tensile tests

The investigation of the tensile behavior of the foams was realized with the same approach than in compression. Two sample size were used in order to quantify a size effect and to evaluate the size of a Representative Volume Element (R.V.E.). Nevertheless the completion of such tests was much more problematic than for compression. The main problem has been to find a way to ensure homogeneous

tensile stress within a determined volume. Direct use of glue (araldite, epoxy...) was success less. Tensile test on dog bones clean samples led to the failure of one of the T-branches. Infiltration of the T-branches by epoxy resin induced stress concentrations at the boundary of strengthened volumes. A combination of techniques was finally found to be convenient. Dog bone samples with double fillet were cut by wire electro erosion. Then the T-branches were reinforced by stacking of small steel plates with araldite glue. T-branches were finally impregnated by epoxy resin. The large distance between the T-branches and the working volume ensure that the sample would not fail due to stress concentrations induced by the strengthening. The working volume chosen were the same than in compression : cubic volumes of respectively 10 mm and 20 mm side size. Figure A.2 shows two samples after the strengthening procedure. A pair of adjustable tensile chucks was used for all the samples. To obtain the strain field within the sample, a digital image correlation technique was developed. The tensile machine and an high resolution camera were synchronized. Pictures of the sample in RAW format with a 3900×2800 resolution were obtained for each machine load value. The post treatment of the pictures with the correlation technique detailed in A.1 gave access to the strain field on the surface of the sample. Since during a long period of the tensile tests the strain field was homogeneous, it is assumed that the surface field transcript the volumic field within the material. The weak transverse strain gives even more weight to this assumption.

A.3 Bending tests

Bending tests were performed on a home designed system. The set of requirements for the system was the following. First it should allow loading in 3-points and 4-points bending tests and it should permit to vary the inner and outer span. In 3-point bending the outer span can be varied from 52 mm to 300 mm. In 4-point bending, the maximum outer span is of 300 mm, minimum inner span is of 50 mm and the minimum difference between outer and inner span is of slightly more than 50 mm. It can be noticed that in 4-points bending configuration, the inner span is given a degree of freedom in rotation in the bending moment direction in order to get an equilibrium of the forces on the rollers. Furthermore

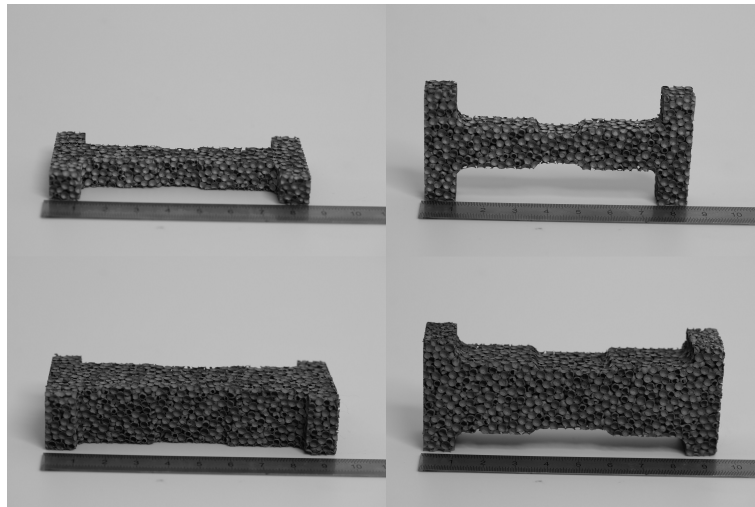


Figure A.2: *Tensile samples after strengthening procedure. Samples have respectively a side size cubic working volume of 10mm for the top one and 20 mm for the bottom one.*

the boundaries conditions have also to be variable. Thus one can perform test on clamped beams or on simply supported beams with variable roller diameter. Within all the tests performed for this Ph.D. the structures were loaded with simply supported boundaries conditions and the rollers diameter was of 19 mm.

The system was used on a ADAMEL DY35 traditional compressive-tensile machine. Outer rollers were unmovable. The load was measured thanks to a 20kN cell on the inner span part. Displacement was also recorded directly on the inner span part by the machine. Nevertheless the machine and of the system are thus in series with the tested samples. Several methods were used to get the real displacement of the inner span part. The simplest one was the measure of the stiffness of both the machine and the system thanks to a test on a beam with well known properties. The stiffness of the machine was around 0.1 mm/kN. Then the use of digital image correlation could also give the relative motion of rollers. Another displacement was recorded during the first 16 mm of deflection of the beam : the motion of the central point of the beam, thanks to a ± 10 mm RDP sensor. Figure A.3 gives an overview of the bending system in 3-points bending tests with clamped outer boundaries conditions and in 4-points bending with simply supported boundaries conditions.

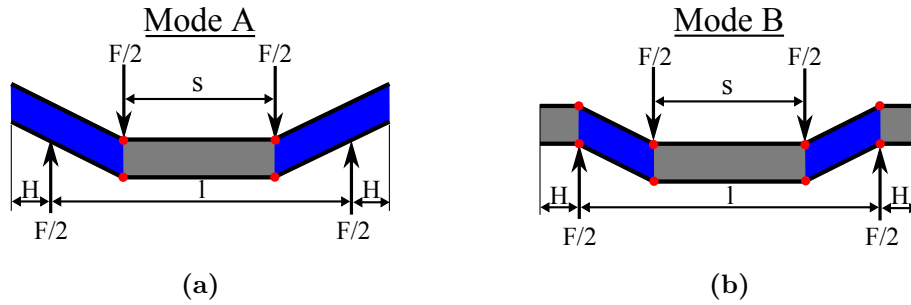


Figure A.3: Bending system. 3-points configuration with clamped outer boundaries (a) and 4-points configuration with simply supported boundaries conditions (b).

A digital camera of resolution 3888x2592 pixels was used to record the tests. The pictures could be synchronized with the machine records. Because the minimal sampling rate is of one picture every 5 seconds, when tests were performed at low speed and up to a small deflection, pictures were synchronized with the machine. But when the speed increased (and therefore the sampling rate had to be more important) or when the number of recorded points became too important (more than 400 points for a test), pictures were decorelated from the machine records. A manual synchronization is operated at initial state. In that latter case, pictures are rather used to follow strain fields in the core and faces shapes during the tests than to correct the displacement values of the rollers. Figure A.4 shows a typical qualitative result of digital image correlation on a part of a sandwich failing by core shear.

A.3.1 Properties quantification

The quantification of the properties of the beam structures are realised thanks to the following procedure.

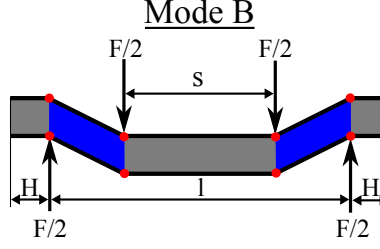


Figure A.4: .

A.3.1.1 Stiffness

First the stiffness is estimated from the load versus the RDP sensor curves during unloading sequences. In order to get the initial slope of unloading, but not to introduce too much error due to the loose tight of the machine, an arbitrary “length” of unloading has to be defined. Here we considers that the linear regression would be applied on the first 1000 N of each unloading sequence. Theses parts of sequences consists in a tenth of points, and the linear regressions quasi systematically presents a correlation factor r^2 superior to 0.95. One can notice that the unloading sequences at low deflection contains only a few points, their accuracy is low. Furthermore, at low deflection the parallelism between the bending system parts and the various faces of the beam has a great influence on the load response, contact might not be perfect at low deflection, thus the stiffness would be underestimated. An increase of the stiffness during the first steps of deflections is observed. From all the stiffness values, the stiffness of the beam can be either the maximal value for a deflection within the elastic domain (which will be defined later), either a mean value around the limit elastic deflection.

Care must also be taken to analytical model used for the stiffness. The well known value of Equation A.4 proposed by Allen [Allen, 1969] assumes the relative displacement of the outer and inner span to be the deflection.

$$\frac{1}{K} = \frac{\delta}{F} = \frac{(L-s)^2(L+2s)}{EI_{eq}} + \frac{(L-s)}{AG_{eq}} \quad (\text{A.4})$$

If on considers the deflection as the displacement of the point of symmetry of the neutral fiber, then the stiffness is the one predicted by Equation A.5.

$$\frac{1}{K} = \frac{\delta}{F} = \frac{(L-s)(L^2 + Ls - s^2/2)}{EI_{eq}} + \frac{(L-s)}{AG_{eq}} \quad (\text{A.5})$$

A.3.1.2 Remarkable loads

If the determination of the maximal load that can carry a structure is obvious and easy, since the tests are carried up to a decrease of the admissible load, the determination of the load that initiates the damaging is more sensitive to the procedure chosen. The non-linear behavior at low deflection forbid the determination of a loading modulus from the initial state. Thus two options are available. First one can extract the loading modulus within a range of load. The bounds has to be within the linear domain. Then a deviation to the linear law obtained gives the damaging load. This method gives values sensitives to the range chosen, but it is quite relevant to compare various structures tested with this method. The second option is to use the stiffness. When a damaging occurs, the stiffness necessarily

decreases. Nevertheless stiffness values are discrete and a their values shows an important dispersion.

Appendix B

Sensitivity of the mechanical behaviour of hollow spheres stacking to the strain rate and to the loading-unloading sequences

B.1 Strain rate sensitivity

The sensitivity of strain-stress response of hollow spheres stackings to the strain rate has been studied. Since the constitutive material (314 AISI) does not present sensibility to the strain rate at room temperature, it was expected that the hollow spheres stackings do so. Figure B.1 presents the stress-strain curves for samples enduring uni-axial compressive loading with varied strain rate. The strain rate $\dot{\epsilon}$ has

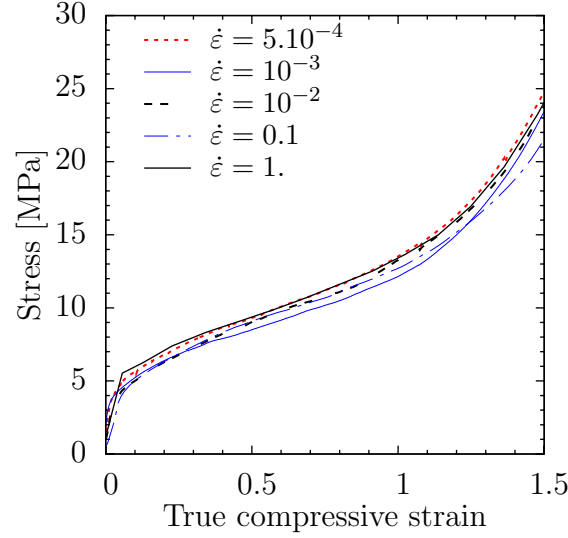


Figure B.1: Stress-strain responses of samples enduring uniaxial compressive loading with varied strain rate.

been varied from 5.10^{-4} up to 1. Samples were cubic with a side size of 15mm. The stackings had a density of about $600g/L$ (Plansee B). There is not significant variation of the response with the strain rate. Thus the material can be considered insensitive to the strain rate, at least up to a strain rate of 1, which corresponds to an impact at roughly $10mm/s$.

B.2 Unloading sequences sensitivity

The various loading-unloading sequences performed to measure the unloading modulus evolution with strain could have some influence on the mechanical response. Thus in order to quantify this influence, uni-axial compression tests have been carried out both with and without loading-unloading sequences. Figure B.2 presents the stress-strain curves for samples enduring uni-axial compressive loading with or without cycles. The strain rate $\dot{\epsilon}$ was of 10^{-2} . Samples were cubic with a side size of 15mm. The stackings had a density of about $400g/L$ (Plansee A). There is not significant variation of the response with the loading-unloading sequences. Thus this experimental method has no influence on the mechanical response, at least up to about 20 cycles.

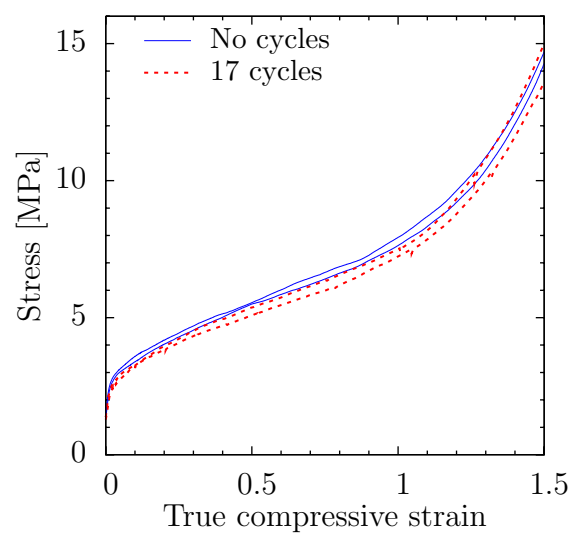


Figure B.2: *Stress-strain responses of samples enduring uniaxial compressive loading with or without loading-unloading sequences.*

Appendix C

Discrete Element Method

C.1 Discrete Element Method

C.1.1 Methodology of elaboration of hollow spheres stacking

The generation of a virtual sample occurs in several steps linked to the real elaboration procedure. First of all, a gas of particles is created. This gas, results in multiple random drawings of potential location into a box. If the location allows the sphere to be put in the box without any contact with other sphere or boundary, it is added to the gas, else another draw is realized. The gas is assumed to be generated when its packing density reaches the one desired. A standard compacity that can be obtain within a few computation time is around 30%.

The second step consists in a densification of the gas of particles by rearranging them. Particles are given an elastic behavior with high Young Modulus in order to remains quasi undeformable. Friction parameters are set to zero as are also cohesive parameters. The rearranging can be computed as periodic or as non-periodic independently in all directions. The periodicity and the isotropicity are used in relation with the process. A compacity of 50 % can easily be obtain is few hours of computing even for large sample of around 200000 particles, but every percent up to 64% is costly to get. As a consequence, an arrangement of particles of packing density of 60% will be used as initial stacking.

The third step consists in an compaction of the initial stacking that can be either isotropic, either periodic in some directions and non-periodic in others. In order to obtain plates, a non-periodic compaction in the transverse direction and periodic conditions in the in-plane directions have been chosen. This compaction is driven by the behavior of the particles that are considered as polystyrene foam balls. Actually during the elaboration process, the polystyrene foam balls are covered by the “powder slurry” and compacted, but the “powder slurry” does not induce any constrain nor geometrical modification. The particles behavior is therefore considered as elasto-plastic with linear hardening. Friction between particles is neglected, since [Fallet, 2008] shown the few influence it had on the stacking. Table C.1 sums numerical parameters of the polystyrene foam behavior. The processing compaction is led up to the packing density desired which is around 72% in the Plansee case. Then, if necessary, the sample

Density	Young Modulus	Poisson ratio	Compressive stress	Hardening Coefficient
$19kg/m^3$	$6MPa$	0.1	$0.09MPa$	$0.1MPa$

Table C.1: Material parameters of the polystyrene foam balls used during the compaction process.

is resized by cutting planes ; extra particles are removed. At that moment, compacity and location of particles centers are completely known. The sintering process of the “powder slurry” can occurs. Numerically, it is realized by creation of bonds between particles. The relative indentation offsets are registered and the mean contact radius is calculated. The initial structure is by that achieved.

Once the boundaries conditions (planes, spherical indent, periodic boundary conditions, free boundary conditions...) are set up, the sample is ready to be loaded. Figure C.1 gives an overview of the whole procedure of generation of the numerical stackings.

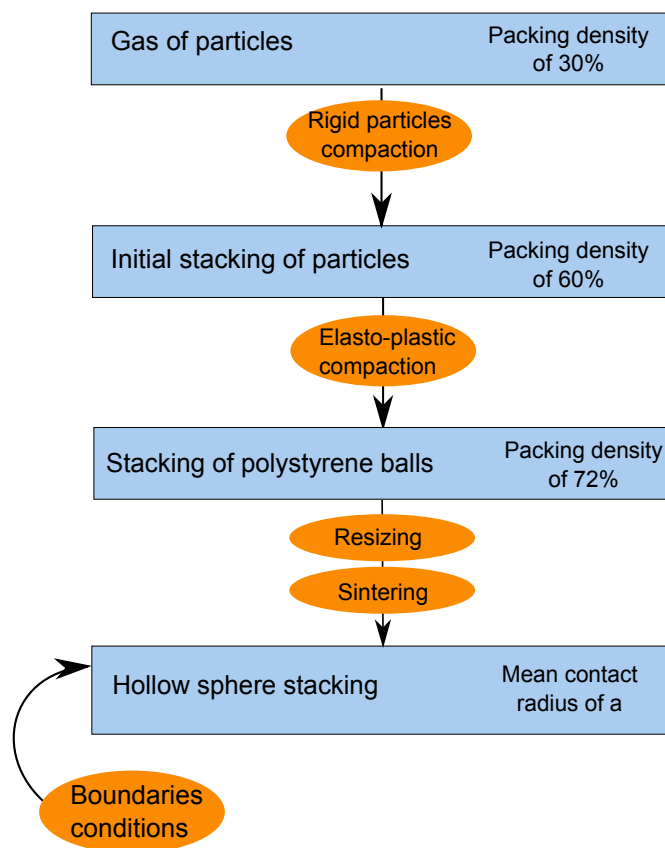


Figure C.1: Procedure of generation of a numerical hollow spheres stacking.

Appendix D

Sandwich structures with architected core

Study of thin sandwich beams with steel faces and perforated polymer core in bending loading : experiments and simulations

P. Lhuissier ^a, J.-P. Masse ^{a,b}, L. Salvo ^{a,*}, Y. Brechet ^a

^a*SIMAP - GPM2, INP Grenoble, CNRS, UJF. 101 rue de la physique BP46 38402 Saint Martin d'Heres, France.*

^b*ArcelorMittal Montataire, R&D Auto Applications. 1 route de Saint Leu 60761 Montataire, France.*

Abstract

The mechanical behaviour of thin sandwich beams with steel faces and porous polymer core have been investigated using *quasi* static four points bending. Classic sandwich models predicting the behaviour and the failure modes are improved to fit the particular configuration of the structure. Numerical simulations were set up in order to investigate damage at large strain. Macroscopic results are compared to analytical models and numerical simulations. Two numerical models of the core allowed confrontation of local behaviour with experiments. Criteria for localisation and damaging depending on core architecture are proposed.

Key words: Steel/polymer sandwich, Failure modes, Porous core, Large deformation behaviour

PACS:

1. Introduction

Reduction of mass and vibrations in car design suggest to use laminated structure such as the combination of polymer and steel in thin plates. However in order to allow classic shaping processes as bending, a more compressible material than massive polymer would be preferable. A possible strategy is to introduce porosity in the core : either a micro structuration as in foam, or a macro structuration of the core *via* drilling macroscopic holes. The last option is the topic of this paper. The scope is to study and predict the behaviour of such sandwich structures in critical use conditions, where the sandwich is carried up to failure in bending load-

ing. A range of sandwich structures with different perforated polymer cores were realised and tested in bending up to irreversible damage.

Allen [Allen1969] proposed a model to predict the elastic deflection of the sandwich structures during bending test. Ashby [Ashby2000], and Zenkert [Zenkert1997] developed analytical models able to predict the main failure modes, by means of an upper bound calculation of the competing collapses modes, and therefore the critical load, which is the load at initiation of irreversible damaging. These models, developed for sandwich structure with thick foam core, and comparatively thin faces, had to be modified considering on the one side materials and typical thicknesses of the structure, and on the other side experimental observations, as it has been done by Mohan [Mohan2005]. These enhanced models will be compared with our experimental results. The analytical approach allows to investigate the behaviour at small strain, with simple materials behaviour laws. Tagarielli [Tagarielli2004] took into

* Corresponding author. Tel: +33 4 76 82 63 79. Fax: +33 4 76 82 63 82

Email address: Luc.Salvo@simap.grenoble-inp.fr (L. Salvo).

URL: <http://www.gpm2.inpg.fr/perso/index.html> (L. Salvo).

account membrane stretching to predict the behaviour at large strain. If the governing phenomenon is different, it is not possible to access to the maximum load or total energy absorption at large deformation and with heterogeneous core. Therefore in a second step numerical simulations will be set up, and compared to experiments. Criteria of transition between failure modes are suggested.

2. Experimental procedures

In all the paper, all properties related to the core will be subscribed with a ‘c’ (E^c , $\sigma_{0.2\%}^c$) and thoses of the faces with a ‘f’.

2.1. Materials of face sheets

Steel of trade name DP780 (production of ArcelorMittal, France) was used as face sheets material. Provided as sheets of thickness of $0.67mm$, it was tested under uniaxial tensile test at low strain rates ($0.01s^{-1}$). The behavior can be accurately described by a Ludwik Law (Eq. 1).

$$R = R_0 + K(\epsilon_0 + \epsilon_p)^n \quad (1)$$

2.2. Core material and structure and sandwich beams elaboration

The core of the sandwich structures is made of non-reinforced polypropylene. It was tested in the same conditions than the face material. A Ludwik Law describes accurately this material. Table 1 gives the material parameters of the steel and the polymer used.

Perforated structures are obtained from massive polymer defined previously. The initial thickness $c_{initial}$ of the material is $1.4mm$. The perforation is made thanks to a square punch of length $q = 6mm$ (Figure 1). Four kinds of perforated structures with different spaces p between perforations are manufactured, $p = 2, 4, 6$ and $12mm$. The sandwich structures are fabricated by positioning the perforated core between two steel sheets whose dimensions are $300mm$ by $50mm$. The assembly is heated in a hot press at a temperature of $180^\circ C$. The steel/polymer adhesion is possible thanks to a special layer on the surface of the polymer. Steel

Table 1

Coefficients of Ludwik Law for the constitutive materials and extracted values for the face and core materials.

Parameter	Polymer DP780			
Young Modulus	E	350	210000	[MPa]
Poisson ratio	ν	0.4	0.3	[]
Strength coefficient	K	17.4	1369	[MPa]
Initial yield stress	R_0	0.	0.01	[MPa]
Strain offset	ϵ_0	$9.2e^{-5}$	$1e^{-4}$	[]
Strain hardening exponent	n	0.12	0.17	[]
Yield stress at 0.2%	$\sigma_{0.2\%}$	8	510	[MPa]
Maximal stress	σ_m	20	843	[MPa]

sheet with fixed thickness are placed between the plates to control the final thickness of the sandwich structure and pressure of the press is regulated at $3bars$. All the sandwiches manufactured have a total thickness of $2.7mm$, and a final core thickness of $c_{final} = 1.3mm$. The edges of the sandwich are rectified in order to obtain the aimed dimension. The net porosity of the core can be calculated taking account of the reduction of thickness during the manufacturing process (Eq. 2) or of the weight of the sample.

$$porosity = \frac{q^2}{(p + q)^2} \cdot \frac{c_{final}}{c_{initial}} \quad (2)$$

2.3. Four points bending experiments

Four-points bending tests were carried out on the sandwich structures. Rollers consisted in stainless steel cylinders of radius $10mm$. The distances were of $210mm$ and $70mm$ between outer and inner rollers respectively, while the total length of the sandwich beams was of $300mm$ for a width of $50mm$. The configuration of the four-points bending test is described in Figure 2. An ADAMEL DY35 with a $20kN$ force sensor was used to carry the tests on. A tesla sensor measured the central deflection of the beam during the first $10mm$ of deflection. A $1024 * 796$ pixels camera registred the part of the sandwich between the outer rollers every second.

Each sandwich geometry was tested on two samples using a deflection rate of $0.1mm/s$. Several loading and unloading sequences were applied to the beam over the first $10mm$ of deflection.

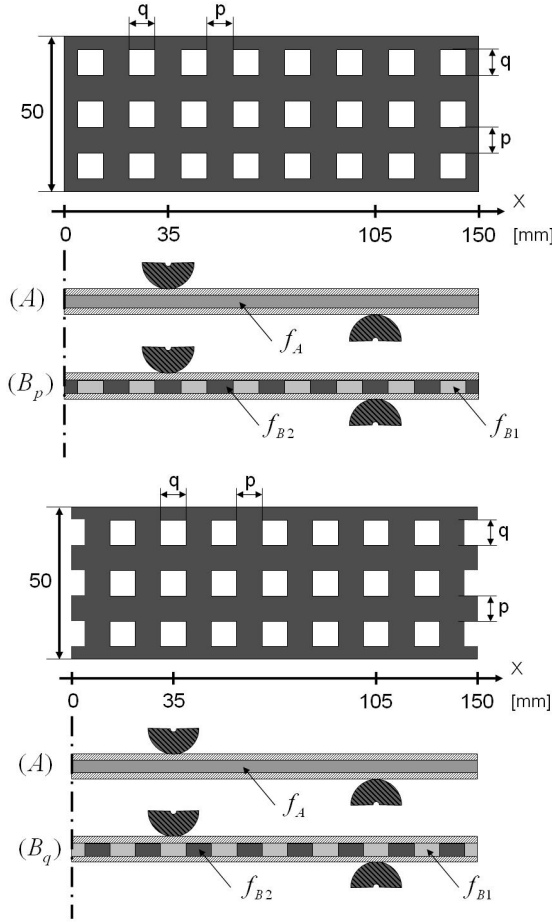


Fig. 1. The two models for the core: (A) Homogeneous core : porosity is $f_A = q^2 / (p + q)^2$; (B) Heterogeneous core : porosities are $f_{B1} = 0$ and $f_{B2} = q / (p + q)$

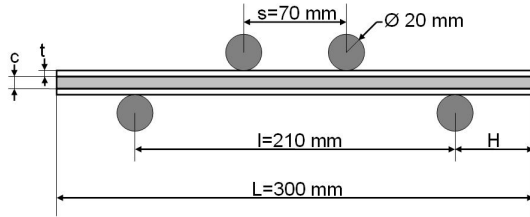


Fig. 2. Configuration of the four-points bending.

2.4. Simulation framework

Finite element simulations were performed using the code ZeBuLoN [ZeBuLoN]. The frame is half of a two dimensions sandwich structure with conditions of symmetry. Rollers are meshed too and they were given the behaviour of a standard stainless steel. In order to perform a simple 2D analysis, a model for the ‘effective core behaviour’ is required. Two models for the core were tested. In the first one (A), the

Table 2

Porosities of core for the different models

Real core		Homogeneous core A	Heterogeneous core B	
q	p	f_A	f_{B1}	f_{B2}
6	2	0.56	0.75	0
6	4	0.36	0.60	0
6	6	0.25	0.50	0
6	9	0.16	0.40	0
6	12	0.11	0.33	0
0	∞	0	0	0

core is considered as an homogeneous medium with properties proportional to the polymer *ratio* in the core. The second one (B) consists in a two phases material, a dense phase of massive polymer, and a equivalent porous one. Figure 1 describes the two configurations and Table 2 references the parameters of porosity of the two models for the different cores simulated and tested.

In model A, only the spacing between rollers matters. By contrast, in model B, the location of the holes alignments in regards to the rollers position can have a great importance. In order to avoid a singular behaviour due to a particular configuration, several configurations have to be simulated. The core should only be cut in the middle of a plot or in the middle of a hole, because of the symmetry of the simulation. So, for sandwich structures with an heterogeneous core, two core configurations were simulated for every geometric parameter. For homogenized core, only one simulation is necessary.

3. Results

3.1. Macroscopic elastic behaviour

The experimental results on the various sandwich structures are shown on Figure 3. Sandwich with spacing of 2mm between the holes in the core, presenting the largest porosity and the lowest contact surface between steel and polymer, failed by delamination. This local debonding between the core and the face translate macroscopically in a sudden softening of the structure. For the other sandwich structures, the influence of the core porosity on the load-deflection curve is less spectacular.

The same methodology was applied to analyse data in real experiments and in numerical simulations. The global behaviour of the structure is com-

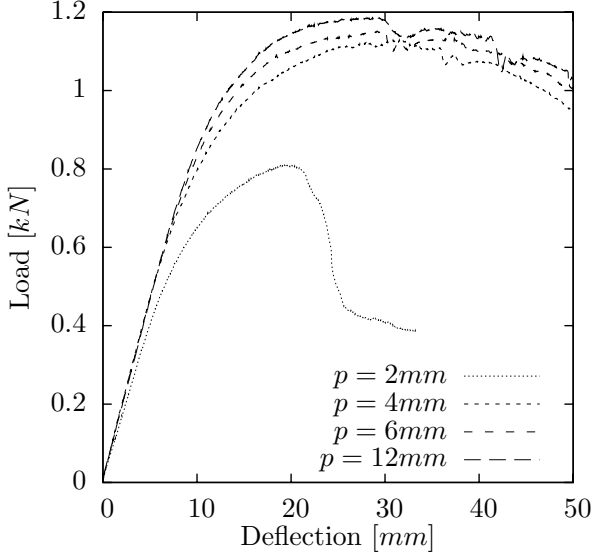


Fig. 3. Response of experiments to bending loading

pared between simulations and real experiments in terms of stiffness, critical load and ultimate load.

An analytical model has been developed by Allen [Allen1969] to determine the stiffness of a sandwich with an homogeneous core, :

$$\delta = \frac{F(l-s)^2(l+2s)}{48(EI)_{eq}} + \frac{F(l-s)}{4(AG)_{eq}} \quad (3)$$

where the equivalent flexural rigidity $(EI)_{eq}$ is

$$(EI)_{eq} = \frac{E^f b t d^2}{2} + \frac{E^f b t^3}{6} + \frac{E^c b c^3}{12} \quad (4)$$

and the equivalent shear rigidity $(AG)_{eq}$ is

$$(AG)_{eq} = \frac{b d^2 G^c}{c} \quad (5)$$

A good correlation is found between this analytical model and the experiments results concerning the loading stiffness, assuming for the core properties the polymer properties weighted by $(1-f)$. Both numerical models, accounting or not for the core architecture, allows to obtain stiffness in agreement with experiments (Figure 4).

3.2. Macroscopic failure load

Four failure modes can occur : face wrinkling, face yield, core shear and indentation. For the critical load and collapse mechanisms, preliminary studies based on models developed by Ashby [Ashby2000] show that only face yield and core shear must be

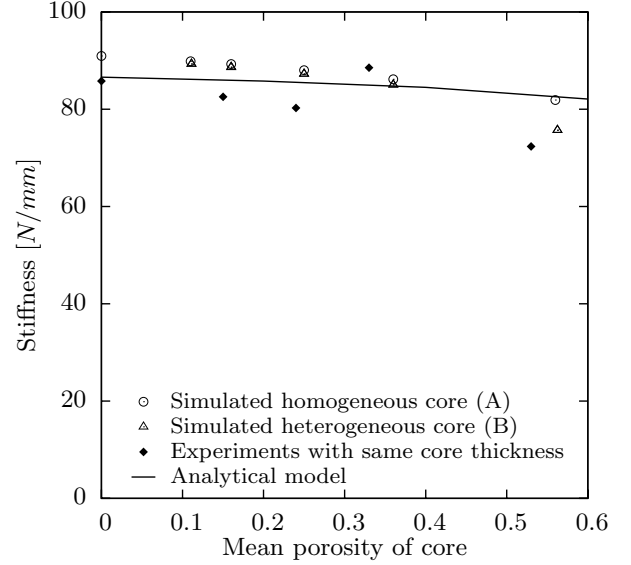


Fig. 4. Comparison of stiffnesses.

considered. The original model considered thin faces and a foam core. For face yield, it assumes that the plastic collapse occurs when the stress into the face sheets reaches the yield strength ($\sigma_{0.2\%}^f$) while the core yields simultaneously at a stress level of $\sigma_{0.2\%}^c$. In our case, post processing of the numerical simulations shows that when the stress into the face reaches $\sigma_{0.2\%}^f$ the stress in the core layer is far from $\sigma_{0.2\%}^c$. The analytical formula for face yield for an homogeneous core is :

$$(F)_{FY} = \frac{4(EI)_{eq}}{(l-s)(c/2+t)E^f} \sigma_{0.2\%}^f \quad (6)$$

The original model for core shear considers two different modes depending on the details of plastic flow in the core. For both mode, shear yield of the core is considered. Mode (I) assumes plastic hinge formation at the inner supports, and mode (II) considers plastic hinge formation both at the inner and outer supports. For our materials and typical dimensions, experiments observations and numerical simulations enable to prove that there is no plastics hinges formation when the core is yielding. The most frequently observed mode is the mode II. The expression of the critical load for this collapse mode is :

$$(F)_{CSB} = 2bc\tau_y^c \quad (7)$$

The graph (Figure 5) presents experimental and numerical simulations results compared with the analytical model. Low porosity of the core induces a

face yield failure of the sandwich. With increasing porosity, the sandwich weakest point becomes the core and the sandwich fails by core shear.

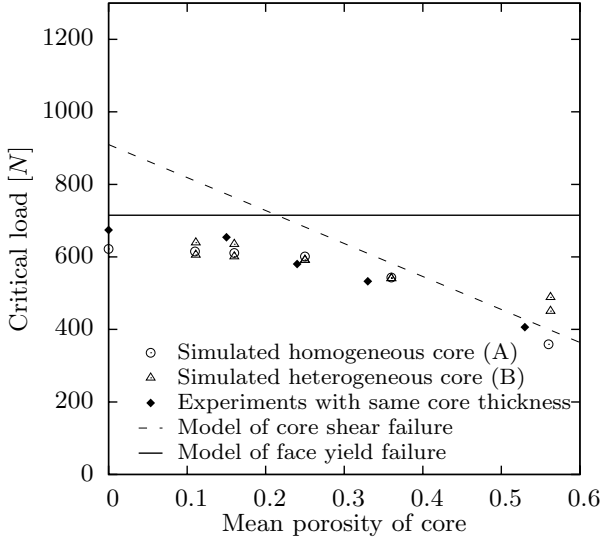


Fig. 5. Comparison of critical loads.

3.3. Macroscopic maximum load

It is not possible to develop analytical model for the maximum load with the same approach as the one used for critical load. However, we observed, numerically and experimentally, that the evolution of the maximal load with the porosity is identical to the one observed for critical load (Figure 6). Replacing $\sigma_{0.2\%}^f$ by $\frac{\sigma_{0.2\%}^f + \sigma_m^f}{2}$ in the face yield equation 6 allows to fit results. The maximal load can be expressed as :

$$(F)_{FY} = \frac{4(EI)_{eq}}{(l-s)(c/2+t)Ef} \frac{\sigma_{0.2\%}^f + \sigma_m^f}{2} \quad (8)$$

The simulations with homogenized cores (A) are also in agreement with experiments for the maximum load. The heterogeneous core modelisation (B) is very close to the homogeneous core simulation (A).

3.4. Local damage processes

A closer view on the experimented structures indicates the presence of waves on the upper face (Figure 7). Their periodicity is given by the length scale

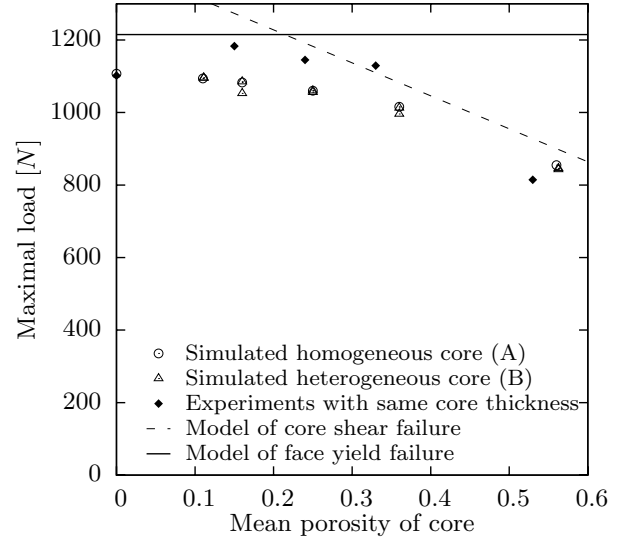


Fig. 6. Comparison of maximal loads.

of the core architecture. Numerical simulations al-

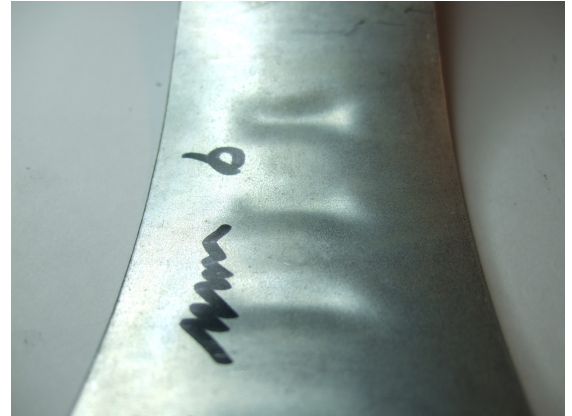


Fig. 7. Waves on the upper face of the sandwich structure ($p = 9mm$, $q = 6mm$) at a deflection of 40 mm.

low to plot the plastic strain on the upper line of the upper face at given deflection. Models are compared for $p = 3mm$ and $q = 3mm$ on Figure 8. It gives an insight into the heterogeneity of the plastic strain in the upper face and on the influence of the position of the holes in regards of the rollers at 15mm of deflection. The homogeneous core translate into : a constant plastic strain in the central part of the structure (submitted to *quasi* constant bending moment), a localisation of strain under the inner rollers, and a decrease of the plastic strain up to zero while leaving the inner rollers area. An heterogeneous core induces a oscillations of strain along

the length of the sandwich X , which phase depends on the holes positions in regards to the rollers.

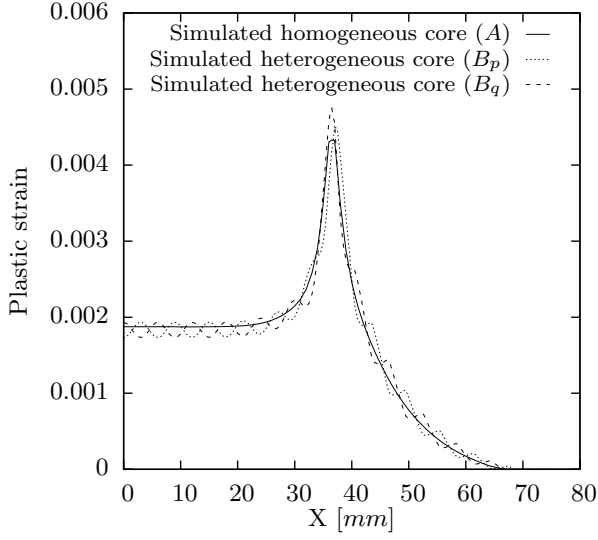


Fig. 8. Plastic strain of the upper face of the sandwich structure at 15mm of deflection ($p = 3mm$, $q = 3mm$).

Plastic strain on the upper face can be plotted as function of the imposed macroscopic deflection. Figure 9 shows the response of the heterogeneous model (B) for a sandwich core with $p = 6mm$ and $q = 6mm$. As expected, these oscillations increase in amplitude with deflection. The core architecture characteristic length is visible and can be directly compared to Figure 8, with the same average porosity of (0.25). The differences only come from the architecture.

One can also notice that the influence of the position of rollers can be important. A possible criterion for the waves is the amplitude of plastic strain in the central part of the structure not to close to rollers in order to avoid the indentation effect. Model (B) was used to plot the *iso* values of plastic strain amplitude as function of the imposed deflection and the hole spacing p deformation. Figure 10 indicates the deflection of initiation of waves on the upper face. The chosen limit is an minimal amplitude of 0.15% of plastic strain waves in the central 45mm of the beam.

The major difference between the two simulations for a spacing of 9mm comes from the localisation which occurs in one core configuration. It is due to a very particular configuration. It remains possible to conclude that waves never occur on sandwich with holes of core spaced by 2mm while the waves at low

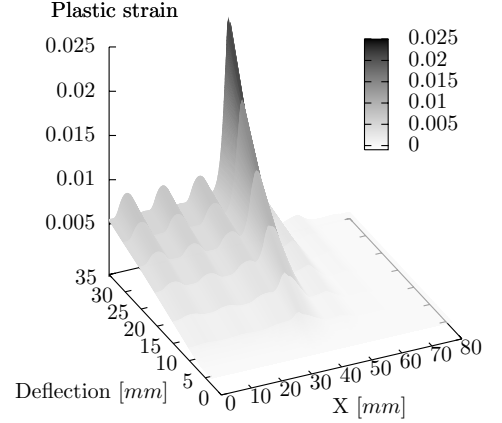


Fig. 9. Plastic strain on the upper face of the sandwich structure with deflection (Heterogeneous core model (B), $p = 6mm$, $q = 6mm$).

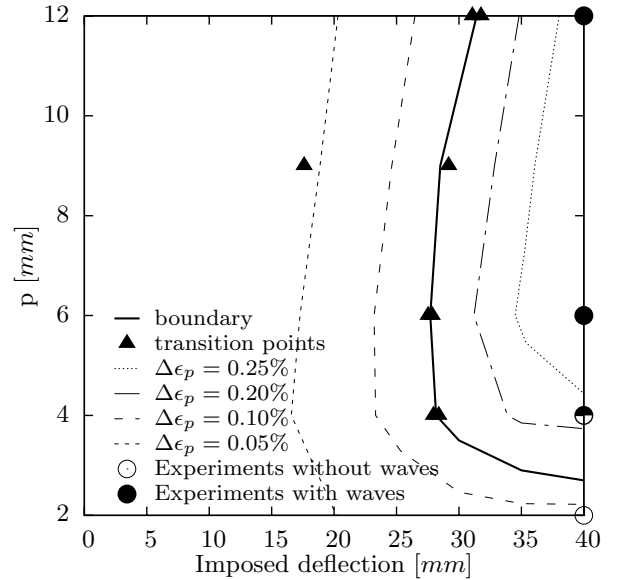


Fig. 10. Limits of initiation of waves with deflection for several threshold. Marks correspond to $\Delta\epsilon_p = 0.15\%$ for several core configurations and define the boundary

deflection are obtained for a spacing around 6mm. Qualitative *post-mortem* observations on the experiments are also reported on figure 10. Transition between waves configurations and smooth configurations is in accordance with numerical simulations.

Another important prediction is to know if localisation of strain occurs or if there is smooth variation in the curvature radius. The criterion is based

on the fact that localisation of strain induce a unloading of the central part of the structure and so a study of the maximal strain in the central part of the upper face is sufficient to predict localisation. Figure 11 indicates the deflection of localisation for several thresholds.

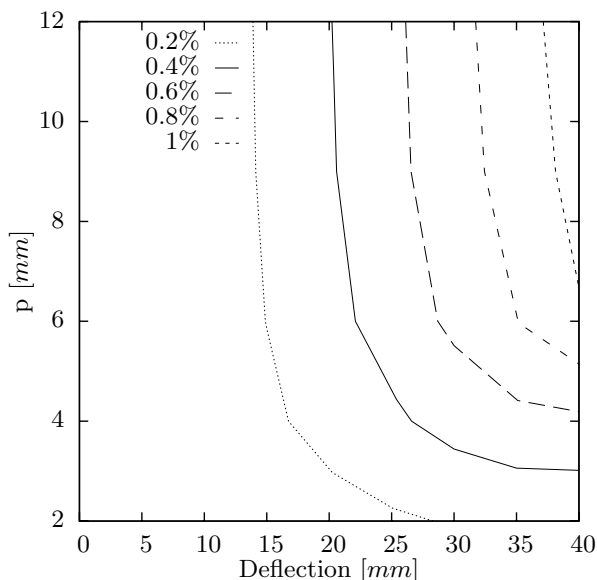


Fig. 11. Limits of initiation of localisation with deflection for several thresholds.

4. Conclusions

Both numerical models considered give very similar results and are in good agreement with experiments at a macroscopic scale for the elastic stiffness, the critical load and the maximum load. The simplest model for the core, corresponding to a mixture law, can be used to predict macroscopic results of the bending curve, while the second model taking into account the core architecture is able to predict local damage occurring during the bending test.

From a structural point of view, it can be conclude that the introduction of porosity in the core of the sandwich structure induces a negligible decrease of the loading stiffness while it leads to a large decrease of critical load and the maximal load. An increase of porosity induces a transition from the face yield to the core shear when porosity is up to 20%. This porosity allows to decrease the amount of polymer used and thus the cost. In stiffness limited design, it can be of interest. However requirement related to sheet aspect after shaping remain important and

the plastic inhomogeneities of the sheets as modeled here require further systematic investigations.

5. Acknowledgments

This work is sponsored by the french government and by ArcelorMittal, which also provided raw materials and manufacturing facilities in Montataire. Numerical simulations were realised thanks to Frederic Feyel and the code ZeBuLoN.

References

- [Allen1969] Allen, H. G., 1969, Analysis and Design of Structural Sandwich Panels, Pergamon Press, New York.
- [Ashby2000] Ashby, M.F. & Evans, A.G. & Fleck, N.A. & Gibson, L.J. & Hutchinson, J.W. & Wadley H.N.G., 2000, Metal Foams : A Design Guide, Butterworth Heinemann.
- [Gibson1984] Gibson, L. J., 1984, Optimization of stiffness in sandwich beams with rigid foam cores, Materials Science and Engineering, 67, 125-135.
- [Mohan2005] Mohan, K. & Hon, Y.T. & Idapalapati, S. & Seow, H.P., 2005, Failure of sandwich beams consisting of alumina face sheet and aluminum foam core in bending, Materials Science and Engineering: A, 409, 292-301.
- [Tagarielli2004] Tagarielli, V. L. & Fleck, N. A. & Deshpande, V. S., 2004, Collapse of clamped and simply supported composite sandwich beams in three-point bending, Composites Part B: Engineering, 35, 523-534.
- [Zenkert1997] Zenkert, D., 1997, The Handbook of Sandwich Construction, Engineering Materials Advisory Services Ltd, UK.
- [ZeBuLoN] Z set package. Available on www.nwnumerics.com.

Bibliography

- [Abrate, 1997] S. Abrate. Localized impact on sandwich structures with laminated facings. *Applied Mechanics Reviews*, 50:69, 1997.
- [Allaire *et al.*, 2007] G. Allaire, P. Destuynder, M. Salaün, and M. Schoenauer. *Conception optimale de structures*. Springer Verlag, 2007.
- [Allen, 1969] H.G. Allen. *Analysis and design of structural sandwich panels*. Pergamon, 1969.
- [Andrews and Moussa, 2009] E.W. Andrews and N.A. Moussa. Failure mode maps for composite sandwich panels subjected to air blast loading. *International Journal of Impact Engineering*, 36(3):418 – 425, 2009.
- [Andrews *et al.*, 1999] E. Andrews, W. Sanders, and L. J. Gibson. Compressive and tensile behaviour of aluminum foams. *Materials Science and Engineering A*, 270(2):113–124, September 1999.
- [Andrews *et al.*, 2001] E. W. Andrews, G. Gioux, P. Onck, and L. J. Gibson. Size effects in ductile cellular solids. part ii: experimental results. *International Journal of Mechanical Sciences*, 43(3):701–713, December 2001.
- [Ashby *et al.*, 2000] M.F. Ashby, A.G. Evans, N.A. Fleck, L.J. Gibson, J.W. Hutchinson, and H.N.G. Wadley. *Metal Foams: A design guide*. Butterworth–Heinemann, 2000.
- [Ashby *et al.*, 2002] Michael F. Ashby, Anthony Evans, Norman A. Fleck, Lorna J. Gibson, John W. Hutchinson, and Hayden N. G. Wadley. Metal foams: a design guide: Butterworth-heinemann, oxford, uk, isbn 0-7506-7219-6, published 2000, hardback, 251 pp. *Materials & Design*, 23(1):119–119, February 2002.
- [Augustin and Hungerbach, 2009] Christian Augustin and Wolfgang Hungerbach. Production of hollow spheres (hs) and hollow sphere structures (hss). *Materials Letters*, 63(13-14):1109 – 1112, 2009.
- [Badiche *et al.*, 2000] X. Badiche, S. Forest, T. Guibert, Y. Bienvenu, J. D. Bartout, P. Ienny, M. Croset, and H. Bernet. Mechanical properties and non-homogeneous deformation of open-cell nickel foams: application of the mechanics of cellular solids and of porous materials. *Materials Science and Engineering A*, 289(1-2):276–288, September 2000.
- [Blottière *et al.*, 1985] Yves Blottière, Bonino Jean-Pierre, Abel Rousset, Claude Rossignol, and Isabelle Gossart. Procédé de fabrication de corps creux, fermes et continus, corps creux obtenus et installation de mise en oeuvre dans le cas de billes creuses. Technical report, Brevet Français 2.585.373, 1985.
- [Blottière *et al.*, 1993] Yves Blottière, Philippe Chapuis, and Mireille Valaud. Method for the manufacture of hollow spherules of synthetic materials. Technical report, U.S Patent 5.205.976, 1993.
- [Caty *et al.*, 2008] O. Caty, E. Maire, S. Youssef, and R. Bouchet. Modeling the properties of closed-cell cellular materials from tomography images using finite shell elements. *Acta Materialia*, 56(19):5524 – 5534, 2008.
- [Cundall and Strack, 1979] PA Cundall and ODL Strack. A discrete numerical model for granular assemblies, 1979.
- [Deshpande and Fleck, 2000] V. S. Deshpande and N. A. Fleck. Isotropic constitutive models for metallic foams. *Journal of the Mechanics and Physics of Solids*, 48(6-7):1253–1283, June 2000.

- [Dillard *et al.*, 2005] T. Dillard, F. Nguyen, E. Maire, L. Salvo, S. Forest, Y. Bienvenu, J.D. Bartout, M. Croset, R. Dendievel, and P. Cloetens. 3D quantitative image analysis of open-cell nickel foams under tension and compression loading using X-ray microtomography. *Philosophical Magazine*, 85(19):2147–2175, 2005.
- [Dillard *et al.*, 2006] T. Dillard, S. Forest, and P. Ienny. Micromorphic continuum modelling of the deformation and fracture behaviour of nickel foams. *European Journal of Mechanics - A/Solids*, 25(3):526–549, 2006.
- [Donev *et al.*, 2004] A. Donev, I. Cisse, D. Sachs, E.A. Variano, F.H. Stillinger, R. Connelly, S. Torquato, and PM Chaikin. Improving the density of jammed disordered packings using ellipsoids. *Science*, 303(5660):990, 2004.
- [Fallet *et al.*, 2008] A. Fallet, P. Lhuissier, L. Salvo, and Y. Brechet. Mechanical behaviour of metallic hollow spheres foam. *ADVANCED ENGINEERING MATERIALS*, 10(9), 2008.
- [Fallet, 2008] Alexandre Fallet. *Structure et propriétés mécaniques d’empilements aléatoires de sphères creuses : caractérisation et modélisation*. Thèse de doctorat, Institut Polytechnique de Grenoble, 2008.
- [Fatt and Park, 2001] Michelle S. Hoo Fatt and Kyong S. Park. Dynamic models for low-velocity impact damage of composite sandwich panels - part a: Deformation. *Composite Structures*, 52(3-4):335 – 351, 2001.
- [Friedl *et al.*, 2008] O. Friedl, C. Motz, H. Peterlik, S. Puchegger, N. Reger, and R. Pippan. Experimental Investigation of Mechanical Properties of Metallic Hollow Sphere Structures. *Metallurgical and Materials Transactions B*, 39(1):135–146, 2008.
- [Gasser *et al.*, 2003] S. Gasser, F. Paun, A. Cayzele, and Y. Brechet. Uniaxial tensile elastic properties of a regular stacking of brazed hollow spheres. *Scripta Materialia*, 48(12):1617–1623, June 2003.
- [Hanssen *et al.*, 2002] A. G. Hanssen, L. Enstock, and M. Langseth. Close-range blast loading of aluminium foam panels. *International Journal of Impact Engineering*, 27(6):593–618, July 2002.
- [Kanit *et al.*, 2003] T. Kanit, S. Forest, I. Galliet, V. Mounoury, and D. Jeulin. Determination of the size of the representative volume element for random composites: statistical and numerical approach. *International Journal of Solids and Structures*, 40(13-14):3647 – 3679, 2003.
- [Lee *et al.*, 2008] D. Lee, JR Barber, and MD Thouless. Indentation of an elastic half space with material properties varying with depth. *International Journal of Engineering Science*, 2008.
- [Lim *et al.*, 2002] T. J. Lim, B. Smith, and D. L. McDowell. Behavior of a random hollow sphere metal foam. *Acta Materialia*, 50(11):2867–2879, June 2002.
- [Mamoud, 2007] Fady Mamoud. *Modélisation de l’élasticité et du fluage des empilements gravitaires de sphères creuses métalliques brasées*. Thèse de doctorat, Institut National Polytechnique de Grenoble, 2007.
- [Marchi and Mortensen, 2001] C. San Marchi and A. Mortensen. Deformation of open-cell aluminum foam. *Acta Materialia*, 49(19):3959 – 3969, 2001.
- [Martin *et al.*, 2003] C. L. Martin, D. Bouvard, and S. Shima. Study of particle rearrangement during powder compaction by the discrete element method. *Journal of the Mechanics and Physics of Solids*, 51(4):667–693, April 2003.
- [McCormack *et al.*, 2001] T. M. McCormack, R. Miller, O. Kesler, and L. J. Gibson. Failure of sandwich beams with metallic foam cores. *International Journal of Solids and Structures*, 38(28-29):4901–4920, July 2001.
- [Miller, 2000] Ronald E. Miller. A continuum plasticity model for the constitutive and indentation behaviour of foamed metals. *International Journal of Mechanical Sciences*, 42(4):729–754, April 2000.
- [Motz and Pippan, 2001] C. Motz and R. Pippan. Deformation behaviour of closed-cell aluminium foams in tension. *Acta Materialia*, 49(13):2463–2470, August 2001.

-
- [Motz *et al.*, 2005] C. Motz, O. Friedl, and R. Pippan. Fatigue crack propagation in cellular metals. *International Journal of Fatigue*, 27(10-12):1571–1581, 2005.
- [Plansee,] Plansee. Metal hollow sphere structures – materials, technology, properties, applications. Technical report, PLANSEE, IFAM, Glatt.
- [Radford *et al.*, 2006] D.D. Radford, G.J. McShane, V.S. Deshpande, and N.A. Fleck. The response of clamped sandwich plates with metallic foam cores to simulated blast loading. *International Journal of Solids and Structures*, 43(7-8):2243–2259, April 2006.
- [Rasband and ImageJ,] WS Rasband and US ImageJ. National Institutes of Health. USA,(available from <http://rsb.info.nih.gov/ij/>, 2004).
- [Reddy, 1984] J.N. Reddy. A simple higher-order theory for laminated composite plates. *ASME, Transactions, Journal of Applied Mechanics*(ISSN 0021-8936), 51:745–752, 1984.
- [Sanders and Gibson, 2003a] W. S. Sanders and L. J. Gibson. Mechanics of bcc and fcc hollow-sphere foams. *Materials Science and Engineering A*, 352(1-2):150–161, July 2003.
- [Sanders and Gibson, 2003b] W. S. Sanders and L. J. Gibson. Mechanics of hollow sphere foams. *Materials Science and Engineering A*, 347(1-2):70–85, April 2003.
- [Shuaeib and Soden, 1997] F. M. Shuaeib and P. D. Soden. Indentation failure of composite sandwich beams. *Composites Science and Technology*, 57(9-10):1249–1259, 1997.
- [Simonsen and Lauridsen, 2000] Bo Cerup Simonsen and Lars Peder Lauridsen. Energy absorption and ductile failure in metal sheets under lateral indentation by a sphere. *International Journal of Impact Engineering*, 24(10):1017 – 1039, 2000.
- [Steeves and Fleck, 2004] Craig A. Steeves and Norman A. Fleck. Collapse mechanisms of sandwich beams with composite faces and a foam core, loaded in three-point bending. part ii: experimental investigation and numerical modelling. *International Journal of Mechanical Sciences*, 46(4):585–608, April 2004.
- [Steinhardt and Ronchetti, 1983] P.J. Steinhardt and M. Ronchetti. Bond-orientational order in liquids and glasses. *Physical Review B*, 28(2):784–805, 1983.
- [Stevanovic *et al.*, 2001] M. Stevanovic, M.M. Yovanovich, and J.R. Culham. Modeling contact between rigid sphere and elastic layer bonded to rigid substrate. *IEEE Transactions on Components and Packaging Technologies*, 24(2):207–212, 2001.
- [Tagarielli *et al.*, 2007] V.L. Tagarielli, V.S. Deshpande, and N.A. Fleck. The dynamic response of composite sandwich beams to transverse impact. *International Journal of Solids and Structures*, 44(7-8):2442 – 2457, 2007.
- [Timoshenko and Young, 1965] S. Timoshenko and D.H. Young. *Theory of structures*. McGraw-Hill New York, 1965.
- [Touratier, 1991] M. Touratier. An efficient standard plate theory. *International Journal of Engineering Science*, 29(8):901 – 916, 1991.
- [Truskett *et al.*, 1998] T.M. Truskett, S. Torquato, S. Sastry, P.G. Debenedetti, and F.H. Stillinger. Structural precursor to freezing in the hard-disk and hard-sphere systems. *Physical Review E*, 58(3):3083–3088, 1998.
- [Türk and Fatt, 1999] Mulla H. Türk and Michelle S. Hoo Fatt. Localized damage response of composite sandwich plates. *Composites Part B: Engineering*, 30(2):157 – 165, 1999.
- [Viggiani *et al.*, 2004] Gioacchino Viggiani, Nicolas Lenoir, Pierre Bésuelle, Marco Di Michiel, Stefania Marello, Jacques Desrues, and Mogens Kretschmer. X-ray microtomography for studying localized deformation in fine-grained geomaterials under triaxial compression. *Comptes Rendus Mecanique*, 332(10):819 – 826, 2004.

- [Yang and Sun, 1982] SH Yang and CT Sun. Indentation law for composite laminates. *Composite Materials: Testing and Design*, pages 425–49, 1982.
- [Zenkert and Fund, 1997] D. Zenkert and Nordic Industrial Fund. *The handbook of sandwich construction*. EMAS publishing, 1997.
- [Zenkert *et al.*, 2004] Dan Zenkert, Andrey Shipsha, and Karl Persson. Static indentation and unloading response of sandwich beams. *Composites Part B: Engineering*, 35(6-8):511–522, 2004.
- [ZéBuLoN,] ZéBuLoN. *ZéBuLoN*, www.nwnumerics.com

Résumé

L'objectif de cette thèse est de caractériser le comportement mécanique des empilements aléatoires de sphères creuses et de proposer des modèles afin de prédire le comportement de structures sandwich avec un tel coeur. La structure du matériau est caractérisée à plusieurs échelles par observation au microscope et par analyse d'images 3D de tomographie aux rayons X. Les lois de contacts entre deux sphères obtenues par Eléments Finis sont implémentées dans un code de Méthode des Eléments Discrets pour simuler des empilements aléatoires. Des essais macroscopiques, pour différentes épaisseurs de coques, sont réalisés tant en compression et traction uni-axiales qu'en compression multi-axiale. Par des essais in situ en tomographie aux rayons X le comportement macroscopique est relié aux mécanismes locaux de déformation. Des essais paramétriques sur des sandwichs sont réalisés aussi bien en flexion 4-points, qu'en indentation, et comparés aux modèles analytiques et numériques.

Mots-clés: Matériau cellulaire, Sphères creuses, Empilements aléatoires, Tomographie aux rayons X, Méthode des Eléments Discrets, Eléments Finis, Structures sandwich, Propriétés mécaniques, Essais mécaniques, Analyse d'image 3D.

Abstract

The aim of this PhD is to characterize the behaviour of random hollow spheres stackings and to propose models in order to predict the behaviour of sandwich structures with such a core. The material structure is characterized at various scales thanks to microscope observations and to 3D images analysis of X-ray tomography. Contact laws between two spheres are obtained by Finite Element and implemented in a Discret Element Method code to model random stackings. Macroscopic tests, with varied shell thickness, are performed for compressive and tensile uni-axial loading and for multi-axial compressive loading. Thanks to in situ X-ray tomograph tests, macroscopic behaviour is linked to local deformation mechanisms. Parametric tests on sandwich structures are performed for 4-points bending loading and for indentation loading, and they are compared to analytical and numerical models.

Keywords: Cellular material, Hollow spheres, Random stackings, X-ray tomography, Discret Element Method, Finite Element, Sandwich structures, Mechanical properties, mechanical tests, 3D image analysis.